Supersonic Gas-Jet Based Beam Profile Monitor

Massimiliano Putignano

Department of Physics

University of Liverpool

A thesis submitted for the degree of

PhilosophiæDoctor (PhD)

July 2012

1. Reviewer: Prof. Dr Paul Nolan

2. Reviewer: Dr Yürgen Pozimski

Day of the defense:

Signature from head of PhD committee:

To my wife Angela, who makes exceptional any ordinary day.

Acknowledgements

or just having a laugh, eaten everything from overcooked pasta to delicious delicacies, go-kart raced and shot paintballs and lasers, installed equipment at 5 in the morning, planned of sending baloons to space and learned a great many things. All this truly will never go forgotten.

Abstract

Ions and in particular antiprotons, stored and cooled at low energies in a storage ring or at rest in traps, are highly desirable for the investigation of a large number of basic questions on fundamental interactions, on the static structure of exotic antiprotonic atomic systems or of (radioactive) nuclei as well as on the time-dependent quantum dynamics of correlated systems. Such low energy, low intensity beams pose, however, new challenges on beam instrumentation, as they require least intrusive diagnostics operating at ultra-high vacuum pressures of the order of 10^{-11} mbar.

This work presents the design and commissioning of a novel transverse beam profile monitor that is based on a supersonic gas-jet screen for use under XHV conditions as well as at higher vacuum pressures in residual gas operating mode. The device has been optimized for operation in the Ultra-low energy Storage Ring (USR) at the future Facility for Low energy Antiproton and Ion Research (FLAIR) in Germany, but its flexible design also allows integration into other accelerator facilities.

In this work the phenomenon of gas expansion is studied both analytically and numerically, and a novel theory of gas expansion is formulated to yield the gas target density and dimension at all points in its travel, as well as the residual gas pressures and required pumping speeds in all vacuum chambers. Furthermore, the technical and particle optical design and assembly of a dedicated experimental stand for the optimization and commissioning of the profile monitor is presented and discussed in detail.

Finally, results from experimental tests are shown that successfully demonstrate the residual gas operation mode of the monitor, reporting a spatial resolution of about 65 μm and a current resolution of about 50 μA.

Contents

CONTENTS

List of Figures

List of Tables

LIST OF TABLES

1

Background

1.1 Overview

Low-energy physics and storage rings are recently attracting growing interest in the scientific community as tools for the study of quantum systems [1, 2]. Indeed, low projectiles energies in the keV range, corresponding to smaller projectile speeds and longer interaction times, make for stronger interactions, allowing experiments to probe regimes in which theoretical models generate predictions for differential cross sections appreciably different from each other: availability of experimental results in this region would thus allow discrimination between the different theories. One of many examples which can be drawn from literature is the theoretical prediction of full differential ionization cross sections at low energies for different projectiles, for which a wealth of different theories has been proposed, and attempts have been done to experimentally discriminate them [3–5].

The limitation met by experimentalists lies now in the need of recording larger statistics in order to reduce experimental uncertainty and discriminate between theories yielding similar results. Dedicated storage rings would prove very beneficial on this account, as the same stored particles could be used over and over, thus greatly increasing luminosity for the same rate of particle creation at the source. In addition, when it comes to antiprotons in particular, interest has been raised for low-energy antiprotons as a valuable tool to study correlated quantum dynamics of few-electron systems in the femtosecond time regime [6]. Moreover, a set of available experimental results for energies between 10 and 100 keV, produced by the ASACUSA collaboration

[7], shows disagreement with any of the theories, hence confirming the need for more detailed experimental documentation and theoretical understanding. An advanced antiproton storage ring and new detection technologies in combination will enable, for the first time, access to kinematically complete antiproton-induced rearrangement and fragmentation measurements.

1.1.1 Storage ring and experiment technology

The USR One such storage ring is the Ultra Low Energy Storage Ring (USR). The USR is part of the Facility for Low energy Antiproton and Ion Research (FLAIR), itself a part of the larger Facility for Antiproton and Ion Research (FAIR) which will be built at GSI, Darmstadt, in Germany.

Within FLAIR the deceleration of antiprotons supplied by the New Experimental Storage Ring (NESR) with the initial energy of 30 MeV is realized in two steps. First, the beam is cooled and slowed down to an energy of 300 keV in the Low energy Storage Ring (LSR), before being transferred into the USR, operating in the variable energy range from 300 down to 20 keV [8]. The storage ring will be operated at room temperature and at a vacuum pressure of 10^{-11} mbar. Such low vacuum pressure is needed to increase beam lifetime to about 10 s. Design and optimization work on the USR lattice has been ongoing since 2005, and resulted in the four-fold symmetry configuration shown in Fig. 1.1.

Reaction Microscope One feature of the USR is the inclusion of a dedicated in-ring experimental station aimed at the measurement of full differential cross sections. This will be a recoil ion spectrometer, developed at the Max Planck Institute for Nuclear Physics in Heidelberg, Germany, and otherwise known as a *Reaction Microscope* (ReMi) [9].

The ReMi is able to collect on two separate Position Sensitive Detectors (PSD) the differently charged products of fragmentation created by the reaction under study. These products are generally composed of relatively slow ions and faster electrons, which are extracted from the interaction region towards the PSDs by means of an electric field. The reaction itself takes place between the projectile ions and a neutral gas target, in the form of a supersonic gas-jet. Collimation of the supersonic gas jet
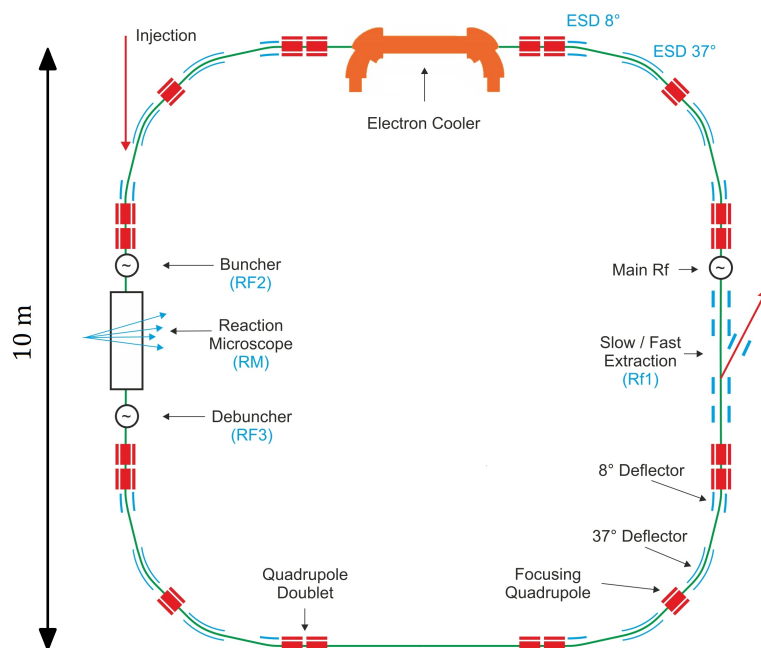
Figure 1.1: Schematic layout of the ultra low energy storage ring [2].

to submillimiter cross sections and focusing of the accelerated beam allow the absolute position where the reaction takes place to be precisely determined and controlled. Therefore, the displacement of the imaged fragment on the PSD with respect to the interaction position yields information on both the direction and the magnitude of the fragment momentum after the reaction. The resolution of the experiment is directly proportional to the inverse of the intensity of the electric extraction field [9], which directly affects the amount of drift of the ionization products before they reach the detector, and hence increases their displacement on the PSD. The electric field is thus kept relatively low, to values generally below 1 kV/m. The electric field is however not sufficient to capture the electrons, because of the much higher initial velocity due to the lower mass; therefore, a homogeneous magnetic field is superimposed to the electric field across the interaction region. The two fields together force the electrons on a helical pattern whose curvature radius is proportional to the magnetic field strength and the initial electron velocity.

Finally, in order to account for the component of velocity parallel to the extraction field, the time of flight needs to be measured as well. The initial trigger is synchronized with the accelerator higher harmonic system used to generate ns bunches [10] (hence

the need of short bunches), and the PSD signal is time monitored to provide the final trigger.

The use of both electric and magnetic field and the design described guarantees a nearly 4π steradian collection angle, and constitutes one of the main advantages of the ReMi over its predecessors. In a typical ReMi experimental setup in-vacuum electrodes are biased to provide a homogeneous electric field, whilst Helmholtz coils outside the vacuum chamber are used to create the magnetic field needed to guide the electrons.

The ReMi has already been used by different groups to investigate full differential cross sections of a number of interactions at medium to high projectile energies, thus constituting a reliable choice for the in-ring experimental station.

1.1.2 Beam diagnostic considerations

Development of low-energy storage rings such as the USR causes widespread beam diagnostic technologies to become obsolete. In particular, as far as transverse beam profile monitoring is concerned, preservation of the beam lifetime and emittance characteristics results in destructive and even perturbing profile monitoring (interceptive foils) to be ruled out [11], due to the stronger interaction resulting from low energy projectiles and the cumulative effects of perturbations in multi-pass machines such as storage rings. Furthermore, existing non-perturbing techniques such as residual gas monitors can take up to about 100 ms [12] to make meaningful measurements, due to the low residual gas density at the expected operating pressure of around 10^{-11} mbar.

A possible solution around these limitations is a neutral[1] supersonic gas jet target shaped into a thin screen and 2-dimensional imaging of the gas ions created by impact with the projectiles, in the same way imaging would be performed using an ordinary interceptive screen. Such monitor, as compared to those based on residual gas, allows injection of additional gas (in order to increase the ionization rate) together with efficient evacuation (to keep the required vacuum levels elsewhere in the storage ring), due to the high directionality of the supersonic jet [13]; furthermore, it allows simultaneous determination of both transverse profiles and imaging of the beam through a direct measurement of local density.

---

[1]i.e. composed of electrically neutral particles, as opposed to plasma or ions jets, used for different purposes in other disciplines

Solving the problem of non-interceptive transverse beam profile diagnostics with a supersonic gas jet based beam profile monitor opens a whole new range of interesting possibilities. First, the monitor is intrinsically very flexible, in that the interaction it relies upon, namely ionization, is well understood and usable with most projectile species. Furthermore, monitoring parameters such as acquisition rate and beam perturbation can be easily scaled by varying the target gas density, and tailored for the particular application. Therefore, the gas jet based beam profile monitor can be used in most accelerators across large energies, current and vacuum ranges, and is not restricted to the monitoring needs of low energy storage rings such as the USR. Secondly, the basic components of the beam profile monitor are very similar to the ones needed for a ReMi: a PSD for imaging of ions, an electric field based extraction system and a supersonic gas jet target. Therefore, the two pieces of equipment can be merged into one, resulting in increased compactness and decreased installation and maintenance cost. Moreover, merging the monitor with the ReMi also brings the additional benefit of being able to measure the transverse beam profile at the very point of interaction, without the need to extrapolate the information across the accelerator lattice. Together, the advantages and options discussed make for a development which goes well beyond the initial motivating scope, encompassing a number of different applications and areas of interest.

Other solutions are already currently available for non interceptive transverse profile monitoring; however, all of them present disadvantages when compared to the gas jet based monitor, mainly in their applicability to only a restricted list of projectile beam parameters and species, or vacuum environments; even though they still retain a number of advantages, mostly in decreased cost, complexity and installation space required. A full discussion about the main alternatives to the gas jet based monitor is presented in the next section, highlighting the different pros and contras of each solution.

1.2   State of the art in transverse profile monitoring

Several different techniques have been developed to achieve non interceptive transverse profile monitoring, based on different principles, ranging from optical properties to ionization and particle detection. However, most of these techniques rely on phenomena

which produce small signals that, even with several stages of amplification, are hardly detectable if the characteristics of the beam or vacuum pipe such as beam density and vacuum levels are not advantageous to their employment. A review of three of these non interceptive transverse profiling methods, namely residual gas, induced beam fluorescence and ion beam monitors are treated in the following. Of these, residual gas monitors in particular deserve a special mention in this work as they more closely resemble the working principle of the supersonic gas jet based beam profile monitor.

1.2.1 Residual gas monitors

Residual Gas Monitors (RGM) rely on the projectile beam ionizing the atoms of the residual gas present in the vacuum vessel, creating positive ions and electrons that can then be extracted to a suitable detector by an external electric field. A scheme of the working principle of a RGM is reported in Fig. 1.2.
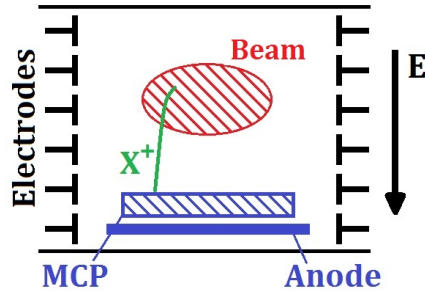
Figure 1.2: Working principle of a residual gas monitor.

The extracted ions or electrons are guided towards some kind of position sensitive detector, which can be either an array of cathode strips which directly collect the current or, should the signal be not sufficiently strong to be detected (low beam currents or low residual gas pressure), a pre-amplifier is used, usually in the form of a Micro Channel Plate (MCP) detector, see section 6.4.1.

This monitoring configuration yields a single transverse profile, given by the integration of the signal acquired in the direction parallel to the position sensitive detector: the information on the beam dimension perpendicular to the beam position monitor is lost. Therefore, usually two monitors in series, tilted by 90° with respect to each other, are used to acquire the two perpendicular profiles.

The main limitations of RGM come from residual gas pressure and beam space charge field. Residual gas pressure limits the count rate of the RGM, and vacuum pressures below 10^{-11} mbar can result in unacceptably high integration times needed to acquire a profile. A full calculation of the count rate expected from an ionization profile monitor is reported in section 1.3.1.

Space charge on the other hand results in an electric field radially distributed around the projectile beam, which is superimposed to the external extraction field, interfering with the trajectories of the extracted ions and distorting the acquired images.

For non relativistic velocities, the radial electrical field E_{sc} of a beam with transverse density Gaussian distributed with standard deviation σ is given by [14]:

$$E_{sc} = \frac{1}{2\pi\epsilon_0} \cdot \frac{qeN}{l} \cdot \frac{1}{r}(1 - e^{r^2/\sigma^2}) \tag{1.1}$$

where r is the radial distance from the beam and qeN/l the number of particle in the charge state q per unit length. Space charge effects prove very influential for high current beams in the hundreds of mA current region, [15, 16] and can lead to major image distortion (drift > 1 mm), even when strong extraction fields in excess of 80 kV/m are employed. However, for low current beams the effect scales linearly, so that for beams with less then 1 mA this is usually negligible.

1.2.2 Beam induced fluorescence monitor

A second effect of collisions between the projectiles and the residual gas molecules, apart from ionization, is fluorescence. Fluorescence results from the decay of the residual gas molecules internal energy level excited in the collision, and the wavelength of the emitted photons depend on the residual gas species. Of particular interest for beam diagnostics is the decay of N_2^+ ions, which shows transition bands in the optical region (blue to near UV: 390÷470 nm). The lifetime of this reaction is about 60 ns, depending on the actual energy levels interested. The ratio of energy lost from the projectile beam to energy emitted radiatively is about 100 [17]. This fluorescence effect, just like the ionization exploited in residual gas monitors, is proportional to the beam density distribution as well as to the residual gas pressure, and can be exploited to image the beam profile. Monitors based on this effect are known as Beam Induced Fluorescence monitors (BIF) [14].

The general working scheme of a BIF monitor is shown in Fig. 1.3.
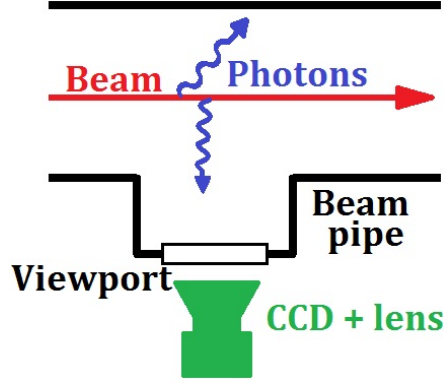
Figure 1.3: General working principle of a BIF monitor.

The parameters affecting the fluorescence signal R_γ, in collected photons per seconds, are given in the following relation [14]:

$$R_\gamma \propto \frac{dE}{dx}\Delta x \cdot P \cdot \frac{I_{beam}}{qe} \cdot \frac{\Omega}{4\pi} \cdot \frac{f}{h\nu} \qquad (1.2)$$

where $\frac{dE}{dx}\Delta x$ is the energy loss of the ions in the observation length Δx, P the residual gas pressure; Ω is the solid angle of observation and f is the fraction of energy converted to photons of energy $h\nu$. Equivalently to the case of RGM, the signal is proportional to the product of beam current and residual gas pressure, which limits potential applications.

An advantage of BIF monitors is that nothing has to be installed in the vacuum pipe and commercially available CCD data acquisition can be used. Similarly to RGM, BIF monitors only provide a 1-dimensional plot of the beam profile integrated on one axis, and two setups at 90° to each other are required for both transverse profiles.

The main limitation of BIF comes again from the reduced signal strength, resulting in both high integration times needed, and very high beam currents or vacuum pressures: residual gas pressures in excess of 10^{-5} mbar have been reported to be required at GSI, Darmstadt, Germany [18, 19], to image a 2.5 mA Ar^{10+} beam even with a double level of MCP pre-amplification.

A review and application examples on beam fluorescence monitors can be found in [14, 20–23].

1.2.3 Ion beam scanner

Another option for obtaining a transverse profile non interceptively is the use of a second ion beam (probe beam) travelling transversally to the projectile beam. The deflection of the probe beam will then be proportional to the charge density in the projectile beam: hence, by scanning the probe beam transversally across the projectile beam, a full transverse profile can be obtained. To measure the deflection, the probe beam is imaged directly on a phosphor screen mounted on the vacuum vessel, and the resulting image acquired by a CCD camera.

In order to avoid the need for scanning the probe beam across the jet, and thus obtain a faster measurement, an option is to use a thin extended ion screen oriented at 45° to the projectile beam. When no projectile beam is present, the projection of the probe beam on the phosphor screen will be a straight line angled at 45°; this pattern will be distorted as shown in Fig. 1.4 when affected by the projectile beam space charge.
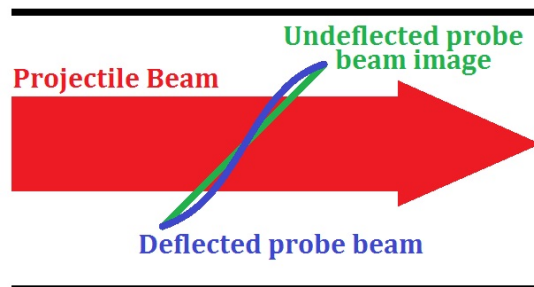
Figure 1.4: Working principle of an ion beam scanner used in the ion screen operation mode. The diagram assumes both beams have the same sign of charge, so that the probe beam is repelled by the projectile beam.

The main advantage with this monitoring configuration lies in the simplicity of the data acquisition system, which does not require any light amplification, the fact that no electric field has to be set up in the beam pipe to extract ionization products, and the independence from vacuum conditions (i.e. residual gas pressure or species). However, the crucial drawback is that in order to obtain a measurable displacement of the probe beam, the charge density of the projectile beam has to be very high, in the hundreds of mA region.

Application examples on ion beam scanners can be found in [24].

1.2.4 Supersonic gas jet based beam profile monitor

As it was mentioned in section 1.1.2, a supersonic gas jet based beam profile monitor overcomes the two main shortcomings of the techniques summarized: namely the need for high intensity beams or high residual gas pressures, while still granting least perturbative operation to both the projectile beam and the vacuum level. The supersonic nature of the jet makes it very directional and easily evacuated from the vacuum chamber. On top of these advantages, a single supersonic gas jet based monitor also provides a full 2-dimensional profile of the projectile beam, whilst all techniques listed require two devices, each of which only acquires a single 1-dimensional profile.

Moreover, the hardware similarities between the profile monitor and a ReMi are such that further design developments, planned to be undertaken after the completion of this project, would allow the two devices to be merged, so that the beam profile can be investigated at the very point of interaction with the experiment and beam line space and costs can be shared.

1.3 Working principle

The transverse beam profile monitor investigated in this work relies on a neutral gas jet, shaped into a thin screen, to cross the beam. In its simplest configuration, shown in Fig. 1.5, the gas screen flows perpendicularly to the projectiles' propagation axis, and the screen plane forms an angle of 45° with the same axis. When the projectile beam crosses the gas jet, ionization occurs and gas ions are created in the jet. These ions are accelerated by an extraction field towards an MCP and imaged via a phosphor screen and a CCD camera. The MCP, see section 6.4.1, is able to provide up to 10^6 amplification while retaining the position information needed for the phosphor screen PSD.

The magnitude of the extraction field is large enough to project the ions on the MCP, minimizing the drift due to the initial momentum acquired during the ionization collision. The details of the design will be discussed in chapter 6. To counterbalance the effects of the extraction field on the main beam, two correction fields of suitable intensity are added both upstream and downstream the detector position in the beamline. After having crossed the beam in the interaction chamber the gas-jet flows into the dumping chamber, where an appropriate vacuum system dumps the jet preventing
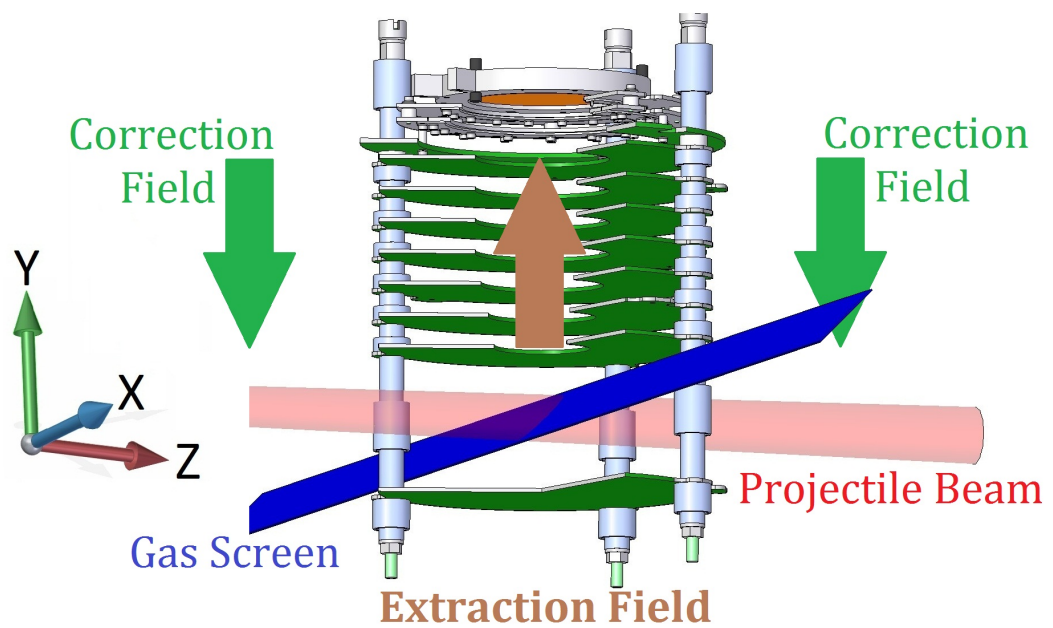
Figure 1.5: Illustration of the working principle of the supersonic gas jet based beam profile monitor. The projectile beam, shown in red, traveling along the z axis, crosses the gas jet screen, shown in blue, traveling along the x axis, directed out of the page, in the middle of the *interaction region*, where an electric field directed towards the detector, along the y axis, extracts the ionization products for profile imaging. A left handed reference system is used.

it from affecting the vacuum in the main accelerator vessel. This transverse profile measurement method allows 2-dimensional imaging of the transverse beam density distribution, hence providing the measured function $\rho(x, y)$. From $\rho(x, y)$, both transverse profiles $\rho_{tot}(x)$ and $\rho_{tot}(y)$ can be computed by direct integration of the measured densities:

$$\rho_{tot}(x) = \int_{-\infty}^{\infty} \rho(x, y)\, dy$$
$$\rho_{tot}(y) = \int_{-\infty}^{\infty} \rho(x, y)\, dx$$

(1.3)

1.3.1 Count rate estimation

The time needed to produce a full profile, i.e. the *acquisition time* of the beam profile monitor, is linked to both the number of events required for a profile and the reaction rate. This time strongly depends on the particular applications, and the features that need to be measured to characterize the investigated beam; However, for a typical application, information on the position and size of the beam will generally be the relevant observables. Assuming a Gaussian shaped beam, this information require the mean and standard deviation of the Gaussian profile to be evaluated.

Gaussian parameters estimation For a normal distribution classic inference analysis leads to the determination of confidence intervals for the sample mean $\bar{x}$ and standard deviation s to be close to the true population mean and standard deviation μ and σ as shown in eqn. (1.4)[25]:

$$\bar{x} - \frac{c\,s}{\sqrt{n}} \leq \mu \leq \bar{x} + \frac{c\,s}{\sqrt{n}}$$

$$Pr\left(-c < T < c\right) = 1 - \alpha$$

(1.4)

$$\sqrt{\frac{(n-1)\,s^2}{\chi^2(n-1),\,\alpha/2}} < \sigma < \sqrt{\frac{(n-1)\,s^2}{\chi^2(n-1),\,1-\alpha/2}}$$

where c is a percentile of the Student t distribution, with variable T, and α is the confidence level for the true mean and standard deviation to fall in the given boundaries. The equations in (1.4) can be rearranged to the more convenient form:

$$\frac{|\mu - \bar{x}|}{s} \leq \frac{c}{\sqrt{n}}$$

(1.5)

$$\sqrt{\frac{\chi^2(n-1),\,\alpha/2}{n-1}} < \frac{s}{\sigma} < \sqrt{\frac{\chi^2(n-1),\,1-\alpha/2}{n-1}}$$

(1.6)

The intervals in eqn. (1.5) and (1.6) only depend on the confidence level chosen and the number of ionization events recorded, rather than on the actual values of the investigated distributions, and can therefore be used to provide general guidelines for the number of ionization events needed to obtain a full profile. In particular, the precision in the measurement of the mean can be defined as the deviation from the mean normalized to the standard deviation, equal to the right hand side of eqn. (1.5), and for the standard deviation as half the difference between the two interval boundaries in eqn. (1.6). Fig. 1.6 shows a plot of the required number of ionization events to obtain a given precision, on the x axis, for different confidence intervals (curve parameter), both expressed in percentages. It is noted that the analysis presented above and leading to the plot in Fig. 1.6, is purely statistical in nature, and allows for the possibility of obtaining arbitrarily small precisions by recording a correspondingly large statistics. In fact, this is not possible in practice due to the effects of unforeseen systematic experimental errors, which would result in vertical asymptotes for the plot in Fig. 1.6, effectivily limiting the precision achieved.
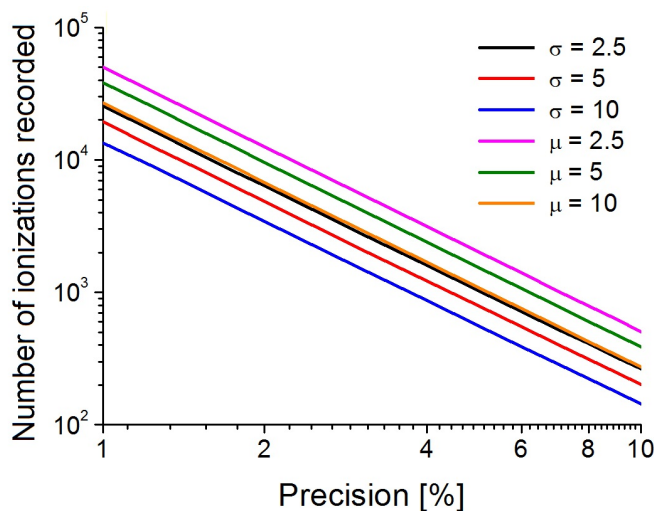
Figure 1.6: Required number of measurements to obtain a given precision (x axis) for different confidence intervals (curve parameter). The plot assumes no systematic experimental errors; in practice, these errors would show as vertical asymptotes on the plot and thus limit the minimum precision achievable, independently of the number of ionization events recorded.

Given the approximate linearity of the plots in Fig. 1.6, the relationship between number of ionization events n and precision p can be approximated with $n \approx hp^k$, with

h decreasing with increasing confidence interval and k (the gradient of the curves in Fig. 1.6) being approximately -1.975 for the standard deviation estimation and -1.995 for the mean. It can also be seen that at a given number of events the estimation of the profile standard deviation, i.e. the beam width, is always more precise than the measurement of the profile mean, i.e. the beam position. In the remainder of this work it will be assumed that for beam diagnostics purposes confidence intervals of 5% in beam position determination can be accepted, corresponding to about 1500 ionization events and 4% precision on the determination of beam profile width.

Ionization cross section Another factor relevant to the acquisition speed is the cross section for ionization interaction between the projectiles and the gas target at the given projectile energies. Cross sections for impact ionization of most gases can be found in literature. Given the wide applicability of the gas jet based beam profile monitor, the range of interesting projectiles and gas species is vast; in the following only a selection of these results, namely Helium, Argon and molecular Nitrogen ionization by slow protons, antiprotons and electrons is reported in Fig. 1.7 through 1.9 [5, 26–31].
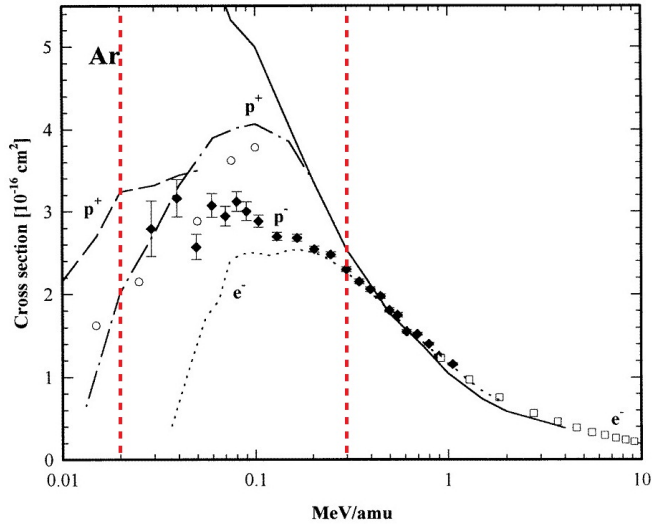
Figure 1.7: Cross section for single ionization of Argon atoms by protons (empty circles), antiprotons (black diamonds) and electrons (empty squares) impact [27]. The energy range of interest for the USR is indicated between dotted lines (20÷300 keV).

As expected, the cross-sections for ionization increase as the velocity of the projectile is decreased to the keV range, due to the longer time of interaction available, only to
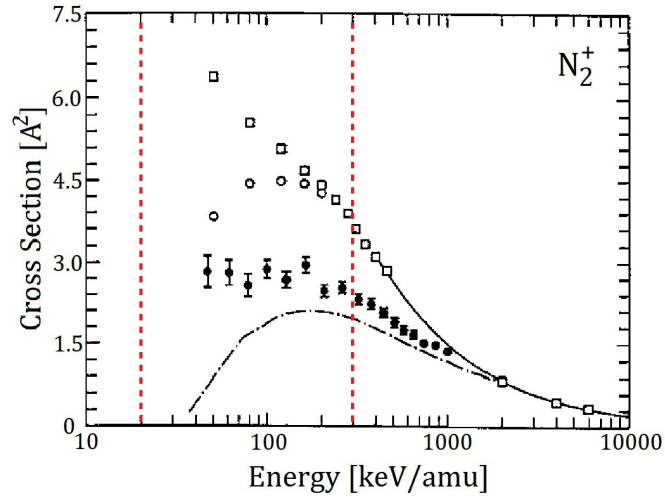
Figure 1.8: Cross section for single ionization of Nitrogen molecules by protons (empty squares), protons excluding electron capture (empty circles) and antiprotons (black circles) impact [5]. Units of cross section reported as used by the authors, in $\mathring{A}^2 = (m^{-10})^2 = cm^{-16}$. The energy range of interest for the USR is indicated between dotted lines $(20 \div 300$ keV).
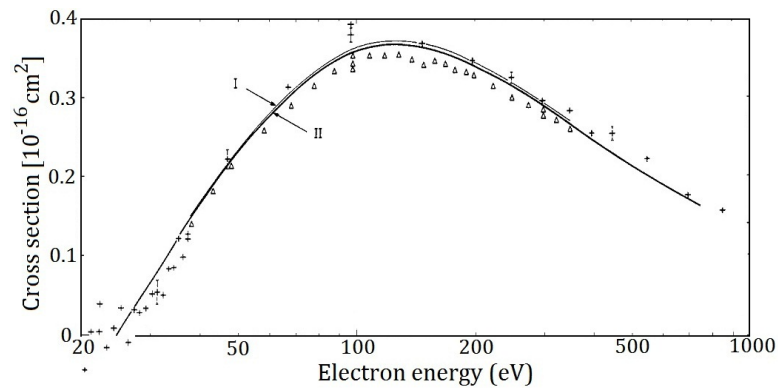
Figure 1.9: Cross section for single ionization of Helium atoms by electrons impact [30].

decrease again for negatively charged projectile after that as the electron cloud repulsion potential becomes comparable with the projectile energy. Analysis of data reported in Fig. 1.7 through 1.9 shows that the cross section for impact ionization of N_2 and Ar by any of the chosen projectiles (protons, antiprotons and electrons) is always in the same order of magnitude of $1 \div 5$ Å^2, whilst this value drops by about one order of magnitude in the case of impact ionization of He, due to its electron cloud being restricted to the 2s orbital, featuring both smaller size and, more important, higher ionization energy.

This data illustrates the flexibility of an ionization based beam profile monitor, in that different projectiles species have little if not negligible impact on the overall performance. In the following, the impact ionization cross section will be assumed to be 1 Å^2. However all results need to be scaled depending on the actual expected cross section for the particular application.

The probability P_{ion} of an incident projectile to ionize a gas atom can then be expressed as the product of the ionization projectile energy dependent cross section $\sigma\left(E_{proj}\right)$, the target gas number density ρ_{gas} and the target gas thickness d_{gas}:

$$P_{ion} \; = \; \sigma\left(E_{proj}\right) \; \rho_{gas} \; d_{gas} \tag{1.7}$$

For typical target thicknesses of about 0.5 mm and gas number densities of about $2.5 \cdot 10^{16}$ particles/m^3 (see Chp. 2 and 4), P_{ion} results in typical values of about $1.3 \cdot 10^{-7}$. This value much smaller than unity justifies the assumption underlying eqn. (1.7) that no gas molecule lies in the shadow of another gas molecule as seen by the projectile. Therefore, the overestimation of P_{ion} as calculated by eqn. (1.7) is negligible. The expected reaction rate R is then given by the product of projectile flux in particles per second, i.e. projectile current I divided by projectile charge q_p, multiplied by P_{ion}:

$$R \; = \; \sigma\left(E_{proj}\right) \; \rho_{gas} \; d_{gas} \; I/q_p \tag{1.8}$$

For the typical values quoted above and singly charged projectiles, the reaction rate per mA of current is about $1.5 \cdot 10^9$ ionizations per second, equivalent to 1 million profile measurements per second, or 1 μs acquisition time[1].

---

[1] This value represents the intrinsic limit in acquisition time dictated by the ionization reaction rate. However, in practical applications this limit can be shadowed, as in the case of the current work, by technological limits such as, e.g., the integration time of the CCD camera used to image the profile.

The projectile beam current will be affected by interaction with the gas screen target, as projectiles undergo scattering interactions which result in beam temperature[1] increase and even in projectiles falling out of the storage ring acceptance and hence be lost. This effect is equivalent to scattering by residual gas particles, only more influent due to the higher density of the gas screen. For the case of the USR, with residual gas pressures of 10^{-11} mbar, corresponding to number densities at room temperature of about $2.5 \cdot 10^{11}$ particles/m^3, the jet to residual gas density ratios $\rho_{jet}/\rho_{res.gas}$ will be about 10^5. The effect of a 0.5 mm gas screen is thus equivalent to 50 m of residual gas, comparable with the circumference of the storage ring. Therefore, with the gas jet operational at a 1 μs acquisition time, the lifetime of the beam in the USR is expected to be halved. Finally, this decrease of stored charge, and hence current, with time will linearly impact on the reaction rate, which will accordingly decrease as per eqn. (1.8).

1.3.2 Resolution

To compute the sensitivity and resolution intrinsic to the monitor itself (i.e. without taking into account the extraction fields and the detection system) an analysis of the monitor in its simplest configuration is performed. With reference to Fig. 1.5, being w the thickness of the gas screen and α its angle with the horizontal, a particle traveling along in the $+z$ direction, and passing through the point $(x, y, 0)$ can ionize a gas atom anywhere in the segment $\left\{ \left(x, y, \frac{y}{tan\alpha} - \frac{w}{2sin\alpha} \right) ; \left(x, y, \frac{y}{tan\alpha} + \frac{w}{2sin\alpha} \right) \right\}$. If the vertical coordinate y of the detector is indicated with y_d, the same ionization would in turn result in a projection on the MCP in the segment $\left\{ \left(x, y_d, \frac{y}{tan\alpha} - \frac{w}{2sin\alpha} \right) ; \left(x, y_d, \frac{y}{tan\alpha} + \frac{w}{2sin\alpha} \right) \right\}$. An effective thickness of the gas screen can then be defined as the distance travelled by a projectile through the gas in a straight line, i.e. $w/sin(\alpha)$. Referring with the subscript s to the coordinates of the image on the sensor and with the subscript i to the initial coordinates of the ionizing particle, the sensitivities of the profile monitor for each direction become:

$$S_x = \frac{dx_s}{dx_i} = 1 = M_x$$
$$S_y = \frac{dz_s}{dy_i} = tan(\alpha)^{-1} = M_y$$

(1.9)

---

[1]Beam temperature can be defined to depend on the velocity spread of the particles in the beam, separately in the direction parallel and perpendicular to beam motion, leading to the definition of parallel and perpendicular beam temperature respectively: $\frac{1}{2}k_B T_\parallel = \frac{1}{2}m\bar{\Delta v}_\parallel^2$; $\frac{1}{2}k_B T_\perp = \frac{1}{2}m\bar{\Delta v}_\perp^2$

which also represent the magnification M_x and M_y of the beam profile image on the position sensitive detector.

The precision can instead be calculated considering the influence of the uncertainty due to the gas screen thickness on the position of ionization. This influences only the vertical (y axis) profile, introducing a flat error distribution with a full width of $w/sin(\alpha)$; which in turn results in an intrinsic final resolution in the y direction poorer than in the x direction, as it has also been reported in the work of Hashimoto [32], where much effort has been devoted to decreasing the screen thickness. It must be noticed that a more correct indication of the precision should take into account the magnification of the beam profile image on the detector. To do this, the modified error distribution full width W_{Err} scaled with the value of magnification must be introduced:

$$W_{Err,y} \;=\; \frac{w/sin\alpha}{y_d} \;=\; \frac{w}{cos\alpha} \tag{1.10}$$

Whilst it is in principle possible to minimize the W_{Err} by decreasing the value of α, hence effectively improving the resolution, eqn. (1.10) shows, however, that it is possible to gain only a factor $1/\sqrt{2}$ as compared to the 45° case. The value of α is then rather chosen in order to have a value of magnification equal in the two directions, leading to a non-deformed image, thus avoiding the need of image post-processing. As the x-axis magnification is equal to unity and independent from the value of α, the y-axis magnification is also chosen to be unity, corresponding to $\alpha = 45^o$. Thus, the extent of the vertical resolution degradation depends only on the width of the screen, which becomes a factor of primary concern in the design of the nozzle skimmer system used for the creation of the gas-jet.

The analysis and results shown in this section have been published in [33].

1.4 Objectives of the project

The project documented in this thesis aims to investigate and characterize the generation scheme of a supersonic gas jet target for transverse profile beam diagnostic, and design a suitable technological apparatus to operate it. To this end, analytical and numerical studies are done to describe the gas jet properties and direct the design effort. Furthermore, the technological issues of designing a working beam diagnostic setup are addressed and solved by means of analytical and numerical calculations as

well as experimental verification. Operation of the beam profile monitor in residual gas mode is finally also demonstrated.

1.4.1   Theory of jet generation and shaping

The successful operation of the gas jet based beam profile monitor depends on the generation of a suitable jet screen target.

The generation of an optimized gas jet target is a topic of high relevance for a number of applications, ranging from reactive engines in aeronautics to laser machining [34, 35]. Such applications have triggered a rich literature analyzing in detail the characteristics of axisymmetric gas jets. Furthermore, due to their properties of low internal temperature and high directionality, gas jets have attracted much interest as suitable targets for interactions in molecular spectroscopy [36], nuclear fusion [37] and atomic physics [9, 38, 39], for which momentum monochromaticity is a very important requisite of the target. In these applications, a pencil like gas beam is extracted from the expanding jet by means of conical skimmers. However, while a remarkable theoretical study has been carried out over the axisymmetric gas-jet system and its interaction with the added conical skimmers, e.g. [40], there have been no studies which expand these analyses to the bi-dimensional case of the planar jet collimated by means of slit skimmers, and a comprehensive review addressing the technicalities of a jet system design optimized for beam diagnostics application is still lacking.

The first objective of this project is to develop a theory of jet generation which takes into account the geometry of the nozzle skimmer system and the vacuum chambers, as well as the thermodynamic variables of pressure and temperature for both the vacuum environment in which the jet expands and the high pressure gas reservoir upstream the nozzle. Such theory produces predictions of the final density and shape of the jet screen, as well as the pressure in each vacuum chamber when the jet is running, which have been proved to agree very well with experiments. It also forms the basis on which the mechanical design of the experimental stand and, ultimately, the actual beam profile monitor is based.

The background of this theory is presented in Chp. 2, whilst the theory itself is introduced in Chp. 4, and used to design the experimental setup.

1.4.2 Development of original jet shaping techniques

In section 4.2 a theory of gas expansion is developed that allows reliable predictions of the expected densities in the jet and its housing vessels. This theory is based on the assumption that no shock wave patterns develop past the skimmer, so that a model based on analytical calculations can be written. However, a shock wave pattern does indeed form beyond the skimmer [40], and control of its structure, which depends on the geometric and thermodynamic design of the nozzle-skimmer system, can be used to improve the performance of the monitor.

To study this shock wave pattern it is necessary to solve the system of Euler's equations which govern the process. This cannot be done analytically, see section 2.2, hence numerical simulations have been performed. A full discussion concerning the results of this study is reported in Chp. 3, whilst a more compact summary has been published in [41].

1.4.3 Realization of a flexible experimental setup

As far as the experiment is concerned, the objective of this work is to use the knowledge acquired on the gas jet physics and technology, through the research outlined in sections 1.4.1 and 1.4.2, to design and commission a flexible experimental stand for the implementation and optimization of a supersonic gas jet based beam profile monitor.

The experimental stand needs to include all the elements needed to run jet based profile monitoring, but also to be configured so that switching to operation as a ReMi is in principle possible. However, the extra detector and magnetic field needed in that case are not included in the present work. They can, nevertheless, be added in the future, by modifying the presented design to include a variation of the extraction system and power supply voltage divider to accommodate a second MCP (see sections 6.1.5, 6.3 and 6.4.2). Design studies would be needed to implement this modification also in terms of the added signal detection complications required in a ReMi, such as synchronization with the projectile beam, time of flight difference compensation, detection of larger displacements and inclusion of magnetic field. However, flexibility to operation as a ReMi is at times conflicting with the optimized operation as a device dedicated solely to profile monitoring, and the trade-offs that need to be found in the design phase are addressed in this work.

The experimental stand is designed so that experimental investigations into the optimization of the gas jet can be carried out. This requires the ability to displace and exchange mechanical elements of the skimming system which would be instead fixed to the optimum position in the final application, resulting in increased cost and complexity of the experimental setup.

Finally, within the scope of this project falls also the test and commissioning of the designed and assembled experimental setup, so that the basis for starting a systematic investigation of the jet generation mechanisms as theorized in this work can be laid. These tests make use of the residual gas of the experimental chamber as target, and hence constitute a demonstration of the operation of the monitor in the residual gas profiling mode.

2

Theory of supersonic jet flow

This chapter presents the background necessary to understand the principles of supersonic expansion that are used for the design of the transverse beam profile monitor presented in this work. Section 2.1 provides an introduction to the fundamentals of fluid dynamics relevant to supersonic jet expansion, highlighting the different flow regimes and describing the shock wave pattern created. Section 2.2 describes the numerical approaches available for investigating jet expansion.

2.1   Theory of supersonic expansion

A supersonic gas jet is generated under suitable pressure conditions when a gas flows from a high pressure region to a lower pressure region through an aperture commonly referred to as *nozzle*, in a process known as *gas expansion*. The gas jet exhibits a series of remarkable properties which make it suitable for diverse applications.

A first classification of such properties can be done in terms of the pressure ratio between the reservoir upstream the nozzle and the base pressure of the environment it expands into, leading to the notion of *underexpanded, overexpanded* or *design* flow regime. This classification is particularly important as the gas jet which will be treated in this work is an underexpanded jet, and its physics differs significantly from the *design jets* which are instead the focus of aerodynamics [1].

2. THEORY OF SUPERSONIC JET FLOW

2.1.1 Gas expansion: equations set

Gas expansion inside a nozzle can be considered a quasi 1-dimensional process, as all the streamlines are confined within the nozzle walls, the flow direction is intrinsically 1-dimensional and perpendicular to the flow area, and no 3D structure develops beside an increase or decrease of the flow area as defined by the diameter of the nozzle at each particular point.

Given the confinement of the streamlines within the nozzle walls, the 1-dimensional nozzle system features conservation of mass in the flow, expressed mathematically by requiring the mass flow at any point along the nozzle to be constant. To express mass flow, one considers the mass which can flow in the unit time through a given nozzle plane perpendicular to the flow direction: this is given by the product of the mass density ρ and the volume swept per unit time, equal to the flow area A times the space covered per unit time by the flow, i.e. the flow velocity. Therefore, one has for the conservation of mass:

$$\dot{m} = \rho v A = constant \tag{2.1}$$

Taking the total differential of the expression above, and dividing by $\rho\, vA$, yields:

$$0 = \frac{d\rho}{\rho} + \frac{dv}{v} + \frac{dA}{A} \tag{2.2}$$

Secondly, momentum is also conserved in nozzle flow. The momentum conservation equation for gas flow can be expressed in terms of ρ, P and v:

$$dP = -\rho v dv \tag{2.3}$$

When nozzle flow in general is studied, the gas cannot always be assumed to be ideal, as many applications require high pressure regimes, for which the ideal gas relation ceases to approximate the flow satisfactorily. However, the ideal gas equation is usually assumed to hold for a first approximation study of nozzle flow, and it definitely holds for the low pressures and densities characterizing the nozzle flow studied in this work. In what follows the ideal gas equation of state will therefore be used.

Finally, viscous and heat conduction effects can in most cases be ignored in nozzle flow; in such high speed flow, indeed, non-equilibrium diffusion processes such as heat conduction have comparatively long characteristic times. Furthermore, since no turbulence is present in non-viscous flows until any shock wave develops, the flow is

also reversible. These assumptions describe an adiabatic and reversible flow, which is therefore isentropic. For isentropic flow of an ideal gas, the following relation holds (see [42]):

$$\frac{dP}{P} = \gamma \frac{d\rho}{\rho} \tag{2.4}$$

Momentum and mass conservation, together with the ideal gas equation of state and the isentropic relation (A.3), (2.2), (2.3) and (2.4) can be combined to get a relation applicable to quasi 1-dimensional nozzle flow, which describes the velocity change of the fluid as it crosses regions of the nozzle with different flow areas A:

$$\left(1 - M^2\right) \frac{dv}{v} = -\frac{dA}{A} \tag{2.5}$$

Thus the velocity of a flow depends on the flow area A in a way which depends on the sub or supersonic nature of the flow. In particular the sign of the velocity change for a given increase in flow area is negative for subsonic flows (M<1), and positive for supersonic ones (M>1). The fact that, differently from what happens in subsonic flow, a supersonic flow accelerates, or *expands*, as the flow area increases has profound consequences in nozzle flows which will be treated in more details in section A.2.

2.1.2   Free jet molecular beams: jet structure

Underexpanded jets and free jets   The categorization introduces in the previous section can be used to place the gas jet used in this work in the wider context of supersonic jets present in the literature. The supersonic gas-jet used in this work is operated under conditions of high vacuum in the ambient: such high value of R results in the jet being underexpanded, as per the definition given in the section above. Moreover, it does not need to produce any thrust, hence the complex design of the CD nozzle is avoided, and a simpler sharp orifice nozzle is preferred. The flow is therefore not guided after the nozzle throat, which leads to referring to this kind of jets as *free jets*. A very comprehensive review of free jet sources, is given by Miller [43], whilst more application specific accounts can be found in [44–46].

Shock wave pattern: equation set   As the free jet exits the nozzle and starts to expand, its pressure is still larger than the pressure of the ambient (underexpanded jet), and shock waves occur.

2. THEORY OF SUPERSONIC JET FLOW

The theory describing the shock wave pattern stems from the equations of mass, momentum and energy conservation, together with the equation of state and the thermal equation of state defined for isentropic, compressible flow: this equation set as a whole is known as *Euler's equations*. Whilst these equations can be used to some extent to provide information about the jet in some rather restrictive assumptions, such as 1-dimensional flow, they cannot be solved analytically for the general case of 2D flow. In free expansion, the flow is transversally confined by shock waves which hence cannot be neglected in the calculation, and rule out the use of the 1-dimensional approximation. Therefore, most of the results presented in the following, including the shock wave pattern formed, rely on numerical simulations, whose details will be treated in Chp. 3. Furthermore, more importantly, they are based on the continuum description on the flow, and can therefore be used only in the initial stages of the expansion of a free jet, when transition to molecular flow still does not occur.

Shock wave pattern: dimensioning A representation of the typical shock wave pattern created at the exit of the nozzle is shown in Fig. 2.1. The normal shock wave downstream the nozzle and perpendicular to the flow direction is called the *Mach disk*, and is equivalent to the shock waves present inside the CD nozzle discussed in the previous section in that it allows the flow to change from supersonic to subsonic.

The shock pattern which surrounds the expanding jet around the Mach disk is instead called the *barrel shock*, and its effect is the transverse confinement of the expanding jet: this is of course not needed in internal nozzle flow as it is the nozzle itself that confines the transverse boundaries of the jet.

The dimensioning of the Mach disk and barrel shock, together with the position of the Mach disk can be used to characterize the particular flow, and have been the subject of both theoretical studies [47] and experimental investigation with density imaging techniques such as Schlieren photography [48], exploiting the fact that shock waves are regions of high pressure and density gradients, and therefore easily imaged by such light scattering techniques. These investigations show that the location of the Mach disk only depends on the pressure ratio and is given by [43]:

$$\frac{x_M}{d} = 0.67\sqrt{\frac{P_0}{P_a}} \tag{2.6}$$
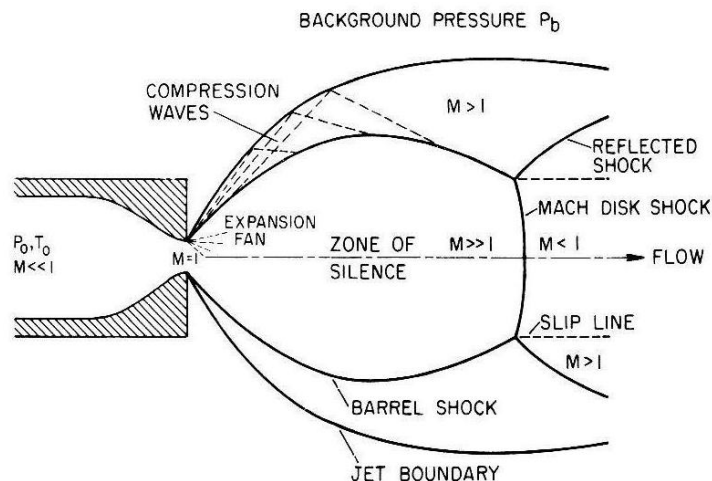
Figure 2.1: Typical shock wave pattern of a free jet [43].

The diameter of the Mach disk d_M and the maximum diameter of the barrel shock d_{Bs} are more difficult to characterize and also depend more strongly on the particular configuration, they can be approximated by $d_M = 0.5\, x_M$ and $d_{Bs} = 0.75\, x_M \pm 25\%$.

Beside the Mach disk and the barrel shock, a more complex pattern of shock waves forms during the jet expansion. These include for example the so-called *expansion fans* at the exit of the nozzle, due to the abrupt ending of the nozzle and resulting abrupt increase in available flow area; the compression waves that are formed between the barrel shock and the outer jet boundary, which provide an extended region for slowing down the jet to the ambient rest gas; the slip lines, which are a series of more complex reiterating phenomena which occur past the Mach disk. These are all region of viscous, non isentropic flow. The region enclosed in the innermost shock waves pattern (barrel shock and Mach disk) is termed the *zone of silence*, referring to the fact that flow in this region is supersonic and therefore not affected by ambient pressure background conditions. The spatial extension of the zone of silence plays a central role in the generation of the supersonic gas jet studied in this work: as the first skimmer needs to be placed within this zone. This allows the jet created beyond the skimmer to be extracted from a region of purely supersonic flow, so as not to allow any subsonic component or shock wave to interfere with the expansion by warming up and slowing down the jet through collisions with subsonic molecules.

Shock wave thickness   Shock waves thickness is of the order of the local mean free path. Therefore, in some laboratory applications characterized by high vacuums such as low density free jets, where the mean free paths are of the order of cm to tens of cm, the shock wave structure is not as neat as the one presented in Fig. 2.1 and rather a slow transition between supersonic and subsonic flow occurs. For the application treated in this work, relatively high density, high mass flow jets are used, resulting in the initial expansion stages of the jet being kept at relatively high pressures of $10^{-2} \div 10^{-4}$ mbar, while the jet itself has a typical pressure of $1 \div 0.1$ mbar, the mean-free path at room temperature lies in the sub-millimeter range. Jet flow in the initial stages of expansion is hence still compatible with the continuum description of the flow (Knudsen number < 0.2), allowing the use of the Navier-Stokes equations. In turn, these reduce to the Euler equations as it has been shown that the gas-jet expansion is a quasi-isentropic process, and viscosity effects can be neglected [40].

2.1.3   Free jet molecular beams: thermodynamics of the expansion

Despite the impossibility of solving analytically the full 2-dimensional system of partial differential equations that describe the 2D isentropic flow, approximated considerations can still be done regarding the centerline properties and some thermodynamic features of the expanding jet.

The result presented in this section include a calculation of the terminal velocity of the free jet, which well approximates the actual jet velocity, affecting the ion recoil in the gas screen, which in turn influences the resolution of the monitor (treated in Chp. 6). Moreover, a set of relations is derived which relate all thermodynamic variables in the jet expansion to the Mach number, thus providing the theoretical basis to justify a choice of observables made in the numerical simulations treated in Chp. 3.

Energy equation and terminal velocity   The equation of conservation of energy is used in the formulation given by the first law of thermodynamics in its formulation in terms of enthalpy, which takes into account the work done by the flow under a pressure gradient. Using the assumptions of negligible viscosity and heat conduction, any change in enthalpy can be only due to a change in kinetic energy. Therefore, defining h as the enthalpy per unit mass, and h_0 as the *stagnation enthalpy per unit mass*, that is the

enthalpy in the chamber reservoir, where the flow is stationary and kinetic energy is null, one can write:

$$h_0 = h + \frac{v^2}{2} \tag{2.7}$$

Also, any change in enthalpy for ideal gases is given by $dh = C_p dT$, with C_p being the specific heat capacity of the gas at constant pressure, and T the temperature. Therefore the difference $h_0 - h$ can be written as the integral of C_p between the stagnation and the local temperature:

$$v^2 = 2(h_0 - h) = 2\int_T^{T_0} C_p dT \tag{2.8}$$

If C_p can be assumed constant in the process, the square of the velocity is simply equal to twice the product of C_p and the temperature difference given by the cooling of the gas jet in its expansion. Since the cooling of the jet is substantial, and T_0/T can be in excess of 100, the final temperature T can as a first approximation be neglected with respect to the stagnation temperature T_0. The resulting velocity is then the velocity corresponding to the whole thermal energy being converted in kinetic energy of the flow, and is known as terminal velocity v_∞. For an ideal gas $C_p = \gamma/(\gamma-1)(R/W)$, therefore v_∞ can be written as [43]:

$$v_\infty = \sqrt{\frac{2R}{W}\frac{\gamma}{\gamma-1}T_0} \tag{2.9}$$

Expansion variables in terms of Mach number   Another result which can be obtained by the analytical study of the isentropic expansion of an ideal gas is the set of equations that relate all the relevant thermodynamic variables of the jet, namely temperature, velocity, pressure and density to one single common variable: the Mach number. This is obtained by recalling that $M = v/a$ and, for an ideal gas, $a = \sqrt{\gamma RT/W}$. These expressions can be substituted in eqn. (2.8), using the ideal gas C_p to yield:

$$(T/T_0) = \left(1 + \frac{\gamma-1}{2}M^2\right)^{-1} \tag{2.10}$$

and

$$v = M\sqrt{\frac{\gamma RT_0}{W}}\left(1 + \frac{\gamma-1}{2}M^2\right)^{-1/2} \tag{2.11}$$

Finally, applying the isentropic relations $(P/P_0) = (T/T_0)^{\gamma/(\gamma-1)} = (\rho/\rho_0)^\gamma$:

$$(P/P_0) = \left(1 + \frac{\gamma-1}{2}M^2\right)^{-\gamma/\gamma-1} \tag{2.12}$$

$$(\rho/\rho_0) = (T/T_0)^{1/\gamma-1} = \left(1 + \frac{\gamma-1}{2}M^2\right)^{-1/\gamma-1} \tag{2.13}$$

Therefore, by computing the Mach number anywhere in the expansion, all thermodynamic variables can be immediately calculated in terms of their stagnation value. It is noted that it is meaningless to combine (2.9) and (2.11) to obtain the final Mach number. The final velocity is defined as the velocity which would be obtained were the temperature of the gas to reach the absolute zero; in turn, this would translate in velocity of sound being zero, and Mach number being infinity. If the definition of the speed of sound is used instead of (2.11) in combination with (2.9), one gets:

$$M_{final} = \sqrt{\frac{2}{\gamma-1}}\sqrt{\frac{T_0}{T_{final}}} \approx 2\sqrt{\frac{T_0}{T_{final}}} \tag{2.14}$$

Which provides a useful simple relation to estimate the Mach number when $T_{final} << T_0$ and monoatomic gases are used. Experience and simulations [9] show that for experimental setups commonly used in laboratory free jets, T_{final} is lower than 20 K in most conditions, and M_{final} can therefore be estimated (for room temperature stagnation sources and monoatomic gases), to be larger than 7.

2.1.4 Free jet molecular beams: mass flow, beam intensity and pumping speed

Mass flow through a nozzle orifice Beside identifying the importance of Mach number in free expansion, eqns. (2.10) to (2.14) can also be combined with the equation of conservation of mass (2.1) and the ideal gas equation of state in terms of ρ, eqn. (A.3), to yield the mass flow through a nozzle orifice in a supersonic expansion in terms of stagnation pressure and temperature P_0 and T_0, nozzle throat area A^* and gas species properties (W and γ). To obtain eqn. (2.15) below, the mass flow is computed at the nozzle throat, where $M = 1$; the relation obtained is however valid anywhere, as mass is conserved along the flow[1]:

$$\dot{m} = \rho v A = P_0 A^* \sqrt{\frac{\gamma W}{R T_0}\left(\frac{2}{\gamma+1}\right)^{(\gamma+1)/(\gamma-1)}} \tag{2.15}$$

---

[1]A full derivation of eqn. (2.15) is reported in appendix B

Eqn. (2.15) has two applications in the design of a free jet source. First, it can be used to estimate pumping requirements and beam intensity: this is done in section 4.2, where eqn. (2.15) is used as a part of a theory modeling the pressure distribution in all vacuum chambers.

Moreover, eqn. (2.15) can be used to compare a supersonic gas-jet system with an effusive gas source, and hence provide a quantitative measure of how much *directional* a supersonic jet is intrinsically, i.e. before collimation is applied. A description of the correlation between effusive and jet sources is therefore reported in section A.3.

2.1.5 Free jet molecular beams: collision rates and transition to molecular flow

The physics of a free supersonic jet changes dramatically depending on whether the flow is continuum or molecular. In this work, the numerical simulations presented in Chp. 3 rely on the continuum description of the flow, whilst the theory which predicts the pressure distribution in the jet system presented in section 4.2 assumes molecular flow. To justify the applicability of the two theories is then necessary to establish the length scale over which transition to molecular flow intervenes. This information on the jet flow can be obtained through numerical solution of the Euler equations, rather than from analytical calculation as it was done in the previous sections. The numerical approaches to the solution of these equations are discussed in more detail in section 2.2, whilst in the following the results are discussed.

Jet properties along the expansion centerline   Solving the Euler equations along the centerline expansion of the jet yields the local values of the thermodynamic variables, shown in Fig. 2.2 [43].

Fig. 2.2 shows an exponential fall of the collision frequency as the expansion progresses. As it was mentioned earlier in this chapter, the collision rate is essential for the establishment of a continuum regime, as opposed to the molecular flow regime. Therefore, for low enough values of collision frequency, the flow turns molecular, and the Euler equations can no longer be used. In molecular flow the thermodynamic properties of the jet are *frozen*, i.e. the exponential fall or rise shown in Fig. 2.2 turns in a straight horizontal line.

31
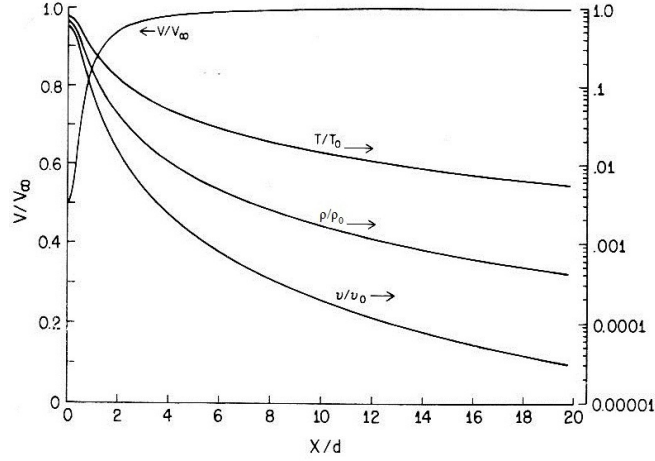
Figure 2.2: Free jet centerline properties versus distance in source diameters for $\gamma = 5/3$; temperature T, density ρ and collision frequency ν (right hand axis) are normalized to the source stagnation values T_0, ρ_0 and ν_0, whilst v is normalized to the terminal velocity v_∞ (left hand axis) [43].

Another feature shown in Fig. 2.2 is that whilst the velocity reaches 99% of the final velocity v_∞ within the first few nozzle diameters of the expansion, the other characteristics, in particular the temperature, take sensibly longer to approach their terminal value. Therefore the velocity of a gas jet can always be assumed for applications to be equal to the terminal velocity. The final temperature instead will depend on where the transition to molecular flow occurs.

The cooling of the jet as it accelerates and expands, described by the curves of temperature and density in Fig. 2.2, is one of the important advantages of high velocity jets. Indeed, since T determines the spread in particle velocities around the mean value, the velocity resolution of a jet is proportional to T/V^2, and this leads to the obtainment of monochromatic jets.

Collision rates and clusters Fig. 2.3 shows the number of collisions remaining in the expansion at any given point along the centerline, a property relevant to the determination of the transition to molecular flow.

An interesting feature of Fig. 2.3 is that in the planar jet the transition to molecular flow occurs far further on in the expansion than in the axisymmetric jet. However, the results shown in Fig. 2.3 are calculated for an ideal planar expansion from an infinite
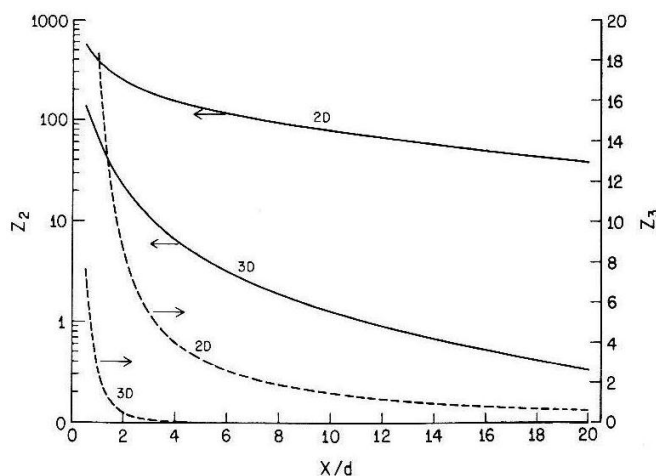
Figure 2.3: Collisions remaining in the expansion in terms of the longitudinal distance from the nozzle in both the axisymmetric and planar expansion (respectively 3D and 2D) for both two-body (solid curves, left hand axis) and three-body (dashed curves, right hand axis) collisions [43].

slit. This assumption is realized satisfactorily only when the longitudinal distance is smaller or comparable with the width of the slit. Further on, an elongated slit can be approximated more and more with a circular one, leading to sharper fall of the collision rate, as in the case of the axysimmetric jet.

Transition to molecular flow occurs when the jet molecules do not undergo any more collisions. This is never fully realized for the complete jet, as the exponential fall in Fig. 2.3 never hits 0. However, when the collision rate is much smaller than 1, only a few molecules will still undergo a collision, and most will on average have reached the condition of molecular flow, which can therefore be considered attained. It is not possible to predict exactly where this transition will occur by using the numerical approach on which Fig. 2.3 is based, as it is no more applicable when the flow approaches the molecular regime. However, analysis of Fig. 2.3 provides an idea of the order of magnitude which can be expected: tens to hundreds of nozzle diameters. For nozzle dimensions of 30 μm, as it is the case in this work, transition to molecular flow happens a few millimeters beyond the nozzle. Hence justifying the use of the numerical simulations of Chp. 3 in the region going from the nozzle to tens of nozzle diameters beyond the first skimmer, and the assumption of molecular flow on the wider scale of the full experimental setup (about 2 m) which is used in section 4.2.

2.2   Numerical approach

The numerical simulations presented in Chp. 3 rely on the Euler equations to solve the flow: this section addresses the numerical methods on which the software used in Chp. 3 is based.

As it was introduced in section 2.1.2, the Euler equations describe the physics of free jet sources with the following set of assumptions:

1. Ideal gas behavior

2. No heat conduction

3. No viscosity effects

4. Constant C_p and γ

5. Continuum flow regime

All of these are satisfied in free jet sources, away from shock waves regions, except for the last one, which only holds so far in the expansion as the collision rates keep high enough for the thermodynamic quantities of temperature and pressure to be defined. Nevertheless, the analysis based on Euler's equations provides results in good agreement with the experiments in most cases, especially when the first stages of expansion are concerned: because of their importance, the Euler equations are reported explicitly in the following [43].

$$\frac{\partial \rho}{\partial t} + \vec{\nabla} \bullet (\rho \vec{v}) = 0 \qquad \text{mass conservation} \qquad (2.16)$$

$$\rho \frac{D\vec{v}}{Dt} = -\vec{\nabla}P + \rho \vec{f} \qquad \text{momentum conservation} \qquad (2.17)$$

$$\rho \frac{D\left(e + v^2/2\right)}{Dt} = -\vec{\nabla} \bullet (P\vec{v}) + \rho \dot{q} + \rho \left(\vec{f} \bullet \vec{v}\right) \qquad \text{energy conservation} \qquad (2.18)$$

$$dh = \hat{C}_p \, dT \qquad \text{thermal eqn. of state} \qquad (2.19)$$

together with the equation of state (eqn. (A.3)). The following notation has been used for the *substantial derivative* D/Dt:

$$\frac{D}{Dt} = \frac{\partial}{\partial t} + \left(\vec{v} \bullet \vec{\nabla}\right) \qquad (2.20)$$

In these equations, e represents internal energy, $\dot{q}$ is the rate of heat added per unit mass and $\vec{f}$ is the body force per unit mass. The characteristics of Euler equations change dramatically with the Mach number, in particular the main difference which concerns this work is that for supersonic flow ($M > 1$), the solution at any point does not depend on the flow downstream that point. Indeed, this feature can be easily understood on physical, rather than mathematical, grounds due to the nature of supersonic flow: the flow itself reaches the downstream point before any perturbation, thus preventing the downstream point condition to influence the supersonic expansion. Mathematically, this translates in the Euler equation being hyperbolic for supersonic flow and elliptic for subsonic flow. However, analytical solutions are not available for the complete solution of the Euler equations without the use of several ad hoc approximations, one of which, namely 1-dimensional flow, was investigated in section 2.1.3 and 2.1.2. For some cases, notably the free jet expansion from a supersonic nozzle, the 1-dimensional flow approximation does not hold, and numerical solutions need to be employed.

Numerical approaches for the solution of flow problems can be categorized in three main methods: the method of characteristics (MOC), the finite-differences method (FD) and the Monte Carlo (MC) approach. These three methods have specific advantages and disadvantages, and rely on different computational principles. A more detailed description of the underlying idea of each method, together with its mathematical structure, together with a qualitative comparative analysis of the different methods is not strictly needed for the following, as commercial codes have been used for the numerical simulations reported in Chapter 3; therefore, this discussion is presented in the appendix, in section A.4.

2.3   Conclusions

The theory presented in this chapter introduces the fundamental of the supersonic gas jet physics and lays the basis for its theoretical analysis as it applies to the present work.

In this work, two different approaches are used for the description of the jet, a numerical approach based on Finite Elements simulations and an original analytical approach based on a mass transport model. The discussion presented in this chapter

introduces the mathematical structure and physical principles needed to construct these approach.

In particular, sections 2.1.1, 2.1.3 and 2.1.4 introduce all the equations needed for the description of the jet flow based on mass transport fully developed in chapter 4. Section 2.1.1 introduces the basic equation of nozzle flow derived from the elementary principles of momentum and energy conservation, and is then used in section 2.1.4 to derive the relation for mass flow through the nozzle orifice. This is complemented by the relations presented in section 2.1.3 which derive the terminal velocity of the gas jet, used, together with the density, to evaluate the mass flow through the skimmer areas in the theory developed in chapter 4.

Section 2.1.2 and the second part of section 2.1.3 focus instead on aspects of the theory needed to plan and benchmark the numerical simulations presented in chapter 3. Section 2.1.2 introduces the equations describing the structure of the expanding jet, which are then used, in section 3.3, for comparison with the numerical results obtained and fine tuning of the simulation boundary conditions. Section 2.1.3 shows instead how all the relevant thermodynamic variables are interlinked and can be derived from knowledge of the Mach Number at any point in the flow. This allows, in chapter 3, to plan the numerical simulations to monitor only the Mach Number, hence saving analysis and computation time.

Finally, in section 2.1.5, the transition to free molecular flow is investigated, and found to be happening few millimeters downstream the nozzle in the expansion. This value sets the limits of applicability of the approaches used: the numerical approach used in chapter 3, based on the Euler equations is only valid before the transition to molecular flow, i.e. in the first few millimeters of the expansion, and hence plays an important role only in the interaction of the jet with the first skimmer; the second approach, presented in chapter 4 is only strictly valid beyond this point.

3

Numerical Simulations

A theory of gas jet expansion simplified enough to be treated analytically is developed and described in Chp. 4, where this same theory is used to design the mechanical components of the experimental stand. The theory relies on the assumption of molecular flow immediately beyond the skimmer, and is based on the equations introduced in Chp. 2. In particular, to describe quantitatively the jet density, extensive use is made of eqn. (A.7), which depends on the value of the peaking factor κ. The peaking factor κ, in turn, can only be approximated by the experimental values found in [49], as these relate to axysimmetric ideal free jets. The real jet does instead present a series of complicated shock wave structures even beyond the skimmer, which gradually fade moving downstream in the expansion, as discussed in Chp. 2.

These shock structures modify the density of the jet along its centerline, as well as the homogeneity of the expansion. On the one hand, they result in jets which have an internal structure, instead of an homogeneous cross section; on the other hand, these structures can be exploited by proper design to achieve higher peaking factor and hence higher beam jet intensities.

Whilst it is not advisable to use the absolute values of CFD simulation results, as these are affected by large uncertainties due not only to numerical error, but mainly to the limits of the theory applied (see Chp. 2), it is still possible to analyze the trends in the observables and identify optimum configurations which maximize jet intensity and density profile homogeneity. Therefore, the error in the final results due to the approximation of the peaking factor (estimated in [49] to be better than 10%) can thus

be considered negligible, as it affects the results only linearly by modifying the found density by no more than 10% in their absolute value.

In this chapter, an numerical analysis of the planar supersonic jet system to be used for beam diagnostics applications is carried out with both a commercial software and custom c++ coded modules, with the aim of investigating the simulated observables with different parameters sets. These parameters are chosen as to fully describe the geometry of the nozzle skimmer system and the thermodynamic variables of the flow, and result in the need to explore a multidimensional variable space.

This chapter describes the characteristics needed by the simulation software and the software which is used in this work, together with presenting a benchmarking study which validates its applicability to known cases similar to the one studied in this work (sections 3.1 through 3.3). In section 3.4, a set of parameters which describe the studied system and original observables to assess its performances are introduced and their significance discussed. Sections 3.5 and 3.5.1 present the simulation plan and the custom c++ modules coded to allow its realization. Finally in section 3.6 the results of the simulations are presented and discussed.

3.1 Software selection

Whilst the theory underlying the time-dependent FD method described in the Chp. 2 is established since some decades, the actual algorithmic implementation of it proves complex. However, well established commercial products are available for CFD calculations; thus this work is carried out using one such commercially available software.

In this work GDT, ANSYS FLUENT and Virtual Device for SIMION have been considered [50–52]. The last one deals with gas jets for accelerator experiments, but is still under development, whilst GDT and ANSYS FLUENT are both feasible for the task and comparable from the point of view of computational efficiency. Of these, GDT has been chosen on the basis of benchmarking provided for shock wave applications and capability of importing CAD files for geometries.

GDT stands for Gas Dynamic Tool, and has been developed by the group of A. Medvedev in Tula, Russia. The code has been widely benchmarked by its creators against known flows, proving very reliable in dealing with high compressibility effects such as shock waves [53].

GDT equations set The GDT package includes both the full Navier-Stokes flow formulation and the special case of the Euler equations. In the application studied in this work, the initial expansion stages of the gas-jet apparatus are housed in vacuum vessels which are kept at relatively high pressures of $10^{-2} \div 10^{-4}$ mbar, while the jet itself has, in these same stages, a typical pressure of $1 \div 0.1$ mbar. At room temperature, these pressures correspond to mean free paths in the sub-millimeter range, still compatible with the continuum description of the flow (Knudsen number < 0.2). This allows the use of Navier-Stokes equations, which reduce to the Euler equations as it has been shown that the gas-jet expansion is a quasi-isentropic process [43], and viscosity effects can be neglected. Hence, the GDT continuum flow solver based on the Euler equations is used.

3.2 GDT benchmarking

A feature crucial to the reliability and efficiency of CFD simulations is the design of the simulation domain in terms of its boundary conditions, dimensions and CFL coefficient. These conditions cannot in general be determined a priori, and need to be optimized for each particular application and algorithm. In this process the main aspects to be taken into account can be obtained by benchmarking the code. This analysis has been performed for the GDT code in the well known 2D case of free expansion (no skimmer) of an axissymmetric jet.

To benchmark the GDT code and the simulation domain design, the conformity of the shock wave and flow pattern to the theory presented in Chp. 2 and the time stability of the pattern formed have been assessed. In particular, the shock wave pattern has been assessed against the following features: formation of Mach disk, barrel shock and reflected shock, all three of which should merge at a point named the triple point. The relative dimensions of the Mach disk and the barrel shock are described by the theory presented in Chp. 2, and the distance nozzle-Mach disk can be characterized in terms of the pressure ratio as in (2.6).

These considerations are complemented by an assessment of the time stability of the numerical simulations, which is monitored to be stable over 1 second. On top of these considerations, the simulation domain has been designed in order to minimize the computing time. Four parameters have been varied: boundary conditions, domain

dimensions, grid finesse and CFL constant. Furthermore, a detailed analysis of the effect of nozzle-shape on the jet expansion has been carried out.

The optimization of boundary conditions and domain dimensions prove to be closely intermingled, and of outmost importance to the reliability and stability of the numerical analysis: thus the study which leads to their optimization deserves a detailed discussion and is postponed to section 3.3. In the following subsections the influence of grid finesse, CFL constant and the effects of nozzle shape will be analysed on the basis of the optimized boundary conditions and domain dimensions as they are determined in the section 3.3.

3.2.1 Grid Finesse

To analyze the effect of grid finesse on the simulations variables, 6 different tests were run for an axisymmetric expansion, using grids with equivalent geometrical proportions and increasing number of points. The smallest number of points corresponded to a 180k points grid, with the nozzle being 1 point thick; whilst the final grid has 6.5 million points (i.e. 180k x Grid $\#^2$) and a 6 points thick nozzle. The variables observed are the geometrical proportions of the shock wave pattern, i.e. the Mach disk and the barrel shock diameter; the longitudinal distance from the nozzle to the Mach disk; and the maximum Mach number achieved in the expansion.

Fig. 3.1 shows a plot of these 4 variables for the different values of nozzle thickness, corresponding to different mesh sizes (i.e. grid finesse), identified by the nozzle diameter length measured in grid points on the x axis.

It can be seen from Fig.3.1 that for all 4 observables there is indeed a dependence on the grid finesse. In particular, all 4 series in the plot are compatible with a stronger and bigger expansion as the grid finesse is improved: the linear dimensions grow together with the maximum Mach number. However, the gradient of the growth decreases as the grid finesse is improved, suggesting a saturation value for better grid finesses. A strong indication of the proximity of this plateau is given by the comparison of the calculated value with the theory expressed in section 2.1.2: the simulated value of the observables corresponding to the best grid finesse tested is within 2.5% of the theoretical value for all observables except the barrel shock diameter, which is instead within 4.3% of the theoretical value.
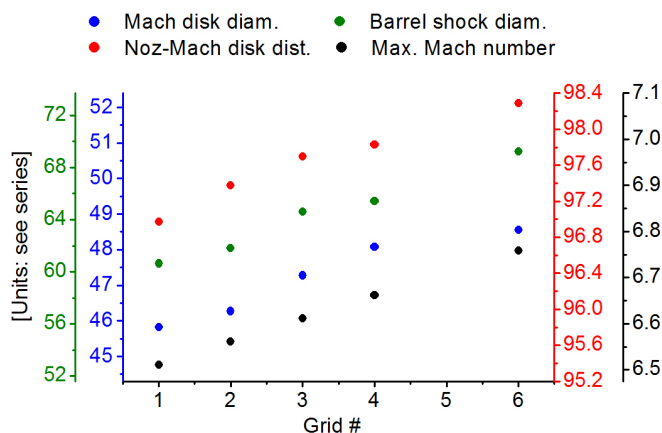
Figure 3.1: Mach disk diameter, barrel shock diameter, nozzle to Mach disk distance and maximum Mach number in the expansion for 5 different grid finesses. The values of length are reported in grid points. The markers for each series match the color of the corresponding vertical axis.

More importantly, increasing the grid points 36 times (i.e. passing from grid number 1 to 6), the percentage variations of all observables with respect to the theoretical value is kept below 5%, with the exception of the barrel shock diameter, which is kept only below 12%, as it can be seen comparing the values of the observables corresponding to the first and last grid finesse values. The higher sensitivity of the barrel shock diameter to the grid finesse can be traced back to the fact that the barrel shock diameter depends on the outer region of the expansion, where the pressure gradients are largest, and hence the numerical error the greatest. However, it is also the observable least relevant to the analysis of jet expansion through a skimmer, as this analysis pivots instead around the central core of the expansion.

Whilst the improvement in precision obtained by larger grids is not larger than 5%, the computation time considerably increases, not only because of the increased number of points, but also due to the smaller time step required (see section A.4.3), according to an exponential curve. Fig. 3.2 shows the measured computing time, in hours, for the 2-dimensional grid tests used in Fig. 3.1 (blue points). Dividing the computing time by the number of grid points and by the number of time steps, the computation time per point per time step can be obtained, and is found to be 43 $\pm$0.3 ns. This value can be used to estimate the computation time needed to solve a 3-dimensional grid with $10^6 \cdot (\text{grid } \#)^3$ points for the same time interval: the result of this estimation

41

is also shown in Fig. 3.2 (red points).
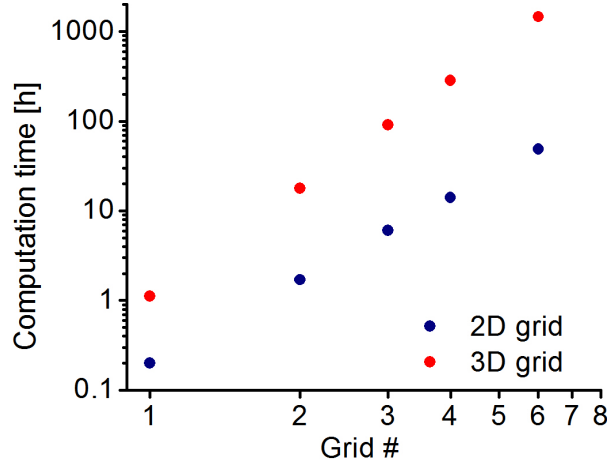
Figure 3.2: Computation time in hours measured for a 2-dimensional grid, and estimated, for a 3-dimensional grid, in terms of grid number, on a Quad-Core Intel® Xeon® 3.40GHz Processor, 64-bit, 16GB RAM, 2X 6MB cache.

It is seen that the 5% improvement in numerical precision comes at the price of an increase in computation time of about 3 orders of magnitude. Therefore, in the interest of saving computation time, it is concluded that the grid can be adjusted so that the nozzle diameter, or nozzle width in the case of rectangular nozzle, only extends for one grid point.

3.2.2   CFL constant

To analyze the effect of the CFL constant on the simulation precision, 9 different simulations were run with decreasing value of CFL constant from 1 to 0.2 in homogeneous steps of 0.1; computing the same 4 observables used in section 3.2.1.

Computing time   These simulations show the computing time to decrease with an approximately hyperbolic trend, like it is expected from theory A.4.3. In particular, for grids of 1 million points similar to the ones which are used for the main body of 3D simulations reported in this work, the best fit of the curve describing the computing time in terms of CFL is given by the equation

$$t_{computing} = k_{CFL}^{-1.12} \tag{3.1}$$

The exponent bigger than one is probably due to numerical errors, as smaller CFL correspond to longer simulations, which are hence more prone to accumulating non negligible errors. To prove this dependence, the computation above was repeated for smaller grids of 125k points, resulting in a best fit exponent of 1.03, closer to the expected value of one than in the case of the 1M point grid, which results in simulations about 10 times longer.

Precision   As for the observables values, the quality factor used is the percentage deviation from the theoretical value. This percentage deviation is found to follow an approximately parabolic law, which is best fitted by the curve:

$$\Delta_\% \,=\, \alpha \, k_{CFL}^\beta + \gamma. \tag{3.2}$$

where the values of the best fit parameters α, β and γ vary from observables to observables and are reported in table 3.1.

Observables	α	β	γ	Optimum CFL
Mach disk diameter	4.5	1.97	1.4	0.9
Barrel Shock diameter	10.2	1.91	3.5	0.9
Nozzle-Mach disk dist.	1.4	2.12	0.4	0.7
Maximum Mach number	3.1	2.03	1.2	0.8

Table 3.1: Best fit parameters α, β and γ describing the percentage deviation from the theoretical value of the 4 test observables in terms of the CFL constant, to be used in the expression given by eqn. (3.2).

Table 3.1 also shows, for each observable, the optimum CFL found corresponding to each observable. The optimum CFL corresponds to the minimum of the curve given by the product of computation time and percentage deviation, serving as the combined quality factor of the simulation. Therefore, the value of CFL = 0.8 is chosen as a best trade off and used throughout the rest of this work for all simulations.

3.2.3   Nozzle shape

As it has been mentioned in Chp. 2, the issue of the influence of nozzle shape on free jet flows has been analysed in the literature, and particularly relevant to this analysis is the pioneering work of Murphy [54]. In this paper, three different nozzle shapes are

compared by means of MOC calculations: sharp edged orifices, convergent nozzle and capillary tube. The calculations show that the effects of precise nozzle shape are only relevant within the first few nozzle diameters of the expansion. In particular, when the centerline Mach number is plotted against the position downstream the expansion, the variations between different nozzles are very small. Therefore, testing the flow structure with different nozzle shapes also proves to be a good indication of GDT code reliability, and has been carried out for all three cases discussed in [54]. Fig. 3.3 shows the Mach number along the centerline of the jet simulated with GDT for these three nozzle configurations. The results obtained in [54] are confirmed also by the GDT analysis, as the differences between different nozzles shapes lie within 8% of their value, which, with reference to the analysis carried out in sections 3.2.1 and 3.2.2, is within the simulation precision of the GDT code in the condition used.

Furthermore, from Fig. 3.3 it can be seen how the Mach number, sharply increasing in the first few nozzle diameters of the expansion, grows asymptotically towards a maximum value, as expected by the theory presented in Chp. 2: this corresponds to the full internal energy of the gas being translated as kinetic energy, i.e. cooling and accelerating the gas. The oscillations in this final value appear to be larger and larger the further the distance from the nozzle: this effect depends on the dimension of the simulation domain and is hence to be attributed to the numerical interference due to the proximity of the simulation boundary, as described in detail in section 3.3. It is hence a numerical artifact of no physical significance.

3.3 Boundary conditions

The influence of boundary conditions has been found to have a dramatic impact on both the geometry and the time stability of the shock wave pattern formed. As it has been seen in Chp. 2, to solve the system of Euler equations for mixed sonic-supersonic flows by finite differences, the simulation needs to run from the initial conditions forward in time until the steady state is reached. Boundary conditions prove influent in such process insofar as the domain dimensions are small enough that a perturbation can travel from the region of interest to the boundary and back before the steady state is reached. This is normally the case, as otherwise too large domains need to be used, critically increasing computation time. In the case of interest in this work, for example,
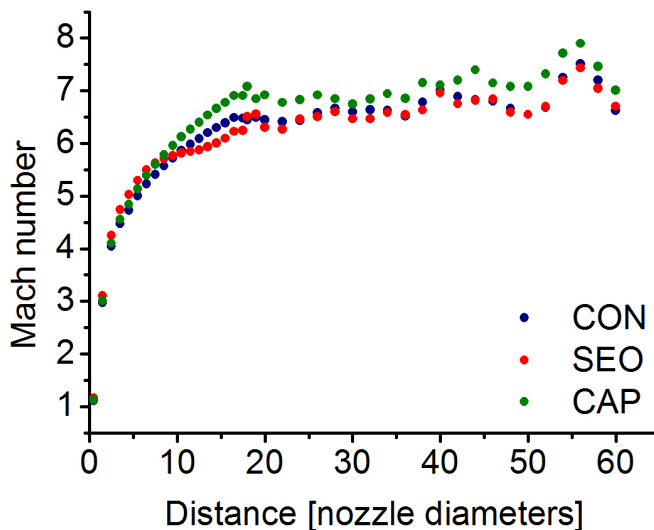
Figure 3.3: Mach number computed along the centerline of the expansion for 3 different nozzle shapes: sharp edged orifice (SEO), capillary (CAP) and convergent (CON). Confirming Murphy's work, the differences are within 8%, with the SEO and CON nozzles being within only 4%, compatible with errors due to GDT precision.

the time needed for a perturbation to travel from the nozzle to the boundary and back can be estimated by using the terminal velocity, eqn. (2.9), and considering that, with a 30 μm nozzle, the domain, which is 100 nozzle diameters long, extends for 3 mm. For a final velocity of about 800 m/s for N_2, this translates in travel times in the order of μs. The equilibrium solution, on the other hand, is achieved (see later in this section) in times of the order of ms: therefore domains three orders of magnitude longer would have to be employed to avoid the effects of reflected perturbations. Thus, a custom solution is to be found to minimize the impact of boundary conditions on the region of interest.

Indeed, the requirement of a small domain results in the need to introduce artificial boundaries in the flow in regions which have no physical significance such as a solid object or another fluid, but are simply the point where one wants the simulation domain to stop. The introduction of these artificial boundaries invariably creates artifact distortions in the simulated flow which are well documented in literature [55]. In particular, these artifacts rise from the spurious reflections of waves from inside the domain on the domain boundaries, if these are not transparent.

Several attempts have been made in literature to achieve a mathematical formula-

tion of transparent boundaries, which minimize the artifact distortions in the simulated flow, and these modified boundaries conditions are known as open boundary conditions, or Non-Reflective Boundary Conditions (NRBC). When there is a large amount of gas flowing at supersonic speed through a border, NRBC boundary conditions are essential as they are transparent to the perturbation, which is lost beyond the boundary, whilst fixed value boundary conditions would instead result in the occurrence of artifact reflected shock waves. The NRBC used by the GDT solver are based on the Sommerfeld radiation condition [56] which is described by Sommerfeld [57] as:

$$\frac{\partial u}{\partial t} + C u_n = 0 \tag{3.3}$$

where u is the generic flow variable, C the waves phase velocity and u_n is normal to the boundary. When there is no considerable gas flow through a boundary, fixed value boundary conditions are preferable over NRBC on the grounds of results stability; if NRBC are used in such situation, local oscillations of pressure and density values are amplified, resulting in unstable motion.

To show the importance of these numerical effects and optimize the boundary conditions, simulations were performed of the well known 2-dimensional solution of free supersonic expansion by a capillary orifice, and the dimensions that describe the shock wave pattern measured (Mach disk diameter, distance from nozzle and barrel shock diameter, similarly to section 3.2). For these simulations the pressure in the gas reservoir is set at 1 bar and the vacuum chamber has an initial base pressure of 0.1 mbar. The domain was chosen to be a rectangle for 2D simulations (shown in Fig. 3.4) and a rectangular box for 3D simulations.
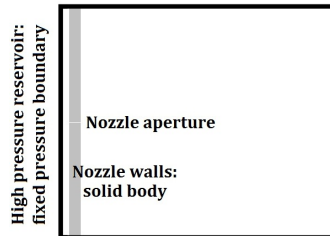
Figure 3.4: Simulation domain before the simulation is run. The grey regions represent solid bodies (in this case the nozzle system), which depending from the simulation to be run can be adjusted (sharp edged orifice, capillary, converging-diverging etc).

The case of the 2D simulations is treated for boundary conditions optimization, as computing time is shorter by about two orders of magnitude. The optimized conditions are then extrapolated and applied to the 3D case for further verification. With reference to Fig. 3.4, the points of interest, as far as boundary conditions are concerned, are the top, bottom and right boundaries, since the left boundary is occupied by the high pressure reservoir of gas and needs hence to be set to fixed value boundary condition.

GDT allows setting different boundary conditions on each of the sides of the rectangle/faces of the box, or even in different regions of the same face. If all three boundaries are set as NRBC, it is observed that the gas jet expands as predicted up to the expected equilibrium condition. This steady state stays stable only over a very short time of less than 100 μs. Soon after, it starts wobbling and becomes unstable until, only about 0.5 ms after the start of the process (depending on the thermodynamic parameters and on the dimensions of the computation domain), it grows out of the steady state and starts expanding up to the filling of the whole domain. Such time instability is shown in Fig. 3.5, where subsequent stages of the process are illustrated.

In principle the optimum configuration should be to have only the right border as open boundary, and top and bottom ones as fixed values. This is due to the consideration that no considerable amount of gas is flowing perpendicularly to the top or bottom boundary at supersonic speed (as the supersonic flow is confined within the barrel shock), while on the other hand the *slip lines* (thin portions of the supersonic flow which extend horizontally from the edges of the Mach disk) result in a considerable portion of gas to be transported out the right boundary at supersonic speed. When such solution is simulated, the time instability of the system is overcome, and the shock wave pattern stays stable (i.e. maintains roughly the same dimensions and does not exceed the simulation domain) over long times (>5ms). However, two problems are observed:

1. The shape of the jet is elongated in the horizontal direction (i.e. the distance of the Mach Disk from the nozzle is far greater than twice the diameter of the disk itself, as expected).

2. A strong wobbling is observed.

Such situation is illustrated in Fig. 3.6:
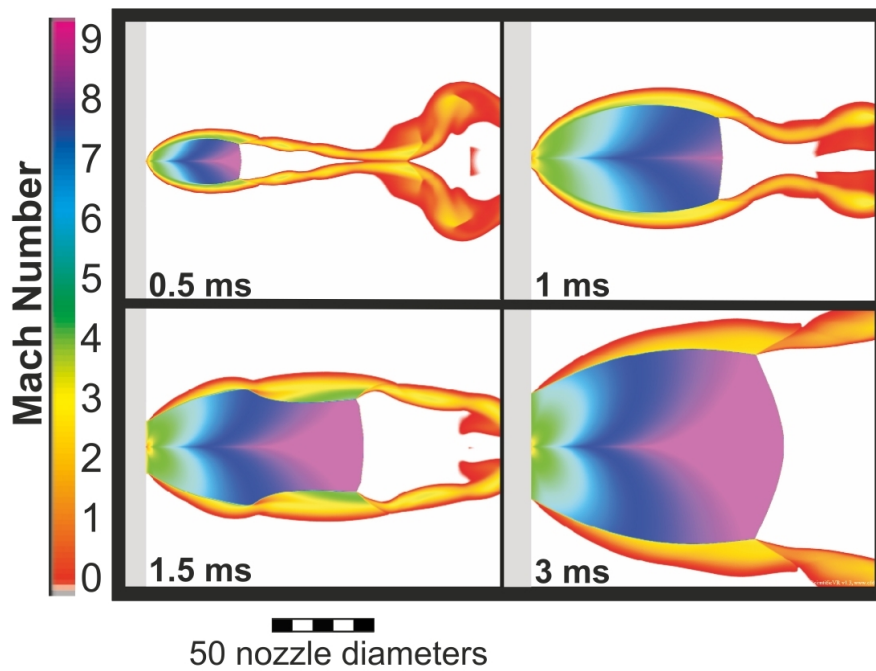
Figure 3.5: Subsequent stages (top line 0.5 ms; 1 ms; bottom line 1.5 ms; 3 ms) of the free expansion of an axis-symmetric gas jet computed by using NRBC conditions on all three gas boundaries. Time instability of the equilibrium pattern is shown. The flow reaches a first condition of equilibrium (top left); then expands further and reaches a second position of equilibrium (top right); only to show some instabilities (bottom left) and finally blowing up (bottom right) until it eventually exceeds the domain. The pressure in the high pressure reservoir is considered to be at full value already before the simulation begins, hence modeling a step pressure rise.
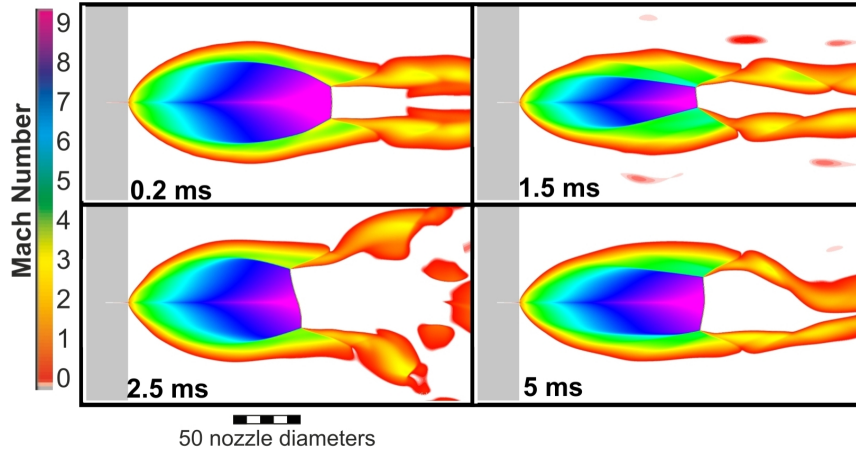
Figure 3.6: Subsequent stages (top line 0.2 ms; 1.5 ms; bottom line 2.5 ms; 5 ms) of the free expansion of an axissymmetric gas jet computed by the GDT code using open boundary conditions only on the right boundary. Elongation and time instability of the equilibrium pattern is shown.

The severe wobbling observed is again a consequence of the instability caused by NRBC in regions were supersonic flow is negligible. Much better results are obtained by setting the boundary regions of the right boundary not exposed to supersonic flow to constant fixed pressure, in order to stabilize the results. In the regions where supersonic flow is not negligible, i.e. downstream the slip lines, NRBC are preferred, to avoid reflection of artifact shock waves formed at the interface between the flow and the constant pressure boundary. Since no knowledge of the exact positioning of the slip lines is known *a priori*, the portions of the right boundary to be set to NRBC needs to be estimated from a simulation in which all boundaries are set as constant value ones. These estimates are used to produce a first simulation with mixed boundary conditions, which is iteratively improved to yield the best performance. When this process is completed, even though spurious reflections by fixed value boundary conditions are not completely eliminated from the right boundary, they are found to interfere mainly with the slip lines, modifying their shape and thickness, but featuring only a negligible influence on the region of interest. This improvement is so pronounced that it is possible to halve the vertical dimension of the simulation domain, bringing the boundary much closer to the region of interest where shock waves are present. This is a proof of the efficiency of the boundary conditions chosen, as proximity of the boundary to the

region of interest without creating large artifact waves is one of the main figures of merit when assessing boundary conditions impact. Quantitatively, the improvement can be seen from the comparison of the shock waves structure, up to the Mach disk, in the 4 different cases, corresponding to different times of the expansion, shown in Fig. 3.7. In particular, monitoring the Mach disk position, the Mach disk diameter and the barrel shock diameter, one finds them to be constant within <7.5 % in all the simulated time (650 ms) after attainment of the equilibrium state (about 300 μs after the beginning of the expansion). This indicates that the system does not change after the time needed for the perturbations to travel to the boundary and back, and thus these artifact reflections are only creating an effect below 7.5 % on the measured shock wave structure.

To further sustain the claim that the wobbling and pattern growth effects observed are indeed due to numerical artifacts and are not a real physical effect of the system, it should be noted that the effect has been shown in this work to decrease for simulations done with a larger grid up to the point of being no more noticeable. This is true regardless of the grid pitch of the simulation domain. Therefore, it is concluded that not only is the wobbling and pattern growth an artifact effect, but also it is only due to the effects of boundary conditions proximity, and is not an effect of numerical instability, which would instead depend on the grid pitch rather than on the proximity of the boundary conditions.

The model described above has been implemented also for the 3D simulations with the same procedure: estimating the regions of supersonic flow by simulating it with fixed value boundary conditions all over, and applying NRBC in the regions affected by it, determined by a reiterative process. The GDT code was furthermore expanded with purpose-written C++ analysis modules which automate variables modification and simulation runs, import data from GDT and compute and display observables of interest, enhancing the ability of GDT to run and compare large numbers of simulations.

3.4   Variables and observables

This sections describes the parameters which are varied in the simulations and hence optimized, together with the observables which are monitored, and serve therefore as the quality parameters for the optimization.
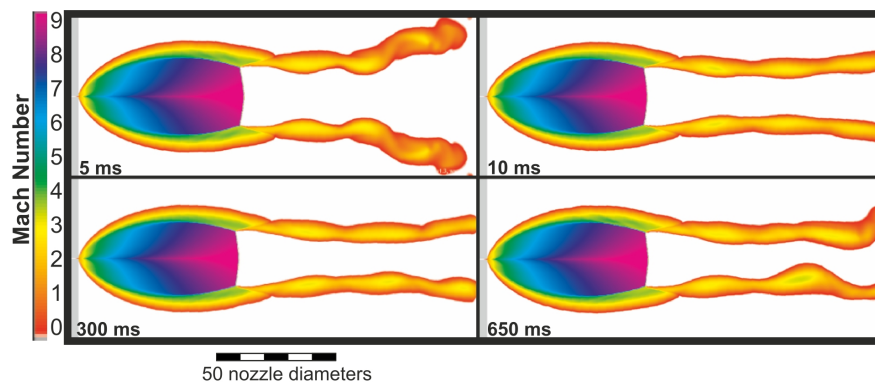
Figure 3.7: Subsequent stages (5 ms, 10 ms, 300 ms, 650 ms) of the free expansion of an axis-symmetric gas jet computed by the GDT code using optimized boundary conditions (NRBC on the right hand side boundary where supersonic flow is present, fixed value boundary conditions on the remaining 3 sides of the domain). The equilibrium pattern is present in the region of interest, while the only differences involving the slip lines. The pressure in the high pressure reservoir is considered to be at full value already before the simulation begins, hence modeling a step rise.

3.4.1 Variables overview

The analyzed system is a generalization of the nozzle-skimmer system for axis-symmetric jets: instead of using circular nozzle and skimmers, the nozzle and skimmer width/height ratio are varied, obtaining the circular configuration as a particular case. Furthermore, the relative orientation between nozzle and skimmer is varied, being tested in both the parallel and the perpendicular configurations. This jet generation system was investigated varying 6 geometric variables, as shown in Fig. 3.8: the skimmer aperture angles (α and β); the width of the skimmer slit (S_W); the depth of the skimmer structure (S_D); the nozzle-skimmer distance (d_{ns}) and the width of the nozzle slit (N_W). For consistency with the existing literature, all length units are normalized to the nozzle slit height, equivalent to the nozzle diameter for standard axis-symmetric setups, and are therefore dimensionless. The skimmer slit height is also kept equal to 1. In addition to these parameters, the pressure ratio between the gas reservoir and the expansion chamber (R) and the common gas temperature in the two environments across the nozzle (T) are also varied.
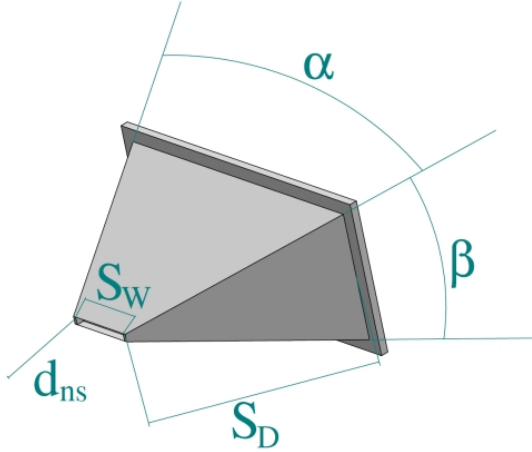
Figure 3.8: Definition of the geometric variables of the skimmer.

3.4.2 Observables overview

Concerning the observables to monitor, in line with current literature, this work includes the Mach number downstream the skimmer (M), which gives an indication of the efficiency of the expansion and hence of the directionality of the jet, as well as the geometrical dimensions of the gas screen: width and depth (W and D respectively), which directly affect the resolution of the monitor as discussed in Chp. 1. However, in this work are also presented three original quality factors, not used in literature, but studied to serve the precise scope of beam instrumentation. Indeed, while elements like the Mach number and thus the temperature play a crucial role in most applications of cold gas jets, they are less relevant to beam instrumentation applications. Indeed, cold gas targets for molecular spectroscopy, for example, need to achieve temperatures in the mK regime to increase the resolution of the measurement, with values as high as a few K being unacceptable. This is also due to the need of relaxing the internal degrees of freedom of the molecule, which is particularly relevant in applications willing to study the roto-vibrational energy levels [58].

On the other hand, in beam instrumentation, the relevance of final temperature is linked to the final velocity: once the final velocity has been nearly reached (within a few percent, i.e. <20K final temperature) and the expansion has reached the point where no more collisions happen between molecules, so that the molecular flow is established, any further reduction of temperature bears little advantage for the operation of the

instrument. Other factors, which are not even mentioned in the literature analyzing applications in spectroscopy and similar fields, are instead more important.

A general formulation of the jet performance along these lines can be done on the basis of the following original three quality factors: jet geometry, density homogeneity and confinement. In short, the quality of the geometry can be assessed by the ratio G_R between the long and the short dimensions of the jet screen, defined as the FWHM of the density profile in the corresponding directions. The region enclosed by these dimensions will henceforth be referred to as *the screen*. The density homogeneity H_ρ is best expressed by the standard deviation of the density profile across the screen region, normalized to the mean density. The confinement K relates to the sharpness with which the tails of the density profile roll off, and is expressed by the percentage of total gas mass past the skimmer enclosed in the screen region. Because of their definitions all three quality parameters are dimensionless.

These quality factors are computed downstream the skimmer at the coordinate when the hard sphere binary collision frequency drops to the point that the computed Knudsen number exceeds 0.2, the continuum description of the flow fails and the system approaches the molecular flow region where inter-gas collisions rarefy until their effect becomes negligible within the scale of up to few meters typical of the jet application. Since only a negligible number of collisions occur past this point, the gas properties are frozen to their terminal value, as it was discussed in Chp. 1. From this point on, the cross section of the jet only scales geometrically due to the spread in momenta, making this the first point in the jet expansion where it is possible to perform a comparison between different nozzle-skimmer systems jet performances. This point can be calculated to occur, from the plot presented in [43], about 5 skimmer diameters beyond the skimmer tip. This is where all quality factors in the following are computed. The following subsections deal with each of these original quality factors separately, delving into the precise inner working of how they are calculated and justifying the choices done in their definition.

3.4.3 System description

Let the gas jet be expanding along the nozzle axis, named the x axis. For the sake of the discussion, assume one can roughly identify, by simple inspection, a geometric plane in which the screen lies. The discussion can be easily generalized to avoid this

assumption, by measuring the screen width for all angles and choosing as the plane in which the screen lies the one which maximizes the screen width. Name this plane the xz plane, with the screen expanding longitudinally in the x direction. A representation of the monitor setup is found by having the projectiles impinge on the screen parallel to the yz bisector, ignoring any focusing effects on the projectile beam which can cause the impinging direction not to be parallel to the yz bisector. The instances of this family of impinging projectiles trajectories can be identified with their y value when z=0 (i.e. the intersection with the y axis of the projection on the xy plane). As there is a 2-dimensional cross section for the projectile beam, one should also include a parameter x to describe the family of trajectories. Nevertheless, while there is a considerable change in density when moving in the yz direction over the screen, the 4 cm of interest for the practical application are a sufficiently small distance if compared to the longitudinal dimension of expansion of the jet, that one can assume no significant change is taking place along this axis, and limit the discussion to the 2D analysis.

As a projectile goes along its yz path, its ionization cross section area will sweep a cylindrical volume whose gas-density at any point is given by the simulation. Therefore, one can define a quantity I, the *integrated density*, proportional to the number of gas atoms encountered by the projectile, and hence to its probability of interaction by simply integrating the density over the full path ξ (normalized to 1):

$$I \; = \; \int_0^I \rho \, d\xi \tag{3.4}$$

It is noted that the discussion leading to eqn. (3.4) can only be applied if the density of the gas times the ionization cross section is sufficiently small, i.e. if it can be safely assumed that no two gas molecules will be shadowing each other from the impinging projectile. This is normally the case for the density achievable in a vacuum system and the cross sections available (see Chp. 1). Also, I will be a function of the parameter y: I(y). A plot of I(y) would yield some bell shaped curve, centered on the axis of the jet. Therefore, the width of this bell shaped curve will be a measure of the longest dimension of the screen, named the *screen height* and indicated with h.

3.4.4 Screen Height

The *screen height* can be defined as the distance between the two projectile paths whose integrated density equals a certain percentage of the maximum integrated density: the

choice of this percentage value, called *cutting percentage*, P_{cut}, is to be further discussed. The screen height defines the region of the screen that will be used in experiments, and is the one which will have to have a particular width, defined by the specifications of the projectile beam; e.g., in the case studied in this work, 40 mm. P_{cut}, on the other hand, defines how homogeneous this region will be and influences the *accuracy* of the monitor. By choosing a $P_{cut} = 50\%$, one is stating that it is acceptable for a certain region of the monitor (in principle) to have half the sensitivity of the most sensitive part, which would bring about the need to normalize the measurements with a previously measured integrated density curve. On the other hand, choosing P_{cut}=90%, though giving a good homogeneity in integrated density over the measurement range, could result in much too short a screen, affecting badly the resolution, as will be clearer when discussing the measurement of the *screen depth*, in the next subsection. P_{cut} will, therefore, be used as an optimization factor, to be fixed after the full equations for the three relevant observable of accuracy, resolution and confinement are derived.

3.4.5   Screen depth

If the density value along each projectile path y is plotted, it results in again a bell shaped curve with a certain width linked to the second transverse dimension of the screen: its *depth*. Similarly to the case of the *screen height*, the screen depth is defined through a cutting percentage $P_{cut,d}$. The screen depth influences mainly the resolution of the system, indeed any interaction taking place at a different depth in the screen images on the detector in a place where a different projectile height images, introducing hence a smear in the image of the beam. Because of this, $P_{cut,d}$ has to be chosen as low as possible, so as to make sure that there is a negligible contribution to smearing from gas outside the screen, as this contribution would not be taken into account in calculations. In this work a value of $P_{cut,d} = 10\%$ is chosen, so that at least an order of magnitude of sensitivity divides regions in the screen from regions outside it.

3.4.6   Accuracy

It is clear from what has been said that the real jet-screen will not be perfectly well located in space, forming a sharp-edged rectangular cross section. Rather, the density profile will have a smoother contour. Since the interaction probability, and hence the sensitivity of the monitor scales linearly with the density, it is clear that it will

not be homogeneous over the whole region of interest for the measurement. This inhomogeneity, when not corrected, will result in practice in an error associated to the measurement, due to the varying sensitivity of the screen in different spots. The accuracy will be the best the least the difference in integrated intensity over the region of interest.
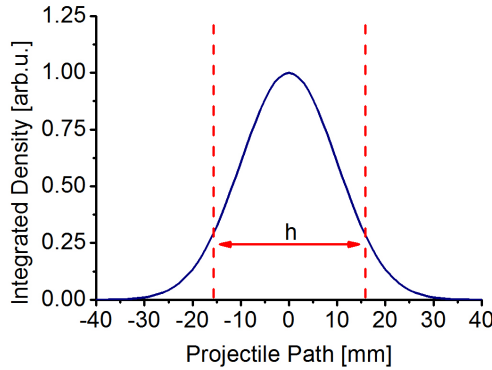
Figure 3.9: Plot of the integrated density against the projectile path (y), showing the extension (exaggerated for clarity) of the screen region.

Fig. 3.9 shows an example of a plot of the integrated intensity for different projectile paths, together with the extension of the screen, h. To assess the accuracy, one is therefore given the choice between a stochastic indicator, such as the standard deviation of the integrated density distribution, and a peak to peak measurement. The standard deviation, in its meaning of average deviation from the average value, provides a best estimate of the expected accuracy error, whilst a peak to peak measurement indicates instead the maximum possible error. In this case, however, to use a peak to peak measurement for the accuracy would be to boldly shift the weight of the measurement only on its upper and lowermost parts, without taking into account the actual distribution, therefore, even in the very convenient case of a quasi-square distribution such as the one in Fig. 3.10, the accuracy would only depend on the extremes, and a peak to peak accuracy indicator would give the same value for both curves in Fig. 3.9 and Fig. 3.10, which is clearly a wrong approach.

On the other hand, applying the standard deviation indicator to both curves yields a value of 0.07 for the curve in Fig. 3.10 and of 0.23 for the curve in Fig. 3.9, well accounting for the difference in shape. Therefore, the standard deviation proves to be a better indicator for accuracy and will be used in the remainder of this work. Actually,
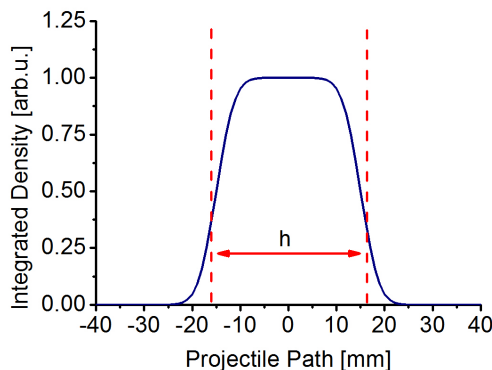
Figure 3.10: Example of a plot of the integrated density against the projectile path (y), showing the extension of the screen region in the case of a more homogeneous screen.

to provide an immediate possibility of comparison, the accuracy will be defined as the standard deviation normalized to the average integrated intensity value over the screen.

3.4.7 Resolution

The resolution of the apparatus is intended as a measure of the smearing of the image of the beam on the detector and is, by the nature of the particular apparatus, different in the horizontal and vertical direction. The horizontal one is due solely to the quality of the extraction electric field and the temperature of the jet molecules. The vertical one is instead due to the thickness of the screen as well, and the following discussion will therefore focus on it, postponing considerations on how the drift of the ions in the extraction field affects the resolution to later chapters. The resolution as treated in this section is intended to be only the resolution intrinsic to the gas screen, which is further worsened by the ion drift. To assess the quality of the geometry of the screen with respect to the resolution, it is necessary to measure its geometrical resemblance to a thin sheet.

To a first approximation, assuming a rectangular cross section, a thicker screen would decrease the resolution, while a thinner one would increase it, as discussed in Chp. 1. Nevertheless, one cannot simply take into account a simple dimension, like, e.g. the screen depth, but rather express the quality of the resolution by a ratio between the depth and the height. This geometric quality factor will be named G_R, and set equal to the ratio h/δ that is height over overall depth (to be defined in the following sub-section, as a generalization of the local depth described above).

The vertical resolution R, intended as the maximum displacement that an event can have on the screen from the point it is supposed to be imaged, has thus the dimensions of a length, and is equal (for a 45° geometry) to the overall depth δ of the screen as seen from the projectile. In order to take into account the scaling factor, one needs to normalize h to the required length L_r, resulting in the following set of simple equations for R:

$$G = \frac{h}{\delta} \tag{3.5}$$

$$R = \frac{L_r}{G} mm \tag{3.6}$$

3.4.8 Overall Depth definition.

When assessing the performances of the screen as a whole, one has to consider that each projectile path has an associated local depth of the screen, and that this depth is in general different for different paths. Again, plotting the local depth in terms of the chosen path y will produce a curve looking like the ones in Fig. 3.9 and Fig. 3.10, from which it is necessary to extract a single number: the overall depth. This can be chosen either to be the average of the local depth over the screen region, or as being the largest. Being the nature of the system stochastic in nature, the average provides a better estimation of the resolution of the system to help finding an optimized solution by giving a more general (as opposed to local) quality indicator.

3.4.9 Confinement

The confinement is the observable which gives an indication of how much the gas is concentrated on the expansion centerline, hence providing a direct link with the peaking factor κ. It is defined as the percentage of total gas mass enclosed in the region of the screen as defined in the previous sub-sections. This definition reflects the understanding that a higher percentage of the gas mass enclosed in the screen region results in smaller halo of the gas jet, and hence a higher peaking factor. Of course, being the definition of the screen dependent on the choice of the cutting percentages, the confinement will also be a function of those parameters.

3.5   Simulation plan

As it was mentioned in Chp. 2, the study of planar flow presents additional computational challenges as compared to the study of axissymmentric flow, mainly due to the need of analysing it in a 3D scheme, which makes the numerical CFD computation extremely time consuming. In the case of interest for this work, even using a dedicated workstation and an optimised CFD code, the vast number of different simulations needed calls for the simulation domain to be carefully considered so as to be able to reduce it to very few grid cells with only an affordable loss in precision.

Analysis of the 2D configuration allows to design a 3D domain compatible with affordable computing times and providing reliable results as well. Such domain will have all boundaries set to fixed value, with only the regions interested by supersonic flow being set to NRBC, as discussed in section 3.3, and be a cube with 100 grid cells at its vertex. Fig. 3.11 shows a sketch of the cubic domain, including the slit and the skimmer.
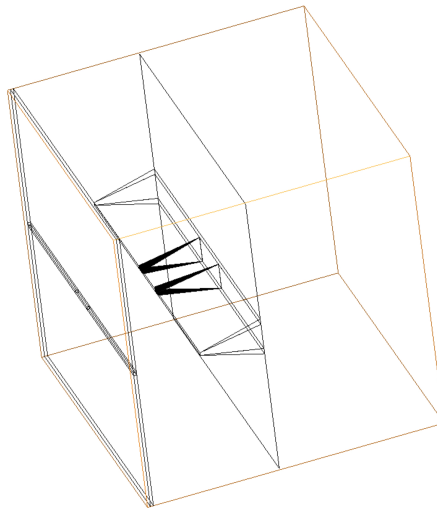
Figure 3.11: 3D simulation domain, slit and skimmer included. Borders of the domain in shades of orange. The distance of the skimmer from the slit (left border) has been exaggerated (roughly doubled) for clarity.

In order to minimize computation time, tests to establish the time needed to reach equilibrium were run. To do that, a set of 100 exploratory simulations with different variables combinations were run. The tests showed that in all conditions tested the
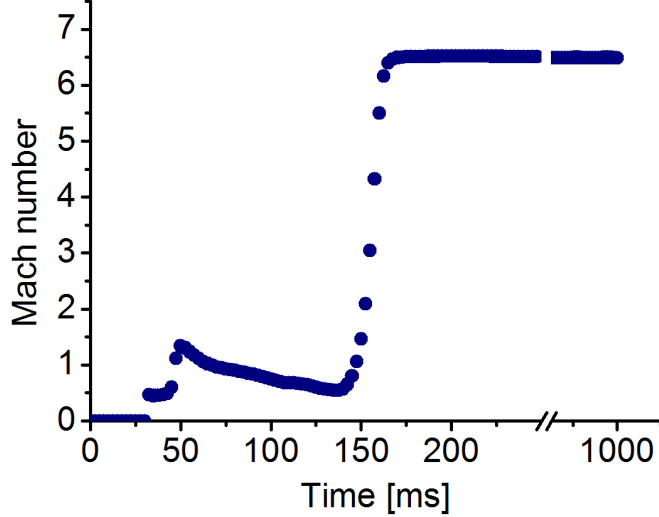
Figure 3.12: Time evolution of the Mach number computed at 5 skimmer diameters downstream the skimmer tip. The initial delay gives an indication of the time taken for the first molecules to travel to the point of computation, from which a velocity 764 m/s can be calculated, compatible with the theoretical prediction of 790 m/s.

density values in the simulation domain fall within 5% of the long term equilibrium solution (simulated up to 10ms) within 750 μs in the worst case, which was thus taken as the simulation runtime, bringing the computation time to about 550s per simulation. Fig. 3.12 shows an example of one such plot, in which the Mach number downstream the expansion, at 5 skimmer diameters downstream the skimmer tip is plotted.

Aside from the quantitative data contained in the plot (i.e. equilibrium is reached to within 5% of the final value within 200 μs in this particular case), qualitative inspection of Fig. 3.12 shows another interesting feature. The time delay before the occurrence of any rise in Mach number is equivalent to the time taken by the first molecules to travel up to the investigated point. This is equal to 32 μs, compatible, as expected, with a travel speed of 764 m/s, just below the calculated terminal velocity of 790 m/s, indicating an incomplete temperature to kinetic energy conversion.

3.5.1 C++ modules

The analysis of the simulations involves a large set of data which calls for an automated analysis procedure. Therefore, a dedicated C++ software was developed, able to read the data directly from GDT, record it in a temporary matrix internal to the program,

rearrange it and finally create a new user readable file with the data conveniently rearranged so as to be able to visualize it with plots. In Appendix C are described the requirements for this software, the GDT analyzer, its protocol layout and part of its implementation.

3.6 Results

3.6.1 Configurations comparison

About 8,000 simulations were run, exploring the whole variable space by assigning 3 different values to each variable, in both the perpendicular and parallel nozzle-skimmer slits configuration. A subset of these simulations, showing only 2 different values for each variable, is shown in Fig. 3.13. On the x-axis is the identification number of each simulation, whose variable set can be read on the y axis in Fig. 3.13a. On the y axis of Fig. 3.13b-d are plotted the resulting density homogeneity H$_\rho$, geometrical ratio G$_R$ and confinement K.

The variables are as discussed previously, the only exception being the pressure, for which a pressure ratio $R = \frac{P_{reservoir}}{P_{chamber}}$ is preferred.

Four combinations turn out to be of particular interest as they resemble commonly used configurations: a) circular nozzle and skimmer; b) circular nozzle and slit skimmer; c) slit nozzle and slit skimmer parallel and d) perpendicular to each other, corresponding respectively (see Fig. 3.13a) to simulations number 1-64; 65-128; 129-192 and 193-256. It must be noted that in configuration a, since the nozzle has circular symmetry, angles α and β are interchangeable, and therefore the simulations with small α and large β have identical results to the ones with small β and large α (the screen long and short dimensions are redefined by the data analysis code depending on the actual orientation of the screen). Furthermore, the geometric ratio for simulations in which $\alpha = \beta$ is always evaluated equal to 1 as the screen formed in this case is symmetric, and in practical applications a collimating slit is needed to form the planar jet. In what follows these configurations are evaluated against each other on the basis of the numerical results, using as quality factors the values of H$^\rho_{-1}$, G$_R$, and K for the configuration under exam, normalized to the values of the same observables obtained for configuration d: slit nozzle and skimmer perpendicular to each other. H^ρ_{-1} is preferred to H$_\rho$ so that higher values mean better performance. In order to give an indication of the overall influence of
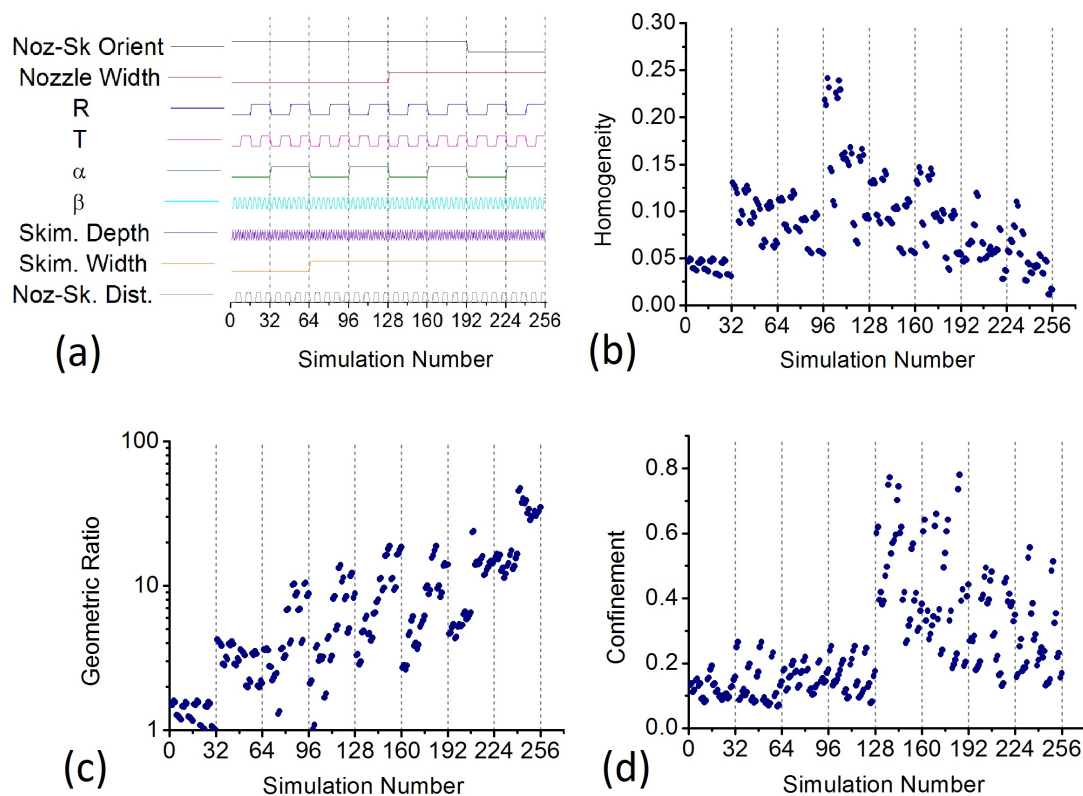
Figure 3.13: Homogeneity *(b)*, geometric ratio *(c)* and confinement *(d)* for each of the 256 simulations plotted on the x axis. The set of variables used for each simulation can be read on the y axis of plot *(a)*. For each of the three graphs, the most influential variable, i.e. the variable whose variation results in the greatest change in the corresponding observable, has been highlighted by using different colors for data points corresponding to different variable values. For homogeneity, it is shown that nozzle width has the greatest influence: i.e. rectangular nozzles perform better than circular ones. For geometric ratio, pressure ratio has the greatest influence, as for rectangular nozzles, increasing the pressure ratio consistently leads to geometric ratio improvement. For Confinement, the most relevant variable is the skimmer depth, whose increment consistently leads to an improvement in confinement.

the configuration change alone, each normalized quality factor has been calculated for each competing configuration, *a*, *b* and *c*, and for all available combinations of other variables, and all these values averaged. For the purpose of optimization, it is instead more interesting to compare the best achievable value for each configuration. Table 3.2 lists both the average values and the best values of H_ρ^{-1}, G_R, and K for the different configurations.

	Average			Best Value		
	a	**b**	**c**	**a**	**b**	**c**
H_ρ^{-1}	0.8	0.46	0.58	0.37	0.21	0.3
G_R	0.13	0.31	0.51	0.09	0.29	0.4
K	0.44	0.55	1.55	0.48	0.45	1.4

Table 3.2: Performance ratio between configuration d (slit nozzle and skimmer perpendicular to each other) and the competing configurations: a (circular nozzle and skimmer), b (circular nozzle and slit skimmer) and c (slit nozzle and skimmer parallel to each other). Ratios lower than 1 indicate a better performance of configuration *d*.

Table performance-comparison shows that configuration *d* performs sensibly better than the others with the exception of the confinement, which is about 50% better in configuration *c*. In particular it can be seen how, by using perpendicular slits for nozzle and skimmer, the homogeneity and the confinement of the planar jet are increased when compared with commonly used configurations with circular nozzle and also outperforms configuration *c* by a similar factor in homogeneity and geometric ratio, at the expenses of losing about 50% in confinement. The geometric ratio also increases when using configuration *d*, in particular when compared to configuration *a*, in which of course one needs to use additional collimating slits to obtain a planar jet.

For practical applications, optimized performance is a more interesting parameter. It can be seen from the right hand side of table 1 that the improvement in homogeneity and geometric ratio is sensibly increased. The same is true to a lesser extent for the confinement. The factor of 2 to 3 that can be gained in geometric ratio by using the proposed configuration *d* results directly in a correspondingly higher density available for the jet in its core (as the gas flowing outside the required geometric ratio does not need to be scraped out). This value can therefore be compared with the effect obtained by Hashimoto and co-workers [32] by use of magnetic focusing, which was reported

to be about 2. It is thus an advantage of the configuration proposed that comparable performance improvement can be obtained without the further complication of an added magnet and corresponding field, beside not being restricted in the choice of gas to a molecular gas with a sizeable magnetic moment.

Finally, it should be mentioned that in practical applications, a further collimating slit or skimmer is used downstream the first skimmer. Given the nature of the flow, which at this point is no more thermodynamic, but molecular, this second skimmer collimates the jet simply geometrically; therefore by increasing the distance from the jet source to the target and reducing the aperture in the second skimmer, is possible to increase the geometric ratio indefinitely. However, this comes at the cost of reduced jet density at the target region. Collimating skimmers placed in the molecular flow region are not included in the simulations, for a two-fold reason. Firstly, they can be applied to any configuration and used to obtain identical effects, geometrically shaping the gas jet, and secondly, continuum flow fails so far out in the expansion, and the Euler equations are no more applicable.

3.6.2   Variable by variable analysis: custom observables

Having identified a nozzle-skimmer configuration yielding best performances, it is possible to narrow down the variable space and run additional simulations with finer details to assess the impact of different geometric variables on the creation of the planar jet. Fig. 3.14 shows two examples of this study: the first three plots (Fig. 3.14a-c) show how H$_\rho$, G$_R$ and K change for increasing angle α (x axis), and angle β (curve parameter). The last three plots (Fig. 3.14d-f) show how H$_\rho$, G$_R$ and K change for increasing skimmer slit width S$_W$ (x axis), and angle α (curve parameter).

It is apparent from the first plot that the homogeneity of the screen slightly worsen when changing from 5° to about 15° as the system moves away from a quasi-axis-symmetric configuration and more marked expansion fans are created past the skimmer, only to improve past 15° due to a dramatic increase in geometric ratio which makes the frontier regions of the screen less influent on the overall homogeneity. Conversely, increasing β only takes the system away from the quasi-axis-symmetric configuration, without the compensating effect of improving G$_R$. Therefore, increasing β consistently leads to homogeneity worsening. Fig. 3.14b shows the behavior of G$_R$ when α and β are increased, confirming the intuitive trend of G$_R$ improving with increasing α and
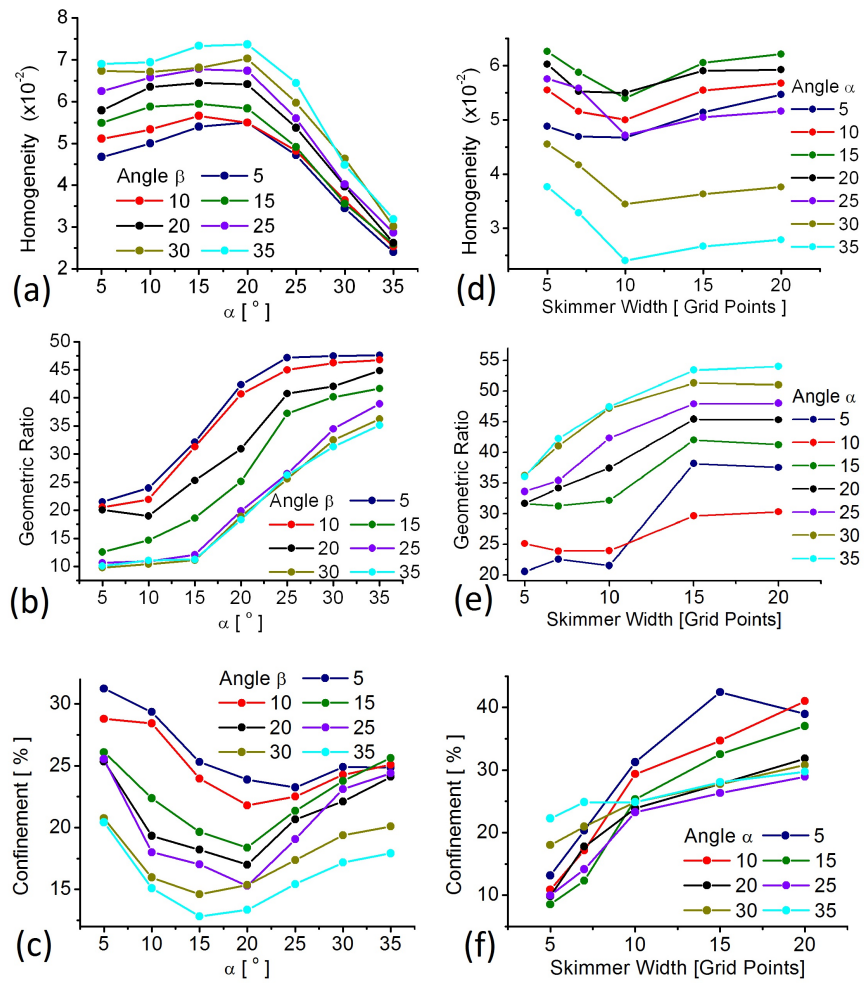
Figure 3.14: Analysis of homogeneity, geometric ratio and confinement for finer variations of angles α and β *(a-c)* and skimmer width *(d-f)*.

decreasing β. Finally, analyzing Fig. 3.14c, it can be seen how extreme values of α lead to better confinement, with K touching a minimum in the $10° \div 20°$ region, depending on β . This can be understood in terms of the density profile fall-off, which is sharper for small α, due to the gas flow being restricted by the inner walls of the skimmer aperture, as it is also proved by the increasing influence of the skimmer depth for smaller and smaller aperture angles α and β (see Fig. 3.14d-f); while conversely confinement improvement is again an effect of having large G_R for large α leading to the creation of a larger screen, hence including more gas mass.

The behavior of α identified for all three observables H_ρ, G_R and K stays consistent also when S_W is changed, as it can be seen in Fig. 3.14d-f, where α is used as curve parameter. Furthermore, Fig. 3.14d shows that homogeneity is optimized for skimmer width matched with about half the Mach disk diameter, due to a trade off between efficient extraction of the coldest, innermost part of the jet, and G_R increasing with larger S_W, which, as discussed above, makes the frontier regions of the screen less influent on the calculation of homogeneity. Indeed, with reference to Fig. 3.14e, G_R improves with increasing skimmer width, as more gas is extracted from the supersonic expansion. This effect decreases as the skimmer width approaches the dimensions of the Mach disk shock wave, and the barrel shock boundary, which defines the boundary of the supersonic flow, is approached, preventing more gas to be extracted from the jet core. A confirmation of this was sought by running the simulations in Fig. 3.14e for increasing values of R, producing a larger jet, with larger Mach disk: in this case the improvement in G_R is linear with R as expected.

Finally, confinement increases almost linearly with skimmer width, due to the skimmer width approaching the dimensions of the barrel shock, where the internal temperature of the jet has an abrupt drop, reflecting in a sharper fall-off of the density profile on which the confinement is calculated. Again, this effect shifts towards larger skimmer dimensions if R is increased, furthering the barrel shock boundary and confirming the explanation above.

In conclusion, from the plots in Fig. 3.14 it can be inferred that the angle α is the most influential variable for both the homogeneity and the geometric ratio observables, where it brings about, in the investigated ranges, a variation of a factor of 2 and 4 respectively, to be compared with the influence of the angle β and the skimmer width, which have factors of 1.5 and 2, and 0.5 and 2 respectively. For most systems, hence,

α should be increased as much as possible, until instabilities in the jet pattern appear, or the worsened confinement becomes a problem. Conversely, the angle β should be decreased as much as possible, bringing about an improvement in all 3 observables. The lower limit to β is posed by the occurrence of instabilities for low β values [41]. Less relevant is the effect of skimmer width, which should be incremented as much as possible until the homogeneity worsening becomes unacceptable.

Given the amount of different variables, and the specificity of the quantitative results to the particular system analyzed, including numerical approach and boundary conditions, the results from a larger set of such plots are best summarized by identifying behavioral trends spotted when changing each variable and representing them schematically in a table.

A trend is intended to be found when the form of the functional relationship between the observable and the variable under investigation is preserved in the simulations regardless of the actual values of the other variables. This way, it is possible to draw a table, shown in Fig. 3.15, which summarizes the simulated behavior of each observable (column entry) when the respective variable is increased (row entry). One can identify linear relationships (straight arrows), parabolic relationships (curved arrows), and more complex relationships (circles), where even the form of the functional relationship depends on the value of some secondary variables (indicated inside the circle), and hence, according to the previous definition, a trend is not found. The latter is a qualitatively different behavior as compared to the first two cases, where the shape of the trend does not depend on the remaining variables, while still the details of the trend, such as the gradient of the linear relationships, will depend on the values of the remaining variables. In the table the bold lines represent very clear trends, defined as those trends where the average over all points of the best fit Pearson value lies above 90%, while the slimmer lines represents less evident trends, where the average best fit Pearson value lies between 75% and 90%.

Amongst other information, this table gives an indication of how sensitive the gas jet is to the geometry of the nozzle-skimmer system. Furthermore, it also gives an insight as to which variables have a stronger impact on the performance of the jet in terms of homogeneity (namely α and S_D), geometric ratio (α, S_W and d_{ns}) and confinement (β, S_W and S_D), beside giving guidance for directing experimental optimization efforts. In particular, the table also shows which of the trends, and corresponding parameters,

Figure 3.15: Table of simulated trends, the arrows schematize the behavior of the column observable when the row variable is increased. Trends shown in red are the most influential ones: by optimizing the relevant parameter, improvements larger than a factor of 2 in the corresponding observable can be obtained.

have the largest impact on the observables: optimization of the parameters of the trends shown in red (i.e. α, SW and $Dist$) leads to improvements of the corresponding observable by more than a factor of 2.

The data shown up to this point allowed to identify an optimized configuration which addresses several trade-offs between the three observables used and the technological limits. The crucial factor for jet performance is the pressure ratio R. Indeed, increasing R always results in better performance for all observables; in particular, homogeneity decreases with the logarithm of R, and similar trends can be observed for geometric ratio and confinement, even if with less clear trends (Pearson Value $< 70\%$). However, improvement with increasing R is limited by cluster creations [9] and vacuum pumping speed available: in practice, ratios larger than 10^6 are difficult to achieve.

The aperture angles of the skimmer also have a very important role. In general, increasing the angle α improves the performance of the jet with respect to H and G_R, sacrificing only slightly the confinement with respect to configurations with small α. However, too large values for α introduce severe distortions in the jet profile which can result at higher temperatures in jet splitting (see next section for details). Further simulations were run at a significantly lower temperature, to confirm this trend, choosing for this purpose the temperature of 77K, in virtue of its ready availability through liquid nitrogen cooling.

These simulations showed that indeed jet splitting does not occur at this temperature even for large ($>$ 20°) apertures angles. However, for stable operation at higher temperatures, α should be chosen between 25° and 30°. Conversely, β should be kept to above 5°: while decreasing β also proves beneficial to all observables, below 5° the density profile becomes unstable, resulting in jet splitting at higher temperatures.

From what has been said, it is clear that temperature is an important parameter insofar as it allows increasing α and decreasing β, thus improving jet performance, without incurring in jet splitting. This result confirms and expands also previous studies which report a temperature dependence of jet performances, in particular transverse momentum spread, which is observed to decrease with jet cooling through nozzle cooling [9]. However, the lower limit on temperature requirement comes from the increased cluster formation efficiency at low temperatures, thus limiting the usable pressure ratios R and hence jet density. The choice of T will therefore depend on the density requirements of the jet and on the cooling systems available. Indeed, higher temperature jets remain more convenient and economical to use if large skimmer apertures are used, and use of room temperature jet has been successfully reported [59].

The simulations confirm the expected requirement of the skimmer depth SD to be as large as possible, preventing skimmed out molecules to affect the supersonic flow in front of the skimmer. SD is therefore only limited by geometrical consideration in the setup and manufacturing technology. Finally, the simulations show that geometric ratio is optimized for normalized nozzle-skimmer distance between 5 and 7 and skimmer width between 16 and 20. Larger skimmer widths sacrifice G_R and K for slightly better H_ρ.

3.6.3 Variable by variable analysis: standard observables

Given the importance that gas speed and internal jet temperature has in many jet applications (e.g. molecular physics and spectroscopy), an analogous analysis as the one discussed above has also been performed focusing on standard observables, and is also reported in [60]. In what follows are shown the results of the same simulations analyzed in the previous section, but using more conventional observables. Only results from 3D simulations with perpendicular slit-skimmer configuration are included, as they provide the best optimized results. Furthermore, the actual quantitative description of the flow depends strongly on the experimental implementation, i.e. the vacuum

chamber effective pumping speed at the nozzle tip, and are therefore less interesting from a general standpoint than the qualitative trends. Therefore, these results are presented, in analogy with the discussion in the previous section, in a table of trends, shown in Fig. 3.16. The parameters chosen are maximum Mach number M; the screen depth D and width W.

Figure 3.16: Table of simulated trends for the standard observables Mach number, depth and width of the curtain.

The results presented in 3.16 can be compared with the custom observables directly only insofar as the geometric ratio is linked to the depth and width of the screen. The significance of this comparison lies in the understanding of where exactly the behavior of G_R comes from. In particular, it can be seen that, as far as α is concerned, the increase in G_R comes from both the decrease of D and the increase of W. On the other hand, the decrease of G_R with β comes mainly from an increase of D, with W being only slightly varied. Similar arguments are valid for the behaviors of the remaining three variables. On the other hand, the Mach number is not immediately relatable to any of the custom observables, as it rather expresses the efficiency of conversion of potential energy to kinetic energy. It is loosely related to the confinement, as the confinement is linked to the temperature: higher temperatures (corresponding to lower mach numbers) result in higher spreading of the jet and so, partly, in worse confinement; therefore smaller Mach numbers should also correspond to smaller confinements. However by definition, the confinement depends very much on the actual shape of the profile of the screen, which is a global indicator related to the shock wave structure of the system, and in many instances shadows the contribution of temperature.

Comparison of Fig. 3.15 and Fig. 3.16 shows indeed that the confinement follows the same trends as the Mach number with changes of α and β, whilst the skimmer width

influences the shock wave structure more than it influences the Mach number, and as a result the confinement increases even as the Mach number decreases, increasing the temperature of the jet.

Finally, the analysis of the standard observables, all of which are proportional to the Mach number as shown in (2.10) through (2.13), proves to be particularly interesting when the dependence of Mach number from the distance nozzle-skimmer is studied. Indeed, the Mach number shows a maximum as the distance nozzle-skimmer is varied, agreeing with the known result in literature relating the jet density, proportional to the Mach number through (2.13), to the nozzle-skimmer distance [61]. This behavior, sketched in Fig. 3.16, is presented in the plots in Fig. 3.17 in more details. Further interesting examples of this analysis through standard observables are also shown in the plot in Fig. 3.18.
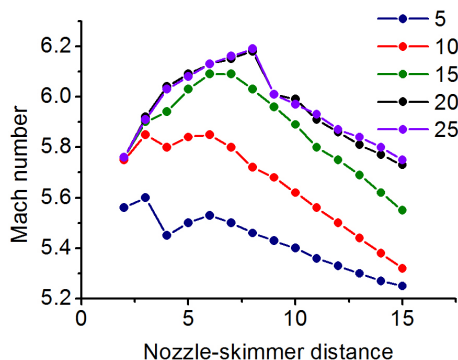
Figure 3.17: Maximum M attained in terms of nozzle-skimmer distance and angle α. A clear pattern is spotted, showing how increasing the angle α increases the maximum M attainable. On the other hand there appears to be an optimum distance nozzle-skimmer (depending on α) for maximizing M.

It can be seen that the nozzle skimmer distance has noticeable effects only on the maximum Mach number and its coordinates. The effects on coordinates is easily explained by the consideration that the second expansion which occurs beyond the skimmer requires some space to be complete, so moving the skimmer further away will shift the coordinates of the maximum accordingly. The gradient of the graph in Fig. 3.18 though is not 1, as the further away the skimmer is set, the more energy is lost by the gas before it reaches it, so the expansion is weaker, and the furthering effect is counterbalanced by this reduction of the expansion.
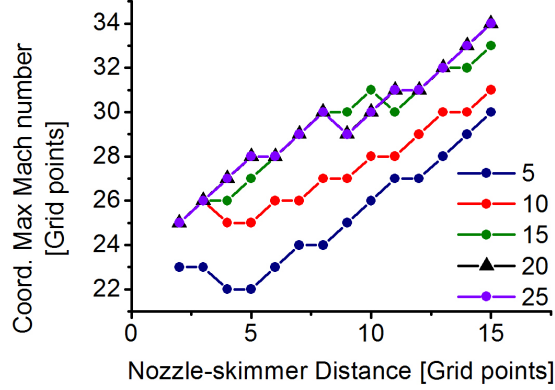
Figure 3.18: Coordinates of maximum M (in terms of grid points) in terms of nozzle-skimmer distance and angle α. As the skimmer is moved further from the nozzle the coordinates of the maximum M also increase. Increasing α also increases the distance of maximum M from the nozzle.

3.6.4 Density profiles

To give a complete description of the jet-flow the density profile shape of the created screen needs to be considered. The features of the density profile change dramatically depending especially on T and R in the perpendicular nozzle-skimmer slits configuration suggested in this work as the most performing. Fig. 3.19 shows typical density profiles of the screen created for high pressure ratios (R=5,000) and aperture angles $\alpha = 25°$ and $\beta = 25°$, when lower (150K) or higher (300K) high pressure reservoir temperatures respectively are used.

The density shown in the picture is calculated by integration of the gas-jet density across the screen short dimension, along coordinate z. The procedure is repeated for all values of the horizontal coordinate x parallel with the jet expansion, and an average is taken and plotted for each y value, with y being hence parallel to the screen long dimension. As there is nearly no variation of the screen density along the x coordinate in the range considered (4 cm), small with respect to the distance to the nozzle ($>$ 60cm), the average reported in Fig. 3.19 does not deviate from any single value by more than about 3.5%. The simulations yielding the results in Fig. 3.19 feature a G_R of about 40, corresponding to a screen depth of about 1 mm for the 40 mm screen width.

A screen splitting phenomenon is clearly seen in Fig. 3.19b, in which the screen density drops abruptly by more than one order of magnitude in the center, due to
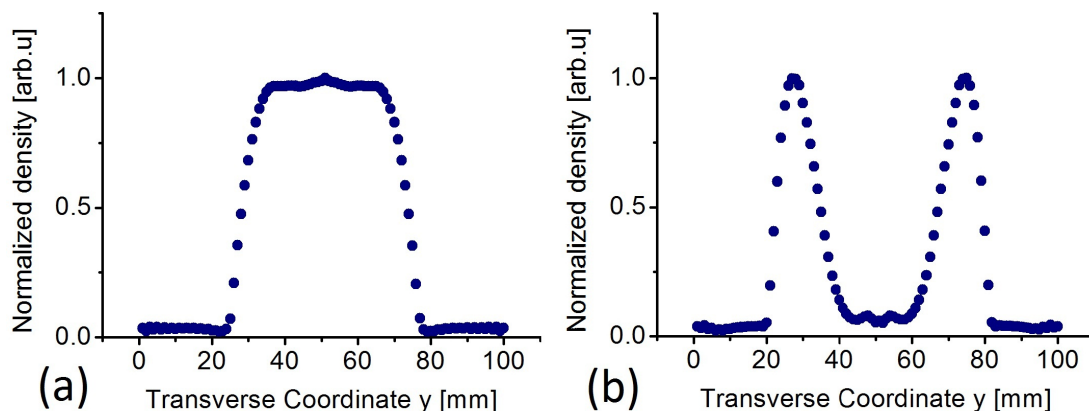
Figure 3.19: Normalized density profiles simulated for R=5000, $\alpha = \beta = 25°$. (a) Normalized density of the screen optimized for beam instrumentation applications, of approximate width 40 mm. The ratio between the average density in the screen region and the base density is about 30. Temperature used T = 150K. (b) Normalized density of an optimized split screen. The ratio between the average density in the screen region and the density between the two tendrils of the screen is about 12. Temperature used T = 300K. The density in both jets is comparable, with the peaks in the two different cases only differing by a factor of ≈ 2.5, with the screen jet peak (a) being more dense than the split one (b).

the development of tendril-like shock wave patterns known to form in the presence of shear layers typical of free jet expansion in the surroundings of the Mach Disk. The simulations show this phenomenon to occur for high temperatures together with high G_R. Such phenomenon bears a potential for application in accelerator beam instrumentation, for beam halo monitoring or even soft beam scraping [60].

As it can be seen from Fig. 3.13a when operating in the regime of simulation #242 it only takes a temperature variation to bring the system in the regime of simulation #250, where screen splitting occurs. This shows another advantage of the proposed system, in the flexibility of changing operation mode by adjusting the thermodynamic properties of the gas reservoir, without having to modify any mechanical feature.

3.7 Conclusions

The study presented in this chapter addresses both the theoretical understanding of the gas-jet physics, tackled through numerical simulations based on the Euler equations, and the jet practical optimization.

73

Sections 3.1 through 3.3 address the problem of identifying a suitable simulation software, capable of implementing the Euler equations and complementing them with non reflective boundary conditions, and suggest an optimized boundary conditions configuration that provides numerical stability and simulation precision, while retaining small domain dimensions and short computation time.

Section 3.4 introduces a set of relevant variables to be investigated for characterizing the jet generation, and also defines a set of three original observables: homogeneity, geometric ratio and confinement. These observables serve to tailor the analysis on the specific application of the thin screen jet target, and complement the more general observables of Mach number and temperature generally used in literature.

Making use of these observables, in section 3.6 different common mechanical configurations for the nozzle-skimmer system are analyzed. The analysis shows that an original configuration, featuring slit nozzle and slit skimmer perpendicular to each other, performs sensibly better (by factors of $2 \div 10$) than the commonly used configurations for the particular application of the jet screen target needed for transverse beam profile monitoring. The analysis, making use of both original and standard observables, is also carried out, in sections 3.6.2 and 3.6.3, for each of the individual variables, providing a information database to direct experimental investigation aimed at optimizing jet performance through modification of the nozzle-skimmer system geometry.

Finally, section 3.6.4 shows one more advantage of the original nozzle-skimmer configuration suggested, namely the ability of changing the gas-jet shape from a thin screen to a double arm screen with a region of low density in the middle by modification of the sole thermodynamic properties of the gas-jet reservoir, without needing any mechanical adjustment, a feature useful for beam halo monitoring or scraping applications.

The results and analysis presented in this chapter have been published in [41].

Outlook Experimental benchmarking of the results presented in this chapter can be obtained by a dedicated experimental setup and such experiment is presently being designed. The setup should be designed to allow control of all the quantities investigated in this chapter. It should thus include a method to measure jet density or a correlated quantity at any point along its initial expansion region (a few cm long); a way to control and monitor the high pressure reservoir temperature; a way to control and monitor the pressure (before jet injection) in both the reservoir and the vacumm chamber and

a set of interchangeable skimmers for investigating the effects of modifying skimmer geometry.

Temperature control can be obtained by enveloping the nozzle holder in a thermostat coolable from outside the chamber. Pressure control requires a leak valve to be installed in the chamber. Monitoring of the jet density is instead less straight forward. Two solutions are being currently investigated: a laser velocimeter to measure gas velocity (directly related to the density, as for eqn. 2.11), and an electron gun coupled with an extraction electric field and a position sensitive detector in a sensing scheme very similar to the one used in this thesis and described in details in Chp. 6. This extraction field should however be placed immediately downstream the nozzle and first skimmer, and the configuration currently used cannot therefore be used directly.

This setup will allow to directly measure a jet density profile immediately past the skimmer and the nozzle, and hence directly benchmark the results presented in this chapter.

4

Mechanical design

In this chapter the mechanical design of the experimental stand is addressed; for brevity, some of the contents of this chapter have been moved to the Annexes. Sections 4.1 and Annex D.2 describe the mechanical details of the main vacuum vessels and the holding stand designed to hold them.

Section 4.2 delves in the workings of the vacuum system, and provides a detailed analysis of the gas flow across it, to the point of deriving equations for the pressures expected in each chamber, the density and size of the created jet. The predictions of the theory concerning the equilibrium pressures in the various vessels lend themselves to straightforward experimental verification: experiments have thus been carried out and are shown to agree remarkably well with the theory. The theory described in this section constitutes a point of originality of the present work and to the author knowledge has not been published in literature to date.

Finally, the following sections focus on the technological accessories of the experimental stand. Section E describes the skimmer design, vacuum gauges, feedthrough and viewports; Annex D.5 describes the operation of a pulsed gas jet together with the equipment design and installation for achieving it and the Annex F describes the design of yet another test stand vessel which allows advanced features to be implemented in the experimental investigation, for research focused on the jet physics beyond the limits of the presently described setup.

4.1 Experimental stand overview

The test stand is composed of 4 main sections, serving different purposes; following the order of the jet travel, these are: the *nozzle chamber* where the jet is generated, the *differential pumping section* which collimates it, the *interaction chamber* where interaction with the electron beam and extraction of the resulting ions occurs and finally the *dumping section* where the jet is finally evacuated from the system. Fig. 4.1 shows a picture of the full setup, highlighting the 4 different sections.
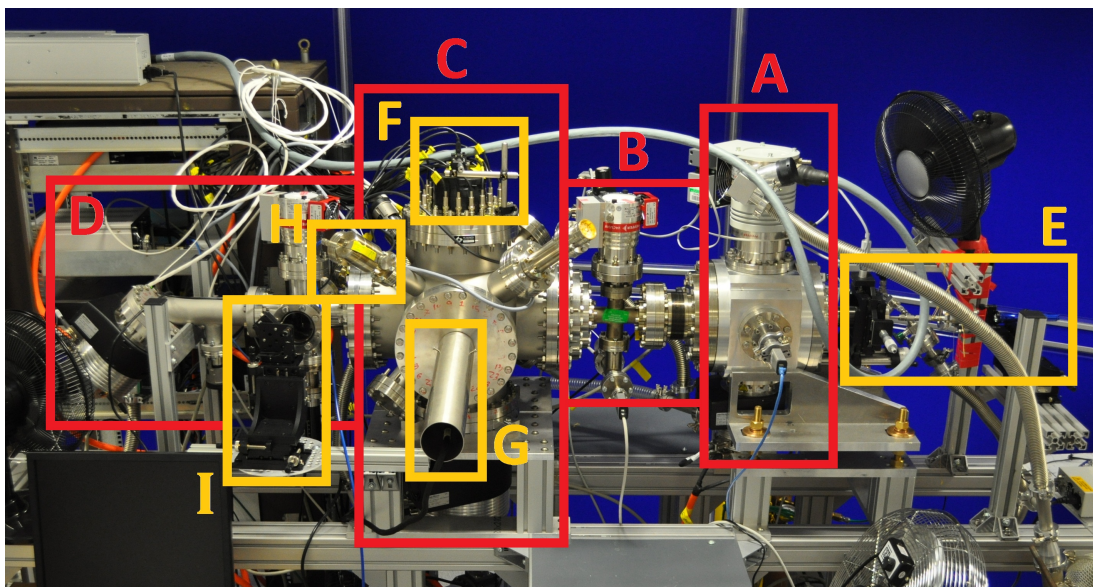
Figure 4.1: Picture of the assembled experimental stand, showing the 4 different sections mentioned in the text and some of the accessories: A - nozzle chamber; B - differential pumping section; C - interaction chamber; D - dumping section; E - gas inlet system and alignment laser/incoherent light source fine positioning stage; F - detector CCD camera; G - electron gun; H - leak valve; I - alignment camera on fine positioning stage.

4.1.1 Nozzle chamber

The nozzle chamber houses the nozzle orifice and the first skimmer. It is provided with a pressure sensor (Pirani, for pressures $> 5 \cdot 10^{-4}$ mbar) and a <u>T</u>urbo <u>M</u>olecular <u>P</u>ump (TMP). A CAD cut view of the nozzle chamber and a zoom on the nozzle tube is provided in Fig. 4.2.

The nozzle orifice, of 30 μm diameter, is laser drilled in a 300 μm thick platinum
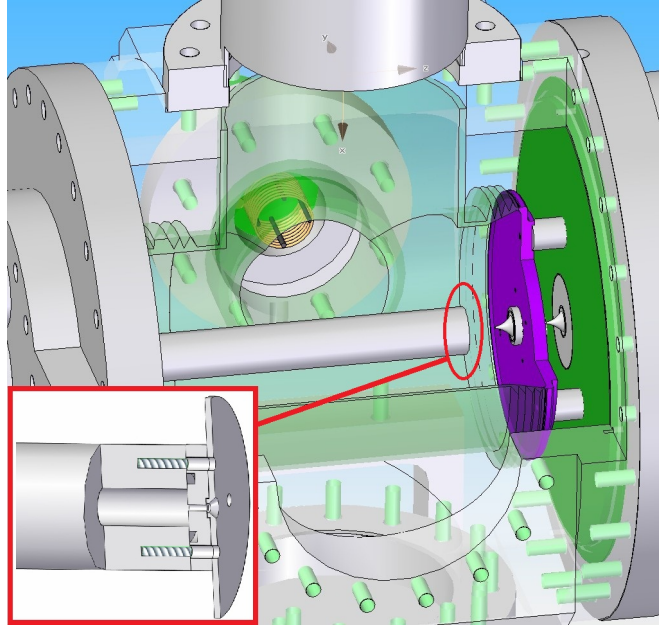
Figure 4.2: CAD cut-out view of the nozzle chamber, showing a zoom on the nozzle tube cross section.

plate of 4 mm diameter. It is mounted at the end of the nozzle tube, a hollow cylinder with 6 mm internal diameter connected to a 3 axes manipulator for fine alignment and with the gas inlet valve. The manipulator for the nozzle, shown in Fig. 4.3, is the *XYZ Miniax*, bought from VGScienta, and features the following characteristics:

- 50 mm travel in the z direction (manual)

- 12.5 mm travel in transverse directions (manual)

- Top flange DN40

- Bottom flange DN100CF with 4x 16CF service ports

- Leak tested to better than 10^{-10} mbar·l·sec^{-1}

At the tip of the nozzle tube there is a holding disk, which has a groove for housing the nozzle and restricts the aperture of the tube to 1 mm diameter only. This restriction is needed in order to be able to push the system to very high pressures (10 bar and more) without distorting the nozzle orifice plate. For the same reason, the nozzle is clamped in place by a thicker (1.5 mm) stainless steel plate, machined to have a countersunk hole

Figure 4.3: 3 degrees of freedom miniax translator from VGScienta.

with 90° full aperture and 1 mm diameter. The countersunk hole is needed to prevent heating of the jet by collisions with the clamping plate. The clamping plate extends beyond the diameter of the nozzle tube, to an outer diameter of 40 mm. This is needed so that screws can be fixed to the skimmer support to mechanically prevent the nozzle tube, which can translate also longitudinally, moving into the skimmer and crashing its tip. The seal between the tube and the nozzle holding plate is obtained by means of an o-ring, while the seal between the nozzle and the holding plate is obtained by means of thin gold wire, plastically squeezed between the nozzle and the holding plate during the clamping procedure. At the atmosphere side of the chamber, the nozzle tube is connected to two different gas lines: a diagram of the gas inlet configuration can be seen in Fig. 4.6.

One gas line connects a small roughing pump (5 m^3/h scroll pump) separate from the rest of the system directly to a 3 way electronically controlled on/off valve. The second gas line connects the high pressure gas cylinder to a pressure gauge, followed by a 0.5 μm mesh gas filter, needed to prevent microscopic metal debris from inside the gas cylinder to be pushed in the nozzle tube thus possibly clogging the nozzle. Fig. 4.4 shows a cylindrical skimmer employed at 10 bar operation of the nozzle before the

filter was installed. Green oxide traces are clearly visible against the copper background from the debris colliding with the skimmer after passing through the nozzle.
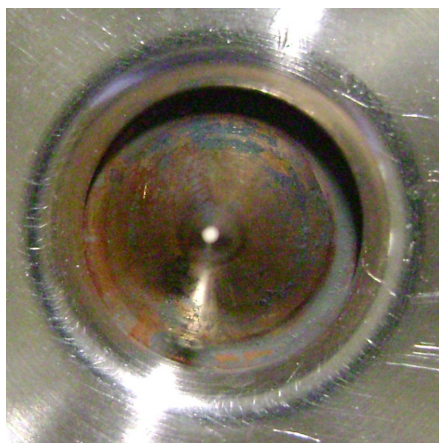
Figure 4.4: Cylindrical skimmer used at 10 bar pressure without small particle filtering, contamination by microscopic metal particles visible in green against the copper background.

Further to the filter is the 3 way on/off valve. This valve normally connects the jet inlet with the roughing pumping line, however when powered it connects instead the gas inlet to the high pressure line, shutting off the connection with the rougher pump. It is a fast acting valve and can be used to inject very short pulses of gas into the nozzle tube, thus producing a pulsed jet target: its design and operation is described in more details in section D.5. When the valve is closed after operation, the connection with the roughing pump ensures that the nozzle tube is quickly evacuated: should this connection not be present, the high pressure gas in the tube would take several minutes to evacuate through the small nozzle orifice, thus effectively preventing pulsed operation.

The nozzle chamber houses the first skimmer, which is clamped and o-ring sealed between two plates few millimeters in front of the nozzle. These plates are fastened to the nozzle chamber with a lip on the outside of the chamber, so that they can be removed towards the outside without having to disconnect the nozzle tube. This allows to conveniently position and align the first skimmer after the nozzle tube has been fixed in position. The skimmer holder also has two tapped holes which can be used to fix the screws intended to brace against the nozzle clamping ring to prevent it crashing against the skimmer. These screws are chosen of a suitable length so that they protrude

from the back of the skimmer holder, and can be used for handling the skimmer holder during alignment.

Finally, the nozzle chamber includes ports of diameters respectively 100 and 70 mm. The smaller port is used for installation of the vacuum gauge, whilst the larger one for pumping: positioning a large aperture as close as possible to the nozzle and skimmer guarantees efficient pumping in this region critical for the generation of the jet.

4.1.2 Differential pumping section

Beyond the first skimmer starts the differential pumping section, composed of 2 different chambers isolated vacuum-wise apart from the small on-axis apertures and pumped by two separate TMP. The first of these chambers houses the second skimmer, whilst the second is composed of a bellow and a cross which houses the third aperture, the TMP and the vacuum gauge.

The chamber housing the second skimmer is the outer nozzle chamber, which top and side ports are connected to the nozzle chamber and o-ring sealed, and the back port is used for the manipulator and the gas inlet. This leaves three ports for use in the differential section. The front port holds a metal disk, o-ring sealed, which supports the second skimmer. This convoluted design, with the outer chamber housing the inner chamber inside, has the advantage of allowing a very small <2 cm distance between the first two skimmers, whilst still providing pumping in between. However, the trade-off is with the pumping speed, which decreases, with respect to the inner nozzle chamber, due to concavity of the geometry. Nevertheless, the pumping requirements beyond the first skimmer are greatly reduced, as only a very small amount of injected gas (about 0.1%, see section 4.2 for calculations) makes it through to the differential pumping section.

Beyond the second skimmer a bellow is placed to allow alignment of the nozzle chamber with the interaction section, and a DN40 6 way cross.

4.1.3 Interaction chamber

The interaction chamber is composed of a main body, a spherical DN200 6 way cross, with 7 additional smaller ports coming in at 45° angles in several directions, an extraction and detection system which is situated on the top flange of the main body and will be discussed in more details in Chp. 6, and a series of diagnostic and insertion

devices treated in the rest of this section. A more detailed description of the interaction chamber is reported in D.1

4.1.4 Dumping section

The dumping section is composed of two different chambers. The first one is a DN70 6 way cross, whilst the second one is a custom made reducer tee, optimized for pumping efficiency.

The 6 way cross is connected to the interaction chamber via a reducer flange: the gasket sealing the connection has a small internal diameter of 10 mm for operation with the cylindrical jet and 40 mm for operation with the screen shaped jet, which serves as a differential pumping aperture. The opposite port connects to the second chamber of the dumping section through an identical reduced inner diameter gasket. The remaining ports of the 6 way cross hold a 80 l/s TMP, a viewport and a retractable mirror which is angled at 45° from the jet path and used to observe the small retractable phosphor screen in the middle of the interaction chamber through the viewport. The optical distance between the viewport and the center of the interaction chamber where the retractable phosphor screen is positioned when in operation is of about 40 cm.

The second chamber of the dumping section, shown in Fig. 4.5, allows the inclusion of a hot cathode gauge for measuring low pressures and the positioning of a DN100 300 l/s TMP at a 45° angle with respect to the impinging jet. This angle is chosen to be equal to the angle formed by the rotor blades, hence maximizing the open area seen by the jet, to increase pumping efficiency of the collimated gas.

4.2 Vacuum system

This section describes the vacuum system of the experimental setup, focusing on the description of all the components and the pumping elements. Based on this description, information on the vacuum level expected in the chamber can be analytically derived by considering the mass flow, the chamber volumes and the pumping speed described. The information obtainable includes the vacuum levels expected as well as their time evolution, which are then used in the design of the pulsed jet operation discussed in Annex D.5. Even though the derivation includes some assumptions and does not
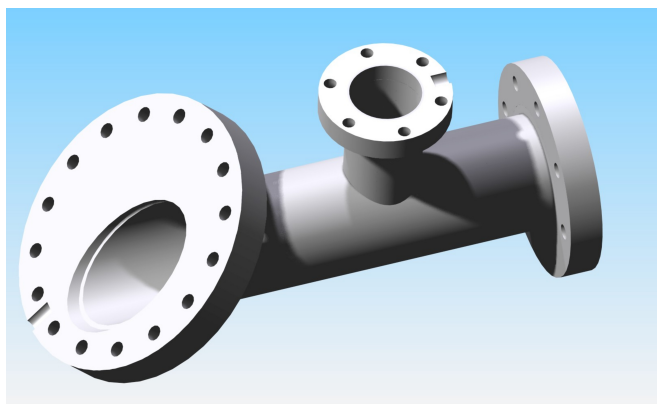
Figure 4.5: End section of the dumping section, with port for the TMP angled at 45° to maximize pumping efficiency.

make use of the full Euler equations, the results prove to be in good agreement with experimental observation.

4.2.1 Description

Fig. 4.6 shows a diagram of the chosen vacuum scheme. The system is composed of 6 different vacuum chambers connected by small apertures.

The values of the most relevant parameters shown in Fig. 4.6 and used in the experimental setup which will be useful in the following discussion are listed in table 4.1 for each chamber.

Chamber #	Skimmer coord. [mm]	Skimmer Dimensions [mm]	Subtended Solid angle [sr]	Chamber Volume [l]	Pumping Speed [l/s]
1	5	ø 0.17	$9.1 \cdot 10^{-4}$	2.2	277
2	25	ø 0.4	$2.0 \cdot 10^{-4}$	4.0	277
3	325	4 x 0.4	$1.5 \cdot 10^{-5}$	1.5	76
4	800	ø 15	$2.8 \cdot 10^{-4}$	30.6	678
5	1010	ø 15	$1.7 \cdot 10^{-4}$	1.9	76
6	––	––	––	1.0	277

Table 4.1: Quantities relevant to vacuum calculations for each chamber.

The pump requirements change with respect to the chamber they are used in. For
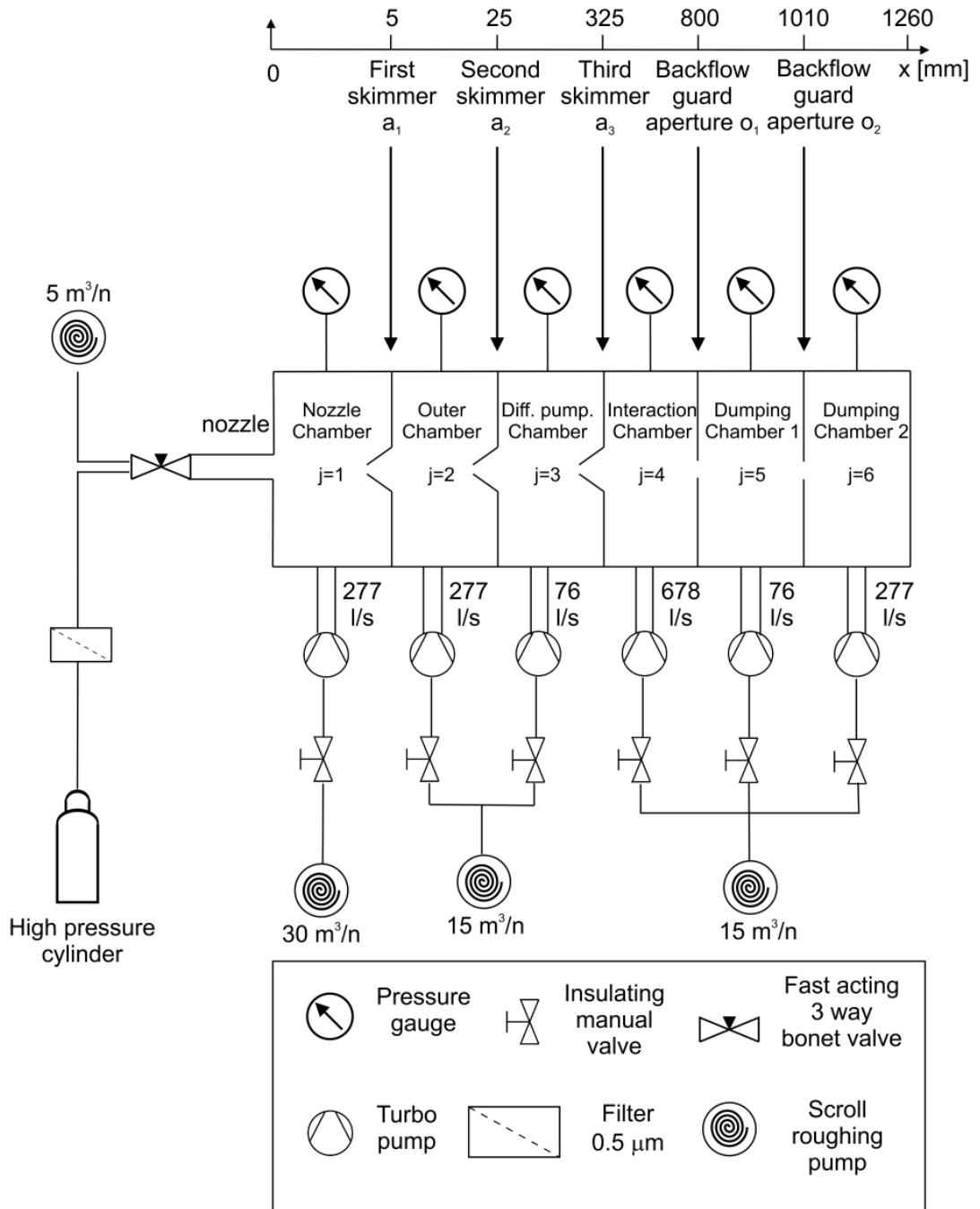
Figure 4.6: Schematic representation of the vacuum scheme used in the beam profile monitor test stand, including aperture identification numbers a_j.

the interaction chamber, there is no need for a large suction power, as no major gas load is expected. Rather, compression ratio becomes an issue to keep the vacuum low against the constant out-gassing of the elements present inside the chamber (detectors, electron gun, movable parts etc.). In the case of the nozzle chamber, instead, the main issue is the ability to dump efficiently the gas load given by the gas jet. The reason for using two different channels of pre-vacuum pumps is to avoid backflow to the dumping and interaction chamber when the jet is turned on and the gas load on the nozzle and skimmer chamber increases drastically.

Given the vacuum to be reached (10^{-8} to 10^{-9} mbar) in the first stages of the experiment, oil-free pumps are essential, and cryopumps are not needed, as almost all commercial TMP can provide a 10^{-9} mbar vacuum. As shown in Fig. 4.6, 9 pumps are employed, 6 TMPs and 3 pre-vacuum pumps (nominal pumping speed reported in the following):

- 1 large TMP (700 l/s) for the interaction chamber on a DN160 flange.

- 2 small TMP (80 l/s) for the first stage of the dumping chamber and for the differential pumping section on a DN70 flange.

- 3 medium TMP (300 l/s) for the remaining chambers, on a DN100 flange.

- 3 Scroll pumps (1 x 30 m^3/h, 2 x 15 m^3/h) for pre-vacuum.

4.2.2 Nozzle chamber

To describe the behavior of pressure in the nozzle chamber the mass flow through the nozzle and the pumping speed need to be taken into account. The mass flow through the nozzle $\dot{m}_{nozzle}$ can be estimated by (2.15). It depends only on orifice geometry, pre-pressure and gas species and is therefore constant in time. On the other hand the mass flow through the TMP depends on the actual pressure in the chamber P_a, and the pumping speed of the pump, which is also a function of P_a. The dependence of the pumping speed from P_a comes from the power limitations of the pump, which increase as the volume swept (proportional to the pumping speed) is filled by more and more gas as the pressure increases, and is given by the manufacturer. The plot in Fig. 4.7 refers to the pumping speed of the TURBOVAC SL300, the 300 l/s TMP (nominal

pumping speed) installed in the nozzle chamber, and is provided by Oerlikon Leybold.
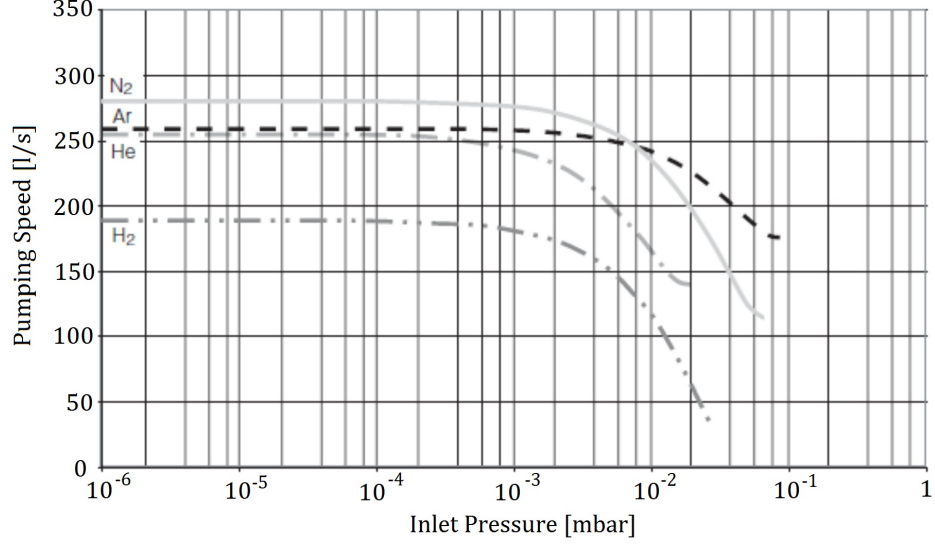
Figure 4.7: Pumping speed in terms of vacuum chamber pressure for the SL300 TUR-BOVAC TMP from Oerlikon Leybold. The pumping speed curve for N_2 is approximated by an exponential relation expressed by (4.1).

The pumping speed can be approximated with an exponential, and in particular the curve for the pumping speed for N_2 can be expressed by (4.1):

$$S_{[l/s]} = 277e^{-10.2\,P_{a[mbar]}} \tag{4.1}$$

Therefore, the mass flow through the pump can be expressed as the product of the mass per liter of gas at the thermodynamic conditions of the ambient chamber times the pumping speed:

$$\dot{m}_{pump} = \frac{nW}{V} \cdot S = \frac{P_a W}{RT_a} \cdot 0.277e^{-0.102P_a} \tag{4.2}$$

where the pumping speed is expressed in m^3/s rather than in l/s for unit coherency and P_a in Pascal. The equilibrium condition will be obtained when $\dot{m}_{pump} = \dot{m}_{nozzle}$, and will correspond to an equilibrium pressure, indicated with P_{a-e}, which is in turn a function of the pre-pressure P_0 and the nozzle diameter d. This calculation ignores the gas mass which escapes the chamber through the skimmer. However, as it was shown in Chp. 2, this mass is less than twice the mass that would escape from the nozzle

in case of an effusive source: thus its ratio to the contained mass is less than twice the solid angle spanned by the skimmer over the full 2π solid angle. For a skimmer aperture of diameter 180 μm at 5 mm distance from the nozzle, this equates to about 0.03%: such low value is negligible in the following calculation. When (4.2) is equated to (2.15) calculated for the nozzle orifice, a transcendental equation is obtained, which can only be solved numerically. Fig. 4.8 shows a plot of the two mass flows, through the pump and through the orifice, calculated for a 30 μm orifice diameter, at 10 bar pre-pressure, with the SL300 TURBOVAC TMP from Leybold.
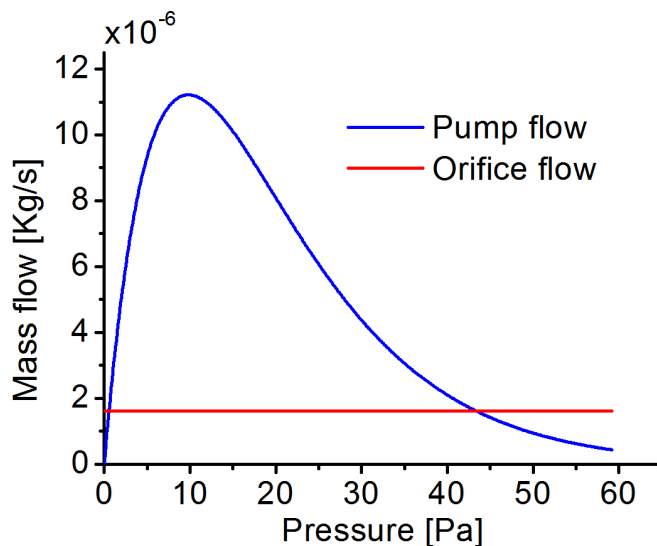
Figure 4.8: Calculated mass flow through the pump and through a 30 μm diameter orifice, at room temperature and 10 bar pre-pressure, with the SL300 TURBOVAC from Leybold, for N_2 gas.

It is possible to identify in Fig. 4.8 two points of equilibrium, in which the two mass flows are equal. However, only the first of such points, the one for lower pressures, is a stable equilibrium point. Indeed, when the mass flow through the pump is smaller than the mass flow from the orifice, the pressure in the chamber rises, so the system moves rightward in the plot, and vice versa. Therefore, any displacement from the equilibrium position pushes the system towards equilibrium for a positive slope of the pumping mass flow and away from equilibrium for a negative slope of the pumping mass flow.

The pressure at which the mass flows are in equilibrium is the expected pressure

which will be reached in the vacuum chamber: something which can be easily measured to provide experimental validation of the theory here described. This experiment was carried out with two different TMP with different pumping speed curves. Fig. 4.9 shows a plot of the calculated equilibrium pressures P_{a-e} for both pumps and different values of pre-pressure P_0, together with the measured data.
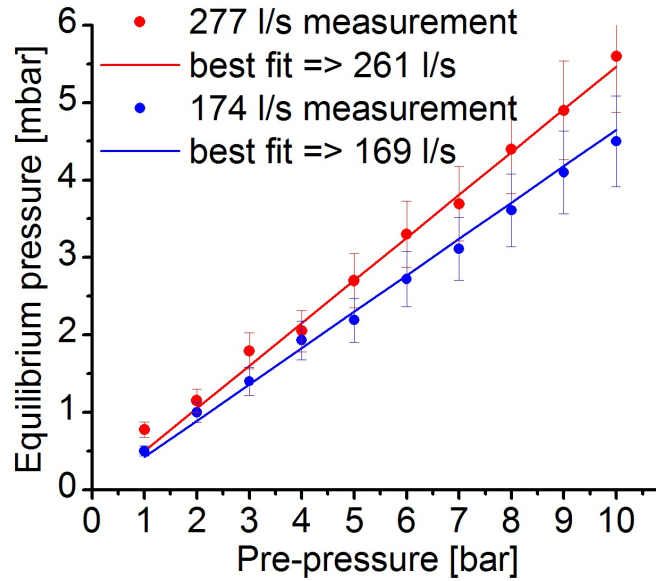
Figure 4.9: Equilibrium pressure P_{a-e} in the nozzle chamber for two different TMP (300 and 180 l/s nominal pumping speed) and for different values of the pre-pressure P_0. Calculations are done for a 30 μm diameter circular orifice at room temperature, with N_2 gas. The continuous line represents the calculation while the points are experimental data. The error bars are quoted from the datasheet specifications of the pressure gauges.

The measured data is in very good agreement with the calculations. To reach this agreement, the nominal pumping speed of the TMP, as derived from the pumping speed curve on the datasheet, was decreased to optimize the agreement with the experimental data, so as to take into account the convoluted geometry of the chamber, which inevitably results in decreased pumping efficiency. That the pumping speeds are only slightly smaller than the ones reported in the manufacturer data is testament to the good design of the chamber, as well as providing an indication of the theory validity. Finally, the mass flow rate can also be expressed in terms of the pressure rate of change:

$$\dot{m} \;=\; \dot{n}W \;=\; \dot{P_a}\frac{V_{chamber}W}{RT_a} \tag{4.3}$$

Therefore if $\dot{m}$ in (4.3) is substituted with the net mass flow rate, given by $\dot{m}_{net} = \dot{m}_{nozzle} - \dot{m}_{pump}$, eqn. (4.2) can be expressed as a differential equation in terms of P_a and its derivative:

$$\dot{P}_a = \left\{ \dot{m}_{nozzle} - \frac{P_a W}{R T_a} 0.277 e^{-0.102 P_a} \right\} \frac{R T_a}{V_{chamber} W} \qquad (4.4)$$

This differential equation can be solved numerically, and provides the time evolution of the system. The relatively simple form of (4.4) comes from the fact that $\dot{m}_{nozzle}$ does not depend on P_a. However, (4.4) also assumes that any mass inflow through the nozzle would be immediately transported to the pump inlet. A rough estimate of how long it takes for the mass entered at the nozzle orifice to reach the vacuum pump is of the order of milliseconds (see section D.5). This can be taken into account in (4.4) by introducing a time delay Δt between the establishment of the pressure in the chamber, calculated in (4.3), and the pressure seen by the vacuum pump, relevant to the pumping speed and appearing in (4.4):

$$\dot{P}_a(t) = \left\{ \dot{m}_{nozzle} - \frac{P_a(t - \Delta t) W}{R T_a} 0.277 e^{-0.102 P_a(t - \Delta t)} \right\} \frac{R T_a}{V_{chamber} W} \qquad (4.5)$$

When (4.5) is solved for varying values of Δt, the transient of the pressure in the chamber can be obtained, giving an estimate of the time needed to reach equilibrium; This is done in Fig. 4.10. Analysis of Fig. 4.10 shows that the rise time, defined as the time needed by the system to reach 90% of the final pressure, is of the order of 20 ns for delays up to a few ms, decreasing down to 10 ms for higher delays. However, the rise time also presents a strong dependence on the effective pumping speed of the TMP, as shown in Fig. 4.11.

Such decrease in pumping speed can come from different factors: geometrically, the aperture where the pump is mounted limits the pumping speed, while mechanically, overheating of the pump causes the rotation speed to decrease as a built-in protection to the bearings and the motor.

4.2.3 Other vacuum sections

The analysis of the complete vacuum system will refer to Fig. 4.6, explicitly using the index j to refer to each chamber, its volume V_j, its exit skimmer area A_j and longitudinal coordinate x_j. To treat the vacuum sections past the nozzle chamber, the mass flow
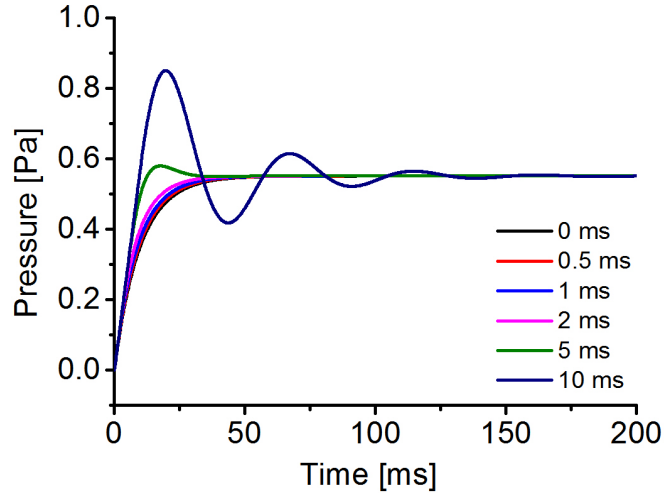
Figure 4.10: Calculated pressure transient for a 2.5 l chamber, flooded with N_2 through a 30 μm diameter nozzle, 10 bar pre-pressure, at room temperature, pumped by a TURBOVAC SL 300. The different plots correspond to different values of time delay between the introduction in the chamber of new gas and the attainment of an overall equilibrium pressure. Calculations done according to eqn. (4.5), to account for a time delay.
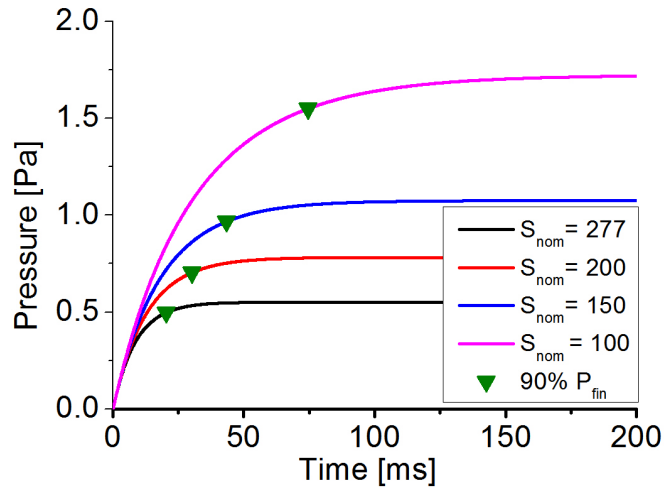
Figure 4.11: Pressure transient for the same characteristics as in Fig. 4.10, with 1 ms time delay and for varying effective pumping speed. Decreasing pumping speed results in an increase of rise time, as well as in a higher final pressure P_{a-e}. The triangular points show the end of the rise time, defined as the time for the pressure to reach 90% of the final value.

rate balance needs to be written. This balance is constituted of 4 different contributions which need to be separately treated: pumping; residual gas flow, outgassing and gas-jet contributions.

Vacuum pumping The pumping contribution to mass flow rate is always negative, and accounts for the effect of the TMP installed in each section. It can be expressed for each chamber through eqn. (4.2), by replacing the two constants present in (4.2), namely 0.277 and 0.102 with the actual values for each TMP. This analysis shows that the exponential factor 0.102 is the same for all pumps, while the nominal pumping speed varies: 3 different pumps are used, with pumping speeds 678, 277 and 76 l/s. The symbol Sp_j will be used in the following to indicate the pumping speed of the TMP in the jth chamber, expressed however in m^3/s for unit consistency with the remaining quantities.

Residual gas flow As for the contribution due to residual gas, past the nozzle chamber molecular flow intervenes, in which the rarefied gas-jet molecules travel in straight lines without any appreciable number of collisions happening between them or also with the residual gas (see Chp. 2). In such conditions, the residual gas and the gas jet coalesce in the same space, their effects sum up and can be treated independently. For molecular flow through an aperture, it is well known that the flow rate due to a pressure differential in terms of molecules per second can be expressed as [62]:

$$\dot{N} = \sqrt{\frac{1}{2\pi WRT}} A_v \cdot A \cdot \Delta P \tag{4.6}$$

where A is the orifice area, A_v the Avogadro's constant and ΔP the pressure differential, leading to the mass flow rate:

$$\dot{m}_{res.gas} = \dot{N}\frac{W}{A_v} = \sqrt{\frac{W}{2\pi RT}} \cdot A \cdot \Delta P \tag{4.7}$$

However, it should be noted that, when the gas-jet is running, this residual gas flow contribution does not apply to the first chamber. Indeed, in this chamber the gas expansion can be still treated as a fluid-dynamic flow, rather than a molecular one, and the gas-jet in its expansion actually displaces the residual gas, so that no residual gas molecule is able to reach the first skimmer.

Outgassing   The third contribution is the one due to outgassing of the vacuum chamber, which makes up for the ultimate pressure that the TMP can achieve when no gas-jet is injected in the system. This is a constant positive mass flow contribution which can be calculated from the set of ultimate pressures for each chamber. Indeed, when no gas jet is running, the mass flow rate balance can be written as the sum of the contributions due to outgassing, pumping and residual gas flow. When the pressures are the ultimate pressures P_{0j}, the equilibrium is reached and the mass flow balance for each chamber is zero:

$$
\begin{aligned}
\dot{m}_{net\_j} &= 0 \\
&= \dot{m}_{out\_j} + \sqrt{\frac{W}{2\pi RT}} \left[A_j \left(P_{0,j+1} - P_{0j} \right) - A_{j-1} \left(P_{0j} - P_{0,j-1} \right) \right] \\
&\quad - P_{0j} \frac{W}{RT} Sp_j e^{-0.102 P_{0j}} \qquad\qquad\qquad\qquad \forall j \qquad (4.8)
\end{aligned}
$$

where for the first and last chamber ($j = 1$, $j = 6$), the term referring to the residual gas flow to the previous and following chamber respectively is ignored (i.e. $A_0 = A_7 = P_0 = P_7 = 0$). When the ultimate pressures are used for all P_j, a set of 6 equations is obtained which allows calculation of the outgassing contribution $\dot{m}_{out\_j}$.

The contribution of outgassing has very different impact on different sections of the experimental chamber: in the jet generation chamber, where gas is externally injected, outgassing is clearly negligible; on the other hand, in the experimental chamber, where the gas jet is not skimmed, and the only contribution to the pressure of the gas jet is due to the gas scattered according to the Beer-Lambert Law (see next subsection), outgassing accounts for a non-negligible portion of the final pressure. Therefore, although the calculation of outgassing might be redundant in some chambers, it needs however to be carried out.

Gas-jet flow   Finally, for the contribution due to the gas-jet it is possible to assume that the jet, collimated by the first skimmer, keeps traveling in a cone defined by the geometric apertures along the path. The flow through each aperture will be given by:

$$
\dot{m}_{aperture} = \kappa \dot{m}_{nozzle} \frac{A_{aperture}}{2\pi x_{aperture}^2} \qquad\qquad (4.9)
$$

where A is the area of the aperture, x its distance from the nozzle and κ the peaking factor. Eqn. (4.9) makes three implicit assumptions.

Firstly, it assumes the size of the aperture to be small enough compared to the distance of the aperture from the nozzle to be able to use its area in (4.9) rather than its projection on a sphere. This assumption also allows the use of the peaking factor in (4.9): indeed, strictly speaking the peaking factor (see Chp. 2) only applies to mass flow along the expansion axis, and steadily decreases as the angle from the axis is increased. However, assuming the size of the aperture being small is equivalent to assuming small angles with the expansion axis, hence the possibility of using the peaking factor to be homogenous and equal to the on-axis value for the jet flow through the apertures.

Secondly, eqn. (4.9) assumes that the aperture considered subtends with the nozzle a smaller solid angle than any of the previous apertures. Should this not be the case, in principle all gas molecules would pass though the aperture, and the mass flow through it would only depends on the mass flow of the previous aperture subtending the smallest solid angle with the nozzle. This is the case of the dumping section apertures, as it can be seen from table 4.1, as they are intended indeed to prevent backflow in the chamber of the effusive gas created when the jet hits the TMP at the end of the dumping chamber, rather than to better collimate the gas jet. This consideration has an important effect when misalignments occur, which lead to smaller effective areas and therefore smaller flows. In order to estimate the precision with which the system is to be aligned if the highest flow for a specific pre-pressure needs to be obtained, a geometrical model can be used. Assuming for simplicity circular apertures, the gas jet diameter d_{fin} at a distance x_{fin} from the nozzle resulting from skimming at an aperture of diameter d_in at distance x_{in} from the nozzle, is given by the shadow cast by the aperture, which scales linearly with the distance:

$$d_{fin} = d_{in} \frac{x_{fin}}{x_{in}} \tag{4.10}$$

Therefore the tolerance on the alignment of a circular aperture of diameter d_{ap} at the distance x_{fin} from the nozzle will be, using (4.10) for the second equality:

$$\Delta = \frac{d_{fin} - d_{ap}}{2} = \frac{d_{in}x_{fin} - d_{ap}x_{in}}{2x_{in}} \tag{4.11}$$

Within these alignment tolerances, eqn. (4.9) can be used to compute the mass flow if the smallest solid angle aperture is used. Fig. 4.12 shows a plot of the cross section of the gas jet everywhere along its path, resulting from the considerations above.
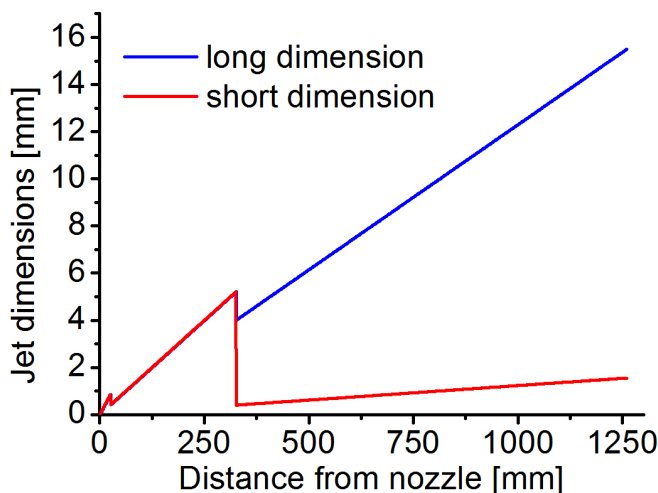
Figure 4.12: Cross section of the gas jet along its path, showing the spot diameter. The line splits beyond the third skimmer as the two curves represent the two dimensions of the rectangular cross section. Note the effects of the first skimmer cannot be seen on the plot as it is the first skimmer itself that defines the initial jet dimensions.

Thirdly, eqn. (4.9) also assumes that the gas jet does not attenuate along its path. In reality, scattering with the residual gas results in attenuation according to Beer-Lambert law [61], which is basically an exponential decay law. This attenuation only occurs, however, past the first skimmer, where the flow becomes molecular and the jet and the residual gas coexist in the same region of space: this does not happen between the nozzle and the first skimmer, where the gas undergoes free expansion and displaces the residual gas until the occurrence of the shock wave pattern.

The attenuation coefficient can be estimated through considerations of the mean free path. Indeed, the scattering probability per unit length of jet path $P_{s/l}$ can be estimated through the product of the residual gas number density ρ_n and the scattering cross section σ:

$$P_{s/l} = \rho_n \cdot \sigma \tag{4.12}$$

Eqn. (4.12) implicitly assumes the scattering probability per unit length to be small enough for the probability of two residual atoms to shadow one another as seen by the impinging gas-jet to be negligible, otherwise it overestimates the true probability. Eqn. (4.12) integrates over distance as an exponential decay with decay constant $P_{s/l}$, similarly to a Beer-Lambert attenuation law. This decay law can then be applied with the scattering cross sections available in literature [63] to correct eqn. (4.9) for each

section. Eqn. (4.12) can be more conveniently expressed in terms of the residual gas
pressure using the ideal gas law:

$$P_{s/l} = p \frac{A_v}{RT} \sigma \tag{4.13}$$

Therefore the gas flow in the jet at the aperture leading into the jth chamber can be
expressed as:

$$\dot{m}_j = \kappa \dot{m}_{noz} \frac{A_{(j-1)^*}}{2\pi x_{(j-1)^*}^2} e^{-\frac{\sigma A_v}{RT} \sum_{t=2}^{j-1} P_t(x_t - x_{t-1})} \tag{4.14}$$

Therefore the net mass flow due to the gas jet in the jth chamber $\dot{m}_{jet\_j}$ can be expressed
as:

$$\dot{m}_{jet\_j} = \kappa \dot{m}_{noz} \frac{A_{(j-1)^*}}{2\pi x_{(j-1)^*}^2} e^{-\frac{\sigma A_v}{RT} \sum_{t=2}^{j-1} P_t(x_t - x_{t-1})}$$

$$- \kappa \dot{m}_{noz} \frac{A_{j^*}}{2\pi x_{j^*}^2} e^{-\frac{\sigma A_v}{RT} \sum_{t=2}^{j} P_t(x_t - x_{t-1})} \tag{4.15}$$

where the star operator is used to account for the minimum aperture correction dis-
cussed above, and therefore, in the particular case of the apparatus described, is defined
as:

$$j^* = min(3, j) \quad \forall j \tag{4.16}$$

Eqn. (4.15) is then more conveniently written as:

$$\dot{m}_{jet\_j} = \kappa \dot{m}_{noz} e^{-\frac{\sigma A_v}{RT} \sum_{t=2}^{j-1} P_t(x_t - x_{t-1})} \left[\frac{A_{(j-1)^*}}{2\pi x_{(j-1)^*}^2} - \frac{A_{j^*}}{2\pi x_{j^*}^2} e^{-\frac{\sigma A_v}{RT} P_j(x_j - x_{j-1})} \right] \tag{4.17}$$

Overall calculation Having identified the 4 contributions to the mass flow rate for
each chamber, expressed in eqn. (4.2), (4.7), (4.8) and (4.17), it is possible to calculate
the expected working pressure for each chamber, together with the number density and
the physical dimension of the gas jet anywhere along its path. This is done by solving
the system of 6 differential equations for the final equilibrium pressures P_{j_fin}:

$$\dot{P}_j = \dot{m}_{net\_j}(P_j) \frac{RT}{V_{chamber} W} \tag{4.18}$$

Having done this calculation for the initial conditions of pressure given by the
ultimate pressures P_{0j} and the values of the other variables listed in table 4.1, the
final equilibrium pressures P_{j_fin} have been obtained and listed in table 4.2, together

Chamber #	$P_{j\text{-}fin}$ [mbar]	Alignment tolerance [μm]	Equilibrium pressure [mbar]
1	5	ø 200	$8.8 \cdot 10^{-3}$
2	25	ø 30	$1.1 \cdot 10^{-6}$
3	325	10^3	$8.5 \cdot 10^{-7}$
4	800	ø $3 \cdot 10^3$	$5.3 \cdot 10^{-9}$
5	1010	ø $3 \cdot 10^3$	$2.3 \cdot 10^{-8}$
6	-	-	$2.7 \cdot 10^{-8}$

Table 4.2: Calculated equilibrium pressure in each chamber, as well as the alignment tolerances needed to reach the predicted pressures.

with the alignment tolerances which need to be met to obtain the equilibrium pressures listed.

Furthermore, through the pressures listed in table 4.2 it is also possible to compute the amount of residual gas scattering the gas jet undergoes along its path and thus plot the expected gas-jet number density everywhere at the equilibrium condition. Indeed, assuming the gas jet travels at the terminal velocity v_∞, see eqn. (2.9), it is possible to express the number density $\rho_\#$ of the gas-jet in terms of the mass flow and the jet cross sectional area:

$$\rho_\# \left[\frac{molecules}{m^3} \right] = \dot{m}_{jet} \frac{A_v}{W A_{jet} v_\infty} \tag{4.19}$$

It is noted that by assuming that the jet travels at velocity v_∞ only an error of few percent is made (see Chp. 2), and that the cross sectional diameter of the jet A_{jet} can be obtained by eqn. (4.10). By substituting in (4.20) $\dot{m}_{jet}$ through (4.14), generalized for the generic position x_j, $\rho_\#$ can be expressed as:

$$\rho_\# \left[\frac{molecules}{m^3} \right] = \kappa \dot{m}_{noz} \frac{A_v}{2\pi W v_\infty x^2} e^{-\frac{\sigma A_v}{RT} \sum_{t=2}^{j} P_t(x_t - x_{t-1})} \tag{4.20}$$

where it is apparent how the jet density depends on κ, the pre-pressure which determines $\dot{m}_{noz}$ and the square of the distance x. This calculation is performed for all positions along the jet expansion and shown in Fig. 4.13:

Analysis of the plot in Fig. 4.13 shows how the expected signal to noise ratio for the gas jet in the interaction chamber is of the order of 10^5. The second factor of importance in establishing whether the jet is easily detectable is its physical size.
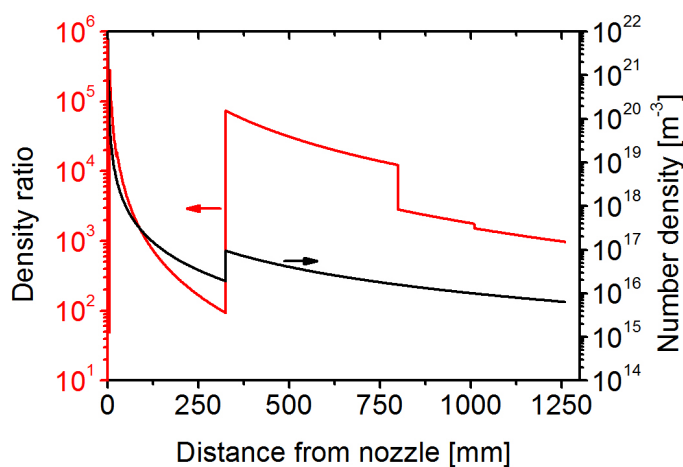
Figure 4.13: Number density of the gas jet everywhere along the jet path (black curve, right-hand axis) and ratio between gas jet and local residual gas number density (red curve, left-hand axis).

Assuming all elements are aligned so that no shadowing effect due to misalignment is present, with reference to Fig. 4.12, in the middle of the interaction chamber the gas-jet has a size of 7.4 by 0.8 mm. These two factors together, signal to noise ratio and physical size, make for a system compatible with very easy detection of the jet through ionization, extraction and imaging on the detector, the experimental complexity laying mainly in the difficulty of practically meeting the alignment tolerances. Although the tolerances themselves as reported in Table 4.2 are not in themselves extremely tight, with the possible exception of the second stage (30 μm), the mechanical design of the different chambers is such that the skimmers are placed in scarcely accessible areas, making it difficult to control the alignment finely. This condition is difficult to change from the point of view of the mechanical design, as it is required that several skimmers be placed at few cm from each other, and are all part of different vacuum environment, differentially pumped. Furthermore, and additional complication lies in the difficulty of maintaining the alignment carefully obtained once the chamber is evacuated and the system is subject to stresses due to atmospheric pressure. This is particularly relevant for the nozzle manipulator, which has a bellow component to allow movement of the nozzle in the chamber, which also results in unavoidable displacements of the nozzle tube during the chamber evacuation. This particular problem has been tackled in the course of this work by aligning only the skimmers between themselves, and postponing

the alignment of the nozzle to after the chamber is evacuated, either by mean of direct laser alignment through a viewport or by observation of the pressure levels in the different chambers.

Summary   The discussion presented in this section is based on the parameters listed in table 4.1. However, the structure given in this section and in Chp. 2 is general and can be applied, with the due modifications, to any jet generation system. In particular, it also immediately applies to the experimental stand discussed in this work when any skimmer position and dimensions are changed.

This flexibility and predictive power proves very valuable for commissioning the jet generation setup. Indeed, as it can be seen from the alignment tolerances shown in table 4.2, mechanical tolerances are very tight, and very likely need to be adjusted after the system has been pumped down, because of possible small distortions due to atmospheric pressure. This can be usually done, if alignment before pumping down was within the listed tolerances, by applying some strain on the vacuum components, which slightly bends the vessel at the welding points and provide a small (few degrees in most systems) angular play. During this procedure, deviations of the observed pressures from the prediction are useful insofar as they show which vessel has a higher pressure than expected, thus indicating which skimmer is misaligned.

4.3   Conclusions

This chapter describes the design and manufacturing of the experimental test stand which is currently operational at the Cockcroft Institute. The details of the mechanical design, including the structural calculations for the holding frame are treated in sections 4.1 and Annex D.2. The stand, complemented by the pressure gauges and vacuum components described in section E and Annex D.5, has been manufactured, installed and commissioned.

Section 4.2 presents instead an original theoretical model to predict the final pressures achieved in each vacuum chamber and the gas screen size and density at any point along the expansion. The model takes into account the contributions due to outgassing, pumping speed, jet and residual gas flow, and provides predictions well in agreement with the experiments. Overall, the model constitutes a novel, valuable tool

for the design and development of supersonic gas jet based systems, and has been used extensively in the design of the setup described.

In Annex F the design of an alternative test stand to be used for the experimental investigation of the jet properties and a further future benchmark of the model presented in section 4.2 is presented and its feature of interest, mainly the possibility to vary chamber volumes and position of the apertures, highlighted.

5

Electron gun calibration

In this work, to simulate the primary beam of antiprotons intended to be monitored in the final application, an electron beam is used as a convenient alternative to an ion or proton beam to cause neutral gas ionization and hence operate the monitor. Electron beams are convenient insofar as they are very easily produced with an electron gun, and do not require access to a full accelerator facility. Furthermore, experimental evidence shows that the cross section for ionization, as well as, more importantly, the momentum transferred to the recoiling ion during ionization do not differ much between electron and proton bombardment; in fact, they are equal to within a factor of 3, amounting in general to a few atomic units of momentum transferred from the projectile to the newly created gas ion. This process is discussed in details in section 6.1.2, where it is shown that the magnitude and direction of the transferred momentum is independent on the energy and type of the projectiles.

This chapter presents the experimental results concerning the characterization and calibration of the electron gun used to simulate the accelerated beam. In section 5.1 a brief overview of the electron gun components and beam specifications is presented, while section 5.2 addresses the experimental results describing the beam characteristics: beam current, spot size, kinetic energy and deflection. The results presented in this chapter form the basis on which the results presented in Chp. 7 for the complete characterization of the residual gas profile monitor operation mode build.

In particular, calibration of the electron beam current allows, in section 7.4.1, to calculate an absolute value for the overall amplification of the monitor and hence for its sensitivity. Beam spot size calibration is useful instead to identify the focus voltage

yielding maximum focusing and evaluating the minimum achievable beam dimensions, used in Chp. 7 to assess image smearing due to ion drift. Kinetic energy directly influences the maximum extraction field that can be used without deflecting the electron beam on the extraction electrodes, hence causing a sharp increase of background noise in the MCP measurement, the calibration presented in this chapter allowed to validate the kinetic energy reading obtained by the display built in the electron gun power supply, hence allowing to adjust the extraction field accordingly. Finally, the measurement of beam deflection was made necessary to insure the proper functioning of the beam steerers, which was initially flawed by a mechanical fault of the gun, preventing the beam from being scanned across the whole active area.

Whilst the electron gun used is a commercial model, limited calibration data from the manufacturer was available, and preliminary tests showed this data not to be reliable anymore due presumably to the combined effects of aging and undertaken repairs.

5.1   Overview and design

The electron gun in use in this work is the ELS 5000 Electron Source and Control Unit manufactured by PSP Vacuum Technology. This gun features a common design, having after the filament three cylindrical plates in an Einzellens configuration; the middle electrode, where the voltage is applied, is 5 times smaller than the other two, kept at ground potential.

Fig. 5.1 shows the main parts of the gun. The filament, first element on the left, is biased with negative voltage and is followed by the grounded anode. Next is the focus plate, and after this, another grounded section of similar length to the anode. Finally come the deflector plates and the grounded end nose.
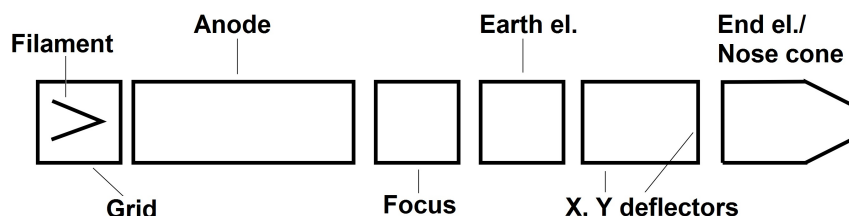
Figure 5.1: Cross-section of the main parts of the electron gun. From the electron gun's manual.

This gun typically produces an electron beam with spot diameter <1 mm, at energies from 1 to 5 keV and currents from 10 nA to 10 μA. Kinetic energies can be as low as 50 eV, but can then achieve less current. The electron gun is also shielded by a mu-metal shield which provides shielding against stray magnetic fields (e.g. earth magnetic field).

5.2 Experimental setup

For the electron gun calibration, three tests have been carried out:

1. Current measurement of the electron beam, dependent on filament current and grid voltage;

2. Spot size measurement, dependent on focus voltage;

3. Beam deflection measurement, dependent on deflector voltage and kinetic energy.

To measure the current of the beam, a detector composed of a biased metal plate connected to a pico-ammeter is used to collect the charge. The detector is movable on a vacuum sealed rotational stage which, through a lever arm, allows horizontal translation in the chamber so as to grant ability to localize the beam. To measure the spot size and beam deflection, a phosphor screen is used in conjunction with a digital camera and a dedicated image analysis software: ImageJ [64]. In the following, the values of the actual voltages set for the grid and the focus are not reported. Instead, use is made of the percentage value, intended as the percentage of the maximum value achievable by the gun supply. The focus actual voltage, indeed, is controlled by the power supply to depend linearly on the kinetic energy, so the percentage is a more suitable descriptor.

ImageJ ImageJ is a Java based open-source software that provides an interface between the most common image formats and a plotting tool, and thus allows to transform the image acquired by the CCD camera in a matrix yielding the gray scale value for each pixel as it is recorded by the camera. In the experiments, the CCD camera, an 8 bit model, hence allowing 0 to 255 gray scale dynamic range, was set to save the acquired image in its native resolution of 1280x1024 pixel, without applying any compression algorithm, so that the ImageJ gray-scale table is equivalent to the CCD pixel

charge map. The digitization error coming from the finite resolution of the CCD camera becomes especially significant when its Poisson distribution is considered, which is particularly influential especially at low signal levels. A full description of Poisson noise in relation to the CCD camera resolution is reported in section 7.4.2.

5.2.1 Current detector and phosphor screen

In order to also identify the position of the beam, the current measuring detector is composed of four plates arranged in quadrants (A to D in Fig. 5.2), whose detected current can be read independently. Balancing of the plates currents corresponds to beam centering for circular cross section beams. In addition, a fifth plate (E) is placed behind the assembly to collect the charge falling between the quadrants.
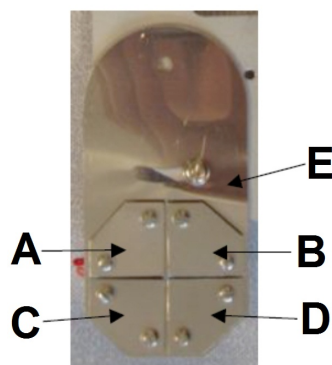
Figure 5.2: Current measurement detector, split in 5 insulated, independently read electrode plates.

This insulation is achieved by ceramic top hat washers on the screws used to connect the plates together, see Fig. 5.3. The screws also hold the signal wires, each wire being curled between two metal washers and held by tightening the nuts on each side of the plates. A piece of PTFE (polytetrafluoroethylene) plastic is used to insulate the detector from the manipulator rod.

A phosphor screen is used to measure the spot size and position of the beam after deflection, hence computing the kinetic energy. The phosphor used is ESPI 311, P31 PHOSPHOR; a combination of zinc sulfide and copper (ZnS:Cu) which produces a yellowish-green glow. It is manufactured by Electronic Space Products, International, Ca USA [65].
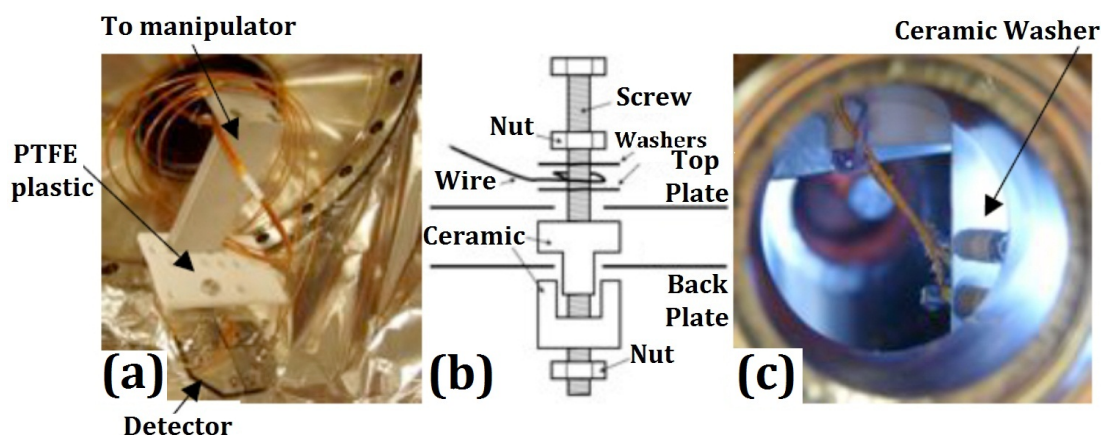
Figure 5.3: Assembly of the current measurement detector. *a)* Detector attached to the manipulator rod; *b)* Cross section of the ceramic washer;*c)* Wiring to PTFE.

5.2.2 Beam current measurement

Only one plate of the detector, plate E in Fig. 5.2, is used to measure the current of the beam. In this operation mode the detector is moved very close to the electron gun tip (10 cm), so as to minimize any possible charge loss. The beam current can be controlled through both the filament current and the grid voltage, controlling respectively the amount of electrons thermally liberated and the collection efficiency.

First, the dependence of beam current from filament current is investigated, and the results shown in Fig. 5.4. This data corresponds to kinetic energy of 3 keV, focus optimized for highest current yield (at 81% of kinetic energy) and grid voltage set to 40% as recommended by the manufacturer. No current is registered at all until the filament current reaches 2.3 A. From 2.4 A to 2.55 A current yield increases steeply and after 2.55 A the rate of increase lessens due to space charge effects that compromise electron collection and saturation of thermal ionization energy.

Second, the influence of grid voltage on beam current is addressed. As in most conventional electron tubes, the cathode is indirectly heated and emits a cloud of electrons. The control grid is a hollow metal tube placed over the cathode; a small opening is located in the center of a baffle at the end opposite the cathode. The control grid is maintained at a negative potential with respect to the cathode to keep the electrons bunched together. A high positive potential on the anodes pulls electrons through the hole in the grid; because the grid is near the cathode, it can control the
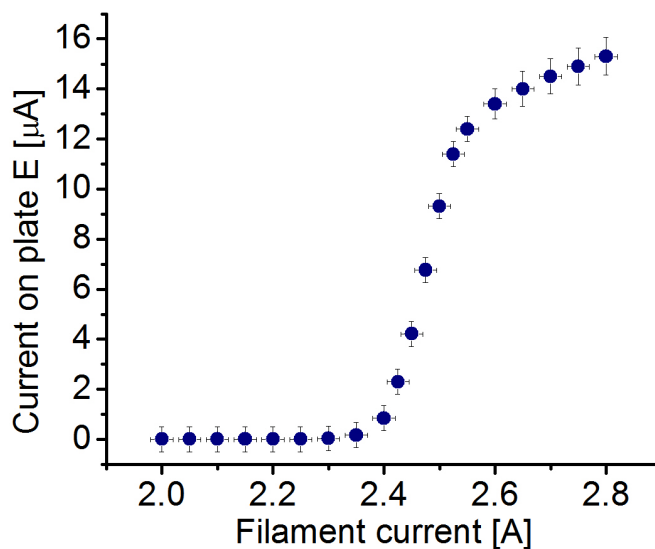
Figure 5.4: Plot of measured current on the detector against filament heating current. Measurements obtained with 3 keV beam, optimum focus and optimum grid potential as specified by the manufacturer.

number of electrons that are emitted. A plot of the measured current for different grid voltage is shown in Fig. 5.5, whilst Fig. 5.6 shows a series of photographs of the beam cross section as imaged on the phosphor screen for different grid voltages. The data is taken with focus at 60%, and filament current at 2.45 A.

5.2.3   Beam spot size measurement.

To investigate how the beam spot cross section changes when changing the focus voltage, the kinetic energy is kept constant at 5 keV, the filament current at 2.3 A in order not to saturate the images taken by the camera and the grid voltage at 40%. Whilst the experiment was run for all values of focus from 0 to 100%, when the focus percentage was more than about 70% the spot size was too big to be measured on the phosphor screen, and those results are hence omitted.

A vacuum vessel of 21 cm flange to flange distance was used for this measurement: this allows measuring the electron gun beam spot at the same distance from the gun tip that there is between gun tip and middle of the interaction chamber in the assembled test stand described in Chp. 4, where the experiments described in Chp. 7 are carried out. The beam resulted to be focused on the phosphor screen when the focus was at
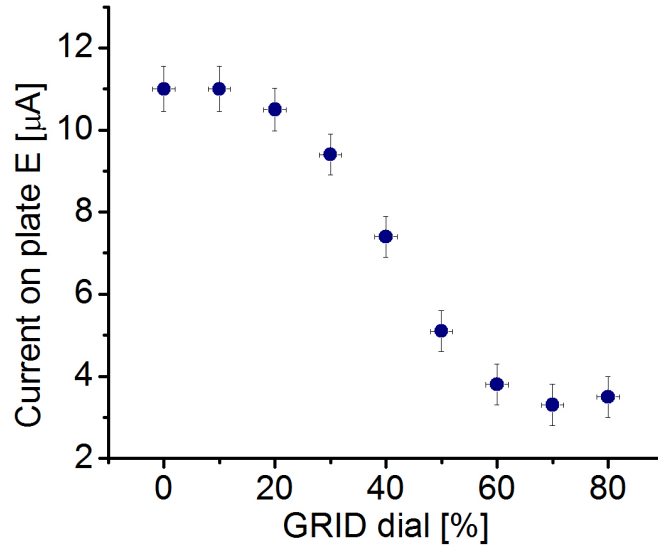
Figure 5.5: Plot of measured current on the detector against grid voltage percentage. Measurements obtained with 3 keV beam, 60% focus voltage and 2.45 A filament current.
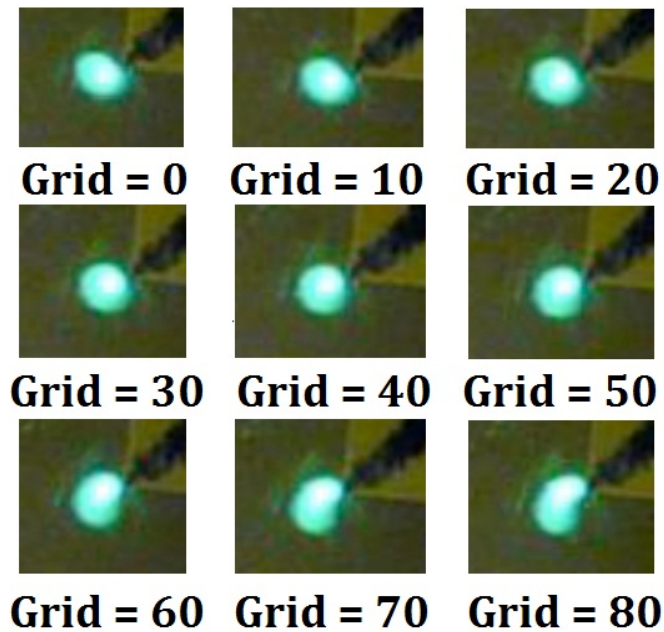
Figure 5.6: Images of the beam cross section as seen on the phosphor screen for different grid voltage percentages. It is seen how the cross section is distorted for high values of grid voltage. Black mark shown for positional reference.

60.4% of kinetic energy, as shown in Fig. 5.7. FWHM of the spot determined using ImageJ.
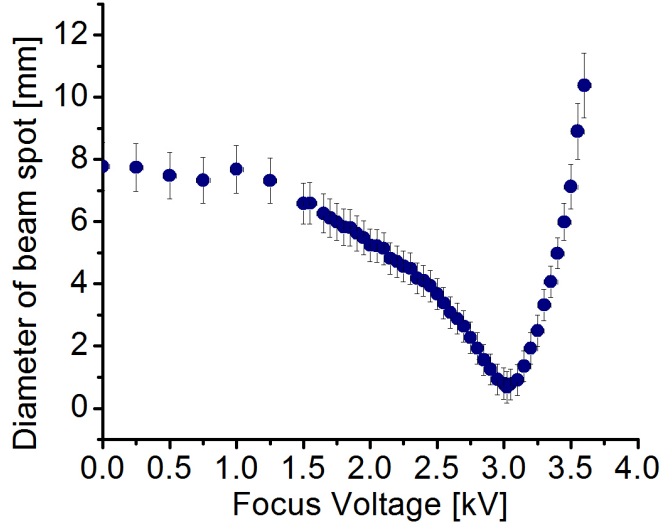
Figure 5.7: Plot of the FWHM spot size 21 cm away from the end of the deflectors with varying focus voltage. Sub millimeter cross section is achieved at optimum operation. Error on focus voltage comparable to data points dimensions.

5.2.4   Beam kinetic energy and deflection measurement.

Changing the kinetic energy dial on the electron gun's controller changes the voltage that the filament is held at and hence the kinetic energy of the beam. To validate the reading obtained by the display built in the electron gun power supply, the kinetic energy of the electron beam is independently measured.

This measurement is carried out by making use of the beam deflectors: they consist of a hollow cylindrical plate divided into four sections at the tip of the electron gun, as shown in Fig. 5.8.

The deflectors are 23 mm long and have an internal diameter of 13 mm. A formula for the kinetic energy in terms of the voltage applied to the electrodes and the observed deviation can be obtained analytically by assuming the plates to be flat and their field to be homogeneous and such that fringe fields effects can be considered negligible. The variables used in this calculations are shown in Fig. 5.9.

The symbols v_x and S_x indicate respectively the initial velocity of the electron in the x direction (parallel to the deflectors) and the length of the deflectors; the voltage on
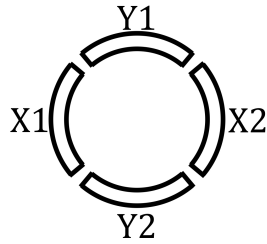
Figure 5.8: Diagram of the cross section of the electron gun deflector plates. This deflection scheme employing curved rather than straight deflecting plates results in non-linear deflection which also changes focusing and emittance properties. However, it has been chosen by the electron gun supplier for manufacturing reasons and it has not been possible to change it.
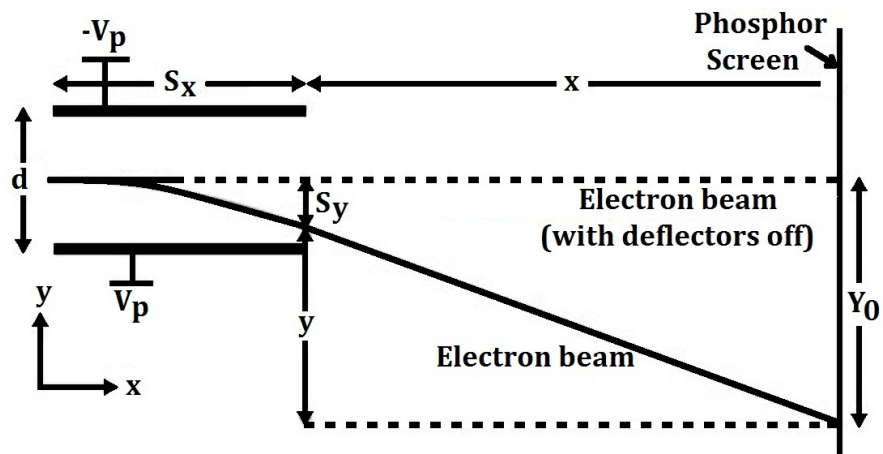
Figure 5.9: Diagram of the simplified system used to derive a formula for the kinetic energy in terms of applied voltage and electron deviation.

one plate is always equal and opposite to the voltage on the opposite plate. Assuming constant field, the field strength between opposite plates biased respectively + and - V_p will be $E = 2V_p/d$, with d being the internal diameter of the plates: 13 mm. By use of the equations of kinematics the distance S_y shown in Fig. 5.9 can then be expressed by:

$$S_y = \frac{eV_pS_x^2}{mdv_x^2} \qquad (5.1)$$

After leaving the deflector the electrons travel in a straight line towards the phosphor screen, covering an additional distance y. The total distance Y_0 expressing the deviation of the electron beam due to the deflecting field can be written as:

$$Y_0 = S_y + y = \frac{eV_pS_x(S_x + 2x)}{mdv_x^2} \qquad (5.2)$$

To introduce the kinetic energy into (5.2), it is not necessary to resort to the relativistic formulation of energy in terms of v_x; indeed, by classical calculation, the velocity of electrons at 5 keV is 0.14 c. At these velocities, the kinetic energy calculated with newtonian physics is only underestimated by less than 2%. Therefore, the simple equation $E_k = \frac{1}{2}mv^2$ is used, where v is obtained by rearranging (5.2). The resulting relation can be used to induce the kinetic energy from the observed deviation Y_0 from the position of the electron beam on the phosphor screen when no field is applied to the deflectors. However, in practice, it is more convenient to use (5.2): a plot of Y_0 in terms of V_p will yield a straight line whose best fit gradient will give the best estimate of v_x and hence the kinetic energy.

A more realistic prediction of the electron beam trajectories, discarding the assumptions of perfectly homogeneous fields and negligible fringe effects, can be obtained by finite elements numerical simulations, realized with OPERA 3D [66]. In the software the four plates of the deflector are constructed with a 10° gap between each plate and 1 mm thickness. Before the deflectors a 60 mm long hollow cylinder is included 1 mm away from the deflectors and held at 0 V. The deflectors length and inner diameter is 23 and 13 mm respectively. An image of the simulated system taken from OPERA is shown in Fig. 5.10, together with an example set of voltages applied.

In the simulation the Y deflectors are grounded and the X deflectors are at ± 12 V: Fig. 5.11 shows the electron tracking.

Beyond the value of 100 mm the trajectories continue to be linear until at $x = 210$ mm the screen is hit. When this happens, Y_0 is computed to be 4.87 mm from its
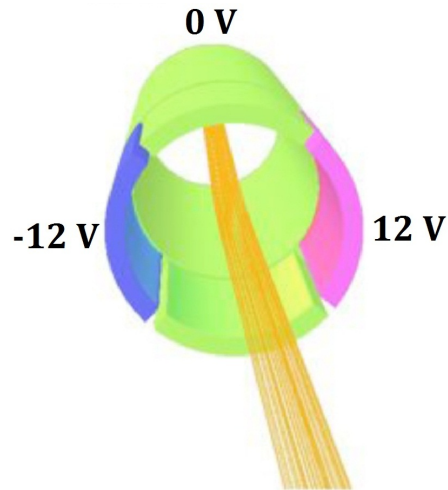
Figure 5.10: Image of the electron gun deflectors simulated in OPERA. The beam coming through the assembly is shown in orange. The colors indicate the applied potentials, with green being ground.
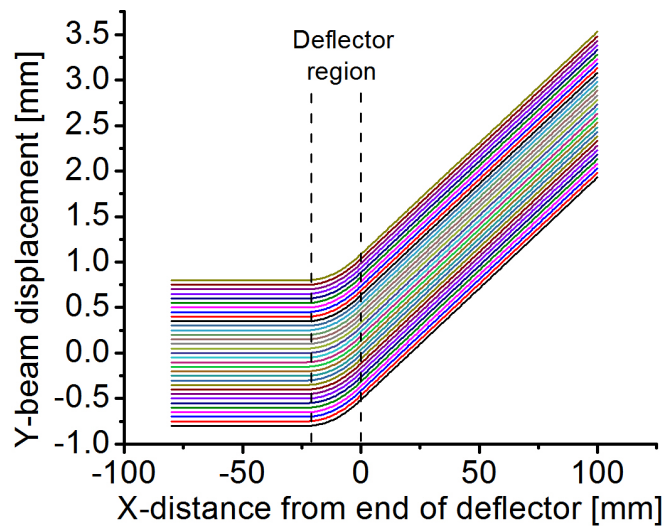
Figure 5.11: Tracking of the electrons in the deflecting plates voltage of ± 12 V for a 2keV beam, 1.6 mm in diameter. Zero on the x axis represents the end of the deflectors. The y axis is instead centered on the electron gun axis.

position with the deflectors off. Further simulations are run to compare the behavior of the electrons when different kinetic energies are employed: these simulations are set up in the same way as the previous one except each line of the resulting plot, shown in Fig. 5.12, represents the center of the beam at different energies.
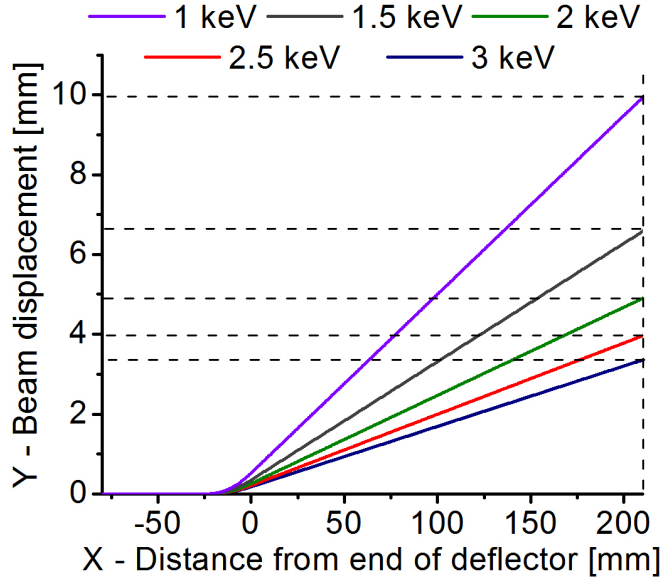
Figure 5.12: Tracking of the central electrons in the deflecting plates voltage for a varying energy beam. ± 12 V deflecting voltage.

The values of beam deflections Y_0 obtained by the simulations can then be compared with the values calculated analytically. The results of the analytical calculation, as expected, underestimates the deflection of the electrons, due to neglecting the fringe fields. This underestimation amounts, on average, to about 8.8% of the simulated value.

Experimental results   The electron gun controller includes two dials that control the deflection of the beam in perpendicular directions. Each dial has a range from 0 to 10 and affects the voltage on the plates that deflect the beam in each direction. When the dial reads 5 the voltage on each plate is 0 V, so there is no deflection, and scales linearly otherwise. The voltages also scale linearly with kinetic energy (so as to maintain the beam position when the kinetic energy is changed). The maximum voltage on the deflector is measured to be 150.2 ± 0.6 V, when the kinetic energy is at its maximum, 5 keV, and the deflectors dial is set to its maximum deflection in either direction, corresponding to 0 or 10 respectively.

The kinetic energy is kept constant at 2 keV and the filament current at 2.3 A to prevent camera saturation. The focus dial is set so that the beam focuses on the screen. The grid is set to 40% and the y deflector is set for no deflection. The x deflector's dial is varied from 5 to 10 taking a photograph every 0.1. All measurements of beam displacement are taken from the position of the beam with the x deflector's off. A graph of the position of the spot on the screen against the deflector's voltage is shown in Fig. 5.13.
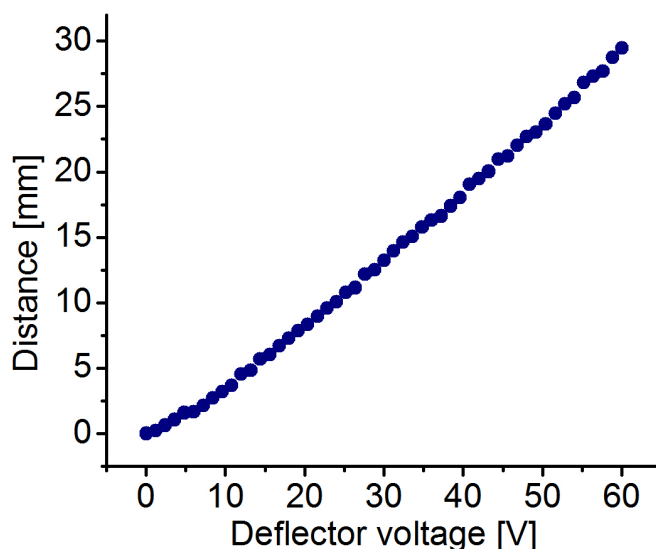
Figure 5.13: Plot of the position of the beam spot on the screen for a 2 keV beam. Errors comparable with data points dimension.

This graph shows a linear behavior, as expected from (5.2). The variations from linearity are due to the error in the measurement of the position on the ImageJ software. Similar graphs have been taken for 3 different values of kinetic energy, for both deflectors and both directions. These measurements are not shown as, when the appropriate modifications on the x axis values are done, they very closely follow the curve shown in Fig. 5.13, due to the mentioned fact that the deflector voltage changes linearly with the kinetic energy to keep the deflection constant at a given deflection voltage dial value, and the symmetry of the deflection.

The measurements show that the nominal value of kinetic energy always overestimates the actual measured energy by an average factor of 3.4% for both deflectors, when the predictions made with OPERA are compared with the measurement. The

result is not due to a difference from the nominal value of the deflector voltage, as this has been tested directly at the connections. However, the difference is so small that it is probably due to differences between real and simulated geometries, and in any case such difference has negligible impact on the following experiments with the gas-jet, both in terms of trajectory and ionization cross section, and can therefore be safely neglected in the following.

5.3 Conclusions

The results presented in this chapter provide a calibration of the electron gun used in the remainder of this work to characterize the beam profile monitor. In particular, beam current measurements show an agreement with the range of currents obtainable from the electron gun, i.e. about 10 μA as quoted by the manufacturer. Furthermore, they provide a way to determine the beam current based on filament current and GRID dial which proves instrumental to measure the profile monitor amplification and sensitivity in section 7.4.1. Beam spot size measurements, beside providing an indication of the beam shape, approximately circular for moderate grid voltages, also prove instrumental in Chp. 7 to assess image smearing due to ion drift. Furthermore, the results shown in section 5.2.4 prove that the repair carried out to the beam deflectors was successful and measurements of monitor linearity across the whole active area can be performed, as it is done in section 7.3.2.

6

Detector system

This chapter describes the detector system used in this work and lays the theoretical foundations for its design.

In section 6.1 a theoretical model to represent the extraction system is introduced and used to predict its performance in terms of image distortion, using this information to optimize the electrical and mechanical design. In section 6.2 the mechanical design of the extraction system is described, while in section 6.3 a simulation software, OPERA 13.0, is used to create a more realistic description of the electric field in the extraction system, and the results obtained with this more complex system are compared with the analogous analysis carried out with a simpler model in section 6.1. Finally, section 6.4 describes the main technological elements of the detector system: the MCP, the voltage divider used for the bias voltages and the phosphor screen.

6.1 Theoretical analysis

6.1.1 Equations set

The extraction system is based, on first approximation, on the simple kinematic equations of motion under constant acceleration. With reference to Fig. 6.1, assuming the screen to be angled at 45° with the horizontal, the gas ions are created by impact ionization at an initial point $\left(x_0,\ y_0,\ y_0 \pm\ k\ \frac{w}{\sqrt{2}}\right)$, $k \in [0,1]$, as described in section 1.3.2.

Through impact ionization, the projectile transfers an initial momentum to the ion, conferring it the initial velocity due to recoil $\vec{v}_{recoil}$. This velocity sums up with the
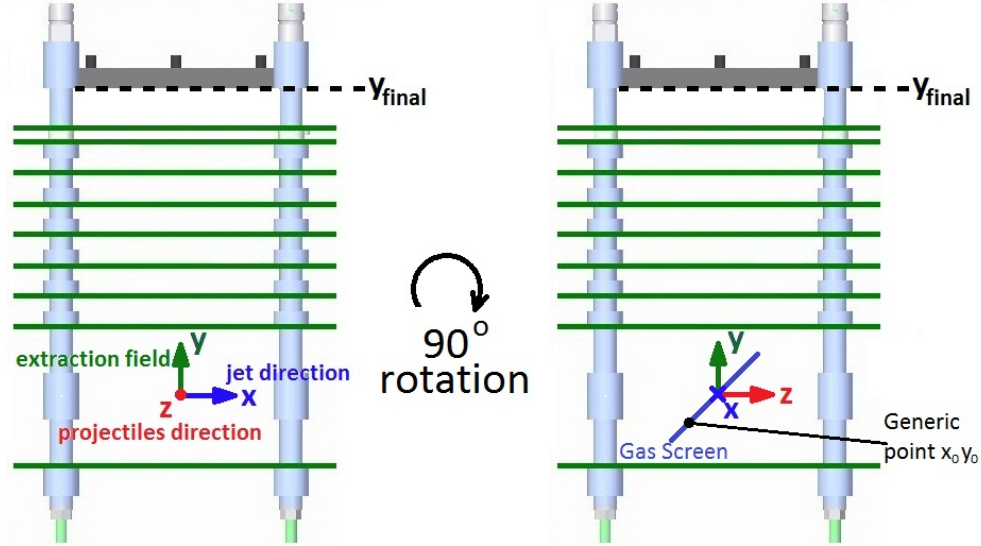
Figure 6.1: Illustrative diagram of the interaction region, showing the directions mentioned in the text as well as the orientation of the gas screen.

initial velocity due to thermal motion $\vec{v}_{th}$, which is negligible in a cold supersonic gas jet, but not in a residual gas monitor. These two initial velocities, $\vec{v}_{recoil}$ and $\vec{v}_{th}$, have in common that their magnitude and direction are random for each collision, and can be therefore merged in a single contribution: the random initial velocity $\vec{v}_r$. Finally, a third component of the initial velocity is due to the gas jet motion $\vec{v}_{jet}$. The total velocity resulting from the sum of all these components will be indicated with $\vec{v}_{tot}$.

The created ions are subsequently accelerated in the homogeneous electric field E provided by the extraction electrodes. This field stops at the vertical coordinate y_1, chosen by assigning suitable biases to the different electrodes, and is followed by a field free drift region extending up to the MCP detector placed at the vertical coordinate y_2. The analysis of the system can then be split in two different regimes: one of motion under constant acceleration, lasting a time t_1, until the particle reaches the vertical coordinate y_1, and one of drift with no acceleration, lasting a time t_2. The total time of flight t will then be given by the sum of t_1 and t_2.

This description of the system results in a set of kinematic equations for the final

positions on the detector x_f and z_f in terms of the initial positions x_0 and y_0:

$$x_f = x_0 + \vec{v}_{tot,x} t$$

$$z_f = y_0 \pm \frac{w}{\sqrt{2}} + \vec{v}_{tot,z} t$$

$$t_1 = \frac{-\vec{v}_{tot,y} + \sqrt{\vec{v}_{tot,y}^2 + 2a\left(y_1 - y_0\right)}}{a} \tag{6.1}$$

$$t_2 = \frac{y_2 - y_1}{\vec{v}_{tot,y} + a t_1}$$

$$a = eE/m_{gas}$$

where e is the elementary charge, equivalent to the total charge of the singly ionized gas ions, and a the ion acceleration. The main assumption underlying these equations is that the electric field in the extraction region is homogeneous and parallel to the y axis, so that constant acceleration along the y axis alone is experienced by the ions. Only discrepancies smaller than 3% are indeed found in the simulated field; the plots obtained through direct applications of eqn. (6.2) have also been recalculated with a particle tracking code making use of the actual simulated field, showing again only very small discrepancies, as shown in section 6.3.

Eqn. (6.2) also assumes that the velocities involved are not relativistic, and hence the classical equations of motions can be used. This last condition is easily satisfied, as ions are accelerated through electrostatic potentials of only a few kV, resulting in speeds some 3 orders of magnitudes smaller than the speed of light.

Before eqn. (6.2) can be applied to characterize the detector resolution and image distortion, and hence optimize the detector design, a more detailed description of the initial velocities distributions is needed, and presented in the following subsection.

6.1.2 Initial ion velocity

As mentioned, the initial ion velocity is composed of 3 different components, due to thermal motion, impact recoil and jet velocity.

Jet velocity component As it has been discussed in Chp. 2, and in particular with reference to Fig. 2.3, most collisions between gas jet molecules occur in the very first few nozzle diameters downstream the expansions. Beyond this point, the number of collisions in the jet decreases dramatically, to the point that is is safe to assume that no more collisions occur when the flow becomes molecular. Given the nozzle diameter used in this work (30 μm), the distance beyond which no more collisions are expected to occur is in the order of millimeters, negligible with respect to the distance from the nozzle to the interaction point of about 600 mm. Therefore, it can be safely assumed that the jet molecules move in a straight line from the nozzle to the interaction point, so that the direction of their velocity is given by the unit vector starting in the nozzle position and pointing at each particle position in the gas screen.

If the longitudinal distance from the nozzle is indicated with d_n; ζ is the angle between the jet axis and the jet molecules reaching the interaction region with y coordinate y_0; h is the elevation on the screen given by $h = y_0/sin\,\alpha$ and α is the screen tilt with respect to the vertical, one can write for the 3 components of the velocity $\vec{v}_{jet}$:

$$
\begin{aligned}
v_{jet,x} &= v_{jet}\,cos\,\zeta & &= v_{jet}\,cos\frac{h}{d_n} = v_{jet}\,cos\left(\frac{y_0}{d_n\,sin\alpha}\right) \\
v_{jet,y} &= v_{jet}\,sin\,\zeta\,sin\,\alpha & &= v_{jet}\,\frac{h}{d_n}\,sin\alpha = v_{jet}\,\frac{y_0}{d_n} \\
v_{jet,z} &= v_{jet}\,sin\,\zeta\,cos\,\alpha & &= v_{jet}\,\frac{h}{d_n}\,cos\alpha = v_{jet}\,\frac{y_0\,cos\alpha}{d_n\,sin\alpha} = v_{jet}\,\frac{y_0}{d_n}
\end{aligned}
\tag{6.2}
$$

where the assumptions of small angles has been used in the y and z components of velocity to substitute $sin\,\zeta$ with $tan\,\zeta$. Moreover, the magnitude of the velocity can be assumed to equal the terminal velocity expressed as per eqn. (2.9).

Thermal velocity component The thermal velocity component comes from the random Brownian motion of molecules in a gas, is completely random in direction, and each of its three orthogonal components $v_{th,i}$ is normally distributed with zero mean (isotropy of space) and standard deviation $\sqrt{RT/W}$ [42]:

$$
f_v\left(v_{th,i}\right) = \sqrt{\frac{W}{2\pi RT}}e^{-\frac{Wv_{th,i}^2}{2RT}}
\tag{6.3}
$$

which is a probability density function for the integration element $dv_{th,i}$. The three velocity components distributed as in eqn. (6.3) integrate together for the speed $v_{th} =$

$\sqrt{v_{th,x}^2 + v_{th,y}^2 + v_{th,z}^2}$ and the volume integration element $dv_{th} = v_{th}^2 \, sin\phi \, dv_{th} \, d\theta \, d\phi$ to yield the well known Maxwell-Boltzmann speed distribution function, for which the most probable speed is given by $v_p = \sqrt{2RT/W}$. In the case of a supersonic gas jet, T can be smaller than 1 K (see Chp. 2), corresponding to about 25 m/s velocity for N$_2$ and 65 m/s for He: i.e. 0.2 and 0.6 a.u. of momentum respectively. The velocity component due to impact recoil, treated in the next section, is shown to correspond to about 1 to a few a.u. of momentum for most collisions, and thus dominates on the thermal velocity component for sufficiently cold jets.

This effect represents a difference with respect to the operation as a residual gas monitor, where thermal velocities equate, for room temperature residual gases, to respectively 3 and 10 a.u. of momentum for He and N$_2$, and hence represent the most influential contribution to ion drift.

Recoil velocity component   When light, singly charged projectiles such as electrons and protons collide with molecules, different reactions can occur, ranging from electron capture to multiple ionization of the target molecule. However, the phenomenon relevant to this work is single impact ionization for projectile energies in excess of few tens of keV, following the reaction $p + X \rightarrow p + X^+ + e^-$ where p is the projectile, X the molecule and e the liberated electron; cross sections for double ionization are $2 \div 3$ orders of mangnitude smaller [4, 9]. Therefore in the following discussion only single ionization will be treated.

The two-body collision system is axis-symmetric around the projectile velocity axis, hence in literature the description of the momentum transfer is done in terms of parallel and transverse momentum components. The actual direction of the transverse momentum is randomly selected with a homogeneous distribution which depends on the impact parameter: however, given the nature of the projectile bombardment, it is safe to assume the impact parameters to be randomly distributed and hence the transverse momentum direction distribution to be homogeneous.

As for the magnitude distributions of the transverse and parallel momenta, these vary depending on the reaction taking place and the projectile and target involved. Nevertheless, it is possible to identify general trends. The longitudinal distribution is usually approximately a Gaussian shaped curve with negative mean for positively charged projectiles (i.e. the recoil ion moves backward, towards the impacting direction

of the projectile) and standard deviation of less than 1 atomic unit. The absolute values of both the mean and the standard deviation increase as the projectile charge or mass is increased [67–74]. However, even when changing from protons to electrons, despite the much lower projectile mass, the momentum transfer is very similar, in the range of 2÷5 atomic units for energies of up to 5keV, see e.g. [75], which investigates the recoiling ion momentum in the ionization of He by electron impact. This observation justifies the use of an electron beam in this work to simulate the behaviour of the jet in presence of an antiproton beam.

The dependence on projectile energy is more complex, as the recoil magnitude presents a peak at low energies where interaction is stronger (few hundreds eV), only to decrease in the keV region and then slightly increase again as the energy is increased in the MeV region. Less influencing is instead changing the neutral target. It is noted that operation of the gas jet monitor can be usually optimized when heavier projectiles are used, as while the recoil increases, the mass also increases, allowing the use of a stronger extraction field.

For the purpose of this work the experimental results for proton impact on Helium will be used as an example of light projectile impact ionization. The choice is motivated by the fact that proton collisions on Helium constitute one of the simplest non-stationary quantum mechanical three-body systems allowing the complexity of double ionization and capture reactions, and are therefore a very important testing ground for theories, which in turn has led to several studies, e.g. [69]. For this special case, the longitudinal momentum distribution of the recoil ion in atomic units can be approximated with a Gaussian curve with $\mu = 0$ and $\sigma = 0.5$.

Theoretical predictions for the transverse momentum distribution are obtained through Monte Carlo techniques, which are presently the only method in the non-perturbative regime that treats the full three-particle problem without any approximation apart from classical scattering for the interaction of charged particles [74]. An example of experimental results for Helium ionization by fast proton collisions, which presents all the plots usually found in this field of study, and from which the distributions used in this work are taken, is shown in Fig. 6.2, 6.3 and 6.4 [69].

However, an analysis of the plots shown in Fig. 6.4, in conjunction with the plot in Fig. 6.3, suggests a simple functional relationship for the transverse momentum. If both components of the transverse momentum are assumed to be Gaussian distributed, with
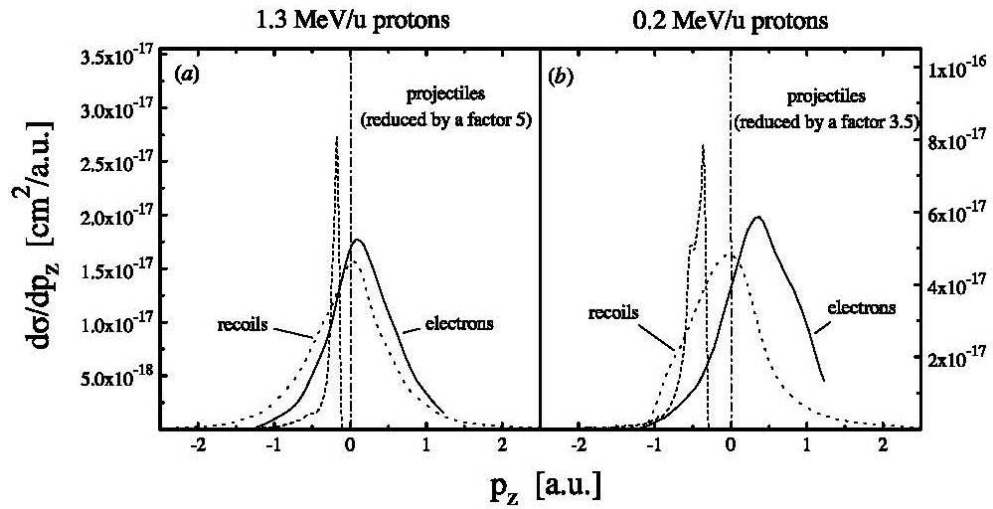
Figure 6.2: Experimental longitudinal momentum distributions of the recoil ions (dotted curve), electrons (full curve) and the loss in momentum of the protons (broken curve) for two different kinetic energies of the projectiles (measured in energy per nucleon): (a) 1.3 MeV u^{-1} and (b) 0.2 MeV u^{-1}. The units of momentum are *atomic units*[2]Taken from [69]
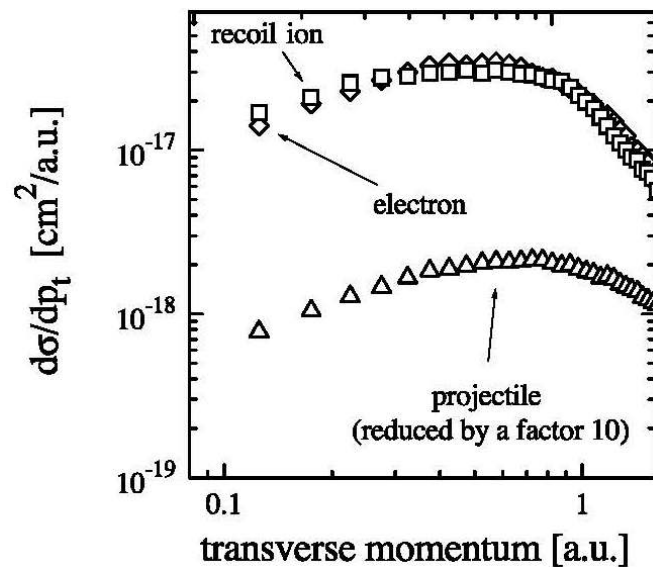
Figure 6.3: Transverse momentum distributions of the recoil ions (squares), electrons (diamonds) and projectiles (triangles) for single ionization of Helium with protons (500 keV kinetic energy). Momentum expressed in atomic units. Taken from [69].
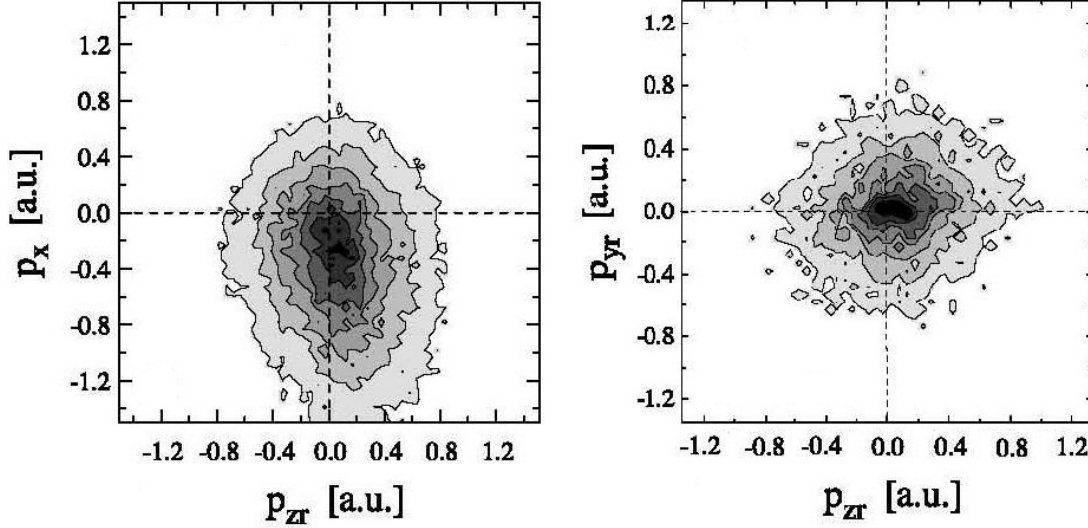
Figure 6.4: Momentum distribution of the recoil ion projected on the collision plane, defined by the incident and outgoing projectile (left) and perpendicularly to the collision and azimuthal plane (right). The doubly differential cross section $d^2\sigma/(dp_x\,dpz)$ is plotted on a linear scale. Momentum expressed in atomic units. Taken from [69].

zero mean, Fig. 6.4 is easily understood, and the right-shifted peak of Fig. 6.3 comes naturally when the vector summation of the two components is performed. For the transverse momentum one has $p_\perp = \sqrt{p_x^2 + p_y^2}$, and for the surface element $dp_x\,dp_y = p_\perp\,dp\,d\vartheta$, with ϑ being the angle lying on the plane perpendicular to the impinging projectile direction. Therefore, integrating ϑ over 2π, yields the expression for the transverse momentum, to be compared with the data plotted in Fig. 6.3:

$$
\begin{aligned}
f\,(p) &= \int_0^{2\pi} A\,e^{-\alpha p^2}\,p\,d\vartheta \\
&= 2\pi\,A\,p\,e^{-\alpha p^2}
\end{aligned}
\tag{6.4}
$$

where the constants A and α need to be tailored to fit the experimental data. The curve in eqn. (6.4) presents, as required, a slow increase from zero to a peak and a comparatively sharp fall beyond the peak. In the particular case of proton collision on Helium as reported in [69], the best fit of the experimental data is obtained with A and α having respectively values of $1.6\cdot 10^{-17}$ cm^2/a.u. and 1.2 a.u, corresponding for each perpendicular component to a Gaussian distribution with $\mu = 0$ and $\sigma = 0.65$.

6.1.3 Calculation

Having defined the probability density distributions for each velocity component forming v_{tot}, it is possible to combine them and substitute into eqn. (6.2) to obtain, rather than the values of x_f and z_f, the probability distributions for the same variables. It is in principle possible to perform this operation analytically, however the calculation becomes very unwieldy and the resulting expression complex enough to mask the physical significance. In what follows the analytical calculation technique is described and the reasons that lead to the choice of a numerical solution explained. The numerical solution itself is also presented.

Analytic solution The distribution of the total y component of velocity $v_{tot,y}$ is the sum of 3 different components, two of which are normally distributed whilst the last one, $v_{jet,y}$ has instead a fixed value, i.e. a Dirac's delta distribution. The distribution of the sum velocity $v_{tot,y}$ is given by the convolution of the three components, made two at a time. The convolution of two functions f and g is defined as:

$$f * g\,(x) \; = \; \int_{-\infty}^{\infty} f\,(t)\; g\,(x - t)\; dt \tag{6.5}$$

therefore, it is by definition equal to the sum of all probabilities $f\,(t)\; g\,(x - t)\; dt$, satisfying the condition $t + (x - t) = x$, i.e., the total probability of the sum of the two random variables yielding x. In the special case needed in this work, this convolution is straightforward, as the convolution of two Gaussians is still a Gaussian with its mean being the sum of the individual means and variance the sum of the individual variances. The convolution of a Gaussian with a Dirac's delta is instead still a Gaussian with mean given by the sum of the Gaussian mean and the Dirac's delta, and same standard deviation as the Gaussian.

Once the distribution of $v_{tot,y}$ is obtained, the distribution of t can be obtained by substituting, in the Gaussian formula for $v_{tot,y}$, the value of $v_{tot,y}$ in terms of t, as obtained from eqn. (6.2). The amplitude of the Gaussian can then be found by normalization.

However, to obtain the distributions for x_f and z_f, the Gaussian distributions for $v_{tot,x}$ and $v_{tot,z}$ respectively need to be combined with the distribution found for t so as to obtain the distribution for their product, as it appears in eqn. (6.2). To do this an

operation similar to convolution need to be performed, but instead of having to satisfy the condition $t + (x - t) = x$ for summation, the condition to satisfy is $t + (x/t) = x$, for multiplication:

$$f \ast' g(x) = \int_{-\infty}^{\infty} f(t) \, g\left(\frac{x}{t}\right) \, dt \tag{6.6}$$

Unfortunately, the integral in eqn. (6.6) is not solvable analytically, therefore the problem of finding the distributions needs to be solved numerically.

Numerical solution To numerically solve the system of eqn. (6.2), and generate a probability distribution for x_f and z_f, it is sufficient to directly solve the system for a homogeneously distributed sample of the constituting distributions for the velocities and the position of ionization in the screen, controlled by the parameter w. A homogeneously distributed sample is obtained by homogeneously dividing the interval $0 \div 1$ in the required number of samples, and then selecting the value X_i of the random variable such that the probability of it assuming a value between $-\infty$ and X_i is equal to the chosen sample value in the interval.

In order to minimize the number of points to be taken and optimize computation time, the 3 distributions for $v_{jet,i}$, $v_{recoil,i}$ and $v_{th,i}$ for each axis i have been merged through the convolution operation described earlier in this section. This allows to minimize the number of degrees of freedom for the initial velocity to the minimum of 3. A 4th degree of freedom needs to be added to account for the finite gas jet screen thickness w.

Each initial velocity degree of freedom has been sampled with $1\dot{\,}000$ points, whilst 50 points only have been used for the distribution of w for a total of $5 \cdot 10^{10}$ points needed to obtain a full distribution for x_f and z_f. The use of a lower number of points for the homogeneous distribution of w comes from the realization that, with reference to Fig. 6.2, the contribution of w to the value of z_f is added directly, instead of being multiplied for t. Therefore the sampling resolution of the distribution of w directly influences the distribution of z_f. For a typical screen thickness of 0.5 mm, 50 points correspond to a sampling resolution of $10 \mu m$, well below the expected spot blurring due to the initial velocity distribution.

6.1.4 Design constraints

The driving equations of the system, eqn. (6.2), include several variables: mechanical dimensions (y_2 and y_1); projectile beam profile (x_0 and y_0); initial velocity contributions due to temperature, ion recoil and initial jet speed (v_{th}, v_{recoil}, v_{jet}); screen width w and electric field strength (coming in the calculation of the acceleration a). However, the values of some of these variables are set by the application, and cannot be modified by the design, namely the initial velocity contributions and the projectile beam profile. Therefore the following analysis will focus on mechanical dimensions, screen width and electric field strength, which, apart from some set constraints, can be optimized through appropriate design.

Extraction system length For the particular application motivating this work, an important constraint is imposed on the mechanical dimensions of the extraction system. Indeed, a shorter extraction system would decrease ion drift and increase resolution for the profile monitor. However, for operation as a ReMi, a long extraction system is needed, so that the ions can be allowed a longer drift space and, hence, a better resolution on transferred momentum can be obtained. The limit used in this work is $y_2 > 150$ mm, a commonly used dimension in ReMi [38]. Therefore, the physical dimension optimization concerns only the variable y_1, i.e. the start of the drift region, which ends at y_2. Indeed, differently from y_2, y_1 can be changed dynamically without resorting to any physical modification of the system, by modifying the applied potentials from outside the vacuum chamber.

Extraction field strength The second relevant limitation concerns the electric field strength. Increasing the field strength results in shorter ion drift and hence improved resolution. However, the field also affects the traversing projectile beam, disrupting its orbit. In the final application in the USR, orbit disruption cannot be tolerated, due to the cumulative effects resulting from multi-pass operation of the ring, and need to be corrected with suitable correction fields. In the test stand, given the much lower energy of the electron beam from the gun, high extraction fields result in the beam hitting the extraction electrodes, resulting in increased background noise from scattered and liberated electrons and in the inability to image the electron beam on the phosphor screen to probe its position.

The limit given by the USR operation can be estimated by calculating the orbit that an on-axis particle would follow passing through the correction fields and extraction fields. The orbit bump setup is depicted in Fig. 6.5. As a first, very rough estimation of the fields upper limits, the fields should be tailored so that at its position of maximum off-axis excursion, the orbit does not approach the electrodes plates more than about $50 \div 60\%$ their inner radius, i.e. $50 \div 60\%$ fill factor. This precaution prevents the beam from getting too close to the electrode plates, where field inhomogeneities are more influential and non linear effect occur which result in beam disruption and decreased lifetime [76–78]. For the USR, whose design is treated in the above references, the electrodes can be assumed to have an inner radius of 100 mm and be 200 mm long, with a 5 mm gap in between.

This configuration is compatible with a 400 kV/m extraction field for 20 keV antiprotons (the lowest energy limit in the USR), and can be increased for higher energies.

However, such extraction field strength cannot be achieved in the test stand, due to the fact that lighter and slower projectiles are used, i.e. electrons with energy ≤ 5 keV. In particular, using the OPERA simulation software for calculating the trajectories of electrons in the extraction system, it is calculated, as summarized in section 6.3.2, that in order to be able to scan the electron beam across a 5 cm gas screen tilted at $45°$ with respect to the horizontal, without hitting the extraction electrodes, the extraction field needs to be ≤ 12 kV/m. Ability to scan the electron beam across the whole 5 cm square of the gas screen is needed to probe the screen density homogeneity with the electron beam and hence demonstrating imaging uniformity.

Screen width Finally, the screen width w is limited by two factors: the mechanical precision available to manufacture the skimmer, and the requirement on reaction rate, which decreases linearly with w. As for the mechanical precision limitation, whilst it is routinely possible to laser cut very thin slits (down to <10 μm), for operation of the gas jet a skimmer is to be preferred to a flat slit, in order to prevent molecules backscattered by the flat wall to cross the jet stream causing intensity decrease as well as temperature increase (resulting in turn in increased w). The quality parameter becomes then the aspect ratio between the skimmer aperture and the thickness of the walls at the skimmer tip. In practice, this limits the available skimmer apertures to
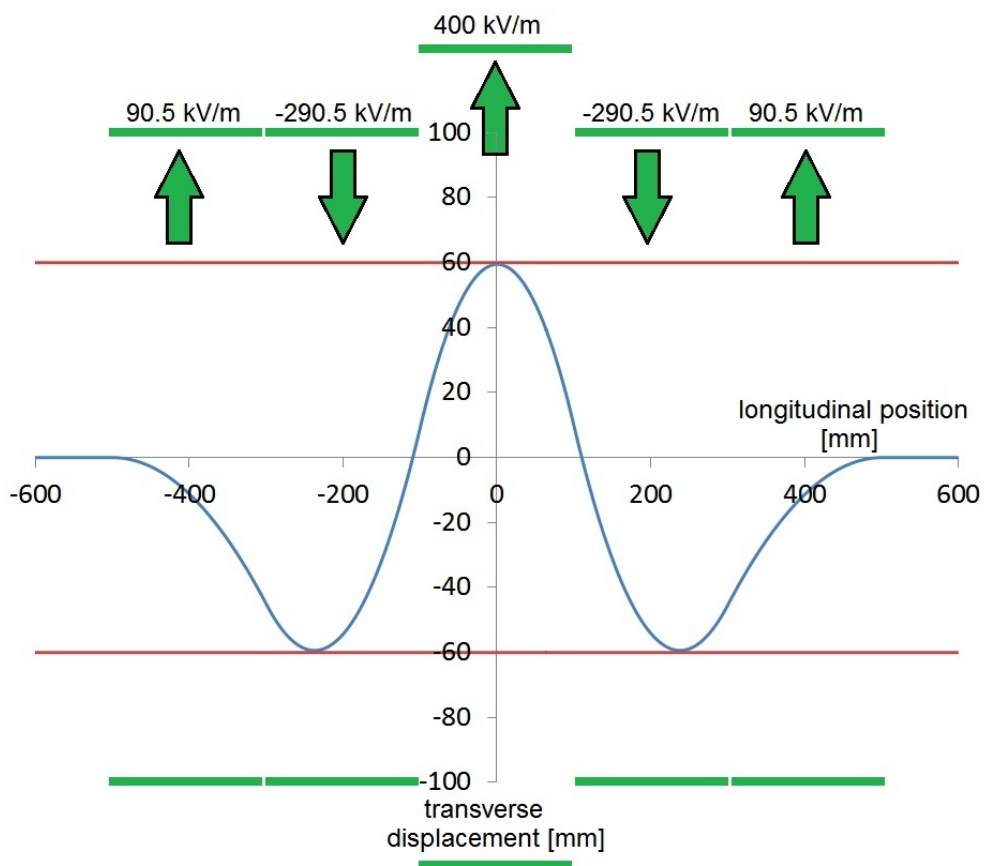
Figure 6.5: Sketch of the orbit bump in the USR needed to correct for the extraction field of the jet profile monitor. Voltages applied to the electrodes (shown in green) and resulting central orbit of 20 keV antiprotons shown as calculated analytically assuming homogeneous fields and no fringe fields effects. Particle trajectory (antiprotons) shown in blue; red lines show the limits for a 60% fill factor.

dimensions in the hundreds of μm scale. For the purpose of this work, the lower limit on w, given by the manufacturing capabilities available, is 400 μm.

6.1.5 Results

Fig. 6.6 shows the probability distribution of a particle ionized in the axes origin to be imaged at the point (x, z), equivalent to the spot created by a beam perfectly localized in the the axes origin. The profile width in the z direction is dominated by the screen width w. The plot is obtained by running the simulations several times, each time with a different samples combination from the Gaussian initial velocity distributions and the flat screen depth position distribution. Furthermore, the low number of counts in the tail regions explains the small statistical ripple observed. The overall distribution resembles the summation of several Gaussian distributions homogeneously distributed along the z axis, i.e. in the direction of the gas screen depth.

The spot size can be characterized in terms of mean μ and standard deviation σ for both transverse profiles, whose values can be plotted to investigate the spot size dependence on the other variables of interest for the design: w, E, and y_1, keeping the condition $y_2 = 150$ mm, as required by the ReMi operation mode. When this is done for the plot in Fig. 6.6, the values obtained are shown in Table 6.1:

Observable	Value
μ_x	1.51 mm
σ_x	41 μm
μ_z	0 mm
σ_z	0.15 mm

Table 6.1: Mean and standard deviation of both simulated x and z profiles. Calculated for $w = 0.5$ mm, $y_1 = 55$ mm, $y_2 = 150$ mm, homogeneous electric field of 12 kV/m and jet speed of 790 m/s.

Screen width   Fig. 6.7 shows a plot of σ_z when the value of w is changed in the range 0.1 to 2.5 mm; the parameter of the curve is the electric field E, increased in 5 steps from 12 kV/m to 60 kV/m.

As the parameter w is increased, the contribution of the Gaussian spread due to the initial velocity, which is the only factor present for $w = 0$, becomes more and more
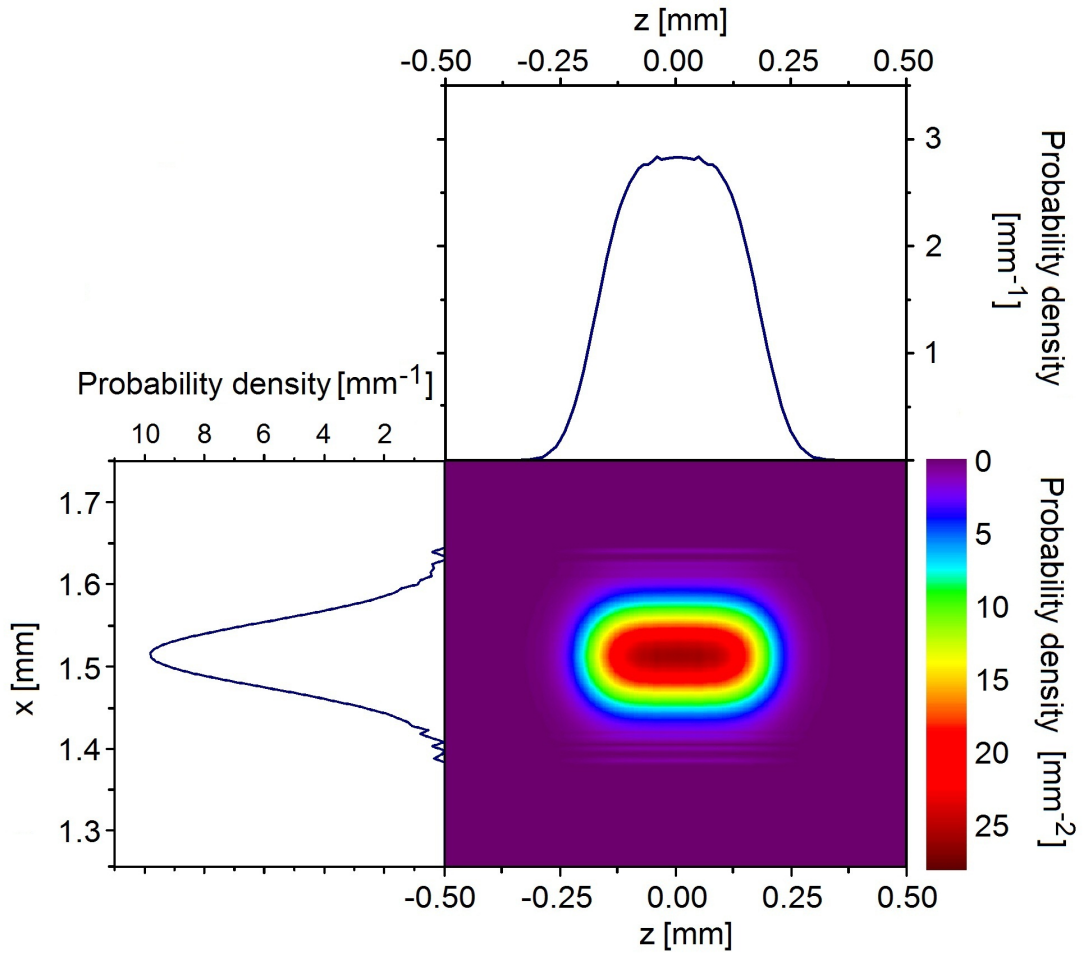
Figure 6.6: Probability distribution function of a particle ionized in $x = y = 0$ to be imaged in the point x, z; equivalent to the 2-dimensional spot resulting from ionizations in $x = y = 0$. 1-dimensional profiles also shown. Statistical ripple due to low counts number is observed at the tail of the distributions; $6.25 \cdot 10^9$ points used. The parameters used are $w = 0.5$ mm, $y_1 = 55$ mm (optimum value, see later in this section), $y_2 = 150$ mm, homogeneous electric field of 12 kV/m and jet speed of 790 m/s.
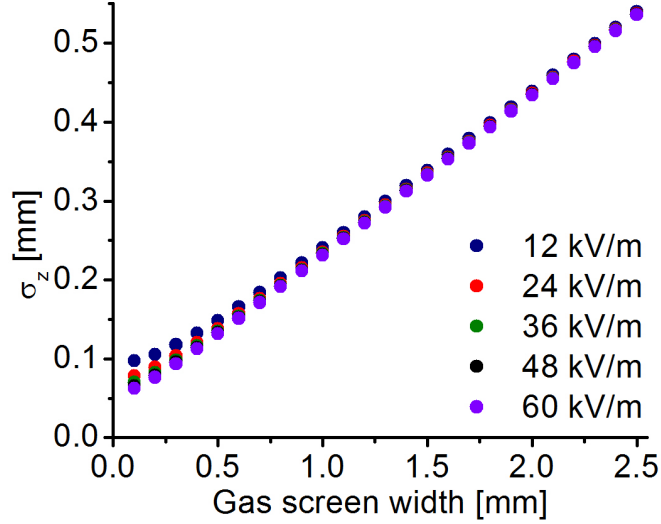
Figure 6.7: σ_z as a function of screen width w, varying from 0 to 2.5 mm, with curve parameter E, varying from 12kV/m to 60kV/m.

negligible, to the point that the plot in Fig. 6.7 becomes a straight line. This effect happens earlier when the electric field is increased, as larger fields decrease the spread due to initial velocity. In particular, for $w = 0.5$ mm it can be seen that σ_z corresponds to about $0.13 \div 0.15$ mm, not depending on E by more than 15%; and still larger than σ_x by a factor of about 4.

Electric field Both μ_x and μ_z are unchanged by variation of the parameter w alone, and so is σ_x. The x profile characteristics are therefore best visualized in the plots shown in Fig. 6.8, which investigate the dependence from E. Being affected only by a random velocity component centered in zero, μ_z is also independent of E and y_1, and stays null.

As compared to the value limited by the electron gun energy as discussed in section 6.1.4, of 12 kV/m, only a factor of 2 to 2.5 can be gained in the x profile observables by increasing the electric field strength 5-fold, and no significant gain is obtained concerning σ_z (see Fig. 6.7), due to the influence of the screen width w. Therefore, the design value of $E = 12$ kV/m is chosen.

Drift region dimension The position y_1 where the drift region starts has an opposite effect on the times t_1 and t_2. This results in leveling of the drift for ions created

130
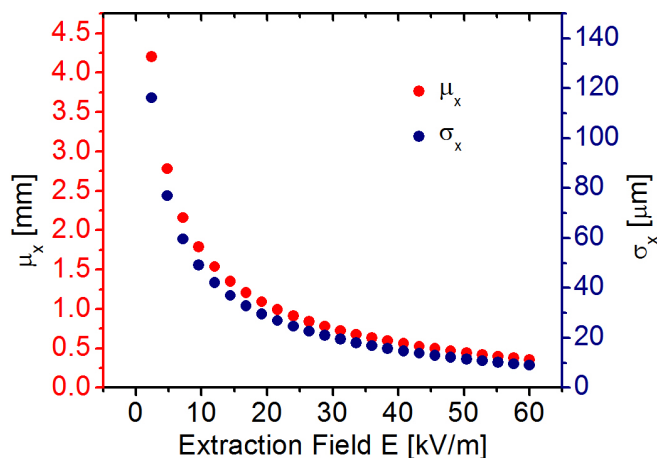
Figure 6.8: Plot of μ_x (blue curve, left axis) and σ_x (red curve, right axis) for varying electric field strength E, from 2.4 to 60 kV/m.

at different y_0 positions. Indeed, in the drift region, ions created further away from the detector, and hence accelerated through a larger potential difference, have the chance to catch up with slower ions, which have reached the drift region earlier, having started closer to it. For each couple of y_0 coordinates, there is an optimum drift region value which equals the times of flight, and hence the drift. However, this optimum value changes from couple to couple and times of flight will still be different over the continuous range. Nevertheless, the maximum to minimum range can be still be optimized by choosing a suitable value for y_1.

When analyzing the x profile, this effect can be seen directly by plotting μ_x: optimization is obtained by choosing the value of y_1 that minimizes the spread of the μ_x values across the y_0 range of interest. In Fig. 6.9 is plotted the difference between the maximum and minimum μ_x across a 5 cm range for y_0, for different values of y_1, showing a minimum at $y_1 = 55$ mm.

The same analysis cannot be repeated in the same terms for the z profile, as μ_z is dominated by the initial position y_0. Moreover, the y resolution of the monitor is linked to the derivative dz/dy_0, which hence needs to be made as homogeneous as possible across the y_0 range. The optimization is therefore better carried out by choosing the y_1 value which maximizes the linear regression coefficient for the plot of z_{mean} against y_1. This plot is also shown in Fig. 6.9, and provides an optimum value of $y_1 = 55$ mm.
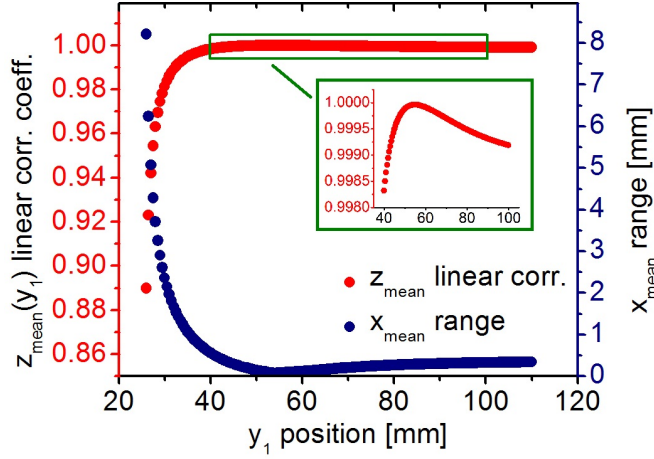
Figure 6.9: Linear regression coefficient for the plot of μ_z against y_0 at different values of y_1 (left axis); and difference between maximum and minimum μ_x in the y_0 range at different values of y_1 (right axis). The range of y_0 used is $-25 \div 25$ mm in both cases. A zoom in view of the linear regression coefficient curve is provided to show the region of the peak.

As for its effect on the profiles spread, the relevant observable is the maximum standard deviation in the y_0 range of interest. This is plotted in Fig. 6.10 for both the x and z profiles. The curves are related solely to the time of flight and thus monotonically decrease as the value of y_1 is increased, as this results in a longer region of field and hence acceleration. However, from $y_1 = 55$ mm to the limit value of $y_1 = 150$ mm, only a decrease in the order of 7% for the x profile and 3% for the z profile can be obtained. Such advantage is overshadowed by the disadvantage illustrated in Fig. 6.9, due to the μ_x difference in values across the y_0 range being increased by a factor of nearly 5. The value of $y_1 = 55$ mm is therefore chosen to be the design value for y_1.

Simulated imaged profile Having determined the optimum values of the detector system parameters, it is possible to reiterate the simulation done for Fig. 6.6 for a set of points sampling an impinging beam, and so create an image of the expected 2-dimensional profile obtained on the detector. Fig. 6.11 shows the result of this simulation, in which the impinging beam has been assumed to be Gaussian distributed in both the x and y direction, centered in x_0, y_0, and having a standard deviation of 5 mm in both directions. These beam dimensions are compatible with the beam dimensions expected in the USR, where emittances in the order of a $1 \div 5\pi$ mm mrad
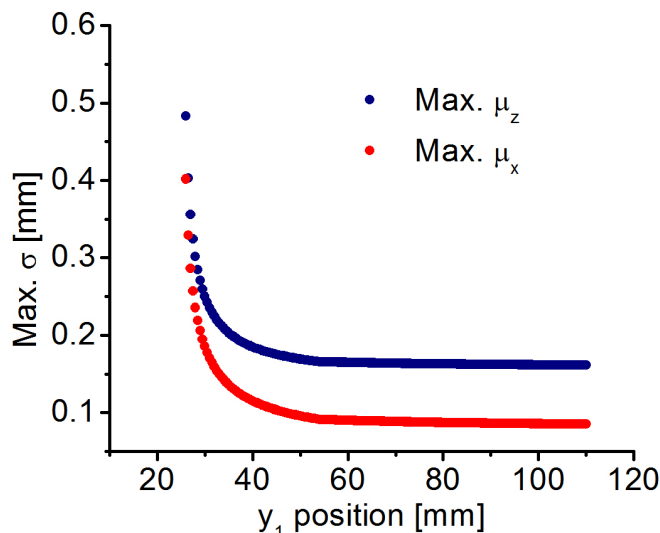
Figure 6.10: Maximum FWHM for the x and z profiles in the y_0 range of interest, at different values of y_1. The range of y_0 used is $-25 \div 25$ mm in both cases.

are expected and the beta function[3] has a value of about 7 m in the symmetric beam operation mode and 16 m in the zero dispersion operation mode [79].

The plot in Fig. 6.11 does not show the elongation along the z axis that characterizes instead the plot in Fig. 6.6. This result is expected, as the profile obtained for the extended beam is the convolution of the profiles for the single incident particles, as

---

[3] Beam emittance ϵ represents the phase space volume occupied by the beam of particles. For unbounded beam distribution (like the Gaussian), it is more convenient to define the beam emittance as phase volume occupied by the beam within one standard deviation from the mean, i.e. the 1-σ beam emittance $\epsilon_{1-\sigma}$. The three components of the emittance, one for each Cartesian coordinate i, are then defined as the area of the phase space ellipse for the corresponding Cartesian coordinate, in terms of the standard deviation values for both distribution of positions (σ_Q) and momentum (σ_P):

$$\epsilon_{1-\sigma,i} \; = \; \pi \sigma_{Q,i} \sigma_{P,i}$$

During motion in the accelerator the phase space ellipse undergoes rotations in phase space. In general, its shape can be characterized in terms of the three *Twiss parameters*: α_i, β_i and γ_i, defined for each Cartesian coordinate i, and leading to the following relation, describing the shape of the phase space ellipse in the i, p_i space:

$$\gamma_i i^2 + 2\alpha_i i p_i + \beta_i p_i \; = \; \epsilon_i$$

Simple geometric considerations on the above equation show that the maximum position i for the ellipse is given by $\sqrt{\beta_i \epsilon_i}$. The value of β_i, which changes along the beam path, gives rise to the so-called *beta function*, which is used, together with the value of emittance, to provide the physical extension of the beam at any point along its path.
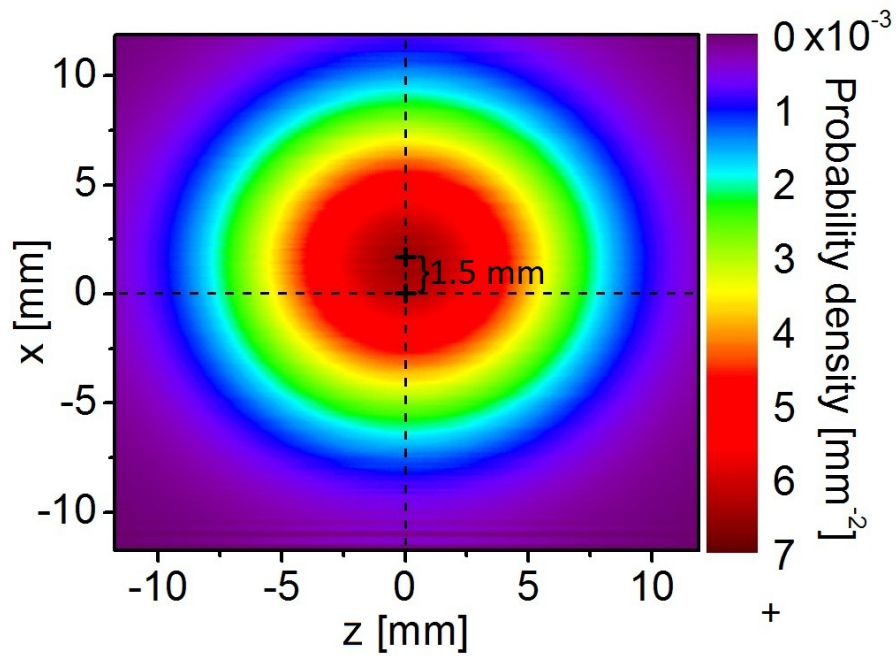
Figure 6.11: 2D plot of the simulated profile imaged on the detector by an ideally Gaussian projectile beam centered in x_0, y_0 with $\sigma = 5$ mm. $4 \cdot 10^{10}$ points used. Offset in the x direction of about 1.5 mm as expected (cf. Fig. 6.6).

they are shown in Fig. 6.6. However, the convolution of two Gaussians is still a Gaussian with a standard deviation given by the square root of the quadratic sum of the single standard deviations. In the case simulated, which in turn is a representation of the expected operating conditions, the standard deviation of the extended beam overshadows the standard deviation of the single particle profile, hence the imaged profile shows no evident distortion. Fig. 6.11 also shows the displacement of the beam image due to the gas jet velocity, resulting in the image being centered about 1.5 mm towards the positive x axis.

6.2 Mechanical design

A CAD illustration of the extraction system is shown in Fig. 1.5. From bottom to top, it is composed of 1 repeller plate, 9 bored electrodes (shown in green), 2 electrodes fitted with a clamping ring for installation of an optional mesh and finally the MCP detector assembly, which includes 2 MCP plates and a phosphor screen. Each electrode has a protruding lip with a clearance hole where the biasing wires can be connected through screws. The repeller plate is only a temporary solution, that will need to be replaced by a second set of electrodes when a second MCP detector will be available to implement a full ReMi.

The electrodes are supported on 4 metal rods which are insulated through ceramic hollow cylinders from the electrodes. The electrodes' position is maintained by a set of precision machined ceramic spacers, whose bore matches the outer diameter of the ceramic insulation tube. These are in turn shielded by a set of metal cylinders separated by 3 mm thick ceramic washers which sit in a groove housed within the shell of the larger metal shield. These metal shields are visible in Fig. 1.5 in turquoise, and are needed to prevent stray electrons hitting the ceramic and hence charge it, resulting in a long lasting field distortion. The metal shields at the $y = 0$ level have a threaded hole in them which allows securing the grounding wire to a screw. One of the 4 metal rods stops before reaching beam level, so that space can be cleared for the retractable phosphor screen to be inserted through port 13 (see section 4.1.3).

The whole assembly is fixed to the top flange, so that it can be easily removed in one piece, by 4 threaded supports, welded to the flange from the inside.

6.3 OPERA simulations

Simulations aimed at predicting a more realistic extraction field than the perfectly homogeneous one used in section 6.1, have been performed numerically making use of two commercially available codes: OPERA 13.0 and SIMION 8.0.

SIMION is an older, lighter program which provides reliable results for simplified geometries and axial symmetries in particular; OPERA instead is fully 3D, includes an optimized meshing algorithm which improves numerical precision for more complex geometries and also presents advanced post-processing capabilities.

A preliminary analysis making use of SIMION has been performed in the early phase of this work [80]. SIMION simulations prove useful to predict the inhomogeneities in the field due to the non negligible separation between electrodes, and in particular the first electrode and the repelling plate, which are separated by 74 mm.

However, SIMION provides only a limited 3D design flexibility, hence 2D analysis only has been carried out, thus restricting its use to the axissymmetric case. Therefore SIMION has not been used to include the field inhomogeneities due to the presence of the supporting rod, one of which is shorter, which adds to the field distortion. These limitations are overcome by the use of the OPERA software, which offers a much improved 3D developing and post-processing environment: for brevity only this more detailed analysis is reported in this work.

6.3.1 Field analysis

Voltage Fig. 6.12 shows a 3D representation of the extraction system including a 2D plot of the simulated voltage on the xy plane, in the x range -50 mm to + 50 mm. Considering that the largest bore in the electrodes has a diameter of 70 mm, the region of interest for ions tracking is only the internal 70 mm of the plane shown.

It is qualitatively visible from Fig. 6.12 that the potential lines are parallel, and no evident distortion is present. A more quantitative analysis is possible through Fig. 6.13, which includes 4 plots showing the potential difference between the on-axis value and 4 extreme values at 20 mm distance from the axis. The positions on the axis angled at 45° from the X and Z axis are chosen because this is the closest that a point at 20 mm distance from the axis can get to the the supporting rods, which constitute the main source of field distortion in the interaction region.
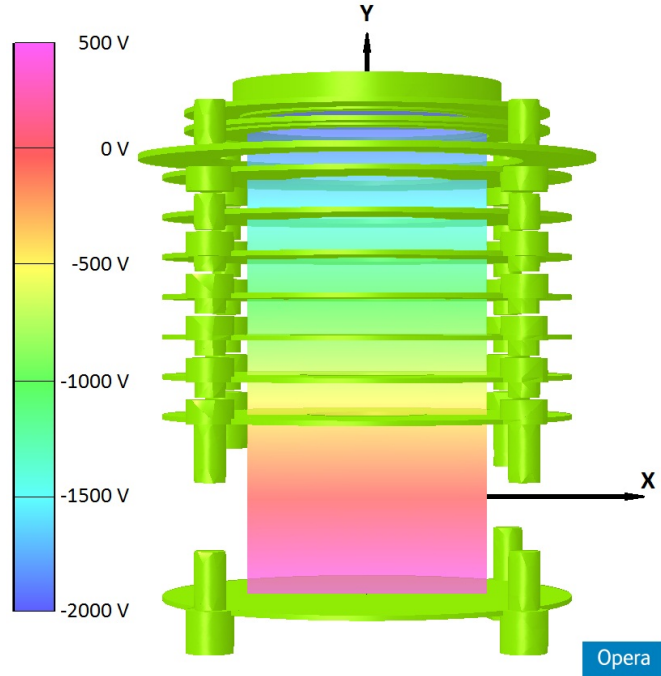
Figure 6.12: 3D representation of the extraction system, showing the voltage on the xy plane.
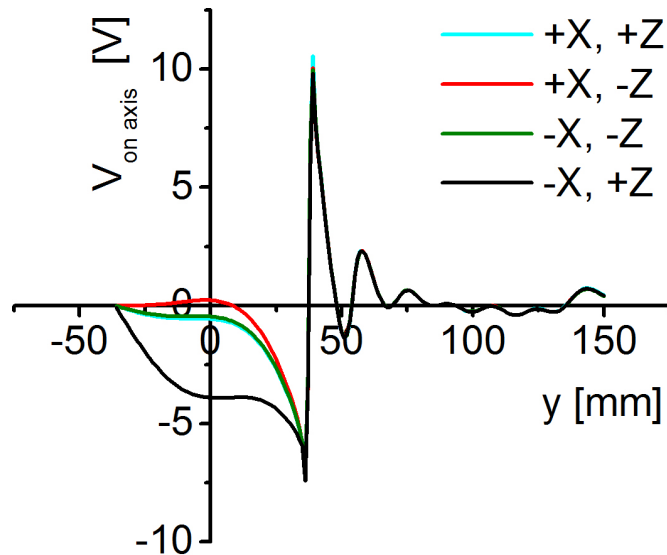
Figure 6.13: Plots of the difference between the potential along the y axis at the positions (± 14.1; y; ± 14.1), and the on axis value. The different data series correspond to 4 points along the xz axis bisector, each at a total distance from the y axis of 20 mm. The position (-14.1; y; +14.1) is closest to the missing supporting rod.

137

From Fig. 6.13 it is seen how the differences in potential even at the extremes of the extraction field domain are very small. Indeed, the voltage along the vertical line passing through (-14.1; 0; +14.1), i.e. closest to the missing supporting rod, is only smaller than the on axis voltage by 4 V. The discrepancy is larger when the first electrode is reached, and hence the field is disturbed by the proximity of the electrode inner bore. However, even in that case, the voltage difference is limited to less than 10 V, against a total voltage at the first electrode in excess of 460 V. The effects on the imaged beam profile due to this distortion in the ideal field is evaluated later in this section, together with the effects of all other non ideal field components, resulting in an overestimation of beam profile standard deviation of about 2%.

Longitudinal field component More insight in the operation of the extraction system can be gained by studying the electric field components. Fig. 6.14 shows a plot of the on axis longitudinal electric field component E_y.
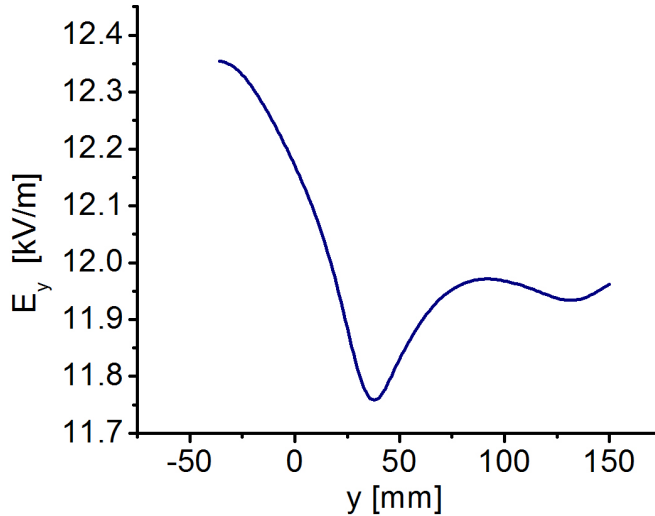
Figure 6.14: Longitudinal field component E_y plotted along the y axis. Deviations from the design value of 12 kV/m within 3%.

The largest deviation from the design value occurs in the region between the first electrode and the repeller plate, where the separation between neighboring electrodes is largest. However, even in the point of maximum deviation, occurring at the surface of the repeller plate, the electric field longitudinal component is within 3% from the design vaue of 12 kV/m.

Transverse field components   The transverse field components on axis are plotted along the y axis in Fig. 6.15.
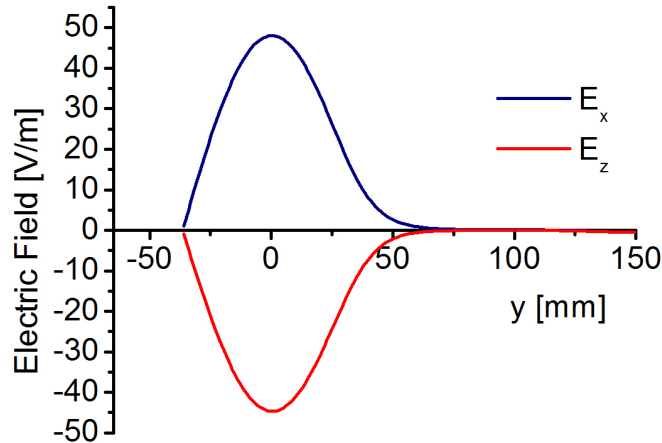
Figure 6.15: Transverse field components E_x and E_z, plotted along the y axis.

The largest deviation from the design value occurs at $y = 0$, in the middle of the central section, where the separation between neighboring electrodes is largest and the asymmetry effect of the missing fourth rod is most apparent. Both transverse profiles show the same behavior, and study of the sign of the deviations identifies the maximum deviation in the quadrant of the missing rod.

However, even at the point of largest deviation, the ratio between the longitudinal and transverse components stays less than $3 \cdot 10^{-3}$, corresponding to an angle formed by the force vector with the vertical of less than $0.2°$. This deviation from the design value results in a particle starting at rest in the origin arriving at destination on the detector being displaced less than 100 nm from the y axis, and is therefore totally obscured by the contribution to the drift due to initial velocity.

Comparison with ideal field   Using the OPERA simulated field, the calculations carried out in section 6.1 making use of constant and uniform acceleration a in eqn. (6.2) can be corrected with the acceleration which is experienced by the ions in the more complex field simulated by OPERA. The most influential effect proves to be the field distortion due to the missing supporting rod, which results in a pull of the ions in its direction. On top of this contribution, the ions also experience a kick as they pass

through the bores in the electrodes, contributing to the final spread attracting each passing ion away from the axis.

To summarize this results quantitatively, the plot in Fig. 6.16 shows the displacement from the expected arrival spot due solely to field distortion as a function of the initial position coordinates x and y.
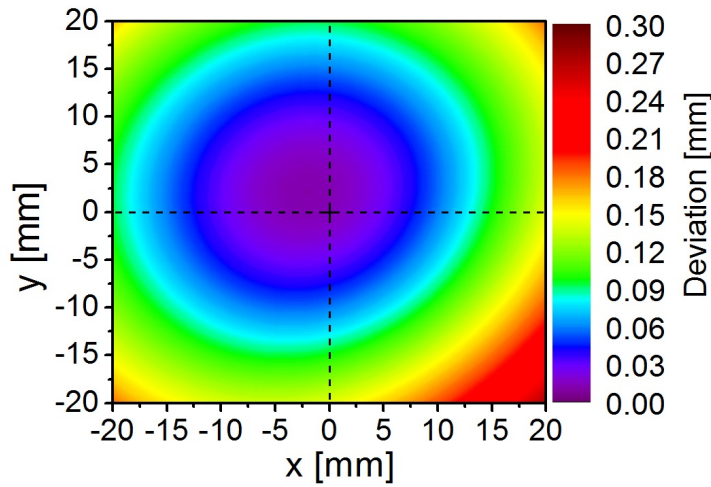
Figure 6.16: Displacement from the expected arrival spot due solely to non-ideal field distortion (i.e. no initial velocity), as a function of the initial position coordinates x and y.

It can be seen how the deviation pattern is not centered in the geometrical center of the extraction system, but rather the points closer to the negative x and positive y direction (i.e. the direction where the missing rod is located) feature larger deviations. Also, the deviation is larger as the points move away from the axis, due to the effect of the electrodes. Nevertheless, the deviations considered are smaller than 200 μm in most of the range of interest, down to less than 100 μm in the inner 2 x 2 cm, and therefore do not contribute significantly to the beam spread.

If the simulation leading to the plot in Fig. 6.11 is repeated taking into account the deviations due to the real field, the difference with the ideal image in plot 6.11 is smaller than 5% at any point. A complete simulation that takes into account also the deviation from ideal behaviour due to the curved trajectories of the electrons in the extraction field is reported in Fig. 6.18. Even taking into account electron trajectories as well, the difference with the ideal behaviour proves to be small ($< 5\%$).

6.3.2 Electron gun trajectories

The last point of interest that can be investigated using OPERA simulations is the trajectory of the probing electrons coming from the electron gun. Indeed the projectile beam will feel the action of the extraction field as well, resulting in an approximately parabolic trajectory in the interaction region. The actual trajectory will depend on the extraction field as well as on the energy and initial direction of the electrons, and has been computed with a custom written c++ tracking code which makes use of the OPERA simulated electric fields. The code computes the eqn. (6.2) at the starting point given by the user, and in 0.1 mm steps therefrom. The particle variables of motions are updated at each step and the time interval to be used calculated from the local value of electric field and particle initial velocity so that the distance traveled in the chosen time interval is 0.1 mm.

The code has been benchmarked against the OPERA native particle tracking code and yields equivalent results for all the fields tested, chosen amongst those treated in this work. Differently from the OPERA native particle tracking software, however, the custom written code allows systematic, automated investigation of several variables, and a more convenient post-processing tailored on the needs of this particular work.

Insofar as the design of the profile monitor test stand is concerned, the energy and initial velocity direction of the electron projectiles has to be chosen so that the maximum possible interaction area is covered by the projectile beam as this is scanned, and therefore the largest possible region of gas screen can be probed. The limit is posed by the need of avoiding the projectile beam hitting any of the electrodes, to prevent the secondaries which would otherwise be released from generating noise by causing spurious ionizations of the residual gas.

Fig. 6.17 shows the extraction system, the vertical component of the extraction field and, superimposed to it, a plot of several possible trajectories spanning the whole range of suitable initial directions for the maximum kinetic energy of the electron gun of 5 keV, corresponding to the minimum obtainable deflection and hence best interaction region coverage.

These settings are compatible with the imaging of a square gas screen tilted at 45° of side 50.5 mm, limited by the lower electron trajectories hitting the repeller plate beyond this range.
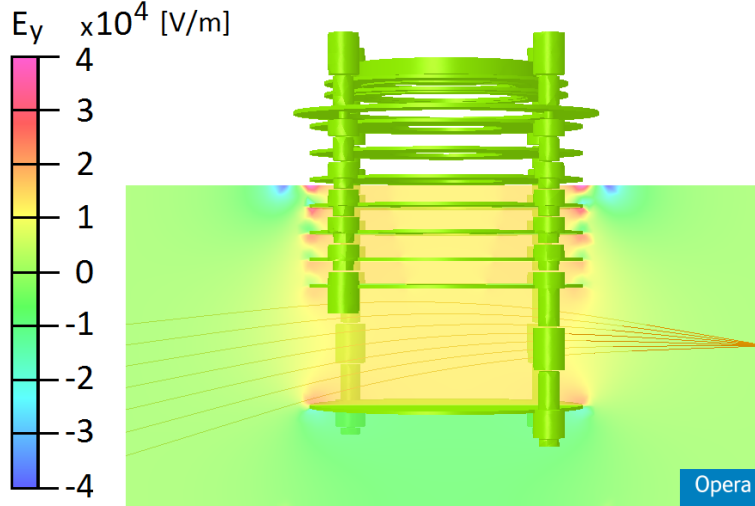
Figure 6.17: Different trajectories of 5 keV projectile electrons, differentiated by initial direction, in the 12kV/m simulated extraction field. The full range of initial directions which do not result in hits against the electrodes is shown. The field shown with the color map is the vertical component of the extraction field.

Effect on initial ion velocity It must be noted that, with reference to Fig. 6.17, the direction of the projectile velocity at the interaction points is not in general parallel to the horizontal, as it is implicitly assumed in the discussion of section 6.1.2. Instead, there is always a deviation which cannot be neglected. However, given the similarity between the distributions of the three initial velocity components (see section 6.1.2), the direction of scatter is almost random, hence all deviations from the horizontal of the impacting projectile occurring in the described setup as simulated with OPERA (see Fig. 6.17) result in negligible effect on the beam image created on the detector.

To prove this claim, the field data taken from the OPERA simulations is fed into the particle tracking code described above, so as to have a prediction of the image created by an ideal Gaussian projectile beam impinging on the gas screen which takes into account a more realistic impacting direction of the projectile, as well as the ions trajectory deviation due to field distortions. The results of this improved model are shown in Fig. 6.18, showing both the simulated imaged profile and the percent differences between the model taking into account projectile direction and field distortion and the simplest ballistic model presented in section 6.1.5. If only field distortion, but not projectile direction is taken into account, the plot on the right of Fig. 6.18 changes only very

slightly, and observed deviations in discrepancy are below 0.2%.
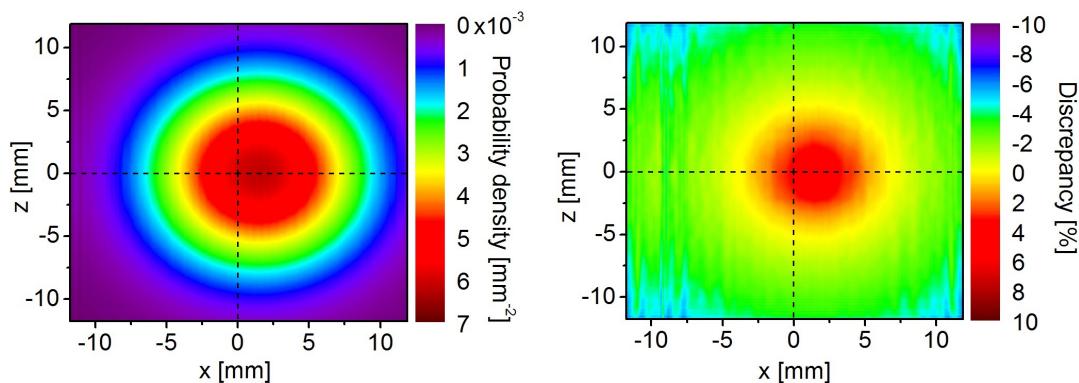
Figure 6.18: Simulation of the image created by an ideally Gaussian projectile beam impinging on the gas screen, and centered in x_0, y_0 and with $\sigma = 5$ mm, equivalent to the one reported in Fig. 6.11, but including field distortion as simulated by OPERA and realistic projectile trajectories (left). Percent differences between the plot of Fig. 6.11 and the plot on the left, showing the discrepancies between the two models (right).

With reference to Fig. 6.18, the net effect of the deviation due to real field calculations and electron trajectory is to move the ions away from the center of the extraction system, hence resulting in the profile in Fig. 6.18 being flatter and more spread out than the one in Fig. 6.11. This difference, however, only counts for less than $\pm 5\%$ at any point in the image, as shown on the right in Fig. 6.18.

A statement on the impact of these effects on the profile measurement can be obtained comparing the mean and standard deviations of both vertical and horizontal 1-dimensional profiles corresponding to the ideal and non ideal fields, i.e. Fig. 6.11 and 6.18. The measured beam profile standard deviation in the non ideal case proves to be 5.11 mm for the z profile and 5.12 mm for the x profile; larger than the true value of 5 by a factor of about 2%.

6.4 Technology

6.4.1 MCP detector

MCP detectors are an established technology in particle detection field, thus many comprehensive reviews exist on the topic [81–83].

The MCP detector is a specialized electron multiplier device, formed by a closely packed array of continuous channel multipliers cells. Each cell is a very small diameter hollow glass tube (10-50 μm diameter in most applications), that acts as an independent electron multiplier. The particle that enters the tube and does not fly straight along its axis will eventually impact on the tube walls, releasing a number of secondary electrons. These electrons will be in turn accelerated by the potential applied across the MCP, colliding with the walls and creating more secondary electrons in an avalanche process that constitutes the signal amplification. This process depends critically on the particles not flying along the axis of the tube without colliding the walls, consequently an important feature of the tube is its aspect ratio, i.e. the ratio of tube length over tube diameter: higher ratios provide larger amplification. Common aspect ratios vary from 20 to 60, resulting in a less than 1 mm thick detector, which is brittle, easily broken and thus hard to handle. Furthermore, the channels are usually tilted with respect to the vertical, to further prevent primaries flying through the holes. The avalanche time is typically of the order of few ns, whilst the spread in transit time is below 100 ps. Fig. 6.19 depicts the working principle of a single amplifier channel [81]: hundreds of thousands channels packed together make up a full MCP plate.
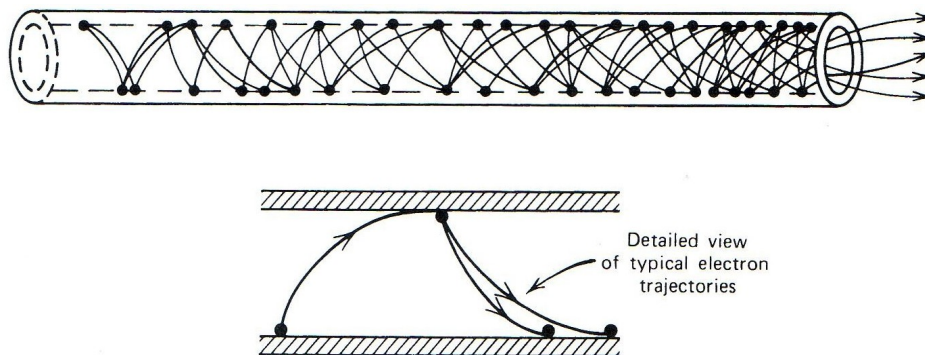
Figure 6.19: Operating principle of a single photomultiplier tube, showing the process of electron multiplication. Image taken from [81]. Clusters of many thousands such tubes allow to maintain the information on the impacting primaries position, constituting a MCP.

In order to increase the amplification of the detector, more plates can be stacked together, with their channels tilted in opposite directions, again to prevent particles flying along the holes axis. When two plates are so stacked, the configuration is said to be of *chevron* type.

It should be noted that when the MCP is used to amplify positive ions, as in the case of interest in this work, it is biased at lower potential than the region where the ions are created, so that the ions are accelerated towards it, but at higher potentials than the region that follows it (i.e. the phosphor screen), as the ions release electrons entering the MCP: it is these electrons that need to be collected, therefore the electric field needs to be directed away from the phosphor screen. Hence the voltage scheme displayed in Fig. 6.21.

The MCP used in this work features a chevron configuration with impedance matched plates: this allows a single voltage to be applied to bias the detector, as impedance matched plates guarantee the voltage to be evenly distributed between the two plates. The active area is circular in shape and its nominal diameter is 80 mm. The plates have a channel diameter of 10 μm, a pitch between channels of 12 μm, which sets the spatial resolution of the device, and a channel tilt of 8°. A total nominal maximum amplification in excess of 10^7 can be obtained, occurring at bias voltages larger than 1 kV per plate. The amplification of the device can be changed by $2 \div 4$ orders of magnitude by changing the voltage applied to the plates. An experiment of the light yield from the detector has been carried out to characterize the impact of bias voltage on the MCP plates, whose results are shown in Fig. 6.20.

The approximately straight line in the logarithmic plot shows an approximately exponential increase of MCP amplification with the bias voltage. The MCP can be biased also above the value of 2 kV, up to a value, quoted by the manufacturer of 2.4 kV, above which sparking is likely to occur and the MCP to be damaged. Bias voltage is usually kept as low as possible and risen with time to counterbalance the effects of MCP aging. Therefore, in this experiment, no bias above 2 kV was provided for preserving the detector: already up to 2 kV, however, the bias voltage allows a tailoring of the MCP gain by over 2 orders of magnitude. If the exponential trend continues up to 2.4 kV, amplification can be increased by another 2 orders of magnitude.

6.4.2 Voltage divider

In order to operate the detector and the extraction system in both the profile monitor and ReMi operation mode, the voltages shown in Fig. 6.21 need to be supplied to the different elements. Not being economical to use separate power supplies for each

145
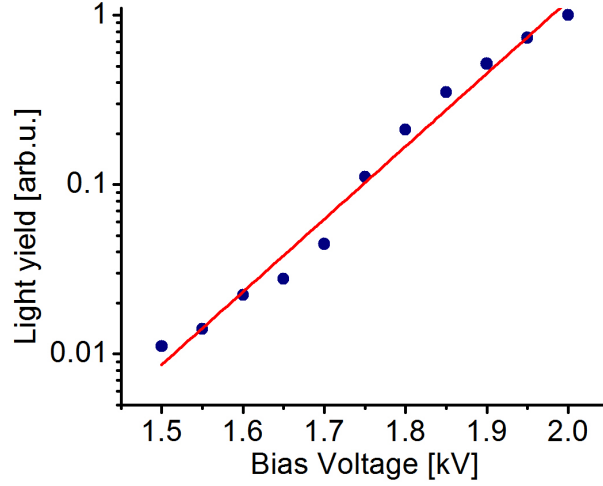
Figure 6.20: Measured amplification of the MCP in terms of the bias voltage applied. The light yield is measured by the gray scale of the image produced on the phosphor screen, and also depends on the residual gas pressure, electron beam current and phosphor screen amplification, hence only relative values carry physical meaning: therefore light yield is reported in arbitrary units normalized to the largest measured value.

different voltage, a voltage divider network has been designed and realized by the author to allow supplying different voltages from a single power supply channel.

The voltage divider network makes use of potentiometer for the fine adjustment needed to compensate resistor tolerances and has a total resistance of about 500 MΩ, compatible with μA currents and mW dissipated power.

Moreover, in order to allow switching between operation modes, a series of high voltage relays has been incorporated in the design. The use of high voltage relays instead of cheaper and easier to implement manual switches is made necessary by the high voltage nature of the application: relays provide a safe contactless environment for the operator, who only interacts with pushbuttons connected to a low voltage 5 V logic circuitry.

Fig. 6.22 shows a diagram of the voltage divider circuitry.

6.4.3   Phosphor screen

A phosphor screen can be categorized as a scintillation detector relying on the principle of luminescence. The theory of scintillators is well studied and can be found in several reviews, e.g. [81].
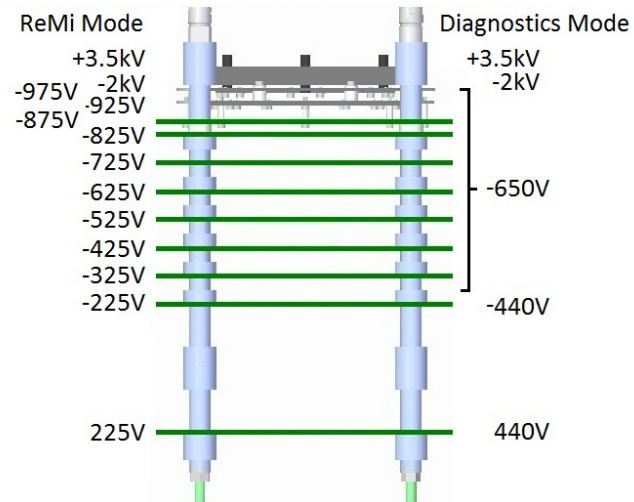
Figure 6.21: Extraction system, showing all electrodes and respective voltages for both the profile monitoring and ReMi operation mode.
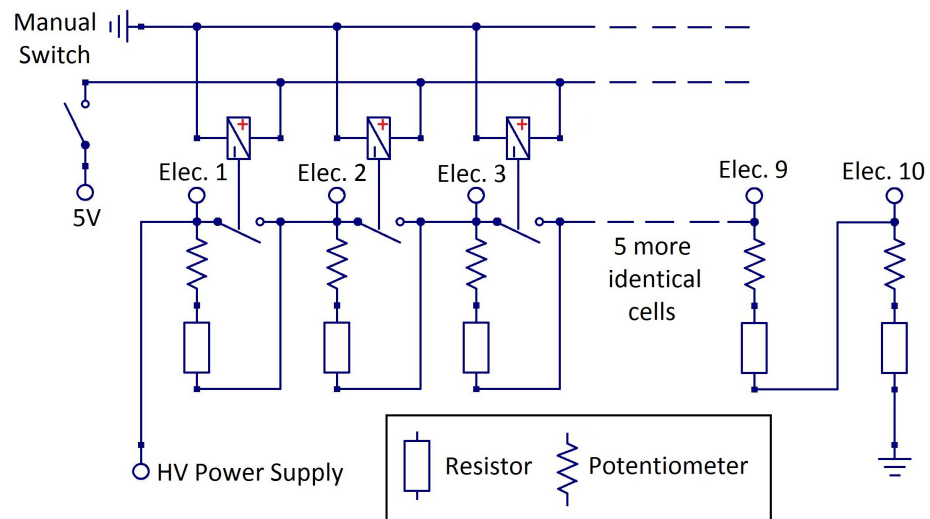
Figure 6.22: Schematics of the voltage divider circuit.

Luminescence results in a light yield from an excited sample which follows an exponential decay law. The phosphor used in this work is the common green glowing P22, an inorganic compound of zinc sulfide doped with copper and aluminium (ZnS:Cu,Al). It features a maximum emission wavelength of 535 nm and a decay time constant given by the manufacturer of 70 μs. Such decay time limits the acquisition rate of the detector for fast pulsed beams. However, the experiments carried out in this work always rely on a continuous beam of electrons, with the ability of pulsing the jet in the ms range, hence the decay time of the phosphor screen is never a limiting factor. Furthermore, the largest limit on the acquisition rate with the setup presented in this work comes from the refresh rate of the CCD camera, featuring 25 frames per second acquisition frequency.

Light yield calibration   Another feature of interest is the light yield of the phosphor screen. This is expected in literature to depend on the energy of the impacting electrons following a power law of the form [81]:

$$I_0 \propto E_{proj}^{\alpha} \tag{6.7}$$

with the exponent α depending on the particular phosphor species. A best fit of the calilbration data provided by the manufacturer is compatible with an exponent of 1.07 for the phosphor used in this work.

The impacting energy of the electrons can be easily tuned in the setup described by changing the bias of the phosphor screen with respect to the back of the MCP plate (held at ground potential), whilst the absolute value of the current hitting the screen can be tuned by either changing the residual gas pressure in the interaction chamber, so as to increase the number of primary ionizations, or by increasing the MCP bias, and hence amplification, until a high enough signal is obtained. Fig. 6.23 shows a plot of the light yield against the impacting energy of the secondary electrons.

The linearity of the plot in Fig. 6.23 is a good indication of the validity of eqn. (6.7). The exponent α can be obtained from the gradient of the double logarithmic plot, and is equal to 0.92. The lower value of α as compared to the value obtained by the manufacturer's data is due to aging. Therefore, whilst it is possible, from the manufacturer specifications, to bias the phosphor screen up to 6 kV, the increase in light yield is only approximately linear, and can only approximately double when moving
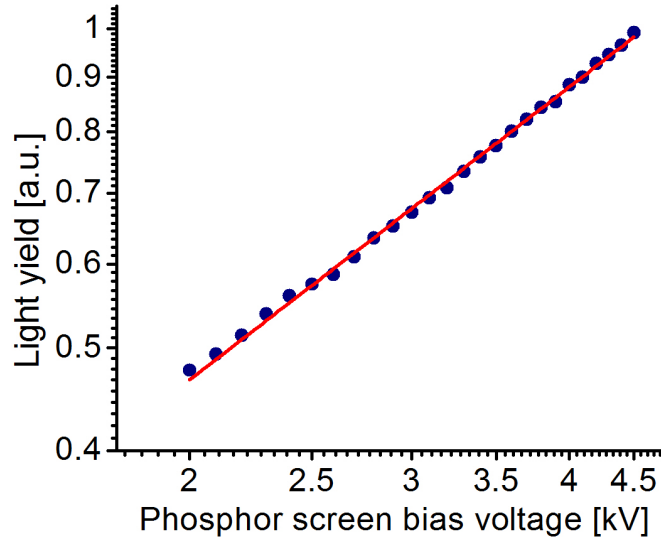
Figure 6.23: Measured light yield of the phosphor screen in terms of the impacting energy of the secondary electrons. The light yield is measured by the gray scale of the image produced, through the ImageJ software, and is reported in arbitrary units normalized to the largest measured value. The plot is in double logarithmic scale so that linearity indicates an exponential law as in eqn. (6.7)

from the manufacturer suggested operating bias of 3.5 kV to the rated maximum. The main gain of the system comes therefore instead from the MCP, which, as discussed in section 6.4.1, can be made to span up to 4 orders of magnitude in amplification by changing its bias voltage.

6.5 Conclusions

In this chapter, a description of the detector system used in the profile monitor is presented.

Section 6.1 is focused on the theoretical analysis of the detection system, presenting the considerations that have driven its design. In this section, the non-relativistic equations of motion under constant acceleration are used to estimate the ion trajectories from the gas screen, where they are ionized, to the MCP detector. The discussion shows the initial ion velocity to be the more influential parameter on the ion trajectories, and takes into account, as well as the thermal component of velocity, also the momentum transfer due to impact ionization, i.e. the recoil. Based on published results, the

recoil momentum is inferred to be the result of 3 Gaussian distributed components, and the parameters of the Gaussians are derived. The limits of an analytic approach are highlighted and a numerical approach described. The constraints on the design given by the application to the USR and by the limits of the test stand available are also discussed. Finally, the results of this analysis are presented and discussed: a shift of the profile centroid due to jet initial velocity of about 1.5 mm is expected; a drift region is added to the extraction field, past the point of $y_1 = 55$ mm; the value of 12 kV/m is set as the working value for the extraction field in the test stand setup, as improvements to both transverse profiles sharpness with higher fields is limited to a factor of $2 \div 2.5$ even for a 5-fold increase of electric field strength, coming at the cost of reduced area spanned by the electron beam. To conclude, the predicted profile from a Gaussian beam compatible with the expected beam from the USR is presented in Fig. 6.11.

In sections 6.2 and 6.4 the mechanical and technological elements of the extraction system are described, including an experimental calibration for the light yield obtained by both the MCP and the phosphor screen, and the description of the divider network designed for supplying the voltages needed by the extraction system.

Section 6.3 complements the analysis performed in section 6.1 by substituting the perfectly homogeneous fields assumed for that analysis with the fields simulated through finite elements methods by OPERA3D. This analysis shows that the discrepancy between the perfectly homogeneous field and the OPERA field model results in displacements in the arrival spot of about 50 μm in the central core of the extraction system, and up to 100 mum outside this. When this data is translated in the effect on the imaged profile, it is shown that an image broadening of about 2% of the real beam profile standard deviation of 5 mm is expected, setting the lower limit to the monitor space resolution. Moreover, simulations of the trajectories of the electron gun beam are performed, and show that with a 12 kV/m extraction field a square area of 50.5 mm side, coplanar with the gas screen, can be probed.

7

Residual gas operation mode

In this chapter, a set of measurements characterizing the residual gas operation mode is carried out, addressing the questions of monitor performance, such as sensitivity, resolution and dynamic range, as well as benchmarking the analysis carried out in Chp. 6. The beam is imaged by means of the three phosphor screens described in section 4.1.3: the detector phosphor screen, positioned downstream the detector and collecting the electrons created by the MCP; the direct hit phosphor screen, positioned in front of the electron gun and the retractable phosphor screen which can be positioned in the middle of the interaction chamber. The image is then acquired by an 8 bits CCD camera with a resolution of 1280 x 1024 pixels.

7.1 Methods and calibration

Residual pressure control   Throughout the experiments of this chapter, the residual gas pressure in the interaction chamber is controlled by use of a precision manual leak valve connected to a N_2 line. The pressure can be controlled within the range $5 \cdot 10^{-9}$ to $1 \cdot 10^{-6}$ mbar. Fig 7.1 shows a plot of the residual gas pressure in the experimental chamber in terms of the aperture of the leak valve, measured in notches on its knob, so as to give an idea of the resolution achievable. By fine tuning the knob against the reading of the pressure gauge it is possible to calibrate the pressure to better than 10% its value even around the 10^{-7} mbar area. Pressures from $5 \cdot 10^{-9}$ mbar to 10^{-6} mbar can be obtained when the leak valve is opened.
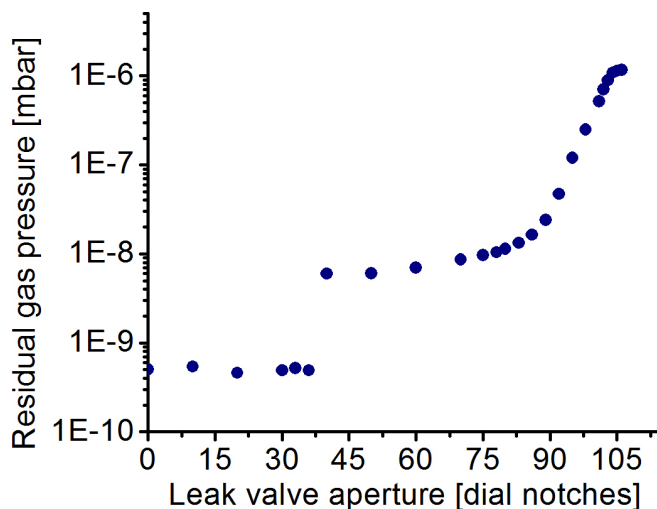
Figure 7.1: Residual gas pressure in the vacuum chamber in terms of the leak valve aperture, measured in notches in the valve's knob. Errors comparable with data points dimension.

Example measurement   The output of a profile measurement is an image captured by the CCD camera focused on the detector phosphor screen. A typical imaged beam profile is shown in Fig. 7.2. The profile is then analysed with the ImageJ software (see section 5.2).

The 1-dimensional profiles shown in Fig. 7.2 are obtained by averaging the CCD camera pixel gray scale value over all the pixel rows or column (depending on the profile axis), imaging the beam[1]. One profile shows the transverse dimension of the beam, and is therefore Gaussian in shape. The other is instead flat as expected, as there is no charge absorption or emission along the path of the beam and therefore the longitudinal profile is not expected to change[2].

---

[1]Averaging is preferred to summation in this work so that saturation effects and resolution limits are more readily apparent as the average has the same units of pixel gray scale of the measured observable. This choice only involves a linear transformation, and the two profiles (obtained by average or summation) hence retain the same shape

[2]Even in presence of a focusing effect, the longitudinal profile obtained would still be flat: indeed, provided the whole beam is included in it, and not only its central part, the profile is directly proportional to the charge in the beam, which is not changed by focusing or defocusing. By including only the central part of the beam in the profiling average, however, it is indeed possible to see focusing effects reflected in a higher luminosity in the central part of the beam.
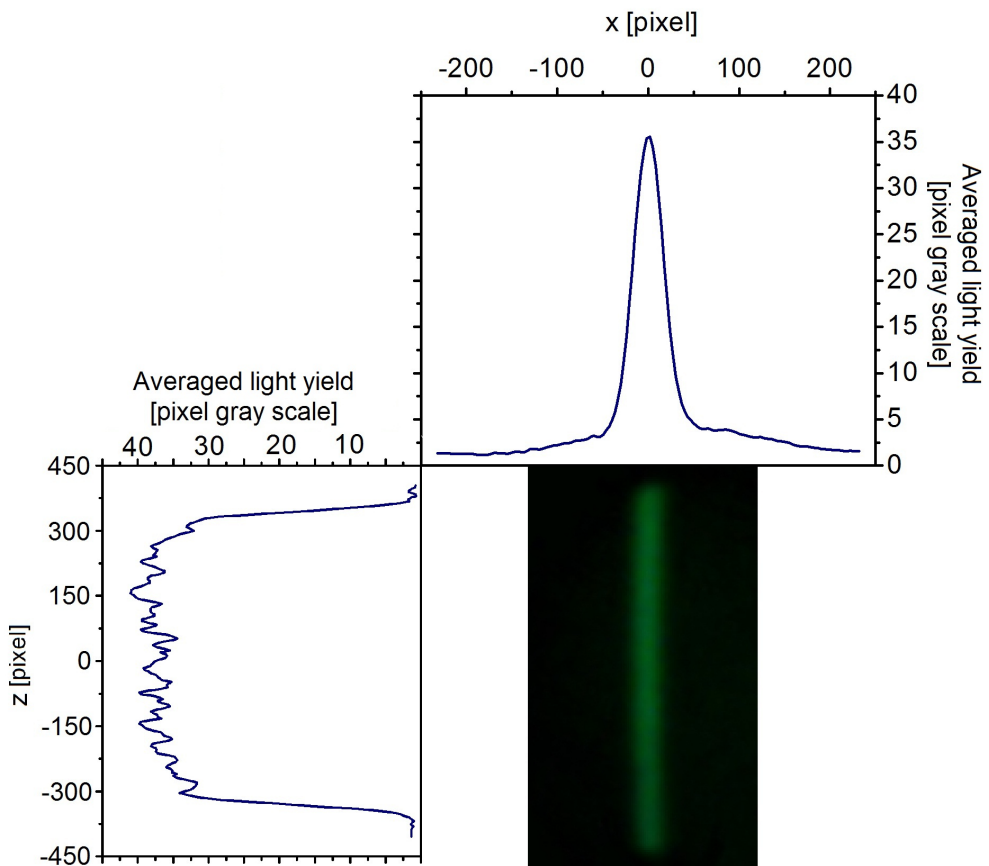
Figure 7.2: Example of a typical imaged profile of the electron gun beam. Two 1-dimensional integrated profiles of the imaged beam are also shown: profiles acquired through the ImageJ software reading the gray scale of the acquired image. The transverse profile follows a Gaussian curve, whilst the longitudinal one is flat, apart from noise. Noise is sensibly higher in the measurement of the longitudinal profile: a theory for noise, presented in section 7.4.2, accounts for this effect.

Pixel to mm conversion   In order to convert the length dimensions from number of pixels on the camera to millimeters, a preliminary measurement is needed. For the direct hit phosphor screen this is done by taking a picture of a measuring tape on top of the phosphor screen detector. For the two remaining screens, though, this is not convenient due to the effects of perspective. Therefore for the detector phosphor screen the known diameter of the phosphor screen itself is measured in pixel, and for the retractable phosphor screen a known displacement is given through the manipulator and measured on the camera. The pixel to mm conversion factors yielded by these experiments are reported in table 7.1. The plots following in this chapter will make use of the conversion factors reported in table 7.1 to express the axis in units of millimeters rather than in pixels.

This conversion factor is not linked to the physical dimension of the pixels on the CCD sensor, due to effect of the objective lens. Rather, the field of view of the camera is first chosen as needed, and then coarsely adjusted using the zoom on the objective lens and the camera position, controlled through a mechanical mounting. The conversion factor from pixels to mm can hence be obtained by dividing the number of pixels in each row or column of the CCD sensor by the dimension of the field of view. The fields of view of all 3 cameras are also shown in table 7.1. The considerably larger field of view of the camera associated with the retractable phosphor screen is due to the distance between the camera and the screen, which is only visible through a viewport and a mirror, 40 cm away from the camera (see section 4.1.4), and the lack of a telescopic objective. The small difference between the other two phosphor screens is instead due to the tolerance of the mechanical mounting, which does not allow fine positioning.

Phosphor screen	Pix/mm factor	CCD field of vision
Detector	16.1	79.5 x 63.6 mm
Direct hit	15.6	82.1 x 65.6 mm
Retractable	4.2	305 x 244 mm

Table 7.1: Pixel to mm conversion factors and CCD camera fields of vision for all three phosphor screens.

7.2 Field of vision

The detector field of vision is defined as the volume where occurring ionizations can be detected. This is limited in principle by the geometrical dimensions of the extraction system and the MCP. In particular, the y dimension of the field of vision is only limited by the first electrode and the repeller plate, and thus measures 75 mm. The x and z dimensions are also limited by the extraction system, rather than by the MCP detector. Indeed, the bore in the first electrode through which the ions must pass has a diameter of 50 mm, smaller than the 80 mm of the MCP nominal active area diameter.

In order to test these predictions, and hence exclude possible field of vision distortions caused by lensing effect associated to field inhomogeneities in the extraction system, a measurement has been carried out. In this measurement, a large downward elevation angle for a 5 keV electron beam has been used, so that the beam hits the rim of the metal flange instead of the direct hit phosphor screen. This causes a shower of electrons to be emitted back in the chamber in a quasi-homogeneous pattern, ionizing residual gas everywhere in the area of extraction. By placing the camera further back from the detector phosphor screen its field of view was increased to include the whole rim of the phosphor screen and of the DN100 viewport. The recorded image is showed in Fig. 7.3.

An estimation of the detector field of vision can be obtained by comparing the diameter of the circle showing a light signal to the known diameter of the phosphor screen. This measurement was repeated for 20 different settings of extraction field strength and MCP amplification, and the results averaged together to yield the estimation of 49.3 ± 0.8 mm, compatible with the prediction of 50 mm mentioned above. It is concluded that it is indeed the bore of the first electrode that acts as a limiting factor for the field of vision.

7.3 Performance characterization

The characterization of the device performance in its operation as a transverse profile monitor can be done in terms of its sensitivity, resolution and noise defined as follows:

- **Sensitivity:** change in readout per unit change of the input signal. In particular, the input signal is the transverse dimension of the beam (measured by the beam
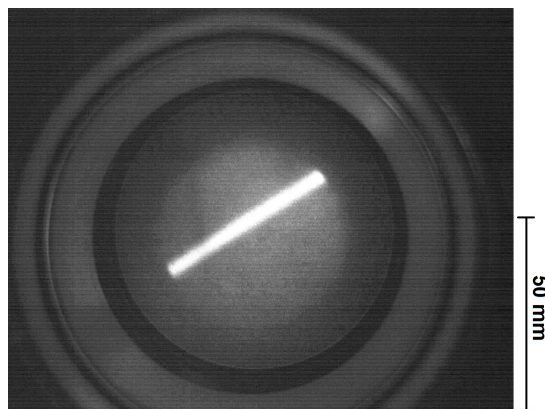
Figure 7.3: The diameter of the field of vision in the xz plane is measured to be equal to 49.3 mm. The image has been adjusted by increasing its luminosity for better visualization in printing, thus relative brightness values do not correspond to reality.

standard deviation σ_{beam}), and the output the standard deviation of the observed beam profile on the detector screen $\sigma_{detector}$, measured in pixels. Therefore, the sensitivity can be defined as the gradient of the curve of $\sigma_{detector}$ in terms of σ_{beam}, which is assumed to be equal to the measured σ_{ret}, i.e. the standard deviation of the profile imaged on the retractable phosphor screen (in mm). The sensitivity has therefore the units of pixel/mm[1].

- **Resolution:** smallest detectable variation in input signal. This translates into the equivalent dimension of 1 pixel in mm, i.e. the numerical inverse of sensitivity, with units of mm.

- **Noise:** the error associated with the measurement. Dominated in this case by the ion drift in the extraction system (see Chp. 6).

---

[1]Although they share the same units, the pixel to mm conversion factor shown in table 7.1 and the sensitivity are two distinct quantities. The pixel to mm conversion factor expresses a relation between the real size of the image appearing on the phosphor screen (in mm) and the pixels of the camera that record it: it does not carry any information on how the image formed on the phosphor screen relates to the actual physical size of the beam, i.e. on the distortion effects due to ion drift treated in section 7.3.2.

7.3.1 Sensitivity and resolution

To obtain the sensitivity of the transverse profile monitor, a measurement of $\sigma_{detector}$ in terms of σ_{ret} was performed. A theoretical model for $\sigma_{detector}$ can be written as :

$$\sigma_{detector} \; = \; S\sqrt{\sigma_{beam}^2 + \sigma_{drift}^2 + \sigma_{MCP}^2} \tag{7.1}$$

where S is the sensitivity and σ_{drift} and σ_{MCP} represent instead the contribution to beam spreading given by the ion drift and MCP spatial resolution.

Eqn. (7.1) can be rearranged to yield a linear relation with S^2 as its gradient and $\sigma_{error}^2 \; = \; \sigma_{drift}^2 + \sigma_{MCP}^2$ being proportional to its intercept:

$$\sigma_{detector}^2 \; = \; S^2 \cdot \sigma_{beam}^2 + S^2 \cdot (\sigma_{drift}^2 + \sigma_{MCP}^2) \tag{7.2}$$

Therefore, the results of the measurements are shown in Fig. 7.4 so that the $\sigma_{detector}^2$ is plotted versus $\sigma_{ret}^2 \equiv \sigma_{beam}^2$. Three different data series have been taken, corresponding to three different extraction field values. To perform this measurement, the spot size was varied by using the focus of the electron gun in the range $\sigma_{beam} \; = \; 0.5 \div 3.5$ mm, and the residual gas pressure kept at $3 \cdot 10^{-7}$ mbar to provide good signal visibility.

The results of the best fit regression carried out on the plots of Fig. 7.4 are reported in table 7.2. The sensitivity of the detector is computed through the gradients of the

Extr. Field [kV/m]	Sensitivity [pix/mm]	$\sqrt{\sigma_{drift}^2 + \sigma_{MCP}^2}$ [mm]
12	15.5 ± 0.24	0.99 ± 0.08
20	15.7 ± 0.25	0.71 ± 0.12
30	16.1 ± 0.30	0.48 ± 0.19

Table 7.2: Detector sensitivity and image spread due to ion drift and MCP as obtained by analysis of the plots in Fig. 7.4. Confidence intervals calculated by standard errors on the linear regression coefficients are also shown.

three plots in Fig. 7.4. Whilst the difference between the three gradients is within 5%, the standard errors associated to the linear regression shown in the table are such that the measurements are incompatible with a single value: thus, the data shows that the sensitivity increases with increasing extraction voltage, increasing by about 4%
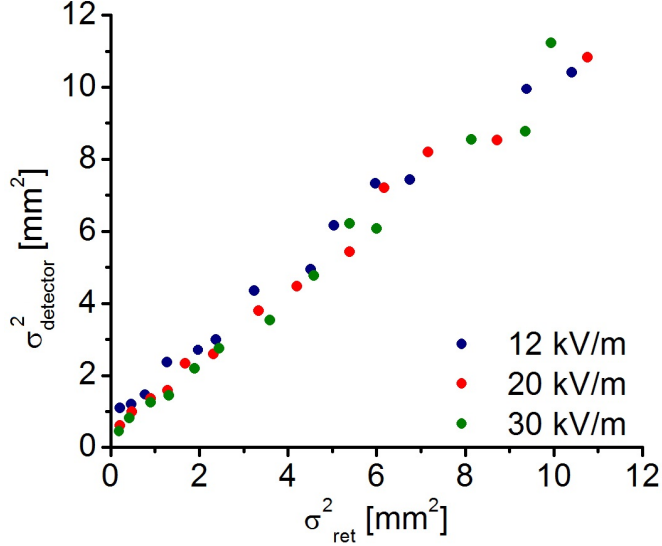
Figure 7.4: σ^2 of the beam transverse profile as seen on the detector phosphor screen in terms of the same quantity observed on the retractable phosphor screen. Three different measurements are shown, corresponding to different extraction voltages: lower extraction voltages correspond to larger ion drifts.

when moving from 12 to 30 kV/m. In particular, when this sensitivity is compared with the pixel to mm factor measured in table 7.1, it can be seen that the sensitivity approaches the pixel to mm factor for stronger extraction fields. The lower value for lower fields implies that the image of the beam undergoes a magnification for low fields. The magnification is relatively small ($<4\%$), and its dependence on the extraction field suggests that it is due to lensing effects in the electrodes system. These effects do not appear in the OPERA simulation (see section 6.3), and must hence be due to the electrodes voltages differing from the bias given by the power supply. An explanation for this effect can be given by considering that, although the electrodes are made of stainless steel, the surface polish specifications at the manufacturing stage were only given to *medium turned polish*, corresponding to about 15 μm roughness, which is compatible with the electrodes retaining machining residues which can be oxidized, lose electrical conductivity and hence trap charge, leading to field distortion, which is more influent at low extraction field voltages, explaining the results of table 7.2.

The intercepts of the plots in Fig. 7.4 are instead linked to the measurement error, as per eqn. (7.2), and are discussed in section 7.3.2.

The resolution of the monitor can be evaluated from the inverse of the sensitivity, resulting in $62 \div 65$ μm, depending on the extraction field used. This value should be compared with the expected beam spot size for the USR, calculated to be 3 cm in diameter at $\pm$ 3σ. The resolution quoted for the monitor in the residual gas operation mode allows thus to obtain more than 450 bins for each profile.

7.3.2 Noise

The noise associated with the spatial mapping of the beam can be traced back to 5 main contributions:

- **Ion drift:** systematic contribution coming from the drift of the created ions in the extraction field. Simulations performed on the model introduced in section 6.1.5, presented later in this section, predict this contribution to smear each point in the image according to a Gaussian distribution with standard deviation of 0.93 mm in any direction.

- **MCP spatial resolution:** introduces a smear of each point whose size is given by the pitch between different channels (12 μm), plus the spread affecting the electrons from each separate channel as they travel between the two MCPs forming the chevron configuration and towards the phosphor screen. The manufacturer quotes a spatial resolution of 80 μm for the particular detector used in this work. This contribution needs to be added in a quadratic sum to the smear due to ion drift, and can be therefore considered negligible.

- **Residual gas pressure fluctuations:** instabilities or inhomogeneities in the residual gas pressure leads to distortion or oscillation of the imaged profile. The effects of this contribution have been tested (see later in this section), but prove negligible when compared to the ion drift contribution.

- **Electric field stability:** the stability of the electric field affects both the electron beam and the extracted ions, and also includes the contribution of the stability of the electron gun power supply, controlling the electron beam energy and intensity. The effects of this contribution have been tested (see later in this section), and can be important when occasional strong spikes occur and the extraction field voltage changes abruptly in intensity. However these are isolated events occurring with

a frequency of few events per hour and lasting about 100-500 ms, and are not detectable during normal operation of the monitor. The most likely cause of these events has been identified in a fault of the communication protocol of the power supply to the computer. Indeed, direct connection with the computer, rather than through the use of a hub, reduces the frequency to about 1 event per hour.

- **Spontaneous residual gas ionizations:** it is in principle possible for the residual gas to self ionize, e.g. following a collision with other residual gas molecules, and hence produce a signal on the detector. To isolate this effect measurement were taken with the electron gun switched off. However, no detectable signal was visible in the pressure range of $5 \cdot 10^{-9} \div 10^{-6}$ mbar: it is concluded that spontaneous residual gas ionizations have a negligible impact on the measurement.

Ion drift and MCP spatial resolution The contributions of ion drift and MCP spatial resolution are intermingled in the measurements, as they have similar effects; however they behave differently with respect to the extraction voltage: increasing the extraction voltage decreases the spread due to ion drift but does not affect the MCP contribution.

With reference to eqn. (7.2), the combined contribution of the two effects can be evaluated from Fig. 7.4, by considering the intercepts of the three curves. The theory presented in section 6.1.5, modeling the extraction with a homogeneous field and the initial velocity distributions with components coming from recoil and thermal motion, can be used to provide a theoretical prediction for the quantities given in table 7.2. The same simulation leading to Fig. 6.6 is run for a 12 kV/m extraction field, assuming gas at room temperature and collectively at rest (as opposed to the jet which has a collective velocity in the x direction); and all ionizations to come from a single point in space (hence omitting the effect of finite gas screen width). For an extraction field of 12 kV/m, the simulation yields the plot shown in Fig. 7.5: the probability distribution for the location of the imaged point resulting from an ionization in the extraction field center.

As compared to Fig. 6.6, Fig. 7.5 shows a more symmetric shape, explained by the absence of the spread due to the gas screen width. The standard deviations of both profiles is equal since strongly dominated by the initial velocity component due to gas temperature, which is isotropic. In particular, σ_{resgas} proves to be almost 6 times larger
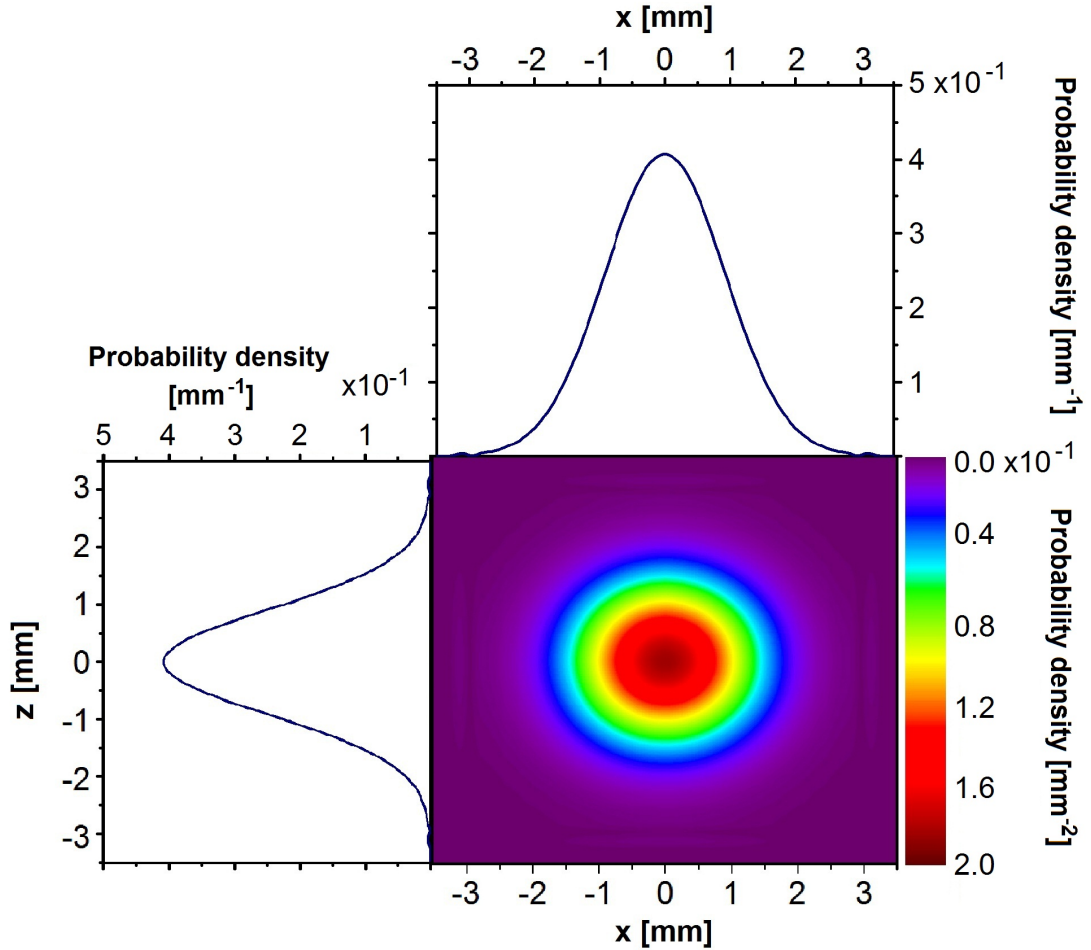
Figure 7.5: Probability distribution function of a particle from the residual gas ionized in $x = y = 0$ to be imaged in the point $x\ z$; equivalent to the 2-dimensional spot resulting from ionizations in $x = y = 0$. 1-dimensional profiles also shown. This image is the residual gas equivalent of Fig. 6.6, which is instead calculated with the parameters of a gas-jet target. The much increased spot size is due to the much higher temperature of the residual gas as compared to the gas jet. This simulation uses the approximation of ideal field and projectile trajectories. Statistical ripple due to low number of counts is observed at the tail of the distributions, in particular along the y axis. The parameters used are a homogeneous electric field of 12 kV/m and a temperature of 300 K. For both 1-dimensional profiles $\sigma = 0.93$ mm.

than σ_z of the jet, and more than an order of magnitude larger than σ_x of the jet as presented in table 6.1. This is due to the low temperatures achieved during the gas jet expansion, and illustrates another advantage of supersonic gas jet profile monitoring over residual gas profile monitoring.

The same simulation leading to Fig. 7.5 is repeated for 20 and 30 kV/m extraction fields, yielding standard deviations for the 1-dimensional density distributions of 0.67 and 0.55 mm respectively, in agreement with the experimental results (c.f. table 7.2). These values of standard deviation confirm the contribution due to MCP channels pitch to be negligible compared to the ion drift due to thermal velocity in a room temperature residual gas.

Another feature of interest in assessing the errors affecting the measurement of the beam profile is the homogeneity of the error due to ion drift contribution across the observation region. Indeed, any inhomogeneity would cause the image being spread more in some places than in others, resulting in profile distortion. To assess this effect the electron beam was scanned across the observation region, and transverse beam profiles traced for several points at different x coordinates. For these measurements, the electron beam was focused at the size of 2 mm FWHM, measured at the center of the observation region on the retractable phosphor screen, so as to make the effect of variation in σ_{drift} most apparent. The results of the experiment are shown in Fig. 7.6.

The points in Fig. 7.6 show a relatively large spread of about 10%. However, translated in pixels, the spread goes from 30 to 33 pixels, and is hence comparable with the resolution error of the monitor of ± 1 pixel. It is concluded that no significant variation in beam size is observed across the monitor field of view.

Medium term stability test A test of the medium term stability of the measurement, intended to evaluate the residual gas pressure and electric field stability, has been performed by recording a video file from the CCD camera and analyzing the image over an observation time of 10 minutes. The same test was repeated 20 times in different days, and the results added together for a total of 200 minutes observation time. During the observation time the monitoring parameters of bias voltages was kept constant and residual gas pressure and focus of the electron gun, coarsely fixed by the position of the control knobs were finely adjusted at each new measurement to match the observation
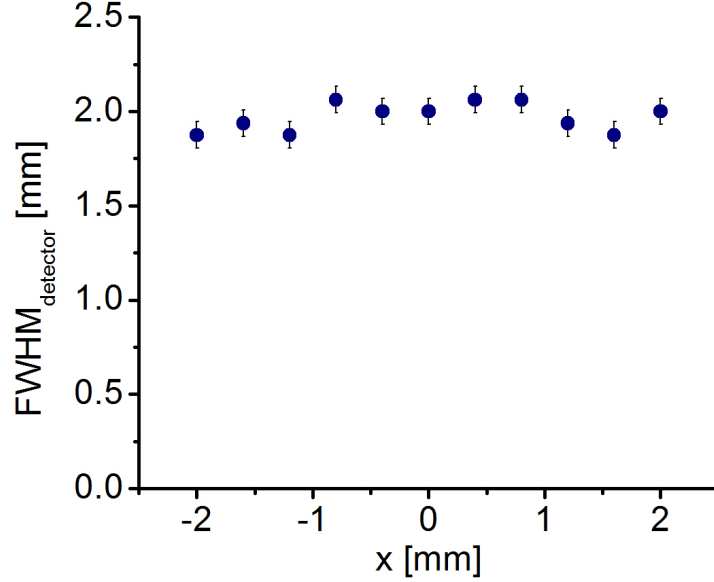
Figure 7.6: FWHM of the beam measured in different points across the observation region.

of the first day. This was made necessary due to an insufficient accuracy of the electron gun focus control and the hot cathode pressure gauge.

An indication that this procedure was needed was given by the fact that in a first set of measurements, in which this calibration was not done, the measured stability on the 10 minutes observation time, in each time window, was consistently better than the stability of the sum of all windows. Also, the percentage oscillation in each 10 minutes window was comparable ($3 \div 4\%$), and better than the overall stability, which was measured up to 19%. Therefore it is concluded that the discrepancy between different observation windows comes from wrong initial setting, given by inaccurate control of the electron gun focus and pressure gauge.

The signal profile was sampled every 10 seconds. The standard deviation of the distribution of oscillation amplitudes between corresponding points was measured to be 4.1% in the tail regions, where the signal is weaker, due to the higher impact of the noise. In the central region, where the signal is larger than half its maximum value, the oscillation amplitude is reduced to 1.6%.

7.4 Current monitoring

The detector also acts as a current monitor, as the light yield is proportional to the beam current. However, for this operation mode, the definitions of sensitivity, resolution and noise lead to different quantities:

- **Sensitivity:** the input is in this case defined as the current, rather than the beam FWHM, and the light yield as the output, rather than the observed FWHM. Therefore the sensitivity is the gradient of the curve of light yield vs beam current. The light yield is expressed in arbitrary units, proportional to the value of the CCD pixel gray scale (from 0 to 255 on the 8 bits digital camera used). However, residual gas pressure also affects linearly the sensitivity: a definition which takes this into account is presented in section 7.4.1.

- **Resolution:** the resolution is given numerically by the inverse of the sensitivity, in units of mA.

- **Noise:** the noise on the light collection comes from two main sources: background light and shot noise, linked to the discretization of the CCD camera pixels, which will be analyzed later in this section.

7.4.1 Sensitivity and resolution

To define the sensitivity of the monitor in its current monitoring operation mode an equation for the light yield L_{yield} in terms of the setup parameters is needed:

$$L_{yield} = R \cdot A_{detector} \cdot \Delta t \qquad (7.3)$$

where R is the reaction rate, in units s^{-1}; $A_{detector}$ is the amplification due to the detector, in units of pixel gray scale levels and Δt is the acquisition time, given by the integration time of the CCD camera: 40 ms from the data sheet. $A_{detector}$ includes the contribution of the MCP and the phosphor screen, which can be controlled through the respective bias voltages, but also the light collection efficiency of the camera, given by the combined contributions of CCD sensor sensitivity, camera position, objective lens transparency.

Eqn. (7.3) can be further expanded by expressing R in terms of its components, as was done in eqn. (1.8), yielding:

$$L_{yield} \; = \; \sigma(E_{proj})\frac{A_v P_{res.gas}}{RT}d_{obs}\frac{I_{beam}}{q_{projectile}}A_{detector}\Delta t \tag{7.4}$$

where d_{obs} corresponds to d_{gas} in eqn. (1.8) and represents the length of the observation region over which ionizations products can be collected on the detector and thus contribute to the signal, hence 50 mm (see section 7.2).

Most of the factors in eqn. (7.4) are fixed by design and cannot be changed during operation; these can be grouped in a single constant k_{design}:

$$k_{design} \; = \; \sigma(E_{proj})\frac{A_v d_{obs}}{RT q_{projectile}}\Delta t \tag{7.5}$$

This definition of k_{design} allows to rewrite eqn. (7.4) in a form best suited for calculating the monitor sensitivity:

$$L_{yield} \; = \; P_{res.gas} \cdot I_{beam} \cdot A_{detector} \cdot k_{design} \tag{7.6}$$

using the same values introduced in Chp. 1 for the reaction rate calculation, eqn. 1.8, the constant k_{design} can be calculated to be equal to $3.0 \cdot 10^{15} \; [mbar^{-1} mA^{-1}]$.

Therefore, the sensitivity $S_{current}$ of the device in the current monitoring mode can be defined as the second derivative of the light output with respect to beam current and residual gas pressure, yielding:

$$S_{current} \; = \; \frac{dL_{yield}}{dP_{res.gas}dI_{beam}} \; = \; A_{detector}k_{design} \tag{7.7}$$

To experimentally determine the factor $A_{detector}$ a measurement of the total light output, integrated over the whole beam profile, was carried out for different values of beam current and residual gas pressure. The beam current was obtained by the electron gun calibration, reported in Fig. 5.4; the residual gas pressure was instead measured by the hot cathode pressure gauge. The acquired data set is illustrated in Fig. 7.7.

If the gradients of the $L_{yield} = f(I_{beam})$ curves are plotted against the corresponding $P_{res.gas}$ values, and the gradient of the obtained curve computed, after dividing for the value of k_{design}, the factor $A_{detector}$ is computed to be equal to $2.88 \cdot 10^{-6}$ pixel gray scale value amplification.

This value of $A_{detector}$ scales with the bias voltages applied to MCP and phosphor screen. Therefore a maximum value of amplification corresponding to the maximum
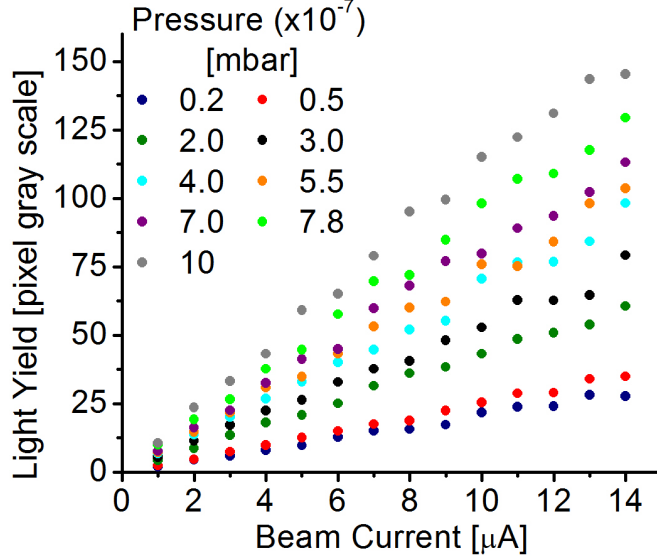
Figure 7.7: Measurement of integrated light output (in CCD pixel gray scale value) in terms of beam current (x axis) and residual gas pressure (curve parameter), taken for 2 kV MCP and 3kV phosphor screen bias voltages.

bias voltage which the detector can support, given by the manufacturer, of 2.4 kV for the MCP and 6 kV for the phosphor screen can be defined as: $A_{det.max} = 5.76 \cdot 10^{-4}$ pixel gray scale value amplification. Finally, the maximum sensitivity of the detector can therefore be computed to be:

$$S_{current} = k_{design} \cdot A_{det.max} = 1.73 \cdot 10^{12} \tag{7.8}$$

and is measured in pixel gray scale value per mbar of residual gas pressure and mA of beam current.

The resolution is given by the inverse of the sensitivity, therefore: $R_{current} = 5.78 \cdot 10^{-13}$ mbar·mA.

7.4.2 Noise

Background noise can be assessed by a measurement with no electron beam on. This is the same measurement carried out to prove that no self-ionization occurs (see section 7.3.2), and shows that no appreciable background light is observed. Therefore background noise can be neglected in the analysis of the device in current monitor operation mode.

A second source of noise is the shot noise, linked to the discretization of charge accumulated in a CCD pixel: when the light level is small, statistical fluctuation have a significant effect on the gray scale value recorded by the pixel. Being a phenomenon linked to discrete statistics, shot noise is a Poisson process, and hence the probability P_n of n events being recorded in the CCD pixel if the expected number of events is λ, is given by a Poisson distribution:

$$P_n = \frac{\lambda^n e^{-\lambda}}{n!} \qquad (7.9)$$

which has standard deviation $\sqrt{\lambda}$. Thus a measure of the relative error Err_{rel} on the measurement is given by the standard deviation of the distribution divided by its expected value:

$$Err_{rel} = \frac{\sqrt{\lambda}}{\lambda} = \frac{1}{\sqrt{\lambda}} \qquad (7.10)$$

The dynamic range of the CCD camera is limited by its 8 bits logic, equivalent to 256 levels of gray scale; thus the relative error is given by (7.10) in the range $Err_{rel} \approx 100\% \div 6\%$, being 22% for $\lambda = 20$.

However, this is only true if a single line, 1 pixel wide, is acquired on the profile. In fact, an advantage of the residual gas monitor analysis is that the transverse profiles of the beam acquired in the observation window can all be summed together, since they are samples of the same traveling beam. The summation process is mathematically equivalent to taking the average of a series of Poisson samples, and reduces the error by a factor of $\sqrt{N}$, with N being the number of samples, i.e. pixel lines averaged together. The number of pixel lines that can be used for beam profile averaging is limited by the camera resolution and the MCP amplification homogeneity. In the system presented in this work it is always possible to take the average on at least 500 pixels on the transverse profile, resulting in an error improvement by a factor of approximately 22. This factor needs to be applied to the calculated value of Err_{rel}, resulting in the shot noise accounting for less than 1% the recorded value for any gray scale value ≥ 20. An indication of the number of samples needed to reduce the shot noise to the point of being negligible can be obtained by considering the standard deviation of the Poisson distribution corrected for averaging over N samples σ_N, rather than Err_{rel}. The condition to be imposed is for $2\sigma_N < 1$, so that with 95% probability

the shot noise will not result in more than 1 gray scale level displacement from the real value:

$$\sigma_N = 2\frac{\sqrt{\sigma}}{\sqrt{N}} < 1 \implies N > 4\sigma \tag{7.11}$$

Thus, the number of samples should be 4 times as large as the signal level.

For the longitudinal profile, instead, averaging is not possible if not over few points along the center of the beam, where the signal is highest, hence resulting in larger Poisson noise. Fig. 7.2 shows an example of such behavior that can be used to test the analysis presented in this section. With reference to eqn. (7.10), the transverse profile is averaged across about 600 points, and hence the condition in eqn. (7.11) is easily satisfied and σ_N is below 1 level of the gray scale. The longitudinal profile is instead only averaged around the 10 pixels which form the peak of the transverse profile: this leads to an expected standard deviation of 1.9 levels of the gray scale. These results are well in agreement with the plots in Fig. 7.2: indeed, the standard deviation of the data points of the longitudinal profile in the beam region (with average value of about 36) is computed to be 2.1, whilst the transverse profile shows a considerably smoother curve. For this profile it is not possible to make a more quantitative statement since the true profile is not known (whilst in the longitudinal case it is assumed to be flat), and the expected spread is smaller than the resolution of the CCD camera.

The Poisson noise reduction through averaging applied to the transverse profile is not possible when the monitor is used in its supersonic gas jet monitoring mode. Thus, if higher precision is needed then the averaging has to be done using profiles taken at different times. If precision better than 3% is to be achieved for all expected values ≥ 20, the profile acquisition rate will be slowed by about 2 orders of magnitude.

7.5 Conclusions

In this chapter the operation of the monitor in the residual gas mode has been characterized. In sections 7.1 and 7.2 the characteristics of the experimental stand built at the Cockcroft Institute are investigated, i.e. the residual gas pressure control valve and the pixel to mm conversion factor of each of the cameras associated with a phosphor screen. Moreover, the field of vision of the detector is found to be consistent with the mechanical bore of the extraction system electrodes, confirming that no major field distortions exist to prevent particles close to the electrodes edges to reach the MCP.

In section 7.3 the performance of the detector with respect to the measurement of the transverse profile is measured. In the same section, a calibration procedure is shown that allows experimental determination of the ion drift due to gas ions initial velocity. It is shown that ion drift is dominated by the thermal component of velocity for operation with residual gas, hence indicating one of the advantages of the use of a supersonic jet. By tailoring the extraction field (limited in these experiments by the use of a low energy electron beam of a few keV energy) the image smearing due to ion drift is demonstrated to achieve sub-mm values. A value of about 65 μm is measured for the spatial resolution of the monitor in this operation mode, well suitable for operation in the USR, where beams with full width at 6σ of approximately 3 cm are expected.

In section 7.4 an equivalent analysis is carried out to characterize the measurement of beam current in the residual gas operation mode. Sensitivity and resolution are redefined to characterize current monitoring, and expressed as the product of two factors, k_{design} and $A_{det.max}$. These factors allow to apply the experimental results for estimating the resolution of other implementations of the monitor, splitting the overall sensitivity and resolution in the components due to monitor design and detector intrinsic limits. The overall maximum resolution is measured to be $5.78 \cdot 10^{-13} mbar \cdot mA$ for the particular experimental setup present at the Cockcroft Institute. For the beam parameters of the USR, where DC beam currents of $160 \div 560$ nA are expected [11] at pressures of 10^{-11} mbar, this results in a resolution of 50 μA, hence about $3 \div 4$ orders of magnitude worse than needed to monitor current as well as transverse profile: operation as a beam current monitor as well as a beam profile monitor is hence restricted to medium to high current machines in the mA current regime. Operation in profile monitoring mode is of course still feasible, due to signal integration times of the order of $1 \div 10$ μs, as calculated in section 1.3.1.

7. RESIDUAL GAS OPERATION MODE

8

Conclusions and Outlook

8.1 Conclusions

The work presented in this thesis constitutes the feasibility study, design, assembly and first commissioning of a novel least interceptive transverse beam profile monitor based on the use of a supersonic neutral gas jet target shaped into a thin screen.

Background In Chp. 1 an overview of the state of the art in non interceptive profile monitoring is presented, and a comparison drawn with the supersonic gas jet based monitor. It is shown that the supersonic gas jet based monitor can be used in regimes of ultra low pressures below 10^{-11} mbar in which operation of other solutions, in particular residual gas monitors and beam induced fluorescence monitors is not feasible. At the same time, the supersonic gas jet based monitor is also applicable in conditions of low current beams such as in the USR (hundreds of nA current), in which conditions ion beam scanners are also not applicable. The supersonic gas-jet based beam profile monitor is hence shown to be the only viable alternative for least-interceptive transverse beam profile monitoring in low energy, low intensity, low vacuum accelerators such as the USR.

The monitor working principle is then described and the obtainable count rate and resolution estimated. A discussion on the actual number of data points needed for each profile is presented, also expressing explicitly the dependence of the number of required profiles on the precision required in the measurement of beam position and profile standard deviation.

Theory of supersonic jet flow   In Chp. 2, a general theory of supersonic jet flow is presented. Section 2.1 introduces the analytical equations that describe the supersonic flow and the results that are obtainable through the study of the Euler equations, applicable due to the isentropic nature of free jets.

The supersonic jet used in this work is categorized as an underexpanded jet, i.e. a jet which keeps expanding also past the nozzle exit, and the influence of nozzle shape is shown to be unimportant to distances of more than a few mm downstream the nozzle. The shock wave pattern created outside the nozzle, characteristic of an underexpanded jet is described and empiric relations for its dimensions quoted. These relations, together with the geometry of the shock wave pattern, are then used in Chp. 3 to benchmark the results obtained by the numerical simulation software employed to study the jet behavior. Finally, the description also yields a relation for the dimension of the *zone of silence*, i.e. the maximum distance that the nozzle can be put from the first skimmer, useful in the mechanical design of the monitor.

Focusing on the flow inside the nozzle, where the jet can be modeled with a 1-dimensional approximation, the equation of mass flow through the nozzle is derived. This equation proves central to the discussion presented in Chp. 4 in which a theory to model the jet expansion is presented.

From energy considerations, the velocity of the jet molecules is shown to approach a terminal value, whose value is given in terms of the high pressure gas reservoir temperature, within few mm of expansion; a fact which will also be used in Chp. 4, to predict the jet number density anywhere in its path across the chamber.

Finally, the peaking factor is introduced as a mean of comparing the intrinsic directionality (i.e. without added collimation) of an ideal diffusive source against the supersonic jet. The discussion shows that the two sources are in fact remarkably similar, and the high directionality obtained in supersonic jets is more an effect of collimation and high pumping speed needed to evacuate the uncollimated part of the flow, rather than an intrinsic property of supersonic flows.

Section 2.2 focuses instead on the numerical approaches used to solve the Euler equations in the mixed sub-supersonic regime applicable to the present work, in particular in the regions close to the occurrence of shock waves. Two different numerical techniques are first introduced, namely the method of characteristics and the Monte

Carlo approach. These techniques are shown not to be ideally suited to the investigated problem due to inability to deal with mixed sub-supersonic flow and unbearable computational weight for the analysis of flow sections with very different densities respectively. The time-dependent finite differences method, used in Chp. 3 to analyse the jet expansion, is then introduced and described.

Numerical Simulations   Whilst a theory of gas jet expansion yielding the required quantities of pressure and density of the jet and vacuum chamber anywhere along the jet expansion is presented in section 4.2, and requires no numerical solution of the Euler equations, this theory relies heavily on the numerical value of the peaking factor, i.e. the directionality of jet flow. The peaking factor depends on the shock wave structure of the flow, and maximization of density flow in the computed Euler flow corresponds to maximization of the peaking factor. The numerical analysis presented in Chp. 3 is therefore aimed at identifying the optimum configuration of the nozzle skimmer through solution of the Euler equations.

Sections 3.1 through 3.3 concern in particular the software tool chosen for solving the Euler equations. The choice of the GDT software is motivated, the software itself successfully benchmarked against the known case of free jet expansion without additional collimating skimmers, and, based on this benchmarking, the parameters of the simulation are fine tuned. In particular, Grid Finesse and CFL constant are fixed, together with the shape and numerical form of the boundary conditions, optimized to minimize the creation of artifact reflected shocks at the boundary. Finally, also the results presented in literature about the insensitivity of longer distance jet flow (> few mm) to nozzle shape are successfully reproduced.

In sections 3.4 and 3.5 the geometric and thermodynamic variables of the collimating system chosen for the investigation are listed and described. Also in these sections is introduced an original set of 3 observables dedicated to the optimization of nozzle-skimmer systems for applications in beam diagnostics, or, in general, for the creation of a homogeneous gas target without stringent requirements on internal temperature.

In section 3.6 an analysis of the jet flow with both the original set of variables and the standard observables used in literature (Mach number and temperature) is performed. An original nozzle skimmer configuration, featuring slit nozzle perpendicular, rather than parallel, to a slit skimmer, is identified as the best performing one when compared

to standard configurations. This presents an improvement factor on the variables of geometric ratio and density homogeneity of 2÷10.

Furthermore, a table showing the response of each observable to variation of each independent variable is also derived as an aid to experimental optimization of the jet target performance. The table identifies the nozzle skimmer geometry, and in particular the opening angles of the skimmer, to play a central role in target optimization.

Finally, density profile maps for the cross section of the target are shown, and the original nozzle-skimmer configuration presented is shown to be able to significantly modify the shape of the jet target from homogeneous to split screen after only a change in high reservoir temperature, without resorting to any geometrical variation. This original feature presents possible applications in beam scraping and halo monitoring.

Mechanical design   Section 4.1 give an overview of the experimental stand, dividing it in 4 operating sub-sections. The mechanical components are introduced and described and justifications are provided for the chosen design. This section is complemented in Annex D.2 by the description and mechanical stability calculation of the holding stand.

Section 4.2 describes the vacuum system in detail. It also presents an original theory of gas jet expansion that relies on the assumption of ideal molecular flow past the first skimmer and the approximation of the peaking factor to compute the jet density and size everywhere along its path, together with the expected vacuum pressures in all different chambers, effectively providing a beyond state of the art, valuable tool for the design of supersonic gas jet target systems in general.

Section E describes in detail the design and operation principle of the skimmers used in the experimental setup. This section is complemented in Annex D.3 and D.5 by equivalent discussions covering the design and operation details of different accessories used in the experimental setup: vacuum gauges, feedthroughs, viewports and the custom made gas valve and respective control electronics for pulsed jet operation.

Finally, reference is made to Annex F, which describes the design and working principle of a modified version of the experimental setup allowing precise relative motioning of the different collimating elements without breaking vacuum. Such setup, of greater mechanical complexity, is intended as a station to investigate systematically the generation of the supersonic gas jet and the validity of the theory introduced in section

4.2, rather than an actual operating monitor, where flexibility is rather surrendered to robustness.

Electron gun calibration Chp. 5 describes the electron gun used in this work to produce a primary beam. The electron gun is experimentally calibrated and values for its current, spot size, kinetic energy and deflection range are provided. These values are then used in Chp. 7, together with the information on residual gas pressure, to evaluate the performance of the monitor in terms of its sensitivity and resolution.

The information on deflection and kinetic energy is also used in Chp. 6 to evaluate the maximum applicable extraction field which still allows the electron beam not to be deflected on one of the metal electrodes and hence be lost.

Detector System In Section 6.1 a simple theory based on the assumption of homogeneous extraction field is introduced and used to derive the equations driving the extraction. To calculate the device performance, the initial ion velocity is identified as a relevant factor, and its components given by impact recoil and initial temperature analyzed. Using this mathematical structure, together with the data on ionization recoil given in literature, the extraction system is characterized in terms of its theoretical spatial resolution and sensitivity, and the mechanical and electric design finalized.

Section 6.2 then describes the mechanical design of the extraction system obtained from the optimization carried out in the previous section, and section 6.4 describes the technological accessories used: namely MCP detector, custom designed and manufactured voltage divider and phosphor screen. In the same section an experimental characterization of the response of MCP and phosphor screen is carried out, confirming a dynamic range of amplification from 2 to 4 orders of magnitude for the MCP (depending on the bias voltage) and only of a factor 2 for the phosphor screen (depending again on the bias voltage applied).

Finally, section 6.3 describes a more realistic theory of extraction, which no longer requires the assumption of homogeneous field, used in the discussion of section 6.1, by considering instead the field simulated with OPERA3D. The results of the two approaches are compared and found compatible to within few percent, and the electron beam trajectories computed to yield the maximum applicable extraction field, set at 12kV/m.

Residual gas operation mode characterization   Sections 7.1 and 7.2 introduce the setup in the residual gas operation mode, and derive the pixel to mm conversion factor for the different phosphor screens as well as the field of vision of the whole detector, confirmed to be 50 mm in diameter.

In section 7.3 the performance of the monitor in terms of its spatial sensitivity, resolution and noise is assessed with a series of experiments in which the beam profile measured on the MCP is compared with the *true* beam profile as seen on the direct hit phosphor screen. The resolution of the monitor is determined to be of about 65 μm, changing of a few μm depending on the extraction field used, significantly exceeding the beam profiling requirements for operation with the USR beam in the commissioning phase, where higher residual gas pressures are envisaged: such monitor would indeed result in sampling of the USR beam with about 450 bins for each profile. Analysis of the noise shows the monitor in this operating mode to yield a noise distribution with $\sigma \approx 0.55$ mm. This standard deviation is quadratically added to the beam standard deviation, and hence sets the limit on minimum beam width suitable for precise measurement.

Section 7.4 focuses instead on the sensitivity and resolution of the monitor to the current signal, and evaluates these by performing measurements of the light yield at different residual gas pressures and beam currents. The current sensitivity S is expressed as the product of the detector amplification $A_{detector}$ and a design constant k_{design}, and found to be given by $1.73 \cdot 10^{12}$ mbar^{-1} mA^{-1}. The resolution is therefore given by $5.78 \cdot 10^{-13}$ mbar·mA, and, at the conditions typical of the USR, found to correspond to 50 μA resolution.

8.2   Outlook

The study presented in this work showed the enormous potential for applications of an ionization beam profile monitor based on a supersonic gas jet. It also indicated that precision alignment of all components is absolutely crucial for the generation of an ultra cold, well defined jet and a dedicated alignment system will constitute an important update to the monitor.

An improved jet generation and shaping scheme has already been designed and manufactured and will form the basis for future studies. As presented in Annex F, this

is a highly flexible experimental setup that will allow to probe the characteristics of the jet for many different configurations of the collimating system in great detail. It will open unique opportunities to benchmark the theory of jet generation and optimization presented in this thesis. Additional developments, such as a laser velocimeter in the frame of the new Marie Curie network LA^{3}NET, will allow extending the research program around this monitor significantly.

The improved setup will also enable optimizing the entire monitor for applications other than the USR. First studies to widen the application of this unique diagnostics element were already launched within the frame of this work and include least intrusive online monitoring of the transverse profile of beams in ion beam cancer treatment facilities, third and fourth generation light sources, as well as beam profile, position and current monitoring in the injection line of the future European Spallation Source (ESS) in Lund, Sweden. In the latter case the primary beam is a 50 mA, 2.2 GeV proton beam [84].

At such high intensity and beam energy most commonly used diagnostics methods will not withstand the beam power: interceptive screens or wire scanners are unsuitable due to monitor damage and fast performance degradation. A supersonic gas jet target monitor could then provide a unique way to include a high resolution monitor into a cryogenic ultra-high vacuum environment. Due to the particular beam parameters at ESS it should allow operating the apparatus also as a current and position monitor, thus potentially providing an all-in-one diagnostics station for the ESS injector.

Appendix A

Theory of supersonic jet flow

A.1 Definitions and glossary

This section introduces the basic quantities used in this work. A more detailed account of these definitions can be found in [42].

- *Particle, continuum and molecular flow.* Fluid dynamics encompasses both the regime of relatively high densities of molecules, or *continuum* regime, where intermolecular collisions are sufficiently numerous to allow the definition of collective properties of the flow such as pressure and temperature; and the *molecular flow* regime, in which each molecule is virtually isolated from the others and needs to be treated individually. In both cases, one refers to the elementary constituent of the flow as a *particle*, referring to a single molecule in the molecular flow regime and to a volume element of fluid in the continuum regime.

- *System dimensioning.* Continuum fluid dynamics is based on the Navier Stokes equations, which are in turn based on basic conservation laws (mass, momentum and energy) applied to *elements of fluid*, i.e. regions of flow composed of a large number of particles. Furthermore, the quantities used are very often ratios, such as the Knudsen, Mach and Reynolds number, which do not depend on absolute dimensional values. Hence the *dimensional theorem* is introduced (see [42]), by which use of dimensionless quantities in the description of flows results in the ability to scale fluid mechanics calculations.

Therefore, the dimensions are normalized to the characteristic dimension of the particular system, usually taken to be the smallest linear dimension. In the case of supersonic gas jets used in beam instrumentation application, this characteristic dimension is best chosen to be the nozzle diameter, which will hence be used in the remainder of this work as the unit for length.

- *Speed of sound a.* The speed of sound a is defined as the speed at which a pressure perturbation, i.e. a *sound wave*, travels across the fluid medium. An equation for the speed of sound in an ideal gas can be derived from kinetic theory [42], and relates a to the temperature T of the medium, the gas constant R, the molar mass W and the adiabatic index of an ideal gas γ :

$$a = \sqrt{\frac{\gamma RT}{W}} \tag{A.1}$$

For real gases a will in general also depend on frequency, pressure and density. However, in the cases discussed in this work, the gases can usually be considered ideal gases, and speed of sound assumed to be given by (A.1).

- *Mach Number M.* Particle velocity in fluid dynamics can be expressed in terms of the dimensionless Mach number M, defined as the ratio between the particle velocity v and a at the local conditions of temperature:

$$M \equiv v/a \tag{A.2}$$

It should be noted that since the velocity of sounds varies with temperature, same velocities can correspond to different Mach numbers. However, flow properties vary dramatically from subsonic speeds ($M < 1$) to supersonic speeds ($M > 1$), due to the possibility (or impossibility) of a perturbation to follow the flow. The effects of sub or supersonic speeds are far more dramatic than those resulting from particle velocity differences alone and it is therefore more appropriate to classify the flow based on M, rather than v.

- *Equation of state for ideal gas.* The equation of state is best expressed in terms of the mass density ρ; if W is the molar mass of the constituent gas and P its pressure, one has:

$$P = \frac{\rho RT}{W} \tag{A.3}$$

- *Mean free path of a particle in an ideal gas* λ. The mean free path λ expresses the average distance traveled by a particle in a gas between two collisions with other molecules. For a Maxwellian velocity distribution, λ is derived from the kinetic theory of gases (see e.g. [85]) and can be expressed as:

$$\lambda = \frac{1}{\sqrt{2}n\sigma} \tag{A.4}$$

where n indicates the number density of the gas and σ the collision cross section.

A.2   Gas expansion: flow regimes

Due to the diverse applications of gas jets, nozzle designs also vary dramatically. A first distinction can be drawn between nozzles with axial symmetry *(axisymmetric)* and slit nozzles for planar flows *(planar)*. For the sake of simplicity, the following discussion only focuses on axisymmetric flow; the conclusions can qualitatively be applied to planar flow as well, although the quantitative details, in particular flow velocity, temperature and collision rates, differ. However, even restricting the discussion to axisymmetric flow, it is still possible to classify the different nozzle designs in 4 main categories: *convergent-divergent (CD) nozzle, convergent nozzle, capillary tube and sharp edged orifice* nozzle. A sketch of all the 4 nozzle designs is shown in Fig. A.1. This discussion will assume a CD nozzle design, where the flow is guided at any point, which simplifies the discussion. Results obtained for the CD nozzle can be as a first approximation extended to all other designs, and even a more detailed analysis, presented in section 3.2.3, shows that the differences are usually negligible for the application treated in this work.

Following the commonly accepted nomenclature for study of nozzle flows in aerodynamics, the terms *chamber* and *ambient* will be used to refer to the high and low pressure reservoirs respectively, and P_0 and P_a to refer to their pressures, always assuming $P_0 > P_a$ [1]. The point of least aperture of the nozzle will be referred to as *nozzle throat*.

Depending on the pressure difference between chamber and ambient, different flow regimes are identified. Fig. A.2(a-g) shows seven possible regimes obtainable by tuning

---

[1]The notation P_0 is preferred to P_c because it will be consistently used in the following text as the initial pressure of the expanding gas, as opposed to the local pressure, indicated with P.
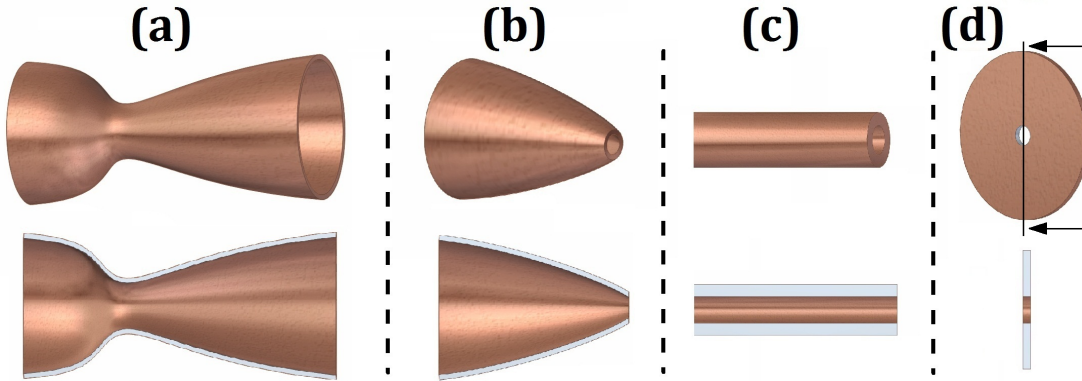
Figure A.1: (a) Convergent-divergent, or *de Laval*, nozzle commonly used for propulsion in supersonic jet aircrafts. Actual proportions vary depending on the speed and altitude to be attained. (b) convergent nozzle, typically used in subsonic aircrafts. (c) capillary tube, and (d) sharp orifice nozzle, commonly used in laboratory experiments.

the pressure difference between *chamber* and *ambient*, indicating also the flow velocities. The relevant quantity for the study of this system is the pressure ratio $R = P_0/P_a$. For low values of R, when P_a is only slightly lower than P_0, subsonic flow occurs, Fig. A.2(a). As expected from eqn. (2.5), the flow accelerates as A decreases until the *nozzle throat*, then it decelerates again as A increases. Flow velocity, and total mass flow rate with it, increase as R increases.

If R is sufficiently increased, eventually the flow velocity increases enough that the Mach Number becomes 1 at the nozzle throat Fig. A.2(b). At this point, no matter what the value of R becomes, the flow will still stay subsonic until the nozzle throat and just become sonic at the throat itself. As it was described in the previous section, nozzle flow can be approximated as 1-dimensional and mass flow is the same everywhere along the flow: the mass flow rate at any point can hence be estimated at the nozzle throat alone. When the Mach Number at the throat is fixed to $M = 1$, unless a change in density occurs, the mass flow rate is fixed for the whole flow: the flow is therefore defined as *choked*. Mass flow rate can of course be changed, if upstream pressure is increased, so that pressure and density increases, even if M is staying unity.

The reason for the occurrence of choked flow and the position of the sonic surface can be qualitatively understood from the analysis of eqn. (2.5). Indeed, should the sonic surface form upstream the nozzle throat, the supersonic flow beyond the sonic surface would see a decreasing flow area A and thus decelerate back to the sonic $M = 1$.

Chamber Throat　　　　**Ambient**

**Flow
accelerating**　M<1　decelerating　M<1

(a)

**Flow
accelerating**　M=1　decelerating　M<1

(b)

**Flow
accelerating**　M=1　acc.　dec.　M<1

M>1　M<1

(c)

**Flow
accelerating**　M=1　accelerating　M<1

M>1　accelerating

(d)

**Flow
accelerating**　M=1　accelerating　**mixed flow
with waves**

M>1

(e)

**Flow
accelerating**　M=1　accelerating　M>1

M>1　**no waves**

(f)

**Flow
accelerating**　M=1　accelerating　M>1

M>1　**with
waves**

(g)

Figure A.2: Representation of 7 different flow regimes obtained in the CD nozzle for increasing values of pressure ratio. Each image shows the position of the sonic surface at M=1, the values of M in the other regions and the regions in which the flow accelerates or decelerates. Regimes depicted: (a) subsonic; (b) flow just choked; (c) shock in nozzle; (d) shock at exit; (e) overexpanded; (f) design condition; (g) under expanded.

A. THEORY OF SUPERSONIC JET FLOW

Conversely, for it to form downstream the nozzle area, the subsonic flow preceding it should have already gone through the nozzle throat, and there hit the largest velocity in the flow, due to the dimension of the nozzle throat being the minimum dimensions anywhere in the nozzle. Therefore, a stable equilibrium solution for the sonic area can only be formed at the point of minimum aperture in the nozzle, i.e. the nozzle throat.

The transition from subsonic to supersonic flow occurs when R exceeds a gas-species dependent critical value G which is given by:

$$G = \left(\frac{\gamma + 1}{2} \right)^{\frac{\gamma}{\gamma - 1}} \tag{A.5}$$

and, since γ never exceeds 2, is smaller than 2.25 for all gases.

Once the flow becomes choked, the sonic surface will stay at the nozzle throat no matter what the ratio R becomes; however, the flow pattern downstream the throat can still change depending on R. As R is increased above the value needed to just choke the flow, supersonic flow occurs beyond the throat, where the flow area increases, Fig. A.2(c). As the flow accelerates, its pressure decreases, to the point that, further downstream, mass flow and pressure are such that the jet can no more displace the rest gas in the ambient whilst keeping its own velocity, density and pressure. The flow must thus adjust to the boundary conditions: a shock wave occurs in the diverging nozzle section. Across the shock wave the thermodynamic properties of pressure, temperature and density, as well as the flow velocity, change abruptly and conform to those of the ambient, with the flow becoming subsonic.

As R is still increased, either the amount of rest gas to displace in the expansion in decreased (lowering P_a) or the amount of gas flowing through the nozzle throat is increased (increasing P_c): as a result the position of the shock wave moves further downstream. Eventually, the shock wave position will reach the exit of the nozzle, Fig. A.2(d). Further increase of the ratio R will see the shock wave bend outwards into the jet Fig. A.2(e). This situation results in the jet exiting the nozzle, and the 1-dimensional approximation to start to break down, which in turn sees the start of a complex shock wave pattern, composed of both normal and oblique shocks which localize the jet transversally and keep it confined outside the nozzle. This regime is referred to as *overexpanded* jet, as the jet pressure at the nozzle exit is lower than the ambient pressure: the jet has expanded too much in the nozzle and needs to readjust to the ambient.

Further increase of R modifies the shock wave pattern, weakening it until a value of R is obtained for which maximum thrust is developed by the expanding jet, and the condition sought by aerodynamic application design is achieved: the flow is therefore known as *design condition*, Fig. A.2(f). In this regime, the pressure at the exit of the nozzle is just matched to the ambient pressure, therefore there is no need for a shock wave to develop. Therefore, no energy is wasted in creating the shock wave *(wave drag)* and the thrust is maximized.

Finally, any further increase of R will result in the pressure at the exit of the nozzle to exceed the ambient pressure, so that more shock waves appear to match the two pressures. These shocks are called *expansion* waves, as the jet keeps expanding past the nozzle exit under the influence of its higher than ambient pressure. Past the nozzle exit, the gas increases its flow area as it progresses, creating the shape known as *plume*. This situation, depicted in Fig. A.2(g), is referred to as *underexpanded* jet, and is the one of interest in this work. Indeed, the need to have very intense target, coupled with the use of nozzles which do not have a divergent section, results in very large values of R. A plot of the pressure distribution along the nozzle for all regimes mentioned is provided in Fig. A.3.

A.3   Intensity along the expansion axis and effusive source comparison

The established form of intensity I in literature is expressed in molecules emitted per second per steradian solid angle centered on the source. I can therefore be interpreted as a solid angle intensity, rather than a surface intensity.A suitable description of the gas-jet solid angle intensity is its intensity along the expansion axis, or *centerline intensity* I_0. This is the intensity that is most interesting for design and applications, as is the one which is extracted through the skimmers and used in the experiment.

I_0 will be a function of the flux of molecules coming out the nozzle orifice: $\dot{N}$, expressed in molecules/sec. The local intensity integrated over 2π solid angle yields $\dot{N}$. 2π is chosen, instead of the full solid angle 4π , because it is assumed that the expansion only happens in the hemisphere downstream the nozzle, and therefore neglects rest gas scattering, which would result in upstream velocities to be eventually acquired by the
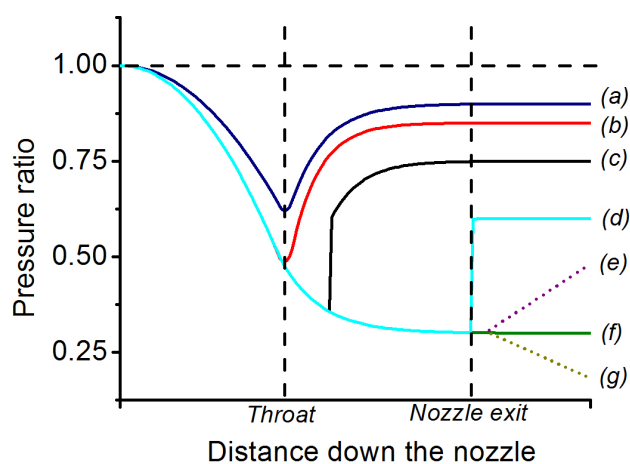
Figure A.3: Plot of the pressure distribution along the nozzle in all 7 flow regimes shown in Fig. A.2, after [1]. In this illustration it is assumed for simplicity that the change in R is only due to the lowering of P_a, rather than the increasing of P_c. Thus the pressure distribution upstream the throat stays constant once the flow has been choked, irrespectively of P_a: a result of supersonic flow being insensitive to downstream conditions and hence isolating the flow upstream the nozzle throat from the ambient. The abrupt pressure changes in the supersonic section of the nozzle represent the occurrence of shock waves. The dashed section indicate regions of complex pressure distributions occurring in the presence of 3-dimensional shock waves pattern (overexpanded and underexpanded jets).

expanding gas. $\dot{N}$ is related to the mass flow by dividing $\dot{m}$ by the mass of each molecule, i.e. the product of Avogadro's constant and the molar weight:

$$\dot{N} \;=\; \frac{\dot{m}}{N_{Av}W} \tag{A.6}$$

It is then further assumed that the expansion pattern, intended as the spatial distribution of local intensities, does not change with $\dot{N}$, but rather that only its intensities scale. Thus, the intensity, and in particular I_0 depends linearly on $\dot{N}$. Experiments by Beijerinck and Verster [49], have established this proportionality factor, known as the *peaking factor* κ, for an axisymmetric ideal free jet:

$$I_0\,[molecules/s \cdot sr] \;=\; \kappa\dot{N}/\pi \tag{A.7}$$

In order to understand the significance of the peaking factor and the reason for the introduction of π at the denominator, it is useful to consider how this relation evaluates in the case of an ideal effusive source. An ideal effusive source can be defined as a source such that the flux coming from it measured at any point in space depends only linearly on the solid angle that the source surface subtends at the point of the measurement, and not on the actual position of the measurement point. This statement is equivalent to requiring that the observed solid angle intensity I_{obs}, i.e. flux per steradian, is constant everywhere around the source[1].

For a mathematical representation, it is needed to calculate the solid angle subtended by the surface at the generic observation point P. For the sake of this calculation, the surface is assumed to be infinitesimally small; it is straightforward to extend all results obtained to a finite surface by integration.

With reference to Fig. A.4, the emitting surface is perpendicular to the x axis (vector $\mathbf{X}$) and the unit vector $\mathbf{P}$ points to the generic point P at distance r from the source surface. If ϑ is the angle between $\mathbf{X}$ and $\mathbf{P}$, and φ the angle between the projection of $\mathbf{P}$ on the yz plane and the y axis (vector $\mathbf{Y}$), the vector $\mathbf{P}$ can be written as:

$$\vec{P} \;=\; \begin{bmatrix} cos\vartheta \\ sen\vartheta cos\varphi \\ sen\vartheta sen\varphi \end{bmatrix} \tag{A.8}$$

---

[1]The definition of I_{obs} is different from the definition of I given above, in that I_{obs} is the flux per steradian of the source as seen from the observation point, and therefore the area which is used to calculate the solid angle is the area of the source, with the solid angle centered on the detector, rather than the area of the observing detector, with the solid angle centered on the source.
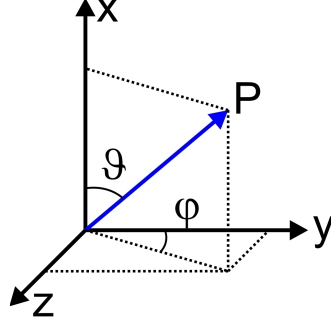
Figure A.4: Definition of the angles ϑ and φ.

The solid angle Ω subtended by the surface at the point P will be given by the surface projection on a plane perpendicular to $\mathbf{P}$ divided by r^2:

$$\Omega \,=\, A\vec{P} \bullet \vec{X}/r^2 \,=\, A cos\vartheta/r^2 \,=\, \Omega_{max} cos\vartheta \tag{A.9}$$

An infinitesimally small detector area through which the incoming molecules are collected is assumed, which subtends an angle $d\Omega_{detector}$ with the source. The intensity I_{obs} seen at the point P by this detector can then be expressed as the source intensity $I(\Omega, \vartheta)$, in molecules per second per steradian, times the angle $d\Omega_{detector}$, divided by the angle Ω subtended by the emitting surface at the point P:

$$I_{obs} \,=\, \frac{I\,(\vartheta, \varphi)\, d\Omega_{detector}}{\Omega_{max} cos\vartheta} \tag{A.10}$$

And the requirement of ideal effusive source implies that I_{obs} should not depend on $\mathbf{P}$ (therefore not depend on ϑ or φ). Thus, the intensity $I(\Omega, \vartheta)$ of the ideal effusive source, also called *Lambertian source*, should be given by $I_0\, cos\vartheta$ so that the two cosines cancel out and the observed intensity is independent on ϑ and φ and, thus, on the direction of the point P. Once the formula for the source intensity I_0 is known, it is possible to integrate it over the full 2π hemisphere and equate the result to the flux through the nozzle, as described above. One has:

$$\vec{N} \,=\, \int_{2\pi} I_0\, cos\vartheta\, d\Omega \,=\, \int_{2\pi} I_0\, cos\vartheta\, \frac{A\,(\vartheta, \varphi)}{r^2}\, d\vartheta\, d\varphi \tag{A.11}$$

where A is the infinitesimal element of area defining the solid angle $d\Omega$, i.e. of the sphere centered in the source. Thus A(ϑ, φ)=r^2 senϑ, to be integrated over ϑ and φ:

$$\vec{N} \,=\, \int_{\vartheta=0}^{\pi/2} \int_{\varphi=0}^{2\pi} I_0\, cos\vartheta\, \frac{r^2\, sen\vartheta}{r^2}\, d\vartheta\, d\varphi \,=\, \pi\, I_0 \tag{A.12}$$

Therefore finally for an ideal effusive source:

$$I_0 = \frac{\kappa \vec{\dot{N}}}{\pi} \tag{A.13}$$

with κ=1. In the case of the supersonic jet, I_0 indicates the centerline intensity. A value of κ larger than 1 indicates that the mass flow is concentrated in the forward direction, as one would expect of a directional jet of gas. However, the values of κ determined experimentally by Beijerinck and Verster, vary only from 1.98 for monoatomic gases to 1.11 for triatomic gases. When one compares this number with the much larger (several orders of magnitude) intensity that can be obtained using supersonic jets instead of effusive sources, it is clear that the difference in intensity is not due to the different values of κ but rather to the different values of $\dot{N}$. Therefore, from the point of view of the gas target intensity, the difference is made by the fact that more mass is pumped through the orifice through larger pressures and pressure differentials, rather than by the supersonic nature of the jet, which just happens to be an effect of larger pressures. This consideration also explains the need for much larger pumping speeds in supersonic jets as compared to effusive sources.

A.4 Numerical Methods

A.4.1 MOC and MC techniques

The MOC has been the first method to be developed [1, 43], and is only suited for the determination of the steady state solution of a given flow.

The MOC relies on the identification of particular curves in space, namely the *characteristics*, along which, through a change of variables, the components of Euler's set of partial differential equations reduce to ordinary differential equations and can be integrated numerically solving them step by step, starting from the initial boundary condition.

Most results available in the literature for free jet expansion in the continuum approximation are derived using the MOC; however these results are unreliable when it comes to a description of the shock waves pattern and the complex regions at the boundary between different shocks, where the flow cannot be considered isentropic anymore, and, past the shock, even becomes subsonic. In subsonic regions, the flow cannot be computed anymore based only on the upstream boundary conditions, but

it also depends on the variables values elsewhere in the flow: i.e. the Euler equation become elliptic, and the MOC fails. This is a severe restriction for an investigation of the free jet source aimed at optimizing the geometry of the nozzle-skimmer system creating the jet, as the isentropic assumption fails at contact with physical boundaries, and regions of subsonic flow are invariably created around the jet in the expansion chamber.

Furthermore, the MOC only provides the steady state of the flow, and has no way to deal with the time transient of the expansion. Therefore this work focuses instead on the time dependent approach, described in section A.4.3.

MC method   One alternative would be the MC method, which does away with the Euler equations altogether, and analyses the system from the interaction of the single particles forming the gas instead. The advantage of the MC method is the ability of overcoming all the assumptions underlying the Euler equations, most important of which is the continuum assumption.

However, two disadvantages of this method make it unsuitable for the project presented in this work. Firstly, MC tools for the study of the free jet supersonic expansion are not readily available, being still the topic of ongoing research [86]. The coding of such software tools requires a considerable R&D effort for both the script and the benchmarking, which make it unsuitable for the time scale of the present work. Secondly, in order to generate sufficient statistics for reliable predictions, the MC simulation needs to be scaled linearly on its whole range so that the region with least particles can still rely on a sufficient number of counts. Given the very high density gradients in the supersonic jet expansion system, which goes from high pressures at the gas reservoir down to the much lower pressures of the outer expansion regions, spanning a range of more than 8 orders of magnitudes, this requirement of the Monte Carlo simulations is likely to result in long computing time [87]. The time dependent FD method is hence preferred in the present work.

A.4.2   Finite differences method

The MOC relies on following the characteristic lines as the Euler equations are integrated: this can become a numerical inconvenience, especially at high Mach numbers,

when the characteristics become particularly elongated and distorted, resulting in numerical errors during the calculation. The FD method allows instead computing the flow on a grid of calculation points that does not follow the characteristics and can be chosen purely on the basis of numerical precision and stability. However, it is based on the same principles underlying the MOC, namely the calculation of the downstream points on the basis of the upstream flow map. Thus, the FD method is also inapplicable when it comes to solving flows which are not supersonic, and hence depend not only on the conditions upstream, but also downstream. Nevertheless, the FD method is at the basis of the time dependent solution of the flow which will be treated in the following section, and is able to overcome these limitations.

The FD method relies on the use of a computational grid, which is usually taken to be rectangular for simplicity. Therefore, points on the FD rectangular computational grid can be identified by a row and a column index, i and j, corresponding respectively to the axes x and y[1].

The main idea underlying the FD method is to use the Taylor expansion to obtain the value of any generic flow variable u at a given grid point in terms of the values of the flow variables at other known grid points. Assuming the boundary conditions are defined on the row $(i, *)$, one has for the unknown vales of the variable u at the grid point $(i + 1, j)$:

$$u_{i+1,j} = u_{i,j} + \left(\frac{\partial u}{\partial x}\right)_{i,j} \Delta x + \left(\frac{\partial^2 u}{\partial x^2}\right)_{i,j} \frac{\Delta x^2}{2} + \dots \tag{A.14}$$

where Δx is the finite difference in x coordinate between the two grid points.

By limiting the discussion to first order, and isolating the derivative term, one gets for positive and negative values of Δx respectively:

$$\left(\frac{\partial u}{\partial x}\right)_{i,j} = \frac{u_{i+1,j} - u_{i,j}}{\Delta x} \tag{A.15}$$

$$\left(\frac{\partial u}{\partial x}\right)_{i,j} = \frac{u_{i,j} - u_{i-1,j}}{\Delta x} \tag{A.16}$$

$$\left(\frac{\partial u}{\partial x}\right)_{i,j} = \frac{u_{i+1,j} - u_{i-1,j}}{2 \cdot \Delta x} \tag{A.17}$$

Eqn. (A.15), (A.16) and (A.17) are referred to respectively as forward, backward and central difference. The actual partial derivatives are obtained from the Euler

---

[1]The discussion is presented in 2D for simplicity, but is easily expanded to include 3D computations.

equations, so that eqn. (A.15) through (A.17) can be used to compute the flow variables at all points.

An example of this procedure is the use of the mass conservation equation (2.16). At the steady state one has $\partial \rho / \partial t = 0$, thus the divergence of $\rho \vec{v}$ is zero, hence:

$$\frac{D}{Dt} \equiv \frac{\partial}{\partial t} + \left(\vec{v} \bullet \vec{\nabla} \right) \tag{A.18}$$

Therefore, expressing (A.18) in terms of (A.15)[1], if the values of v_x and v_y are known on the row $(i, *)$:

$$\left(\frac{\partial v_x}{\partial x} \right)_{(i,j)} = -\frac{v_{y,(i,j+1)} - v_{y,(i,j)}}{\Delta y} \tag{A.19}$$

it is thus possible to write for the unknown value of v_x at the location $(i+1, j)$:

$$v_{x,(i+1,j)} = \left(\frac{\partial v_x}{\partial x} \right)_{(i,j)} \Delta x + v_{x,(i,j)} \tag{A.20}$$

Similarly, the values of v_y and all other flow variables can be calculated through finite differences with the use of partial derivative relations equivalent to that described in (A.18), as they are obtained by the other Euler equations. However, the results obtained will still be only of first order accuracy. In the 1970s a new technique was devised by MacCormack at NASA [88], which is still used today, and allows second order accuracy to be obtained with little computational effort.

In the following the flow variable v_x will be used as an example, the procedure is to be reiterated for all flow variables to have a full description of the flow. MacCormack's method relies on a two step process, rather than a single step one as described above. In the first step, an estimate of the *true* value of $\partial v_x / \partial x$ at point (i, j) is obtained exactly as described above. This estimate is then used, by solving the remaining Euler equations, to similarly compute the values of all other flow variables in the unknown locations: this is the *predictor* step, which is equivalent to the method described above. After the predictor step, MacCormack uses a *corrector* step to improve the calculation accuracy. The value of $\partial v_x / \partial x$ at point $(i+1, j)$ is obtained using a rearward difference (eqn. (A.16)):

$$\left(\frac{\partial v_x}{\partial x} \right)_{(i+1,j)} = \frac{v_{y,(i+1,j)} - v_{y,(i+1,j-1)}}{\Delta y} \tag{A.21}$$

---

[1]The choice is arbitrary: the discussion holds for any of eqn. (A.15) through (A.17)

A more precise estimation of the $\partial v_x/\partial x$ to be used to estimate $v_{x,(i+1,j)}$ in (A.20) can be obtained by averaging between the values of $\partial v_x/\partial x$ in (i,j) and $(i+1,j)$. This estimate $(\partial v_x/\partial x)_{ave}$ is then used to obtain $v_{x,(i+1,j)}$ to second order accuracy, and, through the use of the other Euler's equations, all the other flow variables.

A.4.3 Time dependent solution

The time dependent method provides a solution to solve flow fields in which subsonic and supersonic flow coexist, and hence the flow depends on both the upstream and downstream conditions. The idea underlying the method is to assume an initial flow condition, i.e. a value for all the flow variables everywhere in the flow, and then use the time dependent form of the Euler equations to describe the time evolution of the field point by point. As the number of time steps increases, the variation of the flow variables values in each point per time interval will decrease until it eventually flattens, reaching a steady state condition. The computational method applied is the FD, but the partial derivatives are time derivatives, rather than space derivatives. For the generic flow variable u one writes:

$$u_{t+\Delta t} \;=\; u_t + \frac{\partial u}{\partial t} \cdot \Delta t + \frac{\partial^2 u}{\partial t^2} \cdot \frac{\Delta t^2}{2} + \dots \tag{A.22}$$

which is the equivalent of (A.14) for the time dependent method. Similarly to (A.14), the higher order terms are neglected, and second order precision is instead obtained through the MacCormack method. Again, the values of the time derivatives are obtained from the Euler equations. It is clear from analysis of equations (2.16) through (2.18) that the time derivative of the flow variables can be expressed in terms of the space derivatives. These space derivatives can be obtained from the known configuration of the flow at time t, and used to estimate the flow configuration at time $t + \Delta t$ with the MacCormack method.

The crucial improvement of the time dependent method lies in the fact that the flow at any given time will only depend, on the grounds of causality, on the flow at previous times. In turn, this leads to the corresponding equations in the variable t being *always hyperbolic*, no matter the sonic nature of the flow. Thus not only it is always in principle possible to solve the flow, but it is also possible to describe the time transient from the initial conditions to equilibrium, rather than being able to calculate

the equilibrium state only, like it was the case for previously described FD and MOC techniques.

Impact of grid dimensions Just like a stability criterion on the grid pitch existed for the FD method, a stability criterion for the time step value exists for solving the time dependent analysis. It is shown in literature [1, 89], that the time step Δt should be chosen smaller than the time needed for a sound wave to propagate between any two grid points, similarly to what was mentioned for the stability criterion on the grid pitch. This is known as the Courant, Friedrichs and Lewy (CFL) criterion. If the time Δt is expressed as the product of a constant K and the minimum time needed for a sound wave to travel between any two grid points, K is known as the *stability constant* and is always less than or equal to unity.

If the grid spacing is reduced, the computing time increases because more grid points are present on the same flow field (by a factor of grid pitch squared on a 2-dimensional grid), but it also increases because the time taken from a sound wave to travel between two grid points decreases linearly with grid pitch, and therefore the number of time steps to cover a given time interval increases linearly, bringing the total effect on computing time to the cube of the grid pitch (for a 2-dimensional grid). It is then clear how the requirements on the stability constant need to be considered carefully and optimized case by case.

Appendix B

Derivation of the mass flow equation

In this appendix eqn. (2.15) will be explicitly derived at the nozzle throat, of area A^*, from the equation of conservation of mass, the ideal gas equation of state and the relations deriving from energy conservation, repeated here for completeness:

$$P = \frac{\rho RT}{W} \qquad\qquad \text{ideal gas eqn. of state} \qquad (A.3)$$

$$\dot{m} = \rho v A = constant \qquad\qquad \text{mass conservation} \qquad (2.1)$$

$$(T/T_0) = \left(1 + \frac{\gamma - 1}{2}M^2\right)^{-1} \qquad\qquad \text{temperature-Mach number} \qquad (2.10)$$

$$v = M\sqrt{\frac{\gamma R T_0}{W}}\left(1 + \frac{\gamma - 1}{2}M^2\right)^{-1/2} \qquad\qquad \text{velocity-Mach number} \qquad (2.11)$$

$$(P/P_0) = \left(1 + \frac{\gamma - 1}{2}M^2\right)^{-\gamma/\gamma - 1} \qquad\qquad \text{thermal eqn. of state} \qquad (2.12)$$

B. DERIVATION OF THE MASS FLOW EQUATION

Starting from (2.1), one has:

$$
\begin{aligned}
\dot{m} &= \rho v A \\
&= \frac{PW}{RT} M \sqrt{\frac{\gamma R T_0}{W}} (1 + \frac{\gamma - 1}{2} M^2)^{-1/2} A^* \\
&= P_0 (1 + \frac{\gamma - 1}{2} M^2)^{\frac{-\gamma}{\gamma - 1}} \frac{MW}{RT} \sqrt{\frac{\gamma R T_0}{W}} (1 + \frac{\gamma - 1}{2} M^2)^{-1/2} A^* \\
&= P_0 A^* \sqrt{\frac{\gamma W}{R}} \frac{\sqrt{T_0}}{T_0} (1 + \frac{\gamma - 1}{2} M^2)^{(1 - \frac{\gamma}{\gamma - 1} - \frac{1}{2})} M \\
&= P_0 A^* \sqrt{\frac{\gamma W}{R T_0}} (1 + \frac{\gamma - 1}{2})^{-\frac{\gamma + 1}{2(\gamma - 1)}}
\end{aligned}
$$

(B.1)

the second equality is obtained substituting the isolated values of ρ and v taken respectively from (A.3) and (2.11), and using A^* for A as the flow is computed at the nozzle throat. The third equality is obtained by isolating P in (2.12) and substituting. The fourth equality is obtained by simplifying, rearranging, isolating T in (2.10), substituting and grouping all the factors $1 + \frac{\gamma - 1}{2} M^2$. Finally, in the last equality, all M are substituted with 1 (sonic condition at the nozzle throat), and the exponents summed up.

Appendix C

GDT Analyzer Software

C.1 GDT analyzer requirement plan

The GDT analyser main purposes are:

1. Given the variables to be investigated, create an input file for the geometry and thermodynamic of the system to be opened with GDT.

2. Creation of input files to be automated so that several input files (obtained by permutations of all the variables to be investigated, provided by the user) might be created with a single run of the program.

3. Having saved the GDT results in a suitable TecPlot format, the analyzer is to read the results from the file, store them in random access memory, and analyze them internally, yielding for each file the values of the relevant observables (standard observables as well as accuracy, resolution and confinement).

4. The observables are then to be saved on the mass memory as a comma separated value (.csv) file, that can be opened by the user.

Advanced features of the analyzer are:

- It allows for easy expansion of the database of simulations. Therefore, if new variables are investigated, the analyzer just updates the existing list automatically, rather than creating a new one.

- It allows easy expansion of the study to any newly defined observable.

C.2 GDT analyzer components diagram and description

In what follows there is a description of the different software packages composing the analyzer, how they relate to each other and what tasks they perform. Fig. C.1 shows a diagram in which every component of the software is included together with its interactions with other components. Red circles indicate the user inputs, blue squares identify executable files and green the mass storage files. Counters are presented without any box.
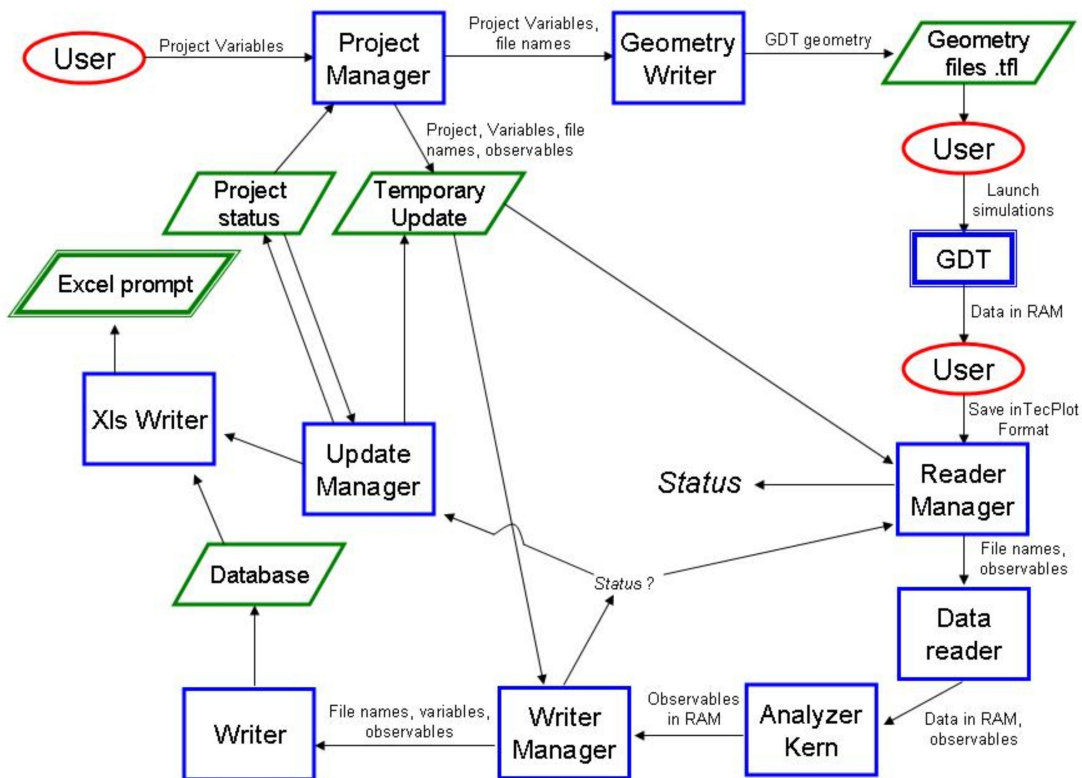
Figure C.1: Block diagram of the GDT analyzer software. Red circles indicate the user inputs, blue squares identify executable files and green the mass storage files. Counters are presented without any box.

a) **Project Manager** - The project manager receives by the user information on the project to be run, and the relevant variables and observables, listed below:

1. Grid dimensions

2. Simulation length

3. Nozzle skimmer orientation (parallel or perpendicular)

4. Base gas pressure and density

5. High pressure gas density

6. Nozzle width

7. Skimmer geometry: α ,β, SD, SW, Dist.

8. Observables to be analyzed.

Having received this information, the **project manager** checks first if there are no other simulation plans already pending, by verifying the existence of the *temporary update*, then, if *temporary update* is not existing, the file *project-status* where information on the variables already simulated for the chosen project are stored, and verifies which of the chosen variables and/or observables still has to be simulated. It then creates a file *temporary-update*, in which the new simulation plan is detailed, together with file name and all the remaining data, and also passes this same information to the **geometry writer**. In addition, should the project be a new one, it will ask the user to confirm it, and if confirmed, will create a new directory to store the relevant files.

b) **Geometry writer** - this program creates a set of *.fld files which can be read by GDT and contain all the relevant information to start a simulation by simply running it on GDT. It saves the *.fld files in an appropriate directory.

c) **Reader manager** - the reader manager is run only after all the data from GDT have been saved in the appropriate directory. Then, the **reader manager** accesses *temporary-update* to find out which files to read and counts them. It then creates a *status* counter to keep count of the files already processed. The file names is then passed to the **data reader**, together with the relevant observables, allowing the **data reader** to store only the needed information.

d) **Data reader** - This program reads from mass memory the files passed by the **reader manager**, recording into the RAM the information therewith contained and relevant to the chosen observables. This information is then passed over to the **analyzer kern**.

e) **Analyzer kern** - uses the data stored in the RAM by the data reader and analyzes it to extract information on the observables specified. It then passes the calculated observables to the **writer manager**.

f) **Writer manager** -passes the observables given by the **analyzer kern** to the **writer** for addition to the *database*, it then checks the *status* counter and goes back to the **reader manager** if some more files need to be read; otherwise, it runs the **update manager**.

g) **Update manager** - The update manager reads the *temporary update* and uses the information there to update the *project status*, after which it deletes the *temporary update*. It then runs the **xls writer**.

h) **Xls writer** - It converts the *database* into a user friendly excel prompt file.

i) *Project status* - Contained in the file "Project Status.dat". It is also used as the Database. It is already existing as a blank file when the GDT-Analyzer is launched for the first time, it is then read by the **Project Manager** to compile the list of the temporary files avoiding repetitions. It is updated by the **Update Manager** and read by the xls writer to create the excel prompt. Its format is such: > $\#_{file}$ a Value$_a$b Value$_b$ v Value$_v$ A Value$_{A1}$ Value$_{A5}$ F Value$_{F5}$. The $\#_{file}$, and small letter values are equivalent to the Temporary Update ones. Then the capital letters value are: Accuracy for the 5 different values of cutting percentage, separated by a space (A); Resolution (B); Confinement (C); Screen Height (D); Screen overall depth (E); flag for the splitting of the screen height (F); flag for the splitting of the screen depth (G).

j) *Temporary Update* - The temporary update file is contained in "Temporary Update.dat". It is created by the **Project Manager**, subsequently read by the **Reader Manager** to find out the total number of files to be read and finally read one last time by **Update Manager** to update the *Project Status*, linking each file name to the relevant variables. **Update Manager** then deletes this file to clear the way for a second set of simulations. Its format is such: > $\#_{file}$ a Value$_a$ b Value$_b$ v Value$_v$ < $\#_{temp.file}$. The $\#_{file}$ refers to the file identification number in the complete scheme of the project status, whilst the $\#_{temp.file}$ refers just to the file identification number in the particular set of simulations

(which could just be an update of the larger project). The parameters a to v refer respectively to: Nozzle-skimmer orientation (0 for perpendicular, 1 for parallel) (a); base pressure (b); base density (c); high pressure gas pressure (d); high pressure gas density (e); nozzle width (f); angle (g); angle (h); skimmer depth (i); skimmer width (j); nozzle-skimmer distance (k); domain width (l); domain height (m); domain depth (n); simulation step count (o); mesh size in meters (p); cutting percentage on screen height value 1 to 5 (q,r,s,t,u); cutting percentage on screen depth value (v).

k) *Geometry files project .fld* - These are the files to be read by GDT in text format.

l *Database* - It is roughly the same as *Project status*, only it has the actual values of the observables in it.

Appendix D

Mechanical design details

D.1 Interaction chamber

The interaction chamber main body was designed by the author, as is the case for the other mechanical parts of the setup, and purchased from VGScienta, completed of Helium firing and leak testing to 10^{-10} mbar·l·s^{-1}. The whole chamber weights just over 50 Kg, has a flange to flange dimension of 406 mm and the central sphere to which the flanges are welded has an inner diameter of 304 mm. The final version of the technical drawing is shown in Fig. D.1

Of the 6 DN200 ports, the top one (port 5) is connected to the detector flange; the bottom one (port 6) houses a DN160 flanged 700 l/s TMP; the front and back (port 1 and 3) ones are connected respectively to the differential pumping and the dumping section, and the side ones (port 2 and 4) are connected to the electron gun and a DN100 phosphor coated viewport to image the electron beam directly. Port 13 has a clear line of sight to the interaction point through the detector electrodes, and houses a longitudinal 15 cm range manipulator holding a small 3 cm diameter phosphor screen that can be positioned in the centre of the interaction chamber to image the electron beam at the point of interaction, thus allowing direct beam imaging and focusing at the interaction point. It must be noted that no clear viewport can be installed which has a clear line of sight to this screen; hence it is observed through a mirror and a viewport in the dumping section, as described later. Port 10 holds a residual gas analyzer, whilst the remaining 2 DN70 ports are blanked and kept for use with additional sensors and connections.

Figure D.1: Technical drawing of the vacuum vessel used for the interaction chamber.

One DN40 port is used for installing the precision leak valve which allows flooding the chamber with a controlled N_2 pressure in the range $1 \cdot 10^{-9}$ to $1 \cdot 10^{-6}$ mbar. The remaining two DN40 ports hold both a high and low pressure sensor (Pirani and hot cathode).

D.2   Holding stand

The whole experimental stand is rested upon a custom designed holding stand, able to supply the needed stability and flexibility to accommodate the experimental needs of a test stand, amongst which the mechanical stability to prevent springing leaks in the vacuum system due to strains in the sealing regions, and the flexibility to accommodate the setup in several different configurations for different tests.

A CAD rendered image of the holding stand is Fig. D.2.

The design of the holding stand for supporting the experimental setup is of importance insofar as the setup prepared in this work is a test stand, and as such needed to be changed and modified often, thus requiring flexibility in the supporting stand, as well
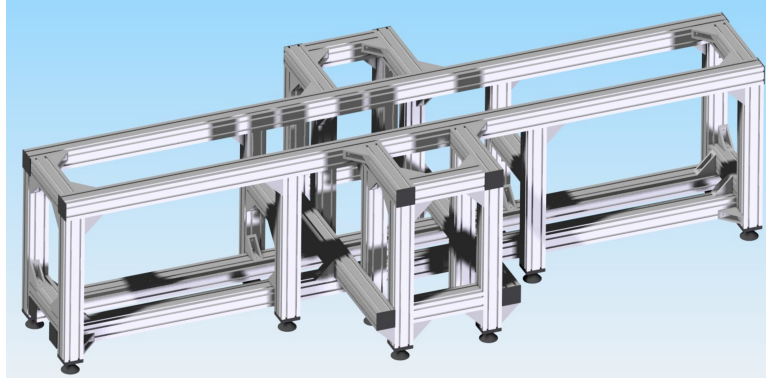
Figure D.2: CAD rendered image of the holding stand used for supporting the experimental test stand.

as sufficient stability to hold the considerable weight of the vacuum chambers (>500kg) without introducing any distortion which could potentially cause leaks or compromise the vacuum welds. The complete design is described in more details in this section.

The holding stand has to comply with the following specifications:

1. Has to accommodate all vacuum vessels and provide flexibility to remove/include other elements which might be needed as the experiment progresses.

2. Provide enough space for the air-cooled turbomolecular pumps to be set under the chambers.

3. It should be immediately adjustable to hold the chamber and gas jet stand in the storage ring where it will be used.

4. Be easily movable, demountable and modifiable for use with different setups.

5. Preferably do not require any machining.

6. Allow for alignment with the horizontal.

7. Be designed to provide high stability even when loaded with the full weight of the setup.

8. Allow fixing the elements in place longitudinally, so as to avoid the chambers being pulled together at the bellow joints when pumped down under the influence of atmospheric pressure.

D.2.1 Design study

The requirements 1, 2 and 3 listed above can be met with proper design, as shown later in this paragraph. The flexibility required by point 4 is obtained by making use, instead of a custom stand, welded together, of a series of modular aluminum profiles which can be fastened together with bolts and (see 5) does not require any machining which is not directly supplied by the company (namely tapping the profiles ends). Furthermore, alignment with the horizontal can be achieved by means of adjustable feet also supplied as accessories by the profiles company. Finally, point 8 can be guaranteed by using aluminum profiles with grooves on their sides: these provide bracing for suitable fasteners which secure each component longitudinally on the aluminum profiles. Having fixed these points, the easiest design, optimizing the trade-off between stability, cost-effectiveness and construction ease, is shown in the Fig. D.3. The holding system
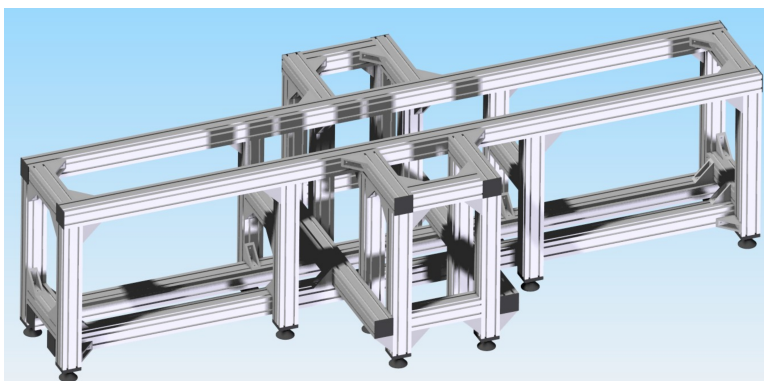
Figure D.3: CAD rendered image of the holding stand used for supporting the experimental test stand.

for the experimental chamber has been realized with aluminum profiles commonly used for frames and construction. The profiles themselves and all the needed accessories are provided by ITEM Ltd. The profiles are cast aluminum beams shaped to have grooves on all sides, where connections with other profiles can be made. In order to make a selection between all the possibilities, it is necessary to estimate the mechanical stress to be sustained by the frame. Two profiles have been chosen for the construction of the holding system, and their cross section is shown in Fig. D.4. The smaller one, Profile 8, 40x40, is used for holding the outermost pieces, while the larger one, Profile 8, 80x80, is used for the heavy duty applications.
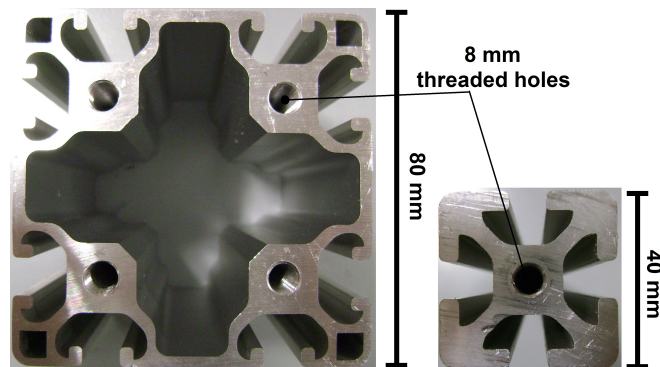
Figure D.4: Cross section of the cast aluminium profiles used for the realization of the holding stand.

Any weight applied longitudinally to the profile is easily bearable from the structure (since a quick calculation shows that even the cheapest 80x80 profile can support longitudinally a weight of more than 30 tons). As for the deflection caused by transversal loads, the most loaded part of the structure (the long 3 m longitudinal profiles) would be able to bear without breaking a weight applied on the center of the stand (where ideally the experimental chamber would stand) of 3.5 tons;

whilst the maximum weight compatible with a 1mm deflection would be 600 Kg. The expected load of the whole chamber in the middle section does not exceed the 500 kg.

D.2.2 Mechanical stress calculation

The bending and stresses of the various profiles can be calculated resorting to the following formulas from classical mechanics, rigid-body physics. The formulas are evaluated in 3 particular cases, useful in this work, and depicted in Fig. D.5:
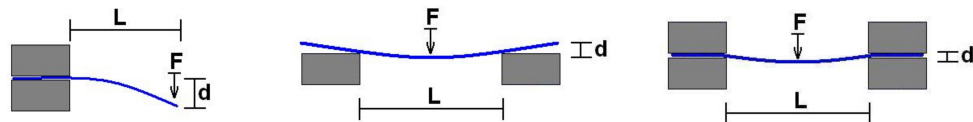
Figure D.5: 3 particular cases of possible deflections corresponding to 3 different ways of supporting the beams.

Where L indicates the length of the profile, shown in blue; F the force applied and

d the deflection. The relevant parameter is the modulus of elasticity E, and the second moment of inertia (or area moment of inertia) I, to be distinguished from the moment of inertia used to calculate the angular inertia. Both numbers can be computed by the material and shape, but are also given by the manufacturer. For completeness, the formula to calculate the second moment of inertia is reported. Given a plane intersecting the beam normal to its axis, being A the region of that plane intersected by the beam and γ a straight line in the plane, then the second moment of inertia of the region A about the line γ is given by the integral:

$$I_\gamma \; = \; \int_A n^2 dA \tag{D.1}$$

with n being the perpendicular distance from the element dA to the line γ. For the three configurations in Fig. D.5, from left to right, respectively:

$$d \; = \; \frac{F \cdot L^3}{3 \cdot E \cdot I \cdot 10^4} \tag{D.2}$$

$$d \; = \; \frac{F \cdot L^3}{48 \cdot E \cdot I \cdot 10^4} \tag{D.3}$$

$$d \; = \; \frac{F \cdot L^3}{192 \cdot E \cdot I \cdot 10^4} \tag{D.4}$$

As it can be seen from the equations, the more one moves right in the configurations, the more stable they become. The moment of inertia for each profile type is provided by the manufacturer, and so is the modulus of elasticity. Using eqn. (D.3) with the values provided, it has been calculated that, with standard profiles, for a load of 500Kg, a distance shorter than 120 cm should be left between each supporting post for the structure to undergo a maximum deflection of 1mm. Hence, 4 sets of supporting posts have been employed, as shown in Fig. D.3, at 1 m distance from each other. Checks for yielding strength were also performed, and all profiles are operated by design way below their yielding strength, so no issues on durability appear.

D.3 Vacuum accessories

D.4 Vacuum gauges

The choice of vacuum gauges depends strongly on the pressure to be measured. For very low pressures (down to 10^{-10} mbar) hot and cold cathode gauges can be considered. In

case of the hot cathode case (also called the *Bayard Alpert gauge*), a heated filament is used as a source of electrons, which are accelerated through a potential difference. In their way from the filament to the anode, the electrons hit and ionize the molecules of the gas; the ions formed move towards the cathode, creating a current proportional to the number of ions, in turn dependent on the pressure of the gas.

The other type of ionization gauge is the cold cathode one: the principle of operation is the same, except that the electrons are created via a high voltage discharge. In order to increase the path of the electrons through the gas, the cold cathode gauges known as Penning gauges, use an axial symmetric magnetic field to force the electron on a helical path. Because of this presence of the magnetic field, such gauges are not suitable to the experiment in this work, as the magnetic field would have a non negligible impact on the trajectories of the electrons used to probe the screen.

It is worth noting that ionization gauges have to be calibrated due to the problem of their composition dependency: indeed the number of atoms ionized will depend not only on the density of the gas, but also on its composition. For this reason it is advisable to use a mass spectrometer in conjunction with the gauge for careful calibration.

For higher pressures (atmosphere down to 10^{-4} mbar) a Pirani gauge can be used. It is composed of a metallic wire (usually platinum) through which a current is made to flow and measured. As the conductivity of metals is dependent on temperature, and temperature in a heated filament in turn depends on the dissipation through conduction (in particular through collision with gas molecules) it is possible to induce the pressure around the filament by measuring the current and hence the conductivity.

Another class of commercially available gauges are the so called wide range gauges: this gauges incorporate both a Pirani gauge and a hot cathode ionization gauge. These devices can be used from atmospheric pressure down to UHV, and result useful in application in which the vacuum is brought down and needs to be measured from the very beginning of the pumping up to the UHV level. In such cases, a straight ionization gauge cannot be used as it would be destroyed when operated at high pressures, whilst a Pirani would give no useful response below 10^{-4} mbar.

Another important point is which flange to use with these gauges. There are two main types of commercially available flanges, namely CF and KF. The KF flanges use rubber o-rings, suitable for insulation of pressures higher than 10^{-7} mbar, whilst the CF flanges use a copper seal: when the flange is screwed in place, a knife edge present

on it bites into the copper seal, digging into it. This creates a strong insulation able to resist much lower vacuum. The drawback is the need to use a different seal every time the chamber is reopened. Both types of flanges have been used in this work, on sections of the setup requiring different vacuum levels.

D.4.1   Feedthroughs

In the main chamber, the detector (whose design description is postponed to Chp. 6), needs power feeds. In particular the following elements need to be biased:

1. Extraction system electrodes (8 main electrodes + 1 mounting disk)

2. Detector meshes (2 different meshes)

3. MCP stack (3 connections: anode, voltage input, voltage output).

This adds up to 13 electrical feedthroughs, totaling 26 as each one of them is to be doubled. The doubling of the feedthroughs is chosen to be able to check that the connection is still active from outside the chamber without breaking vacuum. Some additional feedthroughs are added in case further connections have to be made (for example to increase the electrodes' number). Also, standard Safe High Voltage (SHV) feedthroughs only work up to 5 kV, therefore 2 special SHV feedthroughs rated 10kV are inserted for higher biasing of the MCP meshes.

Moreover, SHV standard feedthroughs have the problem of having a nickel pin, which is highly magnetic, and has been custom ordered to be manufactured out of non magnetic stainless steel SS316LN.

All the needed feedthroughs are placed on the top flange, so that the whole system is removable without having to disconnect pins in remote locations. An image of the top flange, with holes where feedthroughs have been welded is shown in Fig. D.6.

D.4.2   Viewports

The gas screen test stand requires 2 DN100 viewports: one to be placed opposite the electron gun and covered with phosphor to image the electron beam directly, the second to be placed behind the phosphor screen in the detector and looked at with a second CCD camera. A third DN70 viewport is needed in the dumping section to image the
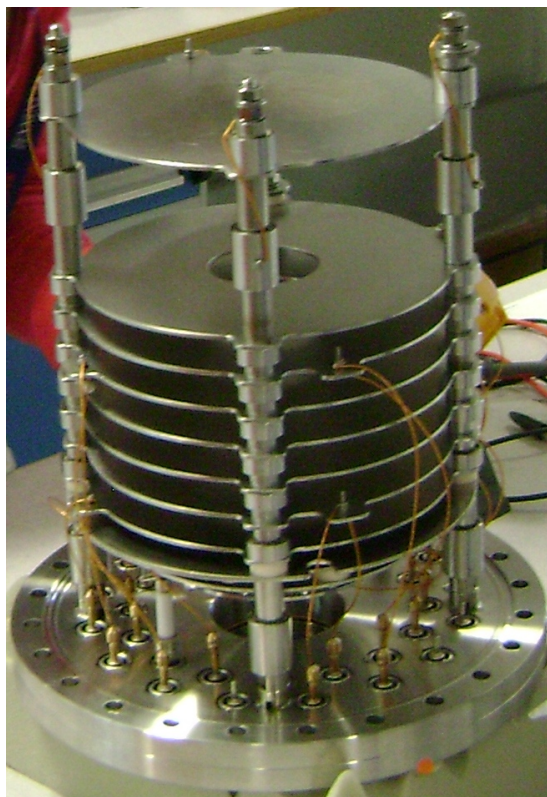
Figure D.6: Top flange of the interaction chamber, with the detector and extraction system mounted in place.

retractable phosphor screen when positioned in the middle of the interaction chamber. The problem arises though with standard viewports as the interface between stainless steel and glass (usually silica) is made of Kovar, which is a Nickel based alloy, and therefore (due to the ferromagneticity of Nickel), strongly magnetic. For the same reason, for example, when operating a reaction microscope, standard feedthroughs are not used, due to the nickel pins that are used. Optional viewports might be used with Kovar substituted by Titanium, with a considerable rise in price. Therefore, no viewport with Titanium skirts has been installed, leaving this step for future application of the monitor.

D.5 Pulsed jet valve and control electronics

The operation of a pulsed jet, as opposed to a continuous one, is interesting for several reasons. Firstly, if the gate time in which the valve is opened is short enough compared to the time needed by the injected gas to fill the nozzle chamber and reach equilibrium in it, pulsing the jet allows relaxing the needs for high pumping speeds. Indeed, high pressure ratios are obtained in the first moments of injection, as the gas injected through the nozzle and skimmed away by the first skimmer flows in the locally lower pressure regions of the chamber which has been previously pumped. The time scale of this geometric pumping process can be estimated by considering the average velocity of an injected gas atom and the typical dimension of the chamber. Indeed, at the pressure at which the nozzle chamber will be kept, of about $10^{-2} \div 10^{-3}$ mbar, the mean free path of N_2 at room temperature, calculated from (A.4) is of the order of 5 cm, therefore on the typical length scale of $10 \div 20$ cm, only a few collisions are likely to occur, and a first estimate of the time taken for the mass injected at the nozzle to reach the pump can be done using the molecular average speed. For room temperature gases, the average speed can be estimated from the Maxwell-Boltzmann velocity distribution. The maximum value (i.e. the mode) of the velocity distribution function expresses the most probable speed that any molecule is likely to have, and can be expressed as:

$$v_p = \sqrt{\frac{2RT}{M}} \tag{D.5}$$

where M is the molar mass of the gas species. In case of N_2, v_p equates to about 422 m/s. For a vacuum chamber of typical dimension 20 cm, the equilibrium can be

estimated to be reached in milliseconds.

The second element that comes into the design of the valve is the rate of change of the pressure in the chamber. Indeed, if the jet is cut off by the valve soon enough, the final pressure in the chamber can be limited to values compatible with the proper expansion of the jet, happening for high enough pressure ratios. To investigate this behavior it is necessary to use the results about the time evolution of the chamber pressure derived in section 4.2. Of relevance to the design of the valve is in particular Fig. 4.11, showing that even in the case of maximum, i.e. nominal, pumping speed, rise times in excess of 20 ms are obtained. This gives an idea of the time scale on which the pulsing valve should be operated.

The valve used in this work is a fast switching poppet valve commercialized by Festo, and features 2 ms response time: it is a 3 way valve which switches position when 230V AC is supplied. The valve is subsequently able to switch again in 2ms when the input tension is cut off. The repetition frequency, due to overheating issues, is limited to 150 Hz. Poppet valves with response times as fast as $100\mu s$ are also available, but they are very expensive custom products, which, given the typical rise times of the system under consideration, are not needed.

The valve connects the nozzle to either the high pressure gas cylinder or a roughing line which evacuates the nozzle tube when the gas cylinder is cut off, hence preventing further flow in the vacuum chamber. Optimal operation of this valve is obtained through dedicated control electronics that allows the user to select both a gate time and a delay. The gate time specifies the time interval in which the gas cylinder will be connected to the nozzle, and the delay the time interval between two successive pulses.

An electronic board to implement these features has been designed in the course of this work, formatted for printing by means of the EAGLE 5.0 CAD software, printed by a fast prototyping PCB milling machine and manually soldered. It relies on a high voltage AC relay to deliver the control signal from a microcontroller to the valve, opening the connection to the mains. The controller board allows switching between manual and remote operation with a dedicated toggle switch. In manual operation, the valve can be opened by pressing and keeping pressed a push-button. In remote operation, a 10 way piano switch is used to select the gate and delay times. 5 channels with weights 1,2,4,8 and 16 are used for each time, allowing changing the gate time in increments of 1 ms from 1 to 32 ms and the delay in increments of 0.5 s from 0.5 to

16 s. Of course it should be kept in mind that gate times shorter than 2 ms are not sufficiently long to have the valve fully open before it starts closing again. A second push-button allows to instruct the microcontroller to update the time settings after they have been set on the piano switch, and a green LED blinks for 3 seconds when the changes are implemented. A red LED lights up when the valve is opened, in both operation modes. These features are obtained by the schematics of the board shown in Fig. D.7 in the EAGLE format.
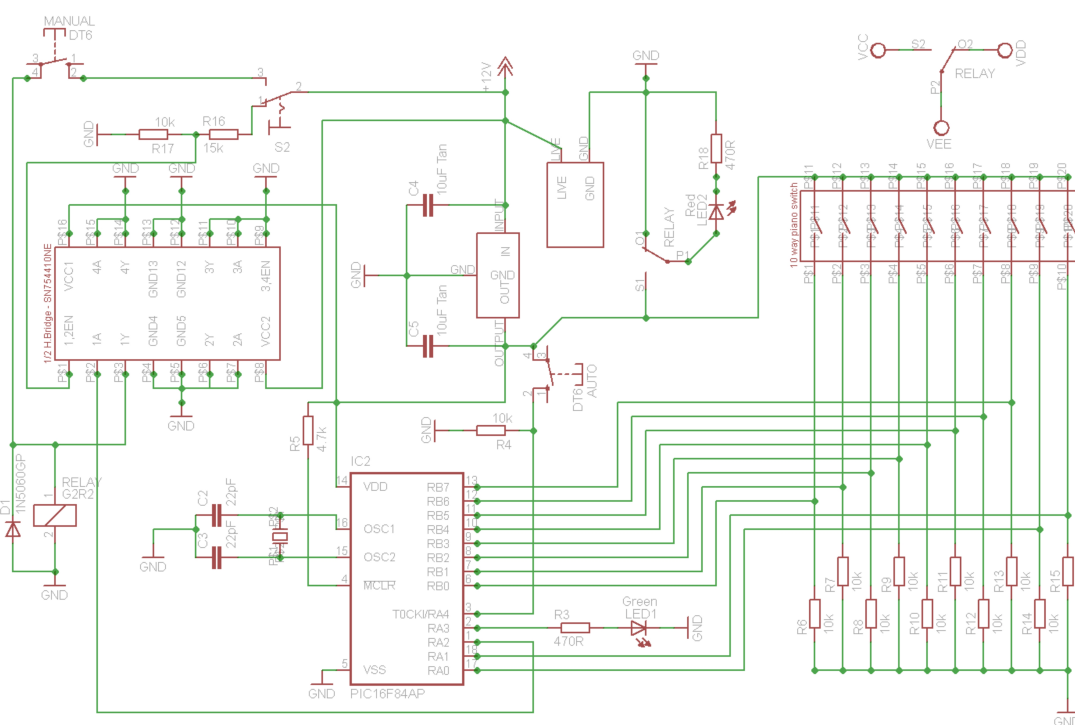
Figure D.7: Schematics of the valve control board formatted by EAGLE 5.0.

Electronic design   With reference to Fig. D.7, the 12V DC supply is fed to a voltage regulator coupled with two tantalum capacitors for preventing supply oscillations from affecting the operation of the microcontroller. This regulated supply provides voltage to the microcontroller, the H-bridge IC used to control the relay, and the 10 way piano switch. Each of the switches on the piano switch is connected to an input pin of the microcontroller through a pull-up resistor, to provide the signal to the microcontroller without saturating its input current tolerance. A toggle switch connected directly to the

12V supply allows switching between applying the tension to the pushbutton *manual* for manual operation of the relay and enabling the use of the H bridge which amplifies and delivers the signal of the microcontroller to the relay.

It is noted the use of a fast Zener diode in parallel to the relay control circuit, to prevent the voltages induced by the changing current in the relay coil from propagating in the system causing instabilities. The green LED is also connected directly to the microcontroller through a current limiting resistor, whilst the red LED is connected directly to the relay second connection, ensuring it follows the behavior of the connection to the valve. The microcontroller itself, a PIC18F84AP used at 4Mhz clock frequency, is mounted on a fast release solderless DIL sockets allowing it to be easily removed and replaced, so that the firmware program can be modified and the ranges for the delay and gate time changed.

The physical board layout, allowing the control board to be housed in a 3"x5" die cast aluminum enclosure, has also been drawn with EAGLE 5.0, and features 2 printing layers (front and back of the board): it is shown in Fig. D.8.
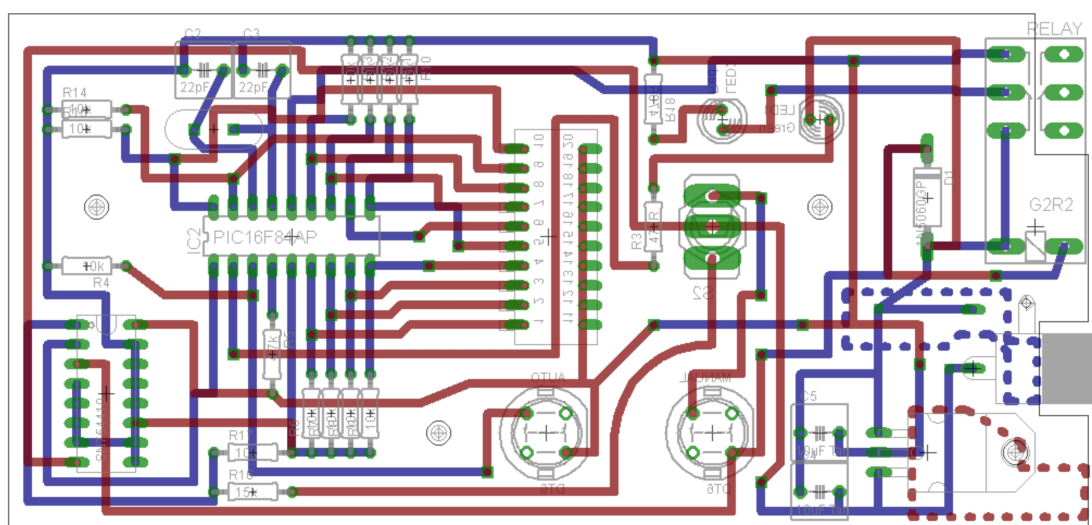
Figure D.8: Board layout of the valve control board produced with EAGLE 5.0. Red and blue traces represent respectively the front and back of the board. Green spots represent electrical pads for soldering, and small green squares vias used for transmitting a signal from one side of the board to the other. Dashed lines represent larger area of copper used to minimize signal noise and improve grounding connections. For ease of soldering, all elements have connections only on one side of the board.

The use of two printing layers is essential to permit crossing between electrical

traces: no crossing of different traces is of course permitted on the same layer. Fig. D.9 is a picture of the actual control board embedded in the custom machined aluminum enclosure.
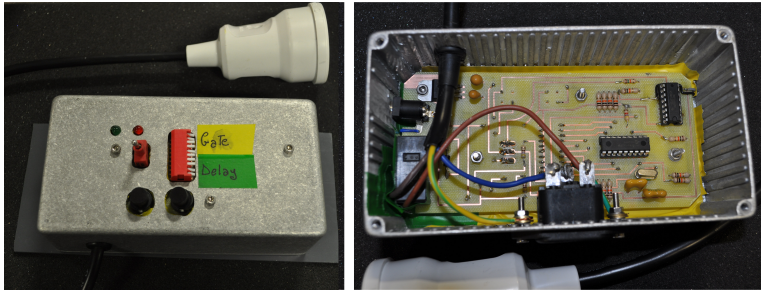
Figure D.9: Valve control board after printing, soldering and installation in aluminum enclosure.

Appendix E

Further mechanical components

E.1 Skimmers

Two different types of skimmers have been employed in the course of this work: circular and rectangular cross section skimmers.

The circular skimmers have been purchased from Beam Dynamics, Inc, Florida, USA. They are manufactured out of copper, and have been specified with double wall thickness (100 ÷ 160 μm) to withstand the large pressure differential and for ease of handling. These skimmers have been chosen as they are commonly used in gas-jet generation experiments (see e.g. [9]), and thus provide a straightforward opportunity to re-create a typical gas-jet setup used in atomic physics experiments and have a system with which to compare the beam profile optimized gas-jet. In particular, the dimensions of the skimmers have been chosen to suit the experimental needs of the Ullrich group at the Max Planck Institute for Nuclear Physics, in Heidelberg, which has pioneered the use of gas-jet targets for atomic physics full differential cross sectional measurements, with the use of the Reaction Microscope recoil ion spectrometer.

The circular skimmers are named *model 7* where 7 is the nominal apex height, and have an orifice diameter of 0.18 ± 0.025 and 0.4 ± 0.025 mm, a height (tip to base) of respectively 6.6 and 6.2 mm and a base diameter of 12.7 mm. The angle at the tip is 25° internally and 30° externally, which becomes 75° at the base.

The rectangular skimmers are more difficult to manufacture, and could not be produced by Beam Dynamics. They were instead manufactured by direct metal laser sintering (DMLS), a laser induced additive layering process usable on different metals,

including stainless steel. The skimmers have been first constructed by additive layering by the *CRDM UK Prototyping & Tooling* and subsequently mechanically polished by *TJW Precision UK*. This process guarantees the possibility of very thin walls (100 μm) at the tip of the skimmer, comparable with the circular skimmers wall thickness, which could instead not be achieved with direct spark erosion based on electrical arcing. Indeed, first trials carried out with spark erosion resulted in the tip of the skimmer melting due to the insufficient wall thickness, as illustrated in Fig. E.1.
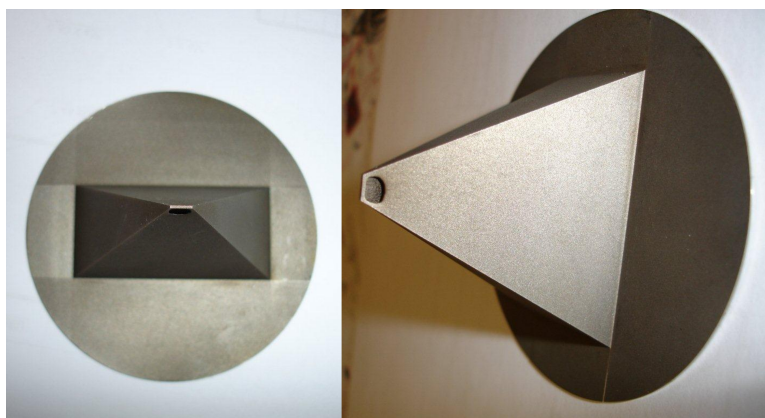
Figure E.1: Illustration of the first prototype of slit skimmer, manufactured through standard machining followed by direct spark erosion. The heat caused by the electrical arc proved to be excessive for the required wall thickness, leading to melting of the skimmer tip.

The rectangular slit skimmers, numerically treated in Chp. 3, are used to produce an extended gas screen, rather than a cylindrical cross section jet. Three of them have been manufactured, with different values of inner and outer angles. The dimensions are reported in table E.1:

Slit Width	Slit Height	Angle α (int/ext)	Angle β (int/ext)
4	0.4	25/60	10/60
4	0.4	25/60	5/55
4	0.4	35/84	10/60

Table E.1: Dimensions of the three rectangular skimmers manufactured. Each of them has a height brim to tip of 47 mm, a base diameter of 74.5 mm and a brim thickness of 2 mm.

The angles α and β of the first skimmer in table E.1 have been chosen on the basis of the optimization described in Chp. 3; the second and third skimmer have instead been chosen so that the influence of the angles α and β can be isolated, and the splitting phenomenon dependent on the temperature described in section 3.6.2 and 3.6.4 investigated.

The rectangular skimmers are higher than the circular skimmers (47 mm tip to brim as opposed to 6.6 mm): this is due to the need of minimizing the effect of the base plate backscattering molecules on the jet path, causing the jet to warm up [32]. However, the need for longer skimmers also brings about the need for a larger brim, therefore different holding systems have been designed for the two different kind of skimmers.

E.2   Additional mechanical components

In addition to the main components of the test stand treated in this chapter, the successful operation of the test setup requires the selection and use of suitable vacuum components and instrumentation, including vacuum gauges, feedthroughs and viewports. A detailed description of such vacuum accessories is presented in the Annex D.3.

Furthermore, in the frame of this work, a pulsed vacuum valve has been selected, and a custom designed electronic control board designed to allow investigation in the pulsed operation of the jet and corresponding reduced pumping requirements. A full discussion on the motivation for such investigation, the choice of the suitable valve and the design, inclusive of circuitry details, of the control board, is reported in Annex D.5.

Finally, a new mechanical design of the jet generation system was completed, to add extra functionalities to the setup described in the remainder of this chapter. The revised design allows to continuously change the longitudinal position of each collimating element, without breaking vacuum. This is achieved by means of movable pistons inside the vacuum chamber sealed with dynamic elastomer seals. Such increased functionality will allow, in future further studies, to extensively benchmark the analytical theory reported in Chp. 4.2 perform a detailed and systematic optimization and characterization study. Such setup has never been employed for characterization of free jets, and thus benefits of a strong element of originality.

E. FURTHER MECHANICAL COMPONENTS

The design, design calculations and drawings for this system as well have all be completed in the frame of this work and are reported in detail in Annex F.

Appendix F

Extended nozzle chamber design

The design discussed in Chp. 4 allows the operation of a supersonic gas jet in both the cylindrical and planar operation modes, since the skimmers and nozzle can be exchanged. However, the longitudinal position of each skimmer and slit aperture is fixed and cannot be varied. This is acceptable for initial testing and would be the choice for the final optimized monitor. However, it would be beneficial to be able to modify continuously the longitudinal position of the collimating elements without breaking vacuum, in order to be able to perform a detailed and systematic optimization and characterization study. Such setup has never been employed for characterization of free jets, and thus benefits of a strong element of originality.

The mechanical design of this system has been completed, the whole setup has already been manufactured, and will form the basis of future studies. This section describes in detail the design of this nozzle chamber, which allows for the following additional degrees of freedom:

- Adjustable distance between the first and second skimmer (between about 20 and 100 mm).

- Differential pumping after every skimming/collimation section.

- Possibility to insert a collimation slit after the double skimming section

- Adjustable distance between the second skimmer and the collimation slit (between about 100 and 500 mm).

- Full axial and planar alignment between the moving elements.

- Automation of the movable parts by means of precision stepper motors.

F.1 Overview

The full assembly of the extended nozzle chamber, shown in Fig. F.1, is composed of 4 main sub-assemblies: shown in green is the first expansion chamber, where the nozzle and the first skimmer are housed; following on its right, in red, is the second expansion chamber, which houses the second skimmer; and finally, in blue, the longer section of the collimating slit chamber. Also, on the leftmost side, behind the first expansion chamber, is shown in gray the fourth subassembly: a custom flange structure that allows the introduction in vacuum of all the moving shafts that transmit the motion to the movable parts.
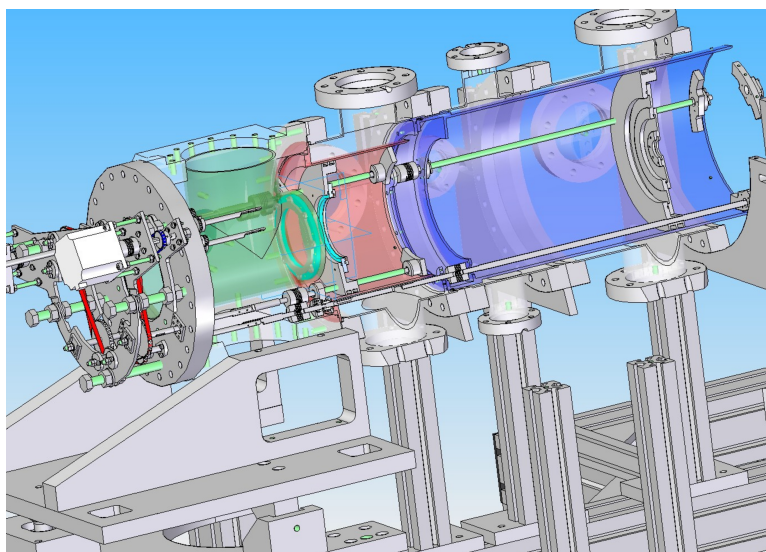
Figure F.1: Overall cut view of the extended nozzle chamber, showing the three different stages of expansion (marked in different colors, green, red and blue, for the first and second skimmer and the collimation slits respectively) and the back-flange assembly in grey. The ports for differential pumping can be seen (two DN70 flanges on top of the red and blue regions and two DN100 flange respectively over and under the green region).

The nozzle is mounted on the same extended tube with 3 degrees of freedom which holds the nozzle in the standard nozzle chamber. The distance from the first to the second skimmer can be varied by moving the longitudinal position of the second skimmer, in the red expansion chamber. Similarly, distance between the second skimmer and the

collimating slit, or third skimmer, can be varied by longitudinally moving the slit in its blue chamber. Movement of the slit and second skimmer is independent and is provided through 6 rotating leadscrew shafts, 3 for each moving plane, which can be motioned from the outside, through the back-flange assembly. In the following sub-sections the whole assembly is described in detail.

F.2   Back-flange assembly

The back-flange assembly is situated at the back of the system, upstream the nozzle tube, on the leftmost position in Fig. F.1. The assembly consists of a modified zero-length CF reducer flange going from DN200, the size of the nozzle chamber connection, to DN100, the size of the XYZ manipulator. The assembly is singled out from the rest of the chamber in Fig. F.2. The back-flange assembly houses the entry holes for the 6 shafts used to transmit the motion to the moving disks in the second and third expansion chamber, and the supports for the motors and gears needed. Each moving disk is motioned by 3 shafts in a 3-fold symmetry, leaving the center of the moving disk free for the jet. For this motioning 3 leadscrews for each disk are used, which move simultaneously by the same amount. This is obviously a more expensive and complex solution both to mount, design and operate, as opposed to having only 1 motioned leadscrew and 2 round shafts used just to have the disk slide on them. This design choice is justified by solving the static problem of the design including only one leadscrew. A diagram on the forces acting on each disk is presented in Fig. F.3.

The driving force of the system is the force applied by the moving leadscrew, F in Fig. F.3. This force creates a torque on the disk, which tends to rotate around its center of mass. This in turn causes the holes in which the shafts are housed to slightly misalign, hence points of contact arise at the two ends of the holes, as shown in the figure. In each of these points of contact two forces are located: the reaction force N and the friction force proportional to N through the coefficient of friction η. Due to the 3-fold geometry of the disk, the lever arm of the leadscrew hole where F is applied is twice the lever arm of the remaining two holes, therefore the torque of the forces in each remaining hole will be halved. However, also the misalignment angle of the remaining holes will be half the one of the leadscrew, so as a first approximation, assuming N to be an elastic force directly proportional on the displacement (in this case proportional
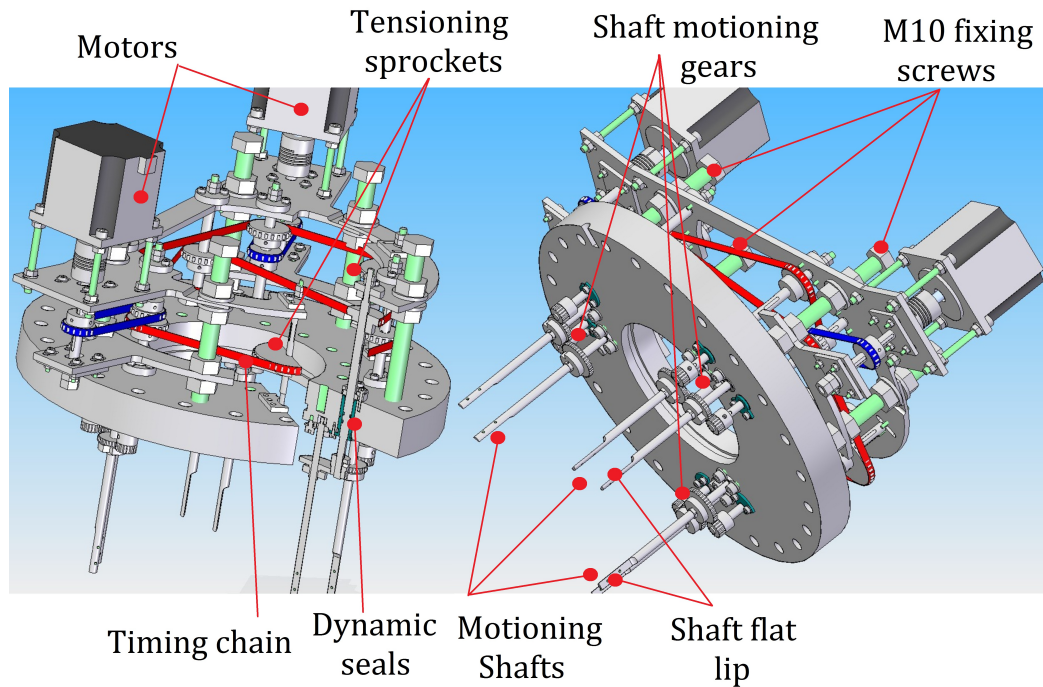
Figure F.2: Two separate views of the back-flange where the motors and the gears are located.
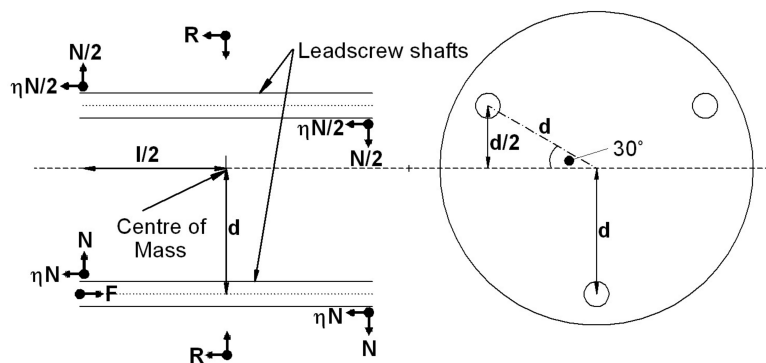
Figure F.3: Diagram of the forces acting on each moving disk, as seen from the front (on the right) and in cut-view cross section (left). The driving force of the leadscrew (F) induces a torsion of the disk around its center, causing the holes in which the shafts are housed to slightly misalign and press on the shafts (forces N), which keep their position due to the constraints at their ends. The shaft reaction creates also a friction force, perpendicular to N, indicated with ηN.

to the misalignment angle), the reaction force on the remaining holes will be half the reaction force on the leadscrew hole, as shown in the figure. Indicating with R the total force due to friction of the outer o-rings, the balance of linear forces and torques respectively can be written as shown in (F.1):

$$\begin{aligned} F &> R + 4\eta N \\ F \cdot d &= 2Nl \end{aligned}$$

(F.1)

Where no friction force appears in the torques balance as they all cancel out. Solving the system in (F.1) by substituting N, eqn. (F.2) is found:

$$d < l \left(1 - \tfrac{R}{F}\right) \tfrac{1}{2\eta}$$

(F.2)

Even in the best case in which a force F >> R is used, d still needs to satisfy $d < l/2\eta$. Even if lubricated, the coefficient of friction of stainless steel screw threads does not fall below 0.2. Therefore, l > d/2.5. For a radius of 70 mm (second expansion chamber) this equates to a hole depth of more than 28 mm, and more than 64 for the 160 mm radius of the third expansion chamber, making for a large, cumbersome construction which would increase the weight of the assembly and decrease the available travel range. Moreover, the design is not completely stable as the point of contact where the friction is applied varies as the thread rotates, possibly causing oscillations which can lead to the disk undergoing a phenomenon known in engineering as *crabbing*: i.e. tilting enough that friction increases, leading to more tilt, and possibly lead to the disk getting jammed. A design with 3 motion shafts would allow unjamming the the disk without braking vacuum, as force can be applied in 3 different places, ultimately providing a more reliable mechanism. Therefore, the solution with 3 leadscrews has been chosen for this work. To ensure joint rotation of the three shafts, a timing chain is used (shown in red in Fig. F.2) tensioned by sprockets and set to motion by a second chain linked to the motor shaft (shown in blue). The standard backslash effect amounts to about 10 degrees in the sprockets, for a maximum mismatch of less than 50 μm, widely compensated by the moving disk tolerances. The feedthroughs to air are dynamic o-ring seals, comprising of two o-rings between the shafts and the bushes and one o-ring for the static sealing of the bush against the flange. This double step sealing which includes the aluminum bush between is necessary to avoid cold welding between the steel components of the flange and the shafts.

The air side of the backflange also incorporates the holding system, fixed by means of 5 M10 screws, which holds the two motors in place and provides bracing for the shafts. On the vacuum side of the backflange is possible to see in Fig. F.2 that each shaft is not directly coupled with the outside, but motioned by a gear. This is necessary due to space restrictions, in order to have the shafts going around the first expansion chamber and into the second or third expansion chamber.

Finally, Fig. F.2 also shows that the shafts motioning the disks end in a flat lip with two threaded holes in it. This lip connects to the mating lip on the second part of the shaft, which goes as far as the disk to be moved. This connection is necessary as an alternative to a one piece shaft to allow assembly of the structure. The screws which hold the two lips together can be fixed through the ports in the outer chamber, shown in transparent white in Fig. F.1, housing the first expansion chamber.

F.3   First expansion chamber (green)

An extract from the assembly technical drawing of the first expansion chamber is shown in Fig. F.4, which also numbers the used parts and specifies their needed quantity: the number in the upper half of the circle markers identify each element part number, whilst the bottom half shows the quantity of items required. The first expansion chamber houses the first skimmer, which is clamped between two holding disks (parts 2 and 3) and sealed by means of o-rings. This assembly is then fixed to the main part (part 1), and sealed with a third o-ring. The port on top of the chamber, connected to the TMP, has an inner diameter of 100 mm, large in comparison with the dimensions of the chamber, to maximize the pumping efficiency on the skimmer tip. Both cylinders forming the chamber are sealed against the outer chamber and back-flange respectively by means of o-rings, hence their edges are tapered to prevent fracture during installation. The whole chamber has a volume of 2.4 liters.

F.4   Second expansion chamber (red)

A close-up 3D view of the second expansion chamber, shown in red, is presented in Fig. F.5. The skimmer (not shown) is clamped between the blue disk and the supporting disk. Like it is the case for the first expansion chamber, the skimmer is not clamped
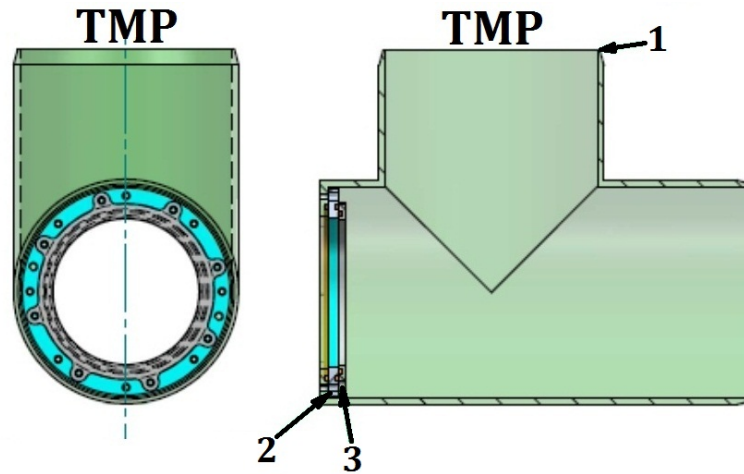
Figure F.4: Extract from the technical drawings of the first expansion chamber, showing the assembly view, and the three components involved.

directly to the moving disk to allow it to be removed and aligned without having to compromise the alignment of the moving disk, so that the two alignments can be done independently. O-rings present in these disks guarantee static vacuum sealing across the skimmer base. The cylinders with spiral pattern at the tips of the shafts are flexible shafts couplings produced by *RULAND*. They have a working angular tolerance of 5° and a linear tolerance once clamped of 1.3 mm, however, the depth range at which the shafts can be clamped in the coupling is of 10 mm.

The three shafts (only two shown, the third is in the cut-out region) which run outside the chamber are directed to the third expansion chamber, and there motion the slit disk. They are provided with a flat lip for assembly, equivalent to the one discussed in section F.2. The three shafts which run inside the chamber are held in place by the 2 end bearings subassemblies, which can be finely aligned by means of the tolerances left in the screw holes in a range of 2 mm. The fine alignment of the 6 subassemblies is instrumental to guarantee smooth operation of the sliding disk, and the procedure is described in more details in appendix G. There is no possibility of axial alignment in the cylinder housing the moving disk of the second expansion chamber: therefore the axis of translation of the second skimmer will define the axis of the whole system in alignment phase. The moving disk itself is sealed with two large cross section (5 mm diameter) o-rings, guaranteeing both large contact surface for better sealing and larger tolerance on motion. The second expansion chamber permits a range of movement of

the second skimmer of 90 mm, taking the second skimmer from 36 to 126 mm from the first one.

Sealing system   Supporting disks   Moving disk   Flat lip

Shaft couplings   Motioning shafts   Bearing subassemblies
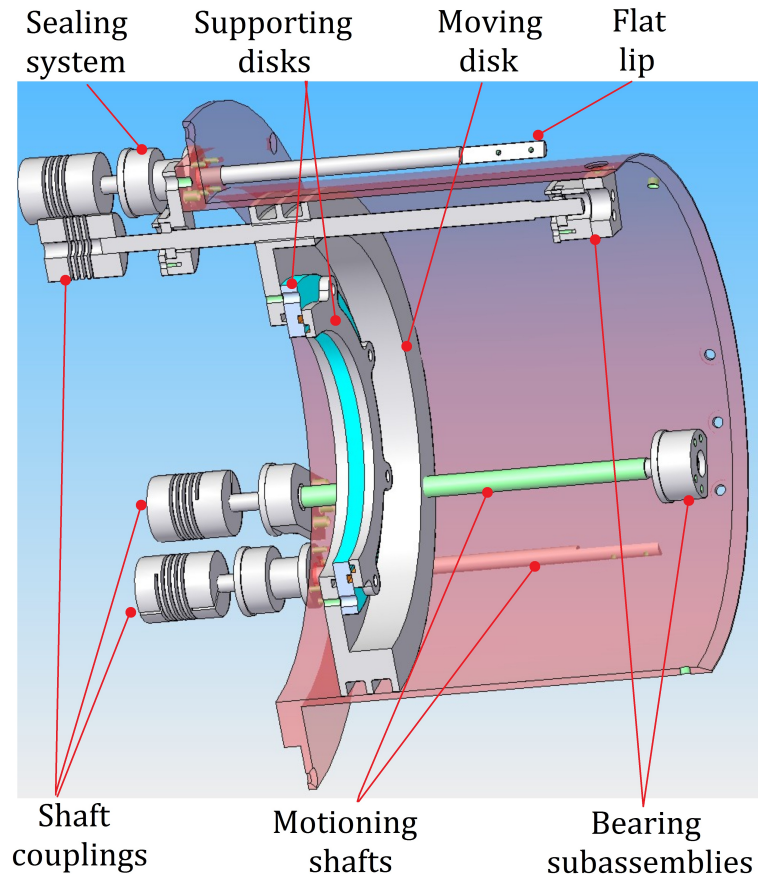
Figure F.5: Cut view of the second skimmer moving section. The moving disk is sealed by two large cross section o-rings, which allow for larger tolerances in the moving parts.

F.5   Third expansion chamber (blue)

The third expansion chamber is shown as a 3D model cut-out view in Fig. F.6. The configuration shown provides support for a slit disk, rather than a skimmer, hence the smaller inner diameter of the supporting disks (parts 12 and 13). The slit is clamped between two disks which can be adjusted independently from the main moving disk, so as to allow separate alignment. The moving disk itself, like it was the case for the second expansion chamber, is sealed by means of two large section o-rings (6 mm).

Also a mechanism of fine alignment of the shafts is made possible by a system of end bearings analogous to the one used in the second expansion chamber. These can be finely aligned by means of the tolerances left in the screw holes in a range of 2 mm.

The third expansion chamber permits a larger range of movement for the slit than the second does for the second skimmer, allowing the slit to travel a range of 305 mm taking the slit from 224 to 529 mm from the first skimmer. Differently from the second expansion chamber, screws placed at the end of the third expansion chamber and pushing against the outer vacuum chamber wall allow fine axial alignment of the cylinder in which the moving disk is translating. This allows aligning the translation axis of the third expansion chamber with the translation axis of the second expansion chamber, which is instead fixed.
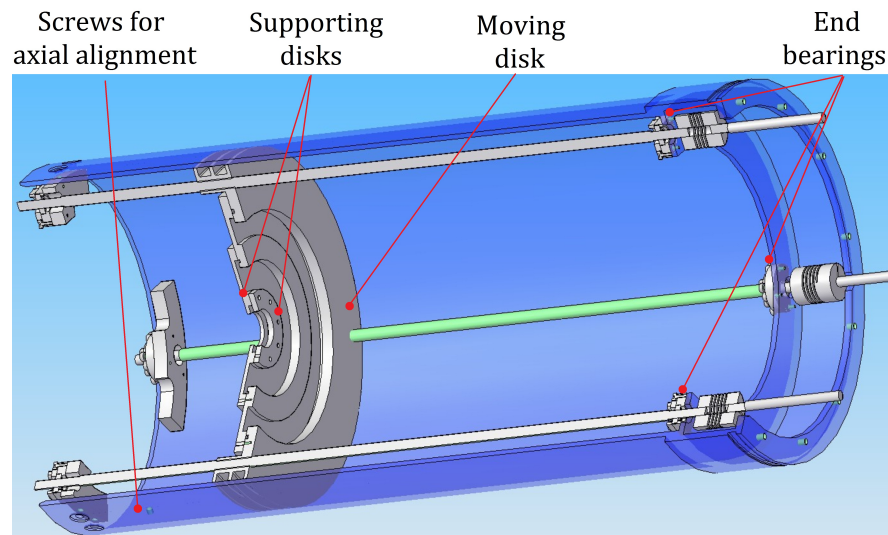
Figure F.6: Cut view of the collimation slit moving sector. The disk is sealed by two large cross section o-rings, similarly to the previous moving part. Furthermore the disk is arranged in such a way that it can be removed and the slit or skimmer exchanged without hindering the alignment of the system.

F. EXTENDED NOZZLE CHAMBER DESIGN

Appendix G

Alignment procedures for the extended nozzle chamber

Given the complexity of the extended nozzle chamber assembly, described in section F, and the number of degrees of freedom that need to be finely aligned, an alignment procedure needs to be studied already at the design phase, so as to allow the necessary modifications in the drawings and design. The degrees of freedom that need alignment are listed below:

- Nozzle: XYZ positioning

- First skimmer: XY positioning

- Second skimmer: XY positioning; smooth run in cylinder.

- Second skimmer cylinder: Z translation axis angular alignment with jet axis.

- Slit: XY positioning; smooth run in cylinder.

- Slit cylinder: Z translation axis angular alignment.

The first degree of freedom to be aligned is the smooth run in cylinder of the second expansion chamber, as it is fixed to the outer nozzle chamber and hence identifies the axis of the whole system. The alignment procedure is composed of the following steps:

- Fix slit shafts and bearings to cylinder.

- Attach leadscrew to shaft couplers and shaft, and insert in front bearings.

G. ALIGNMENT PROCEDURES FOR THE EXTENDED NOZZLE CHAMBER

- Fix cylinder on nozzle chamber.

- Fix alignment male shafts to motors.

- Fix moving disk and bearings to cylinder.

  - TEST - energize motors: make sure moving disk enters and smoothly runs in cylinder.

- Fix and tighten rear and front bearings to fix the smooth run.

  - TEST - energize motors: make sure moving disk still moves smoothly. Failure indicates that the leadscrews have to tilt along their movement: thus the piston chamber is not manufactured to specifications.
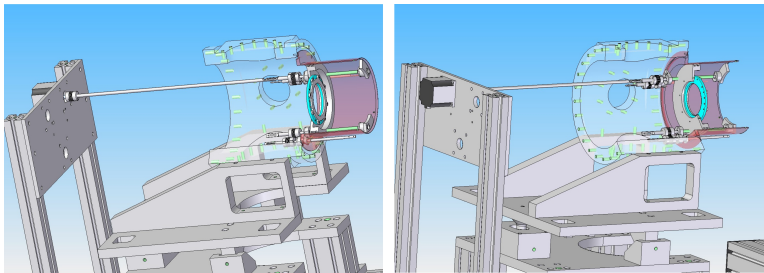
Figure G.1: CAD cut-out view of the first step of alignment, illustrating the alignment of the second skimmer moving disk within its cylinder. For clarity, only one motor is shown, of the three needed.

Secondly, having fixed the axis of the system by fixing the motion of the sliding disk, the smooth run of the third expansion chamber can be fixed, and its motion axis aligned with the system axis. To do this the steps to be followed are very similar to the ones used for the previous degree of freedom. The only difference is that the third expansion chamber is fixed loosely to the outer chamber, in order to allow a small (2°) angular play, which can then be fine tuned with the screws at the end of the chamber. Once the motion of the disk in the cylinder is aligned to the point of being smooth, the motors are set to continuous back and forward motion, and a laser is used, together with a small aperture in place of the slit, to fine align the whole third chamber cylinder to the axis of the system identified by the motion axis of the second expansion chamber. This procedure is illustrated in Fig. G.2.
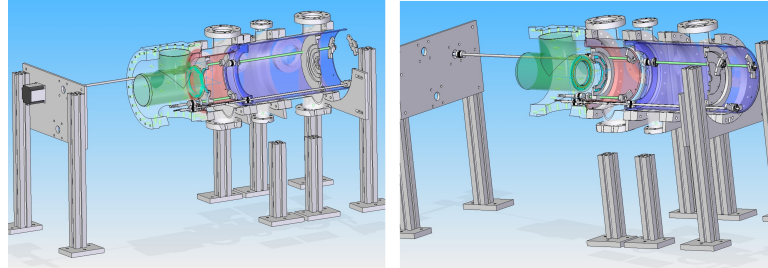
Figure G.2: CAD cut-out view of the second step of alignment, illustrating the alignment of the third skimmer moving disk within its cylinder, and of the cylinder with the system axis. For clarity, only one motor is shown, of the three needed. Notice how the supports for the motors used in the previous step need to be changed for this step as the shafts are in different positions.

In order to align the laser used in this step with the system axis, a dedicated laser alignment system, purchased from Thorlabs, is used. Alignment can be achieved by inserting the skimmer in the first moving disk, and motioning it back and forth, making sure that the laser can be seen through the skimmer aperture at all positions along the translation. This laser is then left in position, and identifies the system axis. Finally, the nozzle tube can be inserted, and positioned, through its own precision manipulators, so that the laser, which has not been moved, shines through it.

G. ALIGNMENT PROCEDURES FOR THE EXTENDED NOZZLE CHAMBER

Bibliography

[1] JOHN D. ANDERSON. *Modern Compressible Flow: With Historical Perspective*. McGraw-Hill Higher Education, 3 edition, June 2004. 1, 23, 186, 189, 194

[2] C. P. WELSCH AND J. ULLRICH. **FLAIR-a facility for low-energy antiproton and ion research**. *Hyperfine Interaction*, **172**:1–3, 2006. 1, 3

[3] H. KNUDSEN, U. MIKKELSEN, K. PALUDAN, K. KIRSEBOM, S. P. MLLER, E. UGGERHJ, J. SLEVIN, M. CHARLTON, AND E. MORENZONI. **Ionization of Atomic Hydrogen by 301000 keV Antiprotons**. *Physical Review Letters*, **74**(23):4627–4630, June 1995. 1

[4] P HVELPLUND, H KNUDSEN, U MIKKELSEN, E MORENZONI, S P MOLLER, E UGGERHOJ, AND T WORM. **Ionization of helium and molecular hydrogen by slow antiprotons**. *Journal of Physics B: Atomic, Molecular and Optical Physics*, **27**(5):925–934, March 1994. 119

[5] H. KNUDSEN AND J.F. READING. **Ionization of atoms by particle and antiparticle impact**. *Physics Reports*, **212**(34):107–222, March 1992. 1, 14, 15

[6] C. P WELSCH, M. GRIESER, A. DORN, R. MOSHAMMER, AND J. ULLRICH. **Exploring SubFemtosecond Correlated Dynamics with an Ultralow Energy Electrostatic Storage Ring**. *AIP Conference Proceedings*, **796**(1):266–271, October 2005. 1

[7] ASACUSA COLLABORATION. **CERN/SPSC 2005-001, SPSC-M-728**. Technical report, CERN, 2005. 2

[8] FLAIR COLLABORATION. **Technical Proposal for the Design, Construction, Commissioning and Operation of**. Technical report, 2005. 2

[9] R. DRNER, V. MERGEL, O. JAGUTZKI, L. SPIELBERGER, J. ULLRICH, R. MOSHAMMER, AND H. SCHMIDT-BCKING. **Cold Target Recoil Ion Momentum Spectroscopy: a momentum microscope to view atomic collision dynamics**. *Physics Reports*, **330**(2-3):95–192, June 2000. 2, 3, 19, 30, 68, 69, 119, 217

[10] A.I. PAPASH AND C.P. WELSCH. **Realization of nanosecond antiproton pulses in the ultra-low energy storage ring**. *Nuclear Instruments and Methods in Physics Research Section A: Accelerators, Spectrometers, Detectors and Associated Equipment*, **620**(23):128–141, August 2010. 3

[11] JANUSZ HARASIMOWICZ AND CARSTEN P. WELSCH. **Beam instrumentation for the future ultra-low energy electrostatic storage ring at FLAIR**. *Hyperfine Interactions*, **194**(1-3):177–181, August 2009. 4, 169

[12] T. HONMA, D. OHSAWA, T. IWASHIMA, H. Y. OGAWA, Y. SANO, E. TAKADA, AND S. YAMADA. **Design and performance of a non-destructive beam-profile monitor utilizing charge-division method at HIMAC**. *Nuclear Instruments and Methods in Physics Research Section A: Accelerators, Spectrometers, Detectors and Associated Equipment*, **490**(3):435–443, 2002. 4

[13] H. KOZIOL. **Beam Diagnostic for Accelerators**. In *Fifth General Accelerator Physics Course*, CERN Accelerator School, pages 565–599. 1994. 4

[14] P. FORCK. **Lecture Notes on Beam Instrumentation and Diagnostics**, 2003. 7, 8

[15] J. EGBERTS, F. ABBON, F. JEANNEAU, J. MARRONCLE, J.-F. MOLS, T. PAPAEVANGELOU, F. BECKER, P. FORCK, AND B. WALASEK-HOHNE. **Detailed Experimental Characterization of an Ionization Profile Monitor**. In *Proceedings of DIPAC2011*, pages 547–549, Hamburg, Germany, 2011. 7

[16] J. EGBERTS. **Detailed Experimental Characterization of an Ionization Profile Monitor**, 2011. 7

[17] M.A PLUM, E BRAVIN, J BOSSER, AND R MACCAFERRI. **N2 and Xe gas scintillation cross-section, spectrum, and lifetime measurements from 50 MeV to 25 GeV at the CERN PS and Booster**. *Nuclear Instruments and Methods in Physics Research Section A: Accelerators, Spectrometers, Detectors and Associated Equipment*, **492**(12):74–90, October 2002. 7

[18] P. FORCK AND A. BANK. **Residual Gas Fluorescence for Profile Measurements at the GSI UNILAC**. In *Proceedings of EPAC 2002*, pages 1885–1887, Paris, France, 2002. 8

[19] A. BANK AND P. FORCK. **Residual Gas Fluorescence for Profile Measurements at the GSI UNILAC**. In *Proceedings of DIPAC 2003*, pages 137–139, Mainz, Germany, 2003. 8

[20] P. FORCK. **Minimal Invasive Beam Profile Monitors for High Intense Hadron Beams**. In *Proceedings of IPAC'10*, pages 1261–1265, Kyoto, Japan, 2010. 8

[21] C. M. MATEO, G. ADROIT, G. FERRAND, R. GOBIN, S. NYCKEES, Y. SAUCE, F. SENEE', AND O. TUSKE. **Non-Interceptive Profile Measurements using an Optical-based Tomography Technique**. In *Proceedings of DIPAC2011*, pages 437–439, Hamburg, Germany, 2011.

[22] A. VARIOLA, R. JUNG, AND G. FERIOLI. **Characterization of a nondestructive beam profile monitor using luminescent emission**. *Physical Review Special Topics - Accelerators and Beams*, **10**(12):122801, December 2007.

[23] F. BECKER. **Beam Induced Fluorescence Monitors**. In *Proceedings of DIPAC2011*, pages 575–579, Hamburg, Germany, 2011. 8

[24] J. BOSSER, C. DIMOPOULOU, A. FESCHENKO, AND R. MACCAFERRI. **Transverse profile monitor using ion probe beams**. *Nuclear Instruments and Methods in Physics Research Section A: Accelerators, Spectrometers, Detectors and Associated Equipment*, **484**(13):1–16, May 2002. 9

BIBLIOGRAPHY

[25] M.G. BULMER. *Principles of Statistics*. Dover Publications, March 1979. 12

[26] HELGE KNUDSEN. **Ionization of atoms and molecules by antiproton impact**. *Hyperfine Interactions*, **109**(1-4):133–143, 1997. 14

[27] K PALUDAN, H BLUHME, H KNUDSEN, U MIKKELSEN, S P MLLER, E UGGERHJ, AND E MORENZONI. **Single, double and triple ionization of Ne, Ar, Kr and Xe by 30 - 1000 keV impact**. *Journal of Physics B: Atomic, Molecular and Optical Physics*, **30**(17):3951–3968, September 1997. 14

[28] F M JACOBSEN, N P FRANDSEN, H KNUDSEN, U MIKKELSEN, AND D M SCHRADER. **Single ionization of He, Ne and Ar by positron impact**. *Journal of Physics B: Atomic, Molecular and Optical Physics*, **28**(21):4691–4695, November 1995.

[29] V KARA, K PALUDAN, J MOXOM, P ASHLEY, AND G LARICCHIA. **Single and double ionization of neon, krypton and xenon by positron impact**. *Journal of Physics B: Atomic, Molecular and Optical Physics*, **30**(17):3933–3949, September 1997.

[30] R G MONTAGUE, M F A HARRISON, AND A C H SMITH. **A measurement of the cross section for ionisation of helium by electron impact using a fast crossed beam technique**. *Journal of Physics B: Atomic and Molecular Physics*, **17**(16):3295–3310, August 1984. 15

[31] FOSTER F. RIEKE AND WILLIAM PREPEJCHAL. **Ionization Cross Sections of Gaseous Atoms and Molecules for High-Energy Electrons and Positrons**. *Physical Review A*, **6**(4):1507–1519, October 1972. 14

[32] Y HASHIMOTO, T FUJISAWA, T MORIMOTO, Y FUJITA, T HONMA, S MUTO, K NODA, Y SATO, AND S YAMADA. **Oxygen gas-sheet beam profile monitor for the synchrotron and storage ring**. *Nuclear Instruments and Methods in Physics Research Section A: Accelerators, Spectrometers, Detectors and Associated Equipment*, **527**(3):289–300, July 2004. 18, 63, 219

[33] M. PUTIGNANO, K. -U. KHNEL, C. -D. SCHRTER, AND C. P. WELSCH. **A fast, low perturbation ionization beam profile monitor based on a gas-jet curtain for the ultra low energy storage ring**. *Hyperfine Interactions*, **194**(1-3):189–193, August 2009. 18

[34] H.C. MAN, J. DUAN, AND T.M. YUE. **Design and characteristic analysis of supersonic nozzles for high gas pressure laser cutting**. *Journal of Materials Processing Technology*, **63**(13):217–222, January 1997. 19

[35] A. V. ZAYTSEV, O. B. KOVALEV, A. G. MALIKOV, A. M. ORISHICH, AND V. B. SHULYAT'EV. **Laser cutting of thick steel sheets using supersonic oxygen jets**. *Quantum Electronics*, **37**(9):891–892, 2007. 19

[36] RICHARD E. SMALLEY, LENNARD WHARTON, AND DONALD H. LEVY. **Molecular optical spectroscopy with supersonic beams and jets**. *Acc. Chem. Res.*, **10**(4):139–145, 1977. 19

[37] V ROZHANSKY, I SENICHENKOV, I VESELOVA, D MOROZOV, AND R SCHNEIDER. **Penetration of supersonic gas jets into a tokamak**. *Nuclear Fusion*, **46**(2):367–382, February 2006. 19

[38] J. ULLRICH, R. MOSHAMMER, A. DORN, R. DORNER, L. PH. H. SCHMIDT, AND H. SCHMIDT-BOCKING. **Recoil-ion and electron momentum spectroscopy: reaction microscopes**. *Rep. Prog. Phys.*, **66**:1463–1545, 2003. 19, 125

[39] V. MERGEL, M. ACHLER, R. DRNER, KH. KHAYYAT, T. KAMBARA, Y. AWAYA, V. ZORAN, B. NYSTRM, L. SPIELBERGER, J. H. MCGUIRE, J. FEAGIN, J. BERAKDAR, Y. AZUMA, AND H. SCHMIDT-BCKING. **Helicity Dependence of the Photon-Induced Three-Body Coulomb Fragmentation of Helium Investigated by Cold Target Recoil Ion Momentum Spectroscopy**. *Physical Review Letters*, **80**(24):5301–5304, June 1998. 19

[40] MANISH JUGROOT, CLINTON P T GROTH, BRUCE A THOMSON, VLADIMIR BARANOV, AND BRUCE A COLLINGS. **Numerical investigation of interface region flows in mass spectrometers: neutral gas transport**. *Journal of Physics D: Applied Physics*, **37**:1289–1300, April 2004. 19, 20, 28

[41] M. PUTIGNANO AND C.P. WELSCH. **Numerical study on the generation of a planar supersonic gas-jet**. *Nuclear Instruments and Methods in Physics Research Section A: Accelerators, Spectrometers, Detectors and Associated Equipment*, **667**(0):44–52, March 2012. 20, 67, 74

[42] WEN-HSIUNG LI AND SAU-HAI LAM. *Principles of fluid mechanics*. Addison-Wesley Pub. Co., 1964. 25, 118, 179, 180

[43] GIACINTO SCOLES, D.C. LAINE, AND U. VALBUSA. *Atomic and Molecular Beam Methods: Vol 1*. Oxford University Press Inc, illustrated edition edition, October 1992. 25, 26, 27, 29, 31, 32, 33, 34, 39, 53, 189

[44] JOHN B FENN. **Collision Kinetics in Gas Dynamics**. *Applied Atomic Collision Physics, Volume 5: Special Topics*, **5**:349, 1982. 25

[45] H. MIKAMI. **Transport phenomena in free-jet expansions**. *Bulletin of the Research Laboratory for Nuclear Reactors*, **7**:151, 1982.

[46] R. CAMPARGUE. **Progress in overexpanded supersonic jets and skimmed molecular beams in free-jet zones of silence**. *J. Phys. Chem.*, **88**(20):4466–4474, 1984. 25

[47] B. MAT, I. A. GRAUR, T. ELIZAROVA, I. CHIROKOV, G. TEJEDA, J. M. FERNNDEZ, AND S. MONTERO. **Experimental and Numerical Investigation of an Axisymmetric Supersonic Jet**. *Journal of Fluid Mechanics*, **426**:177–197, 2001. 26

[48] D. MITCHELL, D. HONNERY, AND J. SORIA. **Study of Underexpanded Supersonic Jets with Optical Techniques**. In *16th Australasian Fluid Mechanics Conference (AFMC)*, pages 217–224, Gold Coast, Queensland, Australia, 2007. 26

[49] H.C.W. BEIJERINCK AND N.F. VERSTER. **Absolute intensities and perpendicular temperatures of supersonic beams of polyatomic gases**. *Physica B+C*, **111**(2-3):327–352, November 1981. 37, 187

[50] GROUP GDT. **GDT Software Group**. http://www.cfd.ru/, 2005. 38

[51] ANSYS. **ANSYS Fluent Software**. http://www.ansys.com/ Products/ Simulation + Technology/Fluid + Dynamics/ANSYS + Fluent, 2001.

[52] SIMION. **SIMION Virtual Device v.21**. http://simion.com/ virtualdevice/, 1995. 38

[53] A. V. Zibarov. **Gas Dynamics Tool Package: System for Numerical Gas Dynamic Non-Steady Process Modeling**. In *Proceedings of ASME*, **397-1**, pages 117–123, 1999. 38

[54] Hylton R. Murphy and David R. Miller. **Effects of nozzle geometry on kinetics in free-jet expansions**. *J. Phys. Chem.*, **88**(20):4474–4478, 1984. 43, 44

[55] Dan Givoli. **Non-reflecting boundary conditions**. *Journal of Computational Physics*, **94**(1):1–29, May 1991. 45

[56] I. Orlanski. **A simple boundary condition for unbounded hyperbolic flows**. *Journal of Computational Physics*, **21**(3):251–269, July 1976. 46

[57] A. Sommerfeld. *Lectures on Theoretical Physics*. Academic press, New York, 1964. 46

[58] R. Drner, J. M. Feagin, C. L. Cocke, H. Bruning, O. Jagutzki, M. Jung, E. P. Kanter, H. Khemliche, S. Kravis, V. Mergel, M. H. Prior, H. Schmidt-Bcking, L. Spielberger, J. Ullrich, M. Unversagt, and T. Vogt. **Fully Differential Cross Sections for Double Photoionization of He Measured by Recoil Ion Momentum Spectroscopy**. *Physical Review Letters*, **77**(6):1024–1027, 1996. 52

[59] Y. Hashimoto, S. Muto, T. Toyama, T. Morimoto, T. Fujisawa, T. Murakami, K. Noda, and D. Ohsawa. **Development of a Nondestructive Beam Profile Monitor using a Sheeted Nitrogen-Molecular Beam**. In *Proceedings of IPAC'10*, pages 987–989, Kyoto, Japan, 2010. 69

[60] M. Putignano and C. P. Welsch. **Numerical studies of curtain gas jet generation for beam profile monitoring applications in the ultra low energy storage ring**. pages 243–246, Santa Fe, New Mexico, US, 2010. 69, 73

[61] Hans Pauly. *Atom, Molecule, and Cluster Beams I*, **1**. Springer, 2000. 71, 95

[62] A Chambers, R Fitch, and B Halliday. *Basic Vacuum Technology, 2nd edition*. Taylor & Francis, January 1998. 92

[63] Erhard W. Rothe and R. H. Neynaber. **Measurements of Absolute Total Cross Sections for Rare-Gas Scattering**. *The Journal of Chemical Physics*, **43**(11):4177, 1965. 95

[64] ImageJ. **ImageJ**. http://rsbweb.nih.gov/ij/, 2008. 103

[65] ESPI Metals. **ESPI Metals**. http://www.espimetals.com/index.php, 1950. 104

[66] Cobham. **Opera - Software for Electromagnetic Design**. http:// www.cobham.com/ media/ 637229/ cts_vectorfields_opera_240610.pdf, 2000. 110

[67] T. Kambara, A. Igarashi, N. Watanabe, Y. Nakai, T. M. Kojima, and Y Awaya. **Recoil-ion momentum distribution of single-electron capture to the ground and excited states in 0.5-1 MeV/u B4+,5+ - He collisions**. *J. Phys. B: At. Mol. Opt. Phys.*, **30**:1251–1260, 1997. 120

[68] R. Moshammer, M. Unverzagt, W. Schmitt, J. Ullrich, and H. Schmidt-Bcking. **A 4 recoil-ion electron momentum analyzer: a high-resolution microscope for the investigation of the dynamics of atomic, molecular and nuclear reactions**. *Nuclear Instruments and Methods in Physics Research Section B: Beam Interactions with Materials and Atoms*, **108**(4):425–445, March 1996.

[69] Th Weber, Kh Khayyat, R Drner, V Mergel, O Jagutzki, L Schmidt, F Afaneh, A Gonzalez, C L Cocke, A L Landers, and H Schmidt-Bcking. **Kinematically complete investigation of momentum transfer for single ionization in fast proton-helium collisions**. *Journal of Physics B: Atomic, Molecular and Optical Physics*, **33**(17):3331–3344, September 2000. 120, 121, 122

[70] Th. Weber, Kh. Khayyat, R. Drner, V. D. Rodrguez, V. Mergel, O. Jagutzki, L. Schmidt, K. A. Mller, F. Afaneh, A. Gonzalez, and H. Schmidt-Bcking. **Abrupt Rise of the Longitudinal Recoil Ion Momentum Distribution for Ionizing Collisions**. *Physical Review Letters*, **86**(2):224–227, January 2001.

[71] H. T. Schmidt, J. Jensen, P. Reinhed, R. Schuch, K. Stchkel, H. Zettergren, H. Cederquist, L. Bagge, H. Danared, A. Kllberg, H. Schmidt-Bcking, and C. L. Cocke. **Recoil-ion momentum distributions for transfer ionization in fast proton-He collisions**. *Physical Review A*, **72**(1):012713, July 2005.

[72] A. Gensmantel, J. Ullrich, R. Drner, R. E. Olson, K. Ullmann, E. Forberich, S. Lencinas, and H. Schmidt-Bcking. **Dynamic mechanisms of He single ionization by fast proton impact**. *Physical Review A*, **45**(7):4572–4575, April 1992.

[73] Kh Khayyat, T Weber, R Drner, M Achler, V Mergel, L Spielberger, O Jagutzki, U Meyer, J Ullrich, R Moshammer, W Schmitt, H Knudsen, U Mikkelsen, P Aggerholm, E Uggerhoej, S P Moeller, V D Rodrguez, S F C O'Rourke, R E Olson, P D Fainstein, J H McGuire, and H Schmidt-Bcking. **Differential cross sections in antiproton- and proton-helium collisions**. *Journal of Physics B: Atomic, Molecular and Optical Physics*, **32**(4):L73–L79, February 1999.

[74] R. Moshammer, J. Ullrich, H. Kollmus, W. Schmitt, M. Unverzagt, H. Schmidt-Bcking, C. J. Wood, and R. E. Olson. **Complete momentum balance for single ionization of helium by fast ion impact: Experiment**. *Physical Review A*, **56**(2):1351–1363, 1997. 120

[75] A. Dorn, R. Moshammer, C. D. Schröter, T. J. M. Zouros, W. Schmitt, H. Kollmus, R. Mann, and J. Ullrich. **Double Ionization of Helium by Fast Electron Impact**. *Phys. Rev. Lett.*, **82**:2496–2499, Mar 1999. 120

[76] G. A. Karamysheva, A. I. Papash, and C. P. Welsch. **Study of slow and fast extraction for the ultralow energy storage ring (USR)**. *Physics of Particles and Nuclei Letters*, **8**(1):50–60, February 2011. 126

[77] A. V. Smirnov and C. P. Welsch. **Ion Kinetics in the Ultra-Low Energy Electrostatic Storage Ring (USR)**. pages 89–91, Alushta, Ukraine, 2011.

[78] A. I. PAPASH, A. V. SMIRNOV, M. R. F. SIGGEL-KING, AND C. P. WELSCH. **Long Term Beam Dynamics in Ultra-Low Energy Storage Rings**. San Sebastian, Spain, 2011. 126

[79] A. I. PAPASH AND C. P. WELSCH. **An update of the USR lattice: towards a true multi-user experimental facility.** In *Proccedings of PAC09*, pages 4335–4337, Vancouver, BC, Canada, 2009. 133

[80] M. PUTIGNANO, K.-U. KUEHNEL, AND C. P. WELSCH. **Design of a Nozzle-Skimmer System for a Low Perturbation Ionization Beam Profile Monitor**. In *Proceedings of DIPAC09*, pages 179–181, Basel, Switzerland, 2009. 136

[81] GLENN F. KNOLL. *Radiation Detection and Measurement 3rd Edition*. John Wiley & Sons, 3rd edition edition, January 2000. 143, 144, 146, 148

[82] S. DHAWAN AND R. MAJKA. **Development Status of Microchannel Plate Photomultipliers**. *IEEE Transactions on Nuclear Science*, **24**(1):270–275, February 1977. 143

[83] C. C LO, PIERRE LECOMTE, AND BRANKO LESKOVAR. **Performance Studies of Prototype Microchannel Plate Photomultipliers**. *IEEE Transactions on Nuclear Science*, **24**(1):302–311, February 1977. 143

[84] M. LINDROOS, S. BOUSSON, R. CALAGA, H. DANARED, G. DEVANZ, R. DUPERRIER, J. EGUIA, M. ESHRAQI, S. GAMMINO, H. HAHN, A. JANSSON, C. OYON, S. PAPE-MLLER, S. PEGGS, A. PONTON, K. RATHSMAN, R. RUBER, T. SATOGATA, AND G. TRAHERN. **The European Spallation Source**. *Nuclear Instruments and Methods in Physics Research Section B: Beam Interactions with Materials and Atoms*, **269**(24):3258–3260, December 2011. 177

[85] ALLEN E. FUHS AND JOSEPH A. SCHETZ, editors. *Handbook of Fluid Dynamics and Fluid Machinery*. Wiley-Interscience, 99 edition, April 1996. 181

[86] FELIX SHARIPOV. **Numerical Simulation of Rarefied Gas Flow Through a Thin Orifice**. *Journal of Fluid Mechanics*, **518**:35–60, 2004. 190

[87] F. SHARIPOV. **Modelling and calculations of rarefied gas flows: DSMC vs kinetic equation, Invited talk**, 2011. 190

[88] R. W MACCORMACK AND B. S BALDWIN. **A numerical method for solving the Navier-Stokes equations with application to shock-boundary layer interactions**. *AIAA, 13th Aerospace Sciences Meeting*, **-1**, January 1975. 192

[89] R. COURANT, K. O. FRIEDRICHS, AND H. LEWY. **Uber die Differenzengleichungen der Mathematischen Physik**. *Math. Ann.*, **100**:32, 1928. 194

Declaration

I herewith declare that I have produced this paper without the prohibited assistance of third parties and without making use of aids other than those specified; notions taken over directly or indirectly from other sources have been identified as such. This paper has not previously been presented in identical or similar form to any other English or foreign examination board.

The thesis work was conducted from February 2009 to July 2012 under the supervision of Prof. Dr Carsten P. Welsch at the Cockcroft Institute, Daresbury, UK, partner of the Liverpool University.

Liverpool, July 2012